The Interplay of Hydrothermal and Tectonic Processes at (Ultra)Slow-Spreading Mid-Ocean Ridges

Dissertation

with the aim of achieving a doctoral degree
at the Faculty of Mathematics, Informatics and Natural Sciences
Department of Earth System Sciences
Institute of Geophysics
at University of Hamburg

submitted by
Arne Glink

Hamburg, 2025

Department of Earth Sciences

Date of Oral Defense:	08.04.2025
Reviewers:	Prof. Dr. Matthias Hort Prof. Dr. Lars Rüpke
Members of the examination commission:	Prof. Dr. Matthias Hort Dr. Jörg Hasenclever Prof. Dr. Lars Rüpke Prof. Dr. Bernd Leitl Prof. Dr. Gerhard Schmiedl

Chair of the Subject Doctoral Committee

Earth System Sciences:	Prof. Dr. Hermann Held
Dean of Faculty MIN:	Dr.-Ing. Norbert Ritter

Abstract

Mid-ocean ridges mark the boundary between divergent tectonic plates, where only a relatively thin brittle lithosphere separates the hot, ductile mantle from the overlying ocean. This unique environment fosters complex interactions among magmatism, tectonic faulting, and hydrothermal circulation within the newly formed seafloor. At slow- and ultraslow-spreading ridges with limited melt supply from the mantle, large, long-lived detachment faults are common, often associated with diverse hydrothermal activity. These systems, which have become a focus of recent research, are the expression of intricate hydro-tectono-magmatic feedbacks. In this thesis, numerical models, ideally suited for unraveling such complex systems, are employed to address unresolved questions about detachment faulting: What governs the subsurface thermal structure, and how does it influence the initiation and persistence of detachment faults? Do these faults merely provide a geometric framework for hydrothermal circulation, or do thermal, hydraulic, and chemical feedbacks actively shape fault evolution?

Building on existing codes, this work presents a refined model to simulate lithosphere faulting, melt emplacement and hydrothermal activity around active fault zones. Two case studies highlight detachment fault dynamics: (1) the magma-poor section of the Southwest Indian Ridge at 64°E, where alternating "flip-flop" detachment faults create large axis-parallel ridges, and (2) the oceanic core complex at 13°30'N on the Mid-Atlantic Ridge, where the domed shear plane of a detachment fault hosts a series of hydrothermal ore deposits. In the first study, hydrothermal cooling within the fault zone is parametrized to investigate the interplay with magmatic sill intrusions and how thermal and rheological effects control flip-flop detachment faulting. The second study examines fluid circulation patterns and high-temperature hydrothermal venting around an active detachment to understand the location of large seafloor sulfide deposits at oceanic core complexes.

Our models contribute to a more comprehensive understanding of oceanic detachment faulting and the associated hydro-tectono-magmatic feedbacks. For instance, large-scale hydrothermal cooling of the active fault zone modifies the subsurface temperature structure and can impact the location of melt accumulation. In turn, location and intensity of footwall magmatism control detachment termination by triggering new fault formation. This feedback applies even in magma-poor settings, where magmatic heat may be insufficient to sustain high-temperature venting. In the second case study, vent field locations and estimates of sulfide accumulation rates indicate significant redirection and focusing of fluid flow below and within the detachment fault zone, controlled by fault zone permeability, heat source distribution, seafloor relief, and interaction of hydrothermal plumes. This leads to the hypothesis that the concave geometry of core complexes confines circulation within the footwall, promoting high-temperature venting around the core complex, whereas elongated fault zones of flip-flop detachments divert fluids to neighboring magmatic segments, explaining reduced hydrothermal venting.

In addition to these insights, this work provides the first open-access version of our numerical model and paves the way for future studies, for example, on the role of the 3-D fault zone structure and coupled hydro-thermo-mechanical feedbacks of fluid-rock interactions on detachment faulting.

Zusammenfassung

Mittelozeanische Rücken markieren die Grenze zwischen divergierenden tektonischen Platten und nur eine relativ dünne spröde Lithosphäre trennt dort den heißen, duktilen Erdmantel vom darüberliegenden Ozean. Diese einzigartige Umgebung ermöglicht ein vielfältiges Wechselspiel zwischen Magmatismus, tektonischen Brüchen und hydrothermaler Zirkulation innerhalb des neu entstehenden Meeresbodens. An langsam spreitzenden Rücken mit geringem Schmelzbudget treten häufig große, langlebige Abscherungen (Detachments) in Verbindung mit vielfältiger hydrothermaler Aktivität auf. Diese komplexen hydro-tektono-magmatischen Systeme sind zunehmend in den Fokus der Forschung gerückt sind. Mit Hilfe von Computermodellen werden in dieser Arbeit folgende Fragen thematisiert: Was bestimmt die thermische Struktur des Untergrundes und wie beeinflusst sie die Entstehung und Dauer von Detachments? Dienen Störungszonen lediglich als geometrischer Rahmen für hydrothermale Zirkulation, oder prägen thermische, hydraulische und chemische Rückkopplungen aktiv deren Entwicklung?

Aufbauend auf bestehenden Codes wird in dieser Arbeit ein verfeinertes Modell vorgestellt, um Bruchprozesse in der Lithosphäre, magmatische Schmelzen und hydrothermale Aktivität zu simulieren. Zwei Fallstudien beleuchten die Dynamik von Detachments: (1) der magma-arme Abschnitt des Südwestindischen Rückens bei 64°E, wo "Flip-Flop" Detachments wechselnder Orientierung gewaltige Kämme senkrecht zur Spreizungsrichtung bilden, und (2) der ozeanische Kernkomplex bei 13°30'N am Mittelatlantischen Rücken, wo eine Reihe hydrothermaler Erzablagerungen entlang der gewölbte Scherfläche eines Detachments identifiziert wurden. In der ersten Studie wird der hydrothermale Kühleffekt innerhalb der Störungszone parametrisiert, um das Zusammenspiel mit magmatischen Intrusionen und die sich daraus ergebenden thermischen sowie rheologischen Einflüsse auf Bruchprozesse zu untersuchen. Die zweite Studie analysiert Strömunsbahnen von Porenwasser um ein aktives Detachment, um die Fundorte großer Sulfidlagerstätten auf dem Meeresboden zu erklären.

Unsere Modelle resultieren in einem umfassenderen Verständnis der Dynamiken von ozeanischen Detachments. Hydrothermale Kühlung der aktiven Störungszone modifiziert die thermische Struktur des Untergrunds und beeinflusst so die Position von Schmelzansammlungen. Umgekehrt kontrollieren Position und Intensität des Magmatismus die Entstehung neuer Brüche und damit das Ende eines Detachments, selbst in magma-armen Umgebungen, wo die magmatische Wärme nicht für hochtemperierte hydrothermale Aktivität ausreicht. Die zweite Fallstudie zeigt anhand der Lage hydrothermaler Schlotfelder und Abschätzungen von Sulfidablagerungssraten, dass eine signifikante Umlenkung und Fokussierung des Wasserflusses unter- und innerhalb der Störungszone stattfindet. Kontrolliert wird dies von deren Permeabilität, der Verteilung von Wärmequellen, der Meeresbodentopographie sowie Interaktionen zwischen hydrothermalen Strömungen. Dies führt zu der Annahme, dass Detachments mit gewölbter Geometrie wie bei Kernkomplexen die hydrothermale Zirkulation darunter abschirmen und fokussieren, während die länglichen Störungszonen von Flip-Flop Detachments das Ableiten der Strömung hin zu benachbarten magmatischen Regionen erlauben.

Neben diesen Erkenntnissen liefert diese Arbeit die erste frei zugängliche Version unseres numerischen Modells und diskutiert mögliche zukünftige Forschungsfragen, beispielsweise zur Rolle der 3-D Struktur von Störungszonen auf Strömungsmuster oder zu Rückkopplungen durch Fluid-Gestein-Interaktionen in Störungszonen.

Acknowledgements

This thesis has been made possible through the support, mentorship, and encouragement of many inspiring individuals, for which I am deeply grateful. I feel incredibly fortunate to have worked with, learned from, and be surrounded by such wonderful people.

First and foremost, I would like to express my heartfelt gratitude to my supervisors: **Jörg Hasenclever**, **Matthias Hort**, and **Lars Rüpke**.

My collaboration with **Jörg Hasenclever** began five years ago when he agreed to supervise my Master's thesis and work on a project proposal with me. Jörg, your guidance has profoundly shaped my understanding and fascination for numerical modeling. You generously entrusted me with your codes, encouraging both creativity and a cautious awareness of their limitations. At all times, you were willing to proofread, to provide feedback, and to help with questions and problems, no matter how big or small. Without your support, this project would not have been possible. I have deeply enjoyed our professional discussions on model details or layout and color schemes of figures just as much as having a coffee over listening to your plans for the next incredible bike tour.

Matthias Hort, your influence on my geophysical career began almost a decade ago in your lecture on fluid dynamics, where you sparked my fascination with using differential equations to describe physical systems. Your genuine curiosity, not only for seemingly every scientific topics, but also for the people you work with, is inspiring. The commitment you show to pass this curiosity to your students, through opportunities like the excursions to Stromboli and Japan, will always stay in my mind. Your frankness and integrity especially in navigating an academic system that so often promotes the opposite, helped me focus on the fascination of science during challenging times. Your wider perspective and thoughtful questions consistently encouraged me to re-examine my assumptions and approaches.

I would like to thank **Lars Rüpke** for believing in our project from our first brainstorming with Jörg. Your broad expertise and network provided invaluable perspectives. Your catching positivity and curiosity made every train journey between Hamburg and Kiel worthwhile.

I would also like to thank the **Volcanology Working Group** in Hamburg for their collegiality and support since my Bachelor's thesis. Our weekly updates and discussions – whether scientific or not – were a great reason to return to the office (at least once a week) as soon as the COVID-19 situation allowed.

Similarly, the **Seafloor Modeling Working Group** at GEOMAR has always been incredibly welcoming and provided me with valuable insights into interdisciplinary applications of our models. My particular thanks go to **Sibiao Liu** for engaging discussions about thermo-mechanical models and for supporting the implementation of diking.

Numerous colleagues have demonstrated interest in my work and offered valuable discussions and feedback. These open-minded interactions provided fresh ideas and inspiration. Among many others, I would like to thank **Sven Petersen**, **Jean-Arthur Olive**, **Antoine Demont**, **Manon Bickert**, **Javier Escartín**, and **Jason Phipps Morgan** for their perspectives and insights. Furthermore, I would like to thank **Rémi Coltat** and four anonymous

reviewers of our two manuscripts for their helpful comments.

In addition, I would like to thank **Bernd Leitl** and **Gerhard Schmiedl** for serving as members of my examination committee, as well as **Franziska Baatz** for her careful proofreading of the manuscript and her constructive feedback.

Mirco Freye, for baking my MacBook when there seemed to be no hope left, you will forever be my hero.

During the most intense and difficult period of my life, my friends and family provided unwavering love and support, helping me to broaden my perspective and to overcome the challenges this project posed to my expectations of myself. I am deeply grateful to you all. Thank you so much, **Merle**, for not ever getting tired of supporting me and for being there in every way! You and **Appa** have been the greatest possible sources of strength.

Funding

This research was funded by the German Science Foundation (DFG) through Grants HO 1411/30-1 and RU 1469/4-1.

The Open Access publication of our first study was supported by the Open Access Publication Fund of the University of Hamburg and Projekt DEAL.

I would also like to thank the organizing team of the 2024 Ada Lovelace Workshop on Modelling Mantle and Lithosphere Dynamics from the Université de Montpellier, especially Fanny Garel and Catherine Thoraval, for hosting the workshop. The recognition with the Best Student Poster Award enabled the Open Access publication of our second study.

Open Research Statement

All simulation results shown in this thesis can be reproduced using our open access MATLAB code `M2TRI_vep` (Hasenclever & Glink, 2025). Snapshots and movies were generated using Tecplot 360 EX, version 2021 R1 (tecplot.com). Simulation movies are found online at https://doi.org/10.25592/uhhfdm.16721.

Folowing figures use color maps from the *Scientific Colour Maps* package by Crameri (2021): *vik* in Figs. 1.1, 4.12 a, 4.13 c, 6.1; *batlowW* for bathymetric maps in Figs. 2.2 and 5.1; *roma* in venting temperature plots in Chapters 5 and 7.

Drafting this thesis involved the use of the DeepL translator (deepl.com) and ChatGPT (chatgpt.com) as writing aids to improve structure and expression. All information originates from my own research or referenced literature, and all outputs of the two tools were carefully reviewed to ensure accuracy and reliability.

Preface on the Value of Numerical Modeling

Starting to work with numerical models feels like stepping into a digital workshop, where you can conduct virtual experiments using an array of tools to deconstruct Earth into its components and reassemble it, adding your own signature along the way. These models offer seemingly unlimited possibilities, allowing you to experiment with different methods, processes, and, of course, visualizations. It does not take long before you find yourself diving deeper into decades of literature, adding layer by layer of complexity to your model.

More than once, after spending days or even weeks refining calculations on a specific process, I found myself questioning the actual value it added to the model. In some cases, I concluded that while the process was fascinating, incorporating it into the model was ultimately useless. However, the term "useless" can carry two distinctly different connotations. First, the process might have no significant impact on the study's outcomes — something that can often be anticipated with experience and preliminary assessments, allowing us to avoid unnecessary work. In such cases, though irrelevant, incorporating the process does not harm the model, aside from increasing computational time. The second meaning of "useless" is more problematic. Here, the process significantly affects the model results, but its influences on a deeper level remain unclear. Incorporating such a process without fully understanding its implications makes the outcome unpredictable and ambiguous—rendering the addition not only useless but potentially harmful to the model's integrity.

"I often worry that simulations may end up just as complicated as the Earth itself."
Jean-Arthur Olive

Since it is simply impossible to explore every interaction between processes from the atomic scale to the global in a single model, we must make reasonable assumptions, simplify certain aspects and disregard others. Because if we do not and let model complexity grow out of control — if we understand our model just as much or little as we understand Earth — which use does it have in the end? This, in my experience, is where most problems with modeling studies originate.

It is easy, not only for students, to become mesmerized by the visual appeal of a detailed 3-D model, crammed with processes, before even formulating a clear, relevant question for the model to address. I cannot absolve myself of this, but I like to think that I have learned some valuable and important lessons over the past four years.

"All models are wrong, but some are useful."
George E. P. Box

The true challenge of numerical modeling, from my perspective, is not about finding the holy grail, a model that replicates Earth in all its complexity. Instead, for every new question that arises, we must identify the model that is "wrong" in just the right way – simple enough to be useful, yet detailed enough to offer meaningful insights. Finding this balance is a challenging process, but when achieved, it can lead to real understanding of the processes involved.

In this thesis, I want to share some models that I found particularly useful, including descriptive and hopefully visually engaging representations. Aside the insights from their practical applications, I aim to convey a bit of the general fascination and potential that numerical modeling holds.

Contents

Chapter 1

Introduction

The Earth's outermost layer is made up of large, rigid plates known as tectonic plates, which are constantly moving relative to each other. Where they collide, either one plate is thrust beneath the other, creating a subduction zone, or the plates may fold upward to form a mountain range. At divergent plate boundaries, however, new oceanic lithosphere is created at mid-ocean ridges (MORs) during the opening of an oceanic basin. The oceans covering around two thirds of the Earth hide the global 65.000 km long system of MORs constituted by 10s to 100s of km long, mainly spreading parallel ridge segments separated by transform faults or non-transform offsets (Fig. 1.1; Searle, 2013). A variety of complex magmatic, tectonic and hydrothermal processes shape the seafloor generated during oceanic spreading, which leads to its complete renewal over a time scale of ∼200 million years.

Divergence of the plates drives upwelling and decompression melting of the underlying hot mantle at the spreading axis, where it feeds 80 % of the Earth's volcanism (Sinha & Evans, 2004). The rising material eventually fills the gap between the diverging plates through either accretion of basaltic crust or faulting of crustal and mantle rocks. As a consequence of mantle upwelling, the brittle lithosphere at mid-ocean ridges is only a few kilometers thick (Escartín & Olive, 2022, and references therein). It thus represents a thin thermal boundary layer that transfers heat not only through conduction, but magmatic heat also drives hydrothermal convection of seawater through the young and porous oceanic lithosphere. This process was first conformed by the observation of the spectacular black smoker vent fields (Corliss et al., 1979; Spiess et al., 1980), where metals dissolved in the venting hot fluids nourish unique deep-sea ecosystems (e.g., Preiner et al., 2020; Shea et al., 2008) and form ore deposits at the seafloor (Hannington et al., 2011). In total, MORs process approximately 18 km^3 of magma per year (Sinha & Evans, 2004), circulate the ocean water volume in much less than a million years (Mottl, 2003) and are responsible for ∼1/4 of the global heat loss of the Earth. Thus, mid-ocean ridges not only shape about 60 % of the Earth's surface, but also act as a major thermal and chemical valve between the geosphere and hydrosphere, significantly contributing to global mass and energy cycles.

As the initially hot and thin lithosphere moves away from the spreading axis, it cools and thickens, causing MORs to buoyantly lift 2-3 km above the surrounding abyssal plains with 5-6 km depth. This eponymous large-scale characteristic has first led to the discovery of MORs through line-soundings in the mid-19th century (Maury, 1860). Since then, mapping techniques have advanced to shipboard multibeam systems capable of measuring swaths approximately five times wider than the local water depth, which has significantly accerlerated seafloor mapping efforts. However, still less than 50 % of the mid-ocean ridge system has been mapped at a resolution of 50-100 m (Escartín & Olive, 2022, and references therein).

Other than at sub-aerial environments, integrated high-resolution data sets that involve

geological sampling as well as ground penetrating methods such as seismics, gravimetry and electro-magnetic methods are limited to relatively few submarine study areas. Furthermore, most measurements represent snapshots in time and repeated surveys or real-time monitoring of hydro-tectono-magmatic activity at MORs are mostly still in their early stages. Focus sites of recent research have been, for example, the East Pacific Rise around 9°N (Fornari et al., 2012), the Juan de Fuca Ride, monitored by the *Ocean Observatories Initiative Regional Cabled Array* and *Ocean Networks Canada*, and the Lucky Strike segment of the Mid-Atlantic Ridge (MAR), monitored by the *EMSO-Azores* seafloor observatory. However, continuous data coverage is more limited at (ultra)slow-spreading ridges of reduced magmatic activity, the focus of this work, while they are characterized by a greater diversity of geophysical processes.

The limitations associated with the sparse direct observations of active processes have made numerical modeling an indispensable tool for reconstructing dynamics at MORs over the past 30 years. Numerous studies have investigated the thermal regime at different spreading rates (e.g., Chen et al., 2022; Fan et al., 2021; Phipps Morgan & Chen, 1993; Theissen-Krah et al., 2011), crustal accretion (e.g., Mezri et al., 2024; Olive et al., 2010; Phipps Morgan &

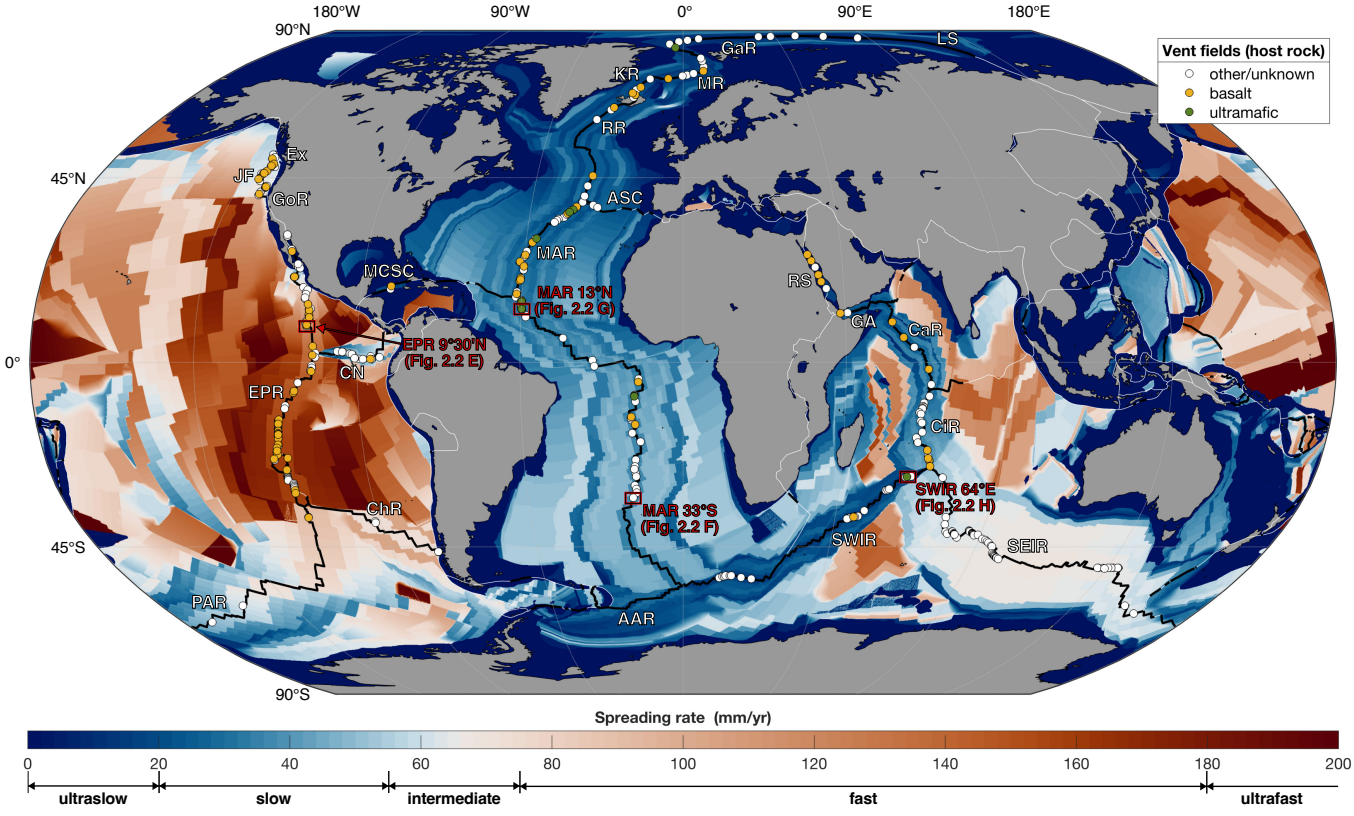

Figure 1.1. Full spreading rate of the oceanic lithosphere (Seton et al., 2020). Mid-ocean ridges and transform faults shown as black lines, white lines represent other plate boundaries (Bird, 2003). Circles represent hydrothermal vents colored by host rock type (see legend; Beaulieu & Szafranski, 2020). Red boxes mark sites shown in Fig. 2.2 F – I. AAR: American-Antarctic Ridge; ASC: Azores Spreading Centre; CaR: Carlsberg Ridge; ChR: Chile Rise; CIR: Central Indian Ridge; CN: Cocos-Nazca Spreading Centre; EPR: East Pacific Rise; Ex: Explorer Ridge; GA: Gulf of Aden; GoR: Gorda Ridge; GaR: Gakkel Ridge; JF: Juan de Fuca Ridge; KR: Kolbeinsey Ridge; LS: Laptev Sea Rift; MAR: Mid-Atlantic Ridge; MCSC: Mid Cayman Spreading Centre; MR: Mohns Ridge; PAR: Pacific-Antarctic Rise; RR: Reykjanes Ridge; RS: Red Sea; SEIR: Southeast Indian Ridge; SWIR: Southwest Indian Ridge.

Chen, 1993; Theissen-Krah et al., 2011) and faulting styles (e.g., Behn & Ito, 2008; Bickert et al., 2020; Buck et al., 2005; Howell et al., 2019; Tucholke et al., 2008), and the resulting seafloor relief (e.g., Ito & Behn, 2008; Z. Liu & Buck, 2020; Phipps Morgan & Chen, 1993). Further research has concentrated on hydrothermal convection patterns (e.g., Andersen et al., 2015; Coumou et al., 2009; Fontaine et al., 2011; Guo et al., 2023; Hasenclever et al., 2014). However, few studies have explicitly examined the dynamic feedbacks between magmatic, tectonic, and hydrothermal processes at MORs (Theissen-Krah et al., 2011, 2016), and none have done so for tectonically dominated segments of slow- and ultraslow-spreading ridges. In these settings, the complex lithosphere structure reports a diverse interplay between large-scale tectonic faults, scattered magmatic heat sources and hydrothermal circulation patterns (Fig. 1.2). With the rapid increase in observational data and computational power, we are now beginning to unravel the complex signatures of hydro-tectono-magmatic interactions in young seafloor – though much work remains to be done.

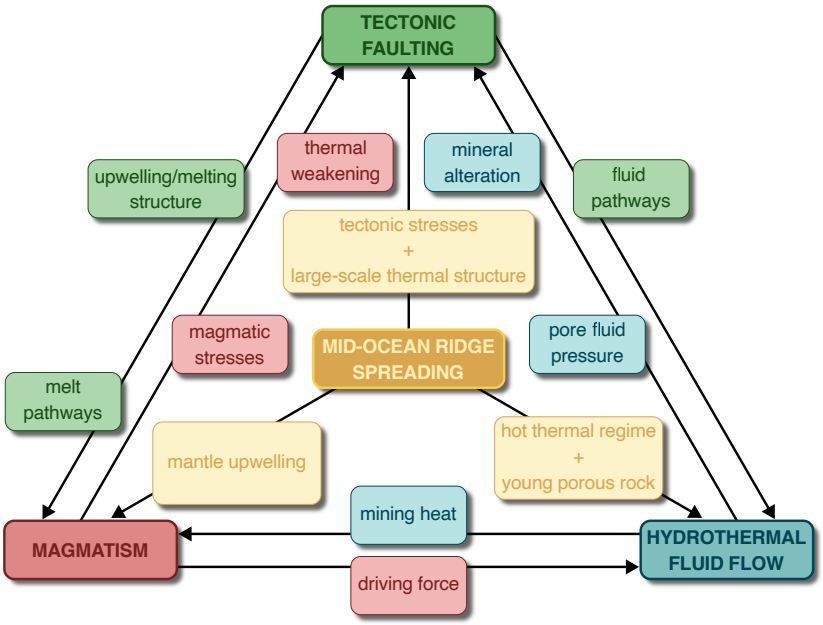

Figure 1.2. Flowchart depicting the interplay between tectonic, magmatic and hydrothermal processes during oceanic spreading.

The research presented in this thesis focuses on the interplay between tectonic detachment faulting and hydrothermal activity at slow- and ultraslow-spreading ridges. Melt budget generally decreases with spreading rate, requiring shear along lithosphere-scale tectonic faults to account for an increasing portion of extension. If the magmatically accommodated fraction of extension drops to around 50 % and below, duration and heave of individual normal faults increase significantly, transforming them into long-lived detachment faults (e.g., Behn & Ito, 2008; Tucholke et al., 2008). At the seafloor, detachment faults manifest in two main forms: As domed and elevated massifs of lower crust and mantle material exhumed along the shear plane, called oceanic core complexes (OCCs) (e.g., Escartín, Smith, et al., 2008; MacLeod et al., 2009), or as a series of large, axis-parallel ridges displaying smooth seafloor composed almost exclusively of serpentinized mantle rocks (Sauter et al., 2013).

Hydrothermal activity around detachment faults is notably diverse. It is characterized

by variations in venting locations relative to fault structures and the ridge axis, venting temperatures ranging from less than 100 °C to over 400 °C, and host rock compositions between basaltic and ultramafic (Früh-Green et al., 2022). This diversity reflects more scattered heat sources and a complex subsurface permeability structure at tectonically-dominated ridge sections compared to more uniform magmatically-dominated fast-spreading ridges.

Interactions between the magmatic, tectonic, and hydrothermal domains raise a series of "chicken-or-egg" questions (Fig. 1.2). For instance: Does the faulted subsurface structure control melt migration, or does melting initiate faulting? To what extent does the hydrothermally controlled temperature structure of the lithosphere affect the emplacement of magmatic intrusions? Does tectonic faulting merely provide a geometric framework for hydrothermal circulation or do thermal, hydraulic and chemical effects significantly influence fault development?

Together with my co-authors, I addressed these questions in two separate studies featured in this dissertation. We coupled a thermo-mechanical visco-elasto-plastic computational model to different implementations of rheological, magmatic, and hydrothermal processes to simulate the dynamics of detachment faulting. The first study (Chapter 4) investigates how active detachment faulting influences the magnitude and spatial distribution of hydrothermal cooling and magmatic intrusions at magma-poor, ultraslow-spreading mid-ocean ridges, and how the resulting thermal structure in turn affects the faulting style. The second study (Chapter 5) focuses on the tectono-magmatic controls governing hydrothermal pathways around oceanic core complexes and their role in determining the size and spatial distribution of sulfide deposits at the seafloor.

Chapter 2

Characterization of Mid-Ocean Ridges

This section reviews the characteristics of mid-ocean ridge processes and the resulting (sub)seafloor structures, drawing on a wide range of profound state-of-the-art literature (e.g., Escartín & Olive, 2022; Früh-Green et al., 2022; Olive, 2023; Searle, 2013). While providing a concise general overview, the primary focus is on detachment-dominated sections of slow- to ultraslow-spreading ridges, which are the subject of the research presented in subsequent chapters. To describe the lithospheric structure and hydrothermal activity in these settings, the following sections will first summarize key concepts of these two aspects, followed by an exploration of different spreading types and their corresponding hydrothermal activity.

Notably, parts of this section are based on the introduction of my master's thesis (Glink, 2020), which covered similar topics. For a broader overview on spreading-related processes including hydrothermal activity, I refer the reader to the aforementioned literature.

2.1 Controls on Lithosphere Structure

The Earth's structure is traditionally described as a series of layers based on composition – core, mantle, crust, hydrosphere, and atmosphere – and thermo-mechanical behavior, such as the distinctions between inner and outer core or between lithosphere and asthenosphere. At mid-ocean ridges, however, this straightforward stratification breaks down due to interactions between different domains. To avoid terminological ambiguity, the key layers relevant to this discussion are briefly defined below.

The **oceanic crust** constitutes the **magmatically formed outermost layer**. Its accretion involves the emplacement and cooling of partial melts extracted from the mantle, which accumulate in magma bodies (e.g., magma chambers or intrusions), form dikes, and erupt to the seafloor. The crust is primarily composed of basalt and gabbro, contrasting with the denser peridotite of the underlying mantle. The crust-mantle boundary, known as the Mohorovičić discontinuity (or Moho), is typically marked by an increase in seismic P-wave velocity to over $7.5\,\mathrm{km\,s^{-1}}$ (Fig. 2.1; Dunn, 2015). While some studies define a seismic crustal thickness for amagmatic ridges with virtually absent magmatic crust (e.g., Momoh et al., 2020), this discussion exclusively refers to magmatic crust when using the term "crust".

The **lithosphere** represents the **outermost mechanical layer** constituting the rigid plates that move over the ductile mantle. At 1200 °C to 1300 °C, ductile creep becomes efficient enough to decouple these plates from the underlying asthenosphere, defining the lithosphere-asthenosphere boundary. The elastic-brittle upper part of the lithosphere is of particular interest for studies of tectonic faulting, and its thickness can be constrained by the maximum depth of (micro-)seismicity (Fig. 2.1; Grevemeyer et al., 2019). The transition from brittle to ductile behavior, which is from now on referred to as the base of the (brittle)

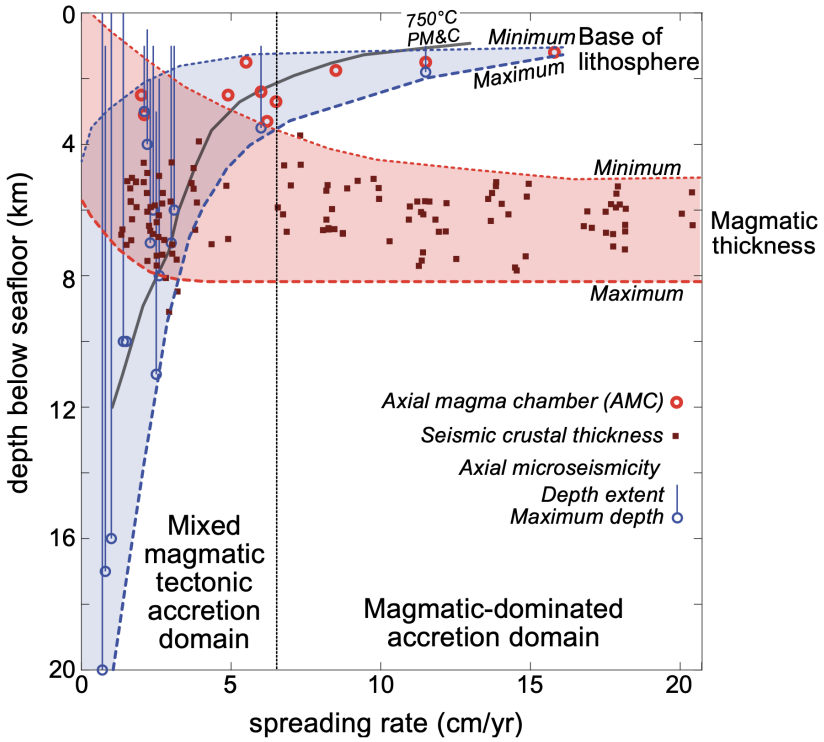

Figure 2.1. Lithosphere and crustal thickness at the ridge axis as a function of full spreading rate, inferred from the maximum depth of microseismicity and seismic velocity, respectively. Further evidence for the base of the brittle lithosphere comes from the depth of the axial magma chamber, if existing. The shaded areas mark plausible ranges for the two parameters. Lithosphere thickness and variability significantly increase with decreasing spreading rate. Axial magma supply, represented by the magmatic thickness, is surprisingly constant with a thickness between 5 - 8 km at fast spreading ridges. At slow- and ultraslow-spreading ridges, melt supply decreases while its variability increases. Reprint with permission from Escartín and Olive (2022), see the original publication for data references.

lithosphere, typically occurs at temperatures of 600 °C to 800 °C, depending on the rock type (e.g., Hirth & Kohlstedt, 2003; Mackwell et al., 1998), and serves as a critical constraint for numerical models. In colder MOR regimes, the brittle lithosphere encompasses both the crust and the upper mantle. In contrast, in hotter, magmatically active settings, only the cold upper part of the crust retains elastic-brittle behavior and forms fractures and faults.

The following sections will examine different styles of oceanic spreading, with a focus on faulting mechanisms and hydrothermal activity. The appearance of a ridge section is largely determined by its mechanical properties and melt budget, which are governed by two key factors: temperature and composition. These factors manifest as the thickness of the axial brittle lithosphere and the crustal thickness, which both show a correlation with spreading rate, even though they a not strictly dependent (Fig. 2.1).

Lithosphere thickness mainly reflects the balance between specific and latent heat supplied from the mantle, and hydrothermal and conductive heat loss to the ocean (e.g., Phipps Morgan et al., 1987; Theissen-Krah et al., 2011). As spreading rate decreases, the upwelling rate of mantle material below the ridge axis slows, reducing heat input and melt generation. This explains the general trend of increasing lithosphere thickness at slower spreading rates.

The crustal thickness in contrast is relatively stable over a wide range of spreading rates. However, a thicker lithosphere can impede the upward migration of melt, preventing it from forming dikes or erupting at the seafloor. Once the lithosphere exceeds the thickness of the magmatic crust that would normally form under continuous magma supply (vertical dashed line in Fig. 2.1), melt is trapped at varying depths and temperatures, creating gabbroic intrusions (see discussion by Chen et al., 2022). Another portion of the generated melt is focused along-axis towards thinner lithosphere generally found at segment centers (Cannat et al., 2003; Kuo & Forsyth, 1988), which can further reduce heat budget and increase lithosphere thickness at spreading rates below this tipping point.

The interplay between lithosphere thickness, melt generation and migration increases the variability of crustal thickness and emphasizes the growing importance of tectonic accretion processes at slower spreading rates. The most common way to classify spreading types is the magmatically accommodated fraction of extension, called the M-factor (Buck et al., 2005). M can be quantified through fault heave measurements at the seafloor (Escartín et al., 1999; C. Liu et al., 2020), while in numerical models and geometric analyses it is often interpreted as the volume of melt added to an on-axis lithospheric dike region relative to the volume opened by spreading (e.g., Behn & Ito, 2008; Howell et al., 2019; Ito & Behn, 2008; Olive et al., 2010; Reston, 2018; Tucholke et al., 2008). Despite some remaining ambiguity in this simple approach (see discussions by Cannat, Sauter, et al., 2019, and Olive & Dublanchet, 2020), it serves well to classify the first order characteristics of spreading and will be used in the following sections.

2.2 Hydrothermal Circulation

The brittle lithosphere formed at MORs is notably porous (e.g., Pruis & Johnson, 2002), allowing seawater to percolate through the seafloor into the crust. While the cold seawater gravitationally sinks towards the brittle-ductile transition, it heats through contact with the surrounding rock. At some point, the fluid has heated enough to initiate buoyant upflow, or in other words, thermal expansion of the fluid causes a pressure gradient driving the fluids upwards. Fluid circulation is strongly controlled by the subsurface permeability structure and limited above the depth, where the rock turns ductile and pores close.

In the simplest case of magmatically active ridge segments, hydrothermal fluid flow is driven by the axial melt region, and upflow and venting are focused on-axis (Hasenclever et al., 2014; Lowell et al., 2013). Observed high-temperature vent fields, which can exceed 400 °C, represent the surface expression of maximized energy transport through narrow, focused upflow zones surrounded by adjacent warm downflow regions (Coumou et al., 2009). Large-scale off-axis recharge flow further sustains axial venting (Hasenclever et al., 2014). Note that while most known submarine hydrothermal vents are venting at high temperatures close to the ridge axis (Baker et al., 2016; Beaulieu & Szafranski, 2020), low-temperature diffuse venting along the ridge flanks presumably constitutes the major portion of mass and energy fluxes by hydrothermal fluids (Elderfield & Schultz, 1996; Mottl, 2003). However, this is not in the focus of this work.

Along the whole fluid path though the crust, reactions between seawater and rock take

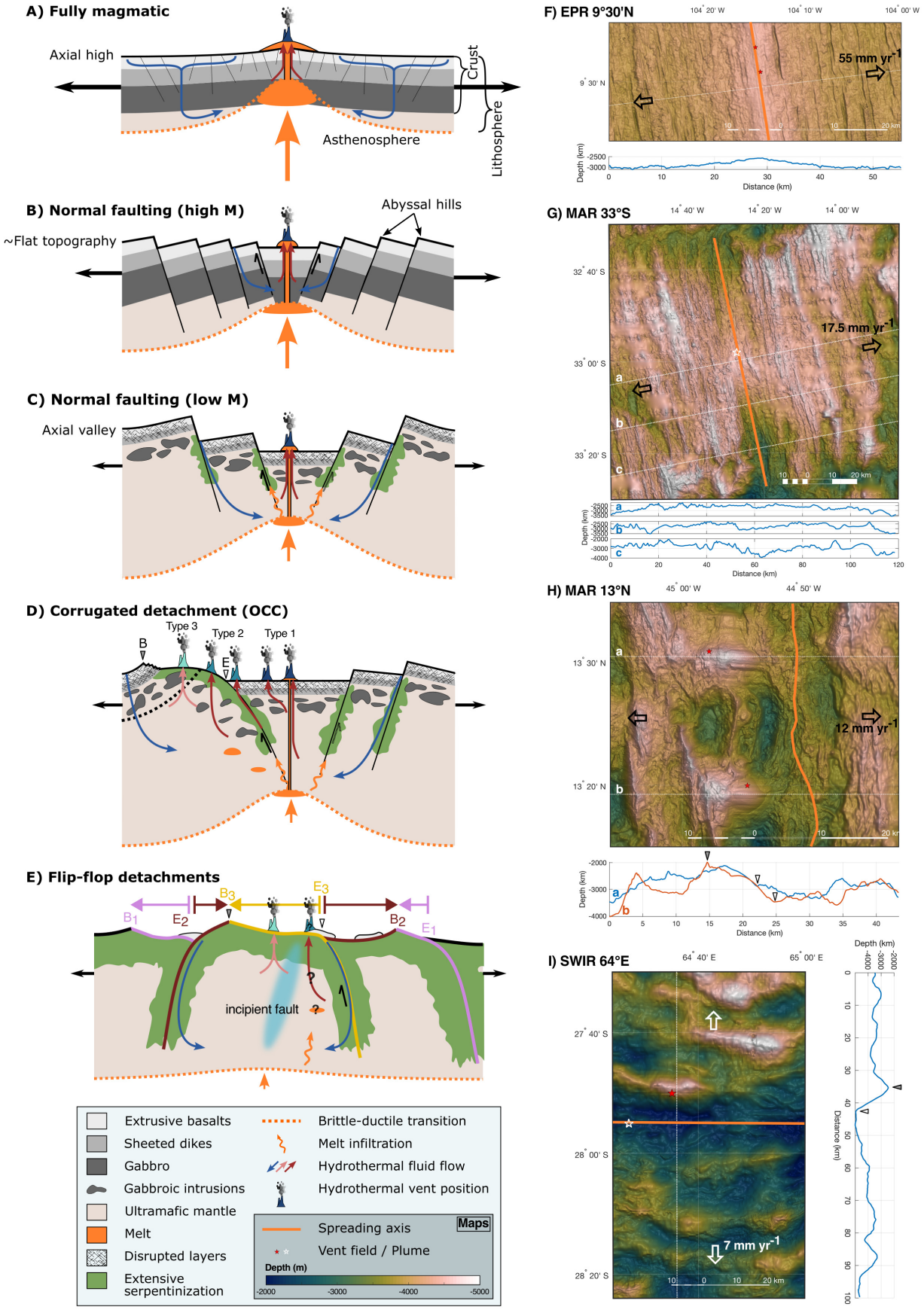

Figure 2.2. Tectono-magmatic spreading modes, illustrated by sketches and examples. Detailed caption on the bottom of the next page.

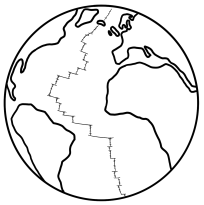

place. Controlled by the different temperature-pressure conditions and host rock type, these reactions modify both fluid and rock chemistry (Früh-Green et al., 2022, and references therein). Upon mixing with cold seawater in the porous uppermost layer and the water column above the vent field, dissolved metals such as Ca, Cu, Fe, Mn, and more precipitate as black or white "smoke" and form edifices and ore deposits at the seafloor. Apart from their direct value for the microbial fauna found around these vents (e.g., Preiner et al., 2020; Shea et al., 2008) and potential economical value (Bang & Trellevik, 2022; Hannington et al., 2011), fluid composition can hint at subsurface processes controlling fluid circulation, which is a valuable tool at more complex settings at slow- and ultraslow MORs discussed later.

2.3 Uniform Lithosphere at Fast-Spreading Ridges

At fast-spreading ridges like the East-Pacific Rise (Fig. 2.2 A + F), extension at the ridge axis is fully accommodated by magmatism (M=1) and the melt budget is large enough to sustain a continuous melt lens at 1 km to 3 km depth that accumulates on top of a mush zone (Carbotte et al., 2021; Marjanović et al., 2014). Cooling of this mush region together with episodic diking events and extrusive lava flows is responsible for the characteristic layered "Penrose" model (Penrose, 1972) also seen in ophiolites (Gass, 1968): Topped by a sedimentary layer, extrusive pillow basalts overlie a diabase sheeted dike complex. The lower crust consists of intrusive gabbroic layers, separated from the ultramafic upper mantle. The resulting crust has a robust mean global thickness of ∼7 km (White et al., 1992), which is significantly thicker than the lithosphere at fast-spreading ridges (Fig. 2.1). Buoyancy associated with the abundant magmatism causes an axial topographic high and volcanism repeatedly overprints the axial seafloor. The resulting lithosphere and seafloor is relatively uniform and along-axis variability is limited to transform faults that account for offsets in the ridge axes. Transform faults cut off the continuous melt supply, leading to less magmatic segment ends. Only minor in- and outward facing faults are observed in the crust at most parts of fast MORs and can be attributed to the buoyant upward bending of the crust (Escartín et al., 2007; Shah & Buck, 2003).

Hydrothermal activity at magmatic ridge segments is characterized by high-temperature, on-axis venting and relatively regular plume spacing (Tivey & Johnson, 2002). Frequent outbursts of magmatic activity lead to phase separations of seawater into vapor and brine, modulating observed vent fluid salinity following volcanic eruptions (e.g., Vehling et al., 2022)

Figure 2.2: A: Sketch of fully magmatic spreading corresponds to the exemplary bathymetric map and profiles from the East Pacific Rise in **F**. **B + C:** Sketches of more and less magmatic normal faulting, respectively, illustrate the segment-scale variability at the Mid-Atlantic Ridge at 33°S shown in **G**. **D:** Sketch of a corrugated detachment fault forming an oceanic core complex. E - Emergence, B - Breakaway. Examples are depicted in **H**, showing the OCCs at the Mid-Atlantic Ridge at 13°20'N and 13°30'N. **E:** Flip flop detachment faulting as observed at the amagmatic corridors at the Southwest Indian Ridge between 62°E and 65°E, shown in **I**. Seafloor in **E** is colored corresponding to the originally exhuming fault zone, arrows indicate increasing seafloor age. This illustrates the multistage formation of the seafloor and the complex seafloor age patterns resulting from flip-flop detachment faulting. Seafloor profiles have a vertical exaggeration of 4:1. Sketches are modified from Glink (2020), bathymetric data from Ryan et al. (2009), vent field locations from Beaulieu and Szafranski (2020) and Lecoeuvre et al. (2021). Ridge axis position in G from Simão et al. (2020).

2.4 Normal Faulting

Melt budget generally decreases with spreading rate. At intermediate-spreading ridges, such as the Southeast Indian Ridge or the Chile Ridge, and at magmatically active slow-spreading ridges like the Mid-Atlantic Ridge at 33°S (Fig. 2.2 B + G), not all extension can be accommodated by the accretion of magmatic crust (M<1). As a result, extensional tectonic stresses build up in the lithosphere, leading to the coalescence of small fissures and fractures. This process gives rise to fewer but larger high-angle normal faults dipping at 45° to 65° (Huang & Solomon, 1988; MacLeod et al., 2009), which dissect and offset the lithosphere, accommodating the portion of extension not supported by magmatism. These inward-dipping faults initiate at the ridge axis and migrate off-axis into cooler and thicker lithosphere. When the lithosphere becomes too thick and strong for efficient fault slip, a new fault forms at the ridge axis leading to sequences of normal faults of alternating polarity (Buck et al., 2005; Shaw & Lin, 1993).

Fault slip is influenced by factors such as fault cohesion, the degree of fault rotation, and lithosphere thickness. Ultimately, fault duration is controlled by the rate at which the fault encounters stronger lithosphere as it migrates off-axis (Olive, 2023, and references therein). Slower spreading rates as well as lower M-values lead to more gentle thermal gradients and slower fault migration, which increases fault spacing and fault displacement. The mafic crust formed by this tectono-magmatic interaction becomes less continuous with decreasing melt budget. Only a thin layer of volcanics extruded through fault-related fissures overlie gabbroic intrusions embedded in peridotite (Fig. 2.2 C; Cannat et al., 1995).

A further characteristic of increasingly tectonic intermediate- and slow-spreading ridges is that the thicker and stronger lithosphere tends to neck under tension, leading to a gradual lowering of the axial topography. While normal faulting at more magmatic, or higher-M ridges results in a flat topography on average (Fig. 2.2 G, profiles 1 + 2), less magmatic, lower-M ridges can display a pronounced axial valley bound by normal faults (Fig. 2.2 G, profile 3; Ito & Behn, 2008; Tapponnier & Francheteau, 1978). Successive normal faults confine solid blocks that are uplifted and tilted away from the spreading axis. That way, axis-parallel ridges, called abyssal hills, form. They comprise 30 % of the ocean floor and thus represent the Earth's most abundant land form (Macdonald et al., 1996).

The style of **hydrothermal activity** does not change significantly as long as magmatism is still very much focused below the spreading axis, which is the case for normal fault dominated ridge sections. However, circulation depth increases with lithosphere thickness. Reduced heat input and increased size of convection cells reflect in wider spacing of discharge sites (Baker et al., 2016).

2.5 Detachment Faulting

Slow- and ultraslow-spreading ridges display far greater variability in M and thus in faulting styles than intermediate-spreading ridges. Here, the influence of ridge segmentation increases as mantle upwelling shows a more 3-D, plume-like behavior (Lin & Phipps Morgan, 1992). At the slow-spreading Mid-Atlantic Ridge, M ranges from 0.2 to 0.8 (Fig. 2.2 G + H; Behn &

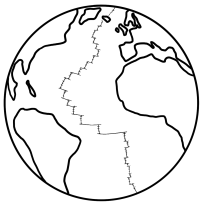

Ito, 2008; Cowie et al., 1993; Ito & Behn, 2008; MacLeod et al., 2009; Olive & Escartín, 2016; Schouten et al., 2010), while the ultraslow-spreading Southwest Indian Ridge (SWIR) even ranges from 0 to >0.9 (Chen et al., 2021; Sauter et al., 2013).

2.5.1 Oceanic Core Complex Formation

At M ratios between 0.3 and 0.6, one side of the ridge axis experiences mostly magmatic spreading including occasional normal faulting, while extension on the opposing side needs to be fully accommodated by faulting (Fig. 2.2 D; Behn & Ito, 2008; MacLeod et al., 2009; Smith et al., 2006). In consequence, spreading at such ridge segments is highly asymmetric with a tectonically and a magmatically spreading ridge side. A normal fault initiated on the tectonic side does not migrate off-axis, since all available melt accretes on the magmatic side. This allows the fault to stay active for a theoretically infinite timespan and thus to accumulate an immense amount of strain.

While the fault root stays in the weak near-axis lithosphere, the breakaway – the tip of the footwall, where the fault first cuts the sea floor – is transported off-axis with plate separation. With increasing displacement on the fault surface, the footwall starts rotating due to buoyancy. This reduces the emergence angle to 20° to 30°, while numerical models and hypocentre locations suggest a steepening of the fault at depth to 70° to 80° (deMartin et al., 2007; Escartín & Canales, 2011; MacLeod et al., 2009; Smith et al., 2006, 2008; Zhao et al., 2013). MacLeod et al. (2009) propose that detachments experience phases of extremely reduced melt supply during their mature stage. This results in an increased asymmetry and migration of the detachment across the ridge axis. Renewed volcanism below the detachment's footwall, for example due to the propagation of an adjacent ridge segment, may subsequently lead to the termination of the detachment.

Large-offset detachment faults exhume lower crust and mantle material to the seafloor, displaying a composition of gabbroic rocks from magmatic intrusions and at least partly serpentinized mantle peridotites indicative of extensive weakening in the fault zone. The exhumed shear plane displays characteristic corrugations in the direction of slip. These domed and corrugated massifs elevated above the surrounding seafloor are known as oceanic core complexes.

Escartín, Smith, et al. (2008) estimate that detachment faulting controls ∼50 % of the MAR between 12°N and 35°N, where it is associated with a large number of different OCCs like those identified at 13°20'N and 13°30'N (Fig. 2.2 H; Escartín, Smith, et al., 2008; Smith et al., 2006), at the Trans-Atlantic Geotraverse (TAG) segment at 26°N (deMartin et al., 2007), and the Rainbow massif (Dunn et al., 2017; Jian et al., 2024). Detachment faulting is prevalent at other slow- and ultraslow-spreading ridges, too. Notable examples include Atlantis Bank and the Dragon Horn area along the Southwest Indian Ridge (Baines et al., 2008; Tao et al., 2020), the region around Loki's Castle vent field at Mohns Ride (Pedersen et al., 2010), as well as Mount Dent at the Mid Cayman Spreading Center (Harding et al., 2017; Haughton et al., 2019), all of which are associated with some kind of hydrothermal activity discussed below.

2.5.2 Flip-Flop Detachment Faulting

Variability between magmatic and tectonic ridge segments is most extreme at ultraslow-spreading ridges. At the Southwest Indian Ridge, 9.5 km thick crust is found at segment 27 at 50°E (Jian et al., 2017), while two corridors between 62°E and 65°E display an extremely thick lithosphere of 15 km (Chen et al., 2023) and appear to be virtually amagmatic (Fig. 2.2 I; Sauter et al., 2013). In the latter case, extension is fully tectonic. After forming at the spreading axis, detachments migrate across the ridge axis towards even thicker lithosphere until breaking a new on-axis fault becomes energetically more favorable. Flexural strain in the footwall associated with rotation provides a weak zone, along which a new fault of opposite polarity emerges (e.g., Bickert et al., 2020; Reston, 2018).

This so-called "flip-flop" detachment mode results in a sequence of successive detachments of alternating polarity cutting their predecessors footwall (Fig. 2.2 E; Reston & McDermott, 2011). The spreading mode expresses as a series of ridges with relief in excess of 3 km parallel to the spreading axis (Fig. 2.2 H). The seafloor is exclusively made of fully serpentinized and exhumed mantle rocks overlain only by isolated volcanic patches and is often termed "smooth" as it lacks the otherwise ubiquitous high-angle fault scarps or corrugations found at other detachments (Canales et al., 2006; Cannat, Sauter, et al., 2019; Sauter et al., 2013).

2.5.3 Variability of Detachment-Related Hydrothermal Activity

The greater diversity and higher structural complexity of lithosphere and magmatic processes at (ultra)slow-spreading ridges also reflects in the style of hydrothermal activity. A close tectonic-hydrothermal relationship is strongly indicated by the irregular distribution of hydrothermal vents, which are found at the ridge axis, but also several kilometers away around the emergence of detachment faults and on the exhumed fault surface (Fig. 2.2 H + I).

Large-scale faults potentially act as permeable pathways, expanding the reach of hydrothermal fluids to depths greater than the typically inferred maximum depth of hydrothermal circulation of 6 km (Andersen et al., 2015; McCaig et al., 2007; Tao et al., 2020). This in turn allows fluids to extract heat from deeper, transient magma bodies and brings them in contact with different rock types at diverse pressure-temperature conditions, giving rise to a variety of chemical reactions between fluid and rock (Früh-Green et al., 2022, and references therein).

Based on venting temperature and fluid chemistry, which are indicators for heat sources and host rock, Kelley and Shank (2010) identify three classes of hydrothermal systems at (ultra)slow-spreading MORs (Fig. 2.2 D):

Type-1 : High-temperature (>300 °C) venting with high metal content, forming sulfide deposits in basalt. Fluid circulation through mafic host rock is driven by cooling and crystallizing axial melts.

Type-2 : High-temperature (>300 °C) venting with high metal content, forming sulfide deposits in gabbro and serpentinized peridotite. Fluid circulation through mixed mafic and ultramafic lithologies inside the detachment footwall is driven by gabbroic intrusions, assisted by serpentinization reaction.

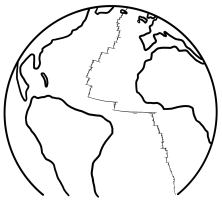

Type-3 : Low-temperature (<120 °C) venting with low metal content, forming carbonate chimneys in serpentinized peridotite. Fluid circulation through dominantly ultramafic lithosphere is driven by residual mantle heat and serpentinization reaction.

McCaig et al. (2007) propose a similar classification based on three archetypes found around OCCs at the MAR: **TAG-type** vents discharge Type-1 fluids on top of the mafic hanging wall of a detachment next to the emergence, with the permeable fault zone presumbaly being the primary channel for hot upflow. **Rainbow-type** and **Lost City-type** vents are equivalent to Type-2 and Type-3 systems, respectively. Maximum measured vent temperatures are 369 °C at TAG (Chiba et al., 2001), 365 °C at Rainbow (Charlou et al., 2002) and 116 °C at Lost City (Früh-Green et al., 2022).

Many other prominent examples of OCC-related venting are found along (ultra)slow-spreading ridges. At smooth seafloor, flip-flop dominated ridge section, however, observations of hydrothermal activity are limited. The only recording of active venting is the Old City vent field on the exhumed shear plane of the currently active detachment (Lecoeuvre et al., 2021). Old City is likely an analogue to the Lost City vent field venting at temperatures below 100 °C (Fan et al., 2021). This supports the idea of very magma-poor spreading with lithosphere cooling and serpentinization being the only drivers of hydrothermal activity. However, the inactive ultramafic-hosted Tianzuo hydrothermal field found in another smooth seafloor corridor presumably vented at temperatures greater than 335 °C (Ding et al., 2021). This could indicate a more diverse and complex system of interacting magmatic, tectonic and hydrothermal processes also in flip-flop detachment dominated ridge segments.

Hydrothermal circulation plays a crucial role in shaping the faulted lithosphere in several ways (Fig. 1.2). It governs lithospheric thickness through large-scale cooling, while the variable fluid pathways create a complex thermal structure that can induce localized cooling or heating, particularly within permeable faults. Elevated pore fluid pressure reduces the confining pressure, further influencing fault dynamics. Interactions between hydrothermal fluids and gabbroic or ultramafic rocks result in the formation of weak hydrous minerals, such as serpentine, talc, chlorite, and amphibole, within detachment fault footwalls (Boschi et al., 2006; Escartín et al., 2003; Picazo et al., 2012; Schroeder & John, 2004). These mineralogical changes alter the lithosphere's strength, directly affecting faulting behavior (Escartín, Andreani, et al., 2008; Escartín et al., 1997a). Moreover, exothermic heating, water consumption, and volumetric expansion during these reactions (Früh-Green et al., 2004; Klein & Le Roux, 2020; Lowell & Rona, 2002), as well as pore space clogging by precipitates (Andreani et al., 2007; Iyer et al., 2010; Lowell & Yao, 2002), create feedback loops that further shape hydrothermal pathways.

Chapter 3

Overview: Research Projects

The contributions of this work to untangling the complex interactions among magmatic, tectonic, and hydrothermal processes at (ultra)slow-spreading mid-ocean ridges, as discussed in previous sections, are highlighted in Fig. 3.1. The two studies presented in this dissertation, outlined below, also include detailed descriptions of the numerical models developed as a core part of this work (Hasenclever & Glink, 2025).

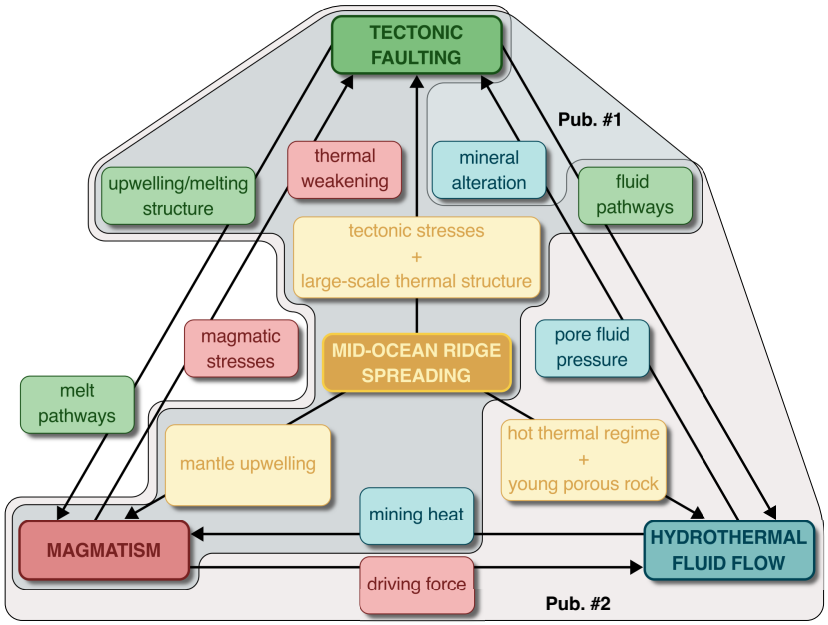

Figure 3.1. Parts of the hydro-tectono-magmatic network covered by the two studies featured in this dissertation.

The first study examines the influence of fault-related hydrothermal cooling and magmatic intrusions on flip-flop detachment faulting in the magma-poor SWIR region between 62°E and 65°E (Glink & Hasenclever, 2024). Two key questions regarding the faulting dynamics in this area are: (1) How does the exceptionally thick lithosphere found in the area support large-slip detachment faulting? (2) What triggers the next on-axis detachment in the absence of a steadily replenished magmatic heat source? Petrological observations and numerical modeling by Bickert et al. (2020) address the first question, attributing it to efficient fault weakening mechanisms. These include grain size reduction by dynamic recrystallization in the ductile mantle and serpentinization at shallower levels. In their model, the prescribed axial thermal structure triggers the shear localizing feedback loop between deformation and weakening. Building on these findings, we investigate the origin of a thermal structure that can explain the periodic formation of new on-axis faults. Our simulations demonstrate that (parametrized) hydrothermal cooling of the active fault zone, combined with periodic sill

intrusions, produce a suitable temperature field: Mantle upwelling is strongest in the footwall close to the active fault, where also hydrothermal cooling is most efficient. The balance between the two processes controls melt accumulation below the central footwall. Thermal and rheological weakening by the melts triggers new on-axis faulting. Our results highlight that even in regions of limited magmatic and hydrothermal activity, such as smooth seafloor areas, both processes can significantly influence detachment faulting dynamics.

Our second study focuses on the factors controlling fluid circulation patterns around oceanic core complexes. Specifically, we are addressing the question, why the largest sulfide deposits found at the seafloor are associated with TAG-like Typ-1 venting in the hanging wall of detachments (Glink et al., 2025). To explore this, we reconstruct the tectono-magmatic history of the core complex at the MAR at 13°30'N and analyze hydrothermal pathways and venting within this framework. The study contributes to the debate on whether permeable detachments can guide high-temperature fluids over long distances, linking Type-1 venting to a distant axial heat source as proposed by McCaig et al. (2007). While highly permeable faults can channel substantial fluid flow, especially when most permeable along the direction of slip, excessive cooling of fluids over long distances may limit metal transport efficiency. Alternatively, we find that relatively shallow intrusions of limited size and persistence are surprisingly effective in focusing large scale fluid flow. This focusing likely occurs across the entire detachment structure, enhanced by the effects of OCC topography and interactions between hydrothermal plumes.

3.1 List of Publications

Glink, A., & Hasenclever, J. (2024). How Hydrothermal Cooling and Magmatic Sill Intrusions Control Flip-Flop Faulting at Ultraslow-Spreading Mid-Ocean Ridges. *Geochemistry, Geophysics, Geosystems, 25* (2), e2023GC011331. doi: 10.1029/2023gc011331

Glink, A., Hasenclever, J., Rüpke, L., Hort, M., & Petersen, S. (2025). Massive Sulfide Deposition at the 13°30'N Oceanic Core Complex: Lessons Learned from Coupled Hydro-Thermo-Mechanical Modeling. *Geochemistry, Geophysics, Geosystems* (under review)

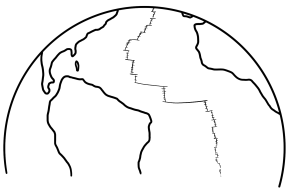

Chapter 4

How Hydrothermal Cooling and Magmatic Sill Intrusions Control Flip-Flop Faulting at Ultraslow-Spreading Mid-Ocean Ridges

Arne Glink and Jörg Hasenclever

Key Points

- We implemented hydrothermal cooling and magmatic intrusion in a thermo-mechanical model to explain detachment faulting at ultraslow ridges
- Stable flip-flop detachment faulting is observed for setups considering both melt input and hydrothermal heat fluxes at realistic magnitudes
- Two other faulting modes frequently observed in our model offer potential alternative interpretations for existing seafloor observations

Author Contributions:

As the first author of the manuscript and primary contributor to the DFG project proposal, I led the core aspects of this study, including its design, execution, and manuscript drafting. **Jörg Hasenclever** made significant contributions across all 14 roles specified by the CRediT taxonomy (National Information Standards Organization, 2022). He was the co-author of the project proposal (*Funding Acquisition*, *Project Administration*) and main supervisor of the PhD project (*Supervision*). Particularly, Jörg Hasenclever provided the original code version and supported its further development through feedback and testing (*Methodology*, *Software*, *Validation*), assisted in the *Conceptualization* of the study through frequent feedback and discussions and contributed in the *Review & Editing* of the manuscript.

This study has been published in 2024 under the same title in *Geochemistry, Geophysics, Geosystems*, Volume 25, Issue 2 (doi: 10.1029/2023gc011331).

Abstract

"Flip-flop" detachment mode represents an endmember type of lithosphere-scale faulting observed at almost amagmatic sections of ultraslow-spreading mid-ocean ridges. Recent numerical experiments using an imposed steady temperature structure show that an axial temperature maximum is essential to trigger flip-flop faults by focusing flexural strain in the footwall of the active fault. However, ridge segments without significant melt budget are more likely to be in a transient thermal state controlled, at least partly, by the faulting dynamics themselves.

Therefore, we investigate which processes control the thermal structure of the lithosphere and how feedbacks with the deformation mechanisms can explain observed faulting patterns. We present results of 2-D thermo-mechanical numerical modeling including serpentinization reactions and denynamic grain size evolution. The model features a novel form of parametrized hydrothermal cooling along fault zones as well as the thermal and rheological effects of periodic sill intrusions.

We find that the interplay of hydrothermal fault zone cooling and periodic sill intrusions in the footwall facilitates the flip-flop detachment mode. Hydrothermal cooling of the fault zone pushes the temperature maximum into the footwall, while intrusions near the temperature maximum further weaken the rock and promote the formation of new faults with opposite polarity. Our model allows us to put constraints on the magnitude of two processes, and we obtain most reasonable melt budgets and hydrothermal heat fluxes if both are considered. Furthermore, we frequently observe two other faulting modes in our experiments complementing flip-flop faulting to yield a potentially more robust alternative interpretation for existing observations.

Plain Language Summary

At mid-ocean ridges, two plates diverge and new seafloor is created. The nature and appearance of this new seafloor strongly depend on spreading velocity and the availability of magmatic melts. At one of the melt-poorest and slowest-spreading ridges, a special form of large-scale tectonic faults, so-called flip-flop detachments, can be observed. Tectonic faults can act as pathways for fluids circulating through the seafloor, which provides a significant cooling effect for the young plate. The interplay of magmatic activity, faulting and fluid circulation is evident at many different ridges with different magmatic activity and spreading rates. Flip-flop faulting is restricted to only a few ridge sections worldwide, and we here investigate the prerequisites for this special spreading mode. To do so, we set up a computer model of an ultraslow-spreading mid-ocean ridge including the effects of sparse magmatism as well as the cooling effect associated with fluid circulation. We find that feedbacks between faulting dynamics, hydrothermal cooling and magmatic activity control the magnitude and spatial distribution of each individual process. Seafloor and subsurface observations are best explained by calculations with moderate melt input and hydrothermal circulation acting together.

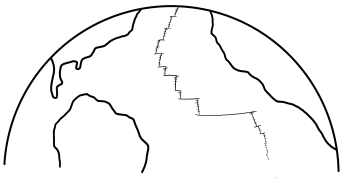

4.1 Introduction

Detachment faulting is a unique spreading mode observed at magma-poor slow- to ultraslow-spreading mid-ocean ridges. It is a highly asymmetric process (MacLeod et al., 2009; Tucholke et al., 2008), where the hanging wall side consists of volcanic crust with moderate normal faulting, while the footwall side is purely tectonic with a long-lived detachment fault rooting in the weak near-axis lithosphere. During plate separation, the breakaway – the tip of the footwall, where the fault first cuts the seafloor – migrates off-axis (Buck et al., 2005). With increasing displacement on the fault plane, the uplifted footwall starts rotating and bending under its own weight (MacLeod et al., 2009; Smith et al., 2006). The domed corrugated shear planes of such detachments, known as oceanic core complexes, emerge to the seafloor at shallow angles where they expose lower crust and mantle rocks (e.g., Escartín et al., 2017; Escartín, Smith, et al., 2008; Hayman et al., 2011; Zhao et al., 2013).

In this study, we focus on an end-member type of detachment faulting observed along almost amagmatic sections of ultraslow MORs, such as the narrow corridors of highly serpentinized seafloor between 62°E to 65°E at the Southwest Indian Ridge. In the absence of melt supply, extension in the hanging wall of a detachment cannot be accommodated by magmatic accretion. The entire fault zone of the active detachment therefore migrates across the ridge axis into thicker lithosphere until the formation of a new on-axis fault in the footwall is energetically more favorable. This new fault is most likely dipping in the opposite direction (i.e. is of opposite polarity) and is oriented along weak zones in the footwall resulting from strain induced by its rotation and flexure. Reston and McDermott (2011) proposed this so-called "flip-flop" detachment mode to be responsible for large areas of exhumed, extensively serpentinized mantle rocks at magma-poor margins and ultraslow-spreading MORs. This extension mode produces regions of unusually smooth seafloor, large ridges that are oriented parallel to the spreading axis, and a pattern of off-axis dipping fault zones that is symmetrical on a large-scale (Cannat, Sauter, et al., 2019; Cannat et al., 2006; Sauter et al., 2013).

A recent numerical study by Bickert et al. (2020) explores the processes causing the flip-flop kinematics. They find that fault zone weakening through mantle serpentinization and grain size reduction in mechanically stressed regions in the lower lithosphere play fundamental roles in stabilizing active tectonic zones and triggering new faults of opposite polarity. A crucial assumption in the aforementioned model is that the near-ridge lithosphere is in a thermal quasi-steady state with prescribed temperature maximum at the ridge axis and fixed depth-dependent temperature profiles. However, gaining further insights into the multifaceted thermo-mechanical interplay of the processes involved in this spreading mode requires a dynamically evolving temperature field. In this study we therefore investigate which processes predominantly shape the near-ridge thermal structure and how the evolving temperature field, in turn, affects the faulting sequence through rheological changes.

The thermal state of (ultra)slow amagmatic ridges is not as well understood as at faster spreading ridges with strong magmatism. A nearly continuous axial melt lens with minor depth variation, for example at the fast-spreading East Pacific Rise (Detrick et al., 1987; Marjanović et al., 2018), indicates a rather stable thermal regime in both space and time. The hot, weak axial region serves as a thermal and mechanical anchor that stabilizes the

ridge axis position and focuses deformation. In contrast, amagmatic ridge sections without a significant melt budget are in a more transient thermal state that is controlled, at least partly, by its faulting dynamics and history (e.g., Behn & Ito, 2008). Here, in the absence of strong magmatic processes, advection of hot mantle material into the footwall of detachments and subsequent cooling by heat conduction and hydrothermal circulation become the main heat distribution mechanisms.

Indirect evidence for hydrothermal cooling is the more than 15 km thick axial brittle lithosphere at ultraslow-spreading ridges (e.g., Grevemeyer et al., 2019), which is incompatible with solely conductive cooling (see also our model without hydrothermal cooling; Section 4.3.2.1). Mapping of thermal plumes in the water column point at a reduced yet still significant hydrothermal activity along sections of the ultraslow Gakkel Ridge and SWIR (Baker et al., 2004). Direct observations of hydrothermal venting in amagmatic settings are limited to the recently discovered low temperature Old City hydrothermal field in the eastern magma-poor corridor of the SWIR (Cannat, Agrinier, et al., 2019; Lecoeuvre et al., 2021). Additional evidence of potentially widespread hydrothermal activity is the inactive ultramafic-hosted Tianzuo hydrothermal field (Ding et al., 2021), located on a detachment surface in a smooth seafloor area between the two corridors investigated by Sauter et al. (2013). Further indicators are the seismically imaged $\sim$5 km thick layer of partially serpentinized material exhumed by the successive detachments (Corbalán et al., 2021; Momoh et al., 2020, 2017; Sauter et al., 2013) and conclusions of other petrological studies (Bickert et al., 2023; Patterson et al., 2021; Vieira Duarte et al., 2020). Observed correlations between fault and vent field positions at more magmatic ridge sections (e.g., TAG, deMartin et al., 2007; Logatchev-1, Petersen et al., 2009; Longqi-1, Tao et al., 2020) suggest that hydrothermal circulation presumably occurs along highly permeable fault zones (McCaig et al., 2007). Potential driving forces for hydrothermal activity at magma-poor ridges are exothermic heat from serpentinization reactions, magmatic heat from sporadic intrusions into the footwall (indicated in recent seismic data by Momoh et al., 2020), and possibly heat mined from deep hot rocks through thermal contraction cracks (Lister, 1974). Fan et al. (2021) suggest that the observed lithosphere thickness results from a thermal balance between deep periodic sill intrusions and hydrothermal circulation in the upper lithosphere driven by their heat. More details on spreading-related processes including hydrothermal activity can be found in the excellent reviews by Olive (2023) and Früh-Green et al. (2022).

Our study is motivated by these recently published data and models, and associated advances in the understanding of the structure and thermal regime of this complex end-member tectonic setting. The key question is, how can the interplay of tectonic, magmatic and hydrothermal processes explain a thermal structure that will lead to flip-flop detachment faulting during ultraslow, magma-poor oceanic spreading. To address this question, we present a thermo-mechanical numerical model for amagmatic oceanic spreading that includes refined implementations of serpentinization and grain size evolution, parametrized hydrothermal cooling (enhanced along active fault zones) and the thermal and rheological effects of sill intrusions into the detachment footwall. Starting with a setup similar to the model by Bickert et al. (2020) with an imposed temperature structure, we increase complexity by calculating the dynamically evolving thermal structure including the effects of hydrothermal fault zone

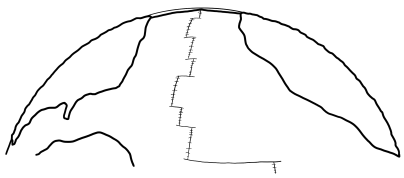

cooling and magmatic intrusions.

4.2 Numerical Model

4.2.1 Numerical Method and Constitutive Equations

The numerical model used in this study applies the finite element method on unstructured meshes to solve for the thermal and mechanical evolution of lithosphere and underlying mantle. The open-source program `M2TRI_vep` (Hasenclever & Glink, 2024) is a successor of the mantle convection code `M2TRI` (Hasenclever, 2010), into which elastic and plastic deformation behavior, serpentinization of mantle rocks and a simple hydrothermal cooling parametrization have been implemented as discussed in previous studies (Hasenclever et al., 2017; Rüpke & Hasenclever, 2017). For the present study, we have further advanced the model by improving the visco-elasto-plastic rheology formulation, which now considers diffusion creep as well as non-linear dislocation creep mechanisms and a viscoplastic regularization (Duretz et al., 2021). Furthermore, we have implemented processes that are critical for lithosphere and upper mantle deformation such as strain softening, deformation-controlled serpentinization, dynamic grain size evolution, periodic emplacement of magmatic intrusions and an advanced hydrothermal cooling parametrization that takes into account the deformation state of the lithosphere. In the following, the relevant equations are written using index notation and Einstein summation convention. All parameters and variables introduced in this section are listed in Table 4.1.

We solve the conservation equations for mass, Eq. (4.1), and momentum, Eq. (4.2), for an incompressible medium using the Boussinesq approximation. The solution variables are displacement velocity components u_i and total pressure P:

$$\frac{\partial u_i}{\partial x_i} = 0, \tag{4.1}$$

$$\frac{\partial \tau_{ij}}{\partial x_j} - \frac{\partial P}{\partial x_i} + \rho g_i = 0, \tag{4.2}$$

where x_i are the spatial coordinates, τ_{ij} are the deviatoric stresses, ρ is the density and g_i are the components of the gravitational acceleration.

Density in the Stokes equation (4.2) is assumed to vary with temperature T and degree of serpentinization s. The latter is used to calculate the volumetric mean between two end-member rock types: mantle peridotite (for which we assume olivine properties; subscript ol) and serpentine (subscript $serp$). This averaging is done for all rock parameters for which two values – one for olivine and one for serpentine – are given in Table 4.1.

$$\rho(T,s) = \rho_{ol}(T)\cdot(1-s) + \rho_{serp}(T)\cdot s, \qquad \rho_c(T) = \rho_{c,0}(1-\alpha_c(T-T_0)). \tag{4.3}$$

Densities $\rho_{c,0}$, with $c \in \{ol, serp\}$, are defined at the reference temperature $T_0 = 0\,^\circ\mathrm{C}$ and α_c are the thermal expansion coefficients. Note that volume changes associated with serpentinization as well as other volume changing processes such as the formation of a fracture

Table 4.1. Description and values of model parameters and variables used in Chapter 4.

Parameter	Description	Unit	Value	
g_i	Gravitational acceleration	$\mathrm{m\,s^{-2}}$	[0, 0, -9.81]	
P	Total pressure	Pa		
P_{ls}	Lithostatic pressure	Pa		
Q	Plastic flow potential	Pa		
R	Gas constant	$\mathrm{J\,kg^{-1}\,mol^{-1}}$	8.314472	
t	Time	s		
Δt	Time step	kyr	0.5 - 5	
T	Temperature	°C		
T_{bd}	Temperature of brittle-ductile transition	°C	750	
u_i	Advection velocity	$\mathrm{m\,s^{-1}}$		
x_i	Spatial coordinates	m		
$\dot{\varepsilon}_{ij}$	Deviatoric strain rate	$\mathrm{s^{-1}}$		
$\varepsilon_{II,p}$	Accumulated plastic strain (2nd invariant)			
$\varepsilon_{p,sw}$	Accumulated plastic strain (full strain weakening)		1.0	
η	Viscosity	Pa s	$10^{18} - 10^{23}$	
η_{vp}	Viscoplastic viscosity for regularization	Pa s	5×10^{19}	
$\dot{\lambda}$	Plastic multiplier	$\mathrm{s^{-1}}$		
τ_{ij}	Deviatoric stresses	Pa		
τ_{yield}	Yield stress	Pa		
	Thermo-mechanical properties		Mantle[a]	Serpentine[b]
C	Cohesion	MPa	60(6)[c]	40(4)
$\frac{\Delta C}{C_0}$	Max. relative cohesion loss		0.9	
C_p	Specific heat capacity	$\mathrm{J\,kg^{-1}\,K^{-1}}$	1200	1200
G	Shear modulus	GPa	30	30
α	Thermal expansion coefficient	$\mathrm{K^{-1}}$	3.0×10^{-5}	2.65×10^{-5}
κ_0	Thermal conductivity	$\mathrm{W\,m^{-1}\,K^{-1}}$	3.3	2.7
ρ_0	Reference density	$\mathrm{kg\,m^{-3}}$	3300	2600
Φ	Friction angle	°	30	15
	Diffusion creep			
A_{dif}	Pre-exponential factor	$\mathrm{MPa^{-n}\,s^{-1}}$	1.5×10^9	
n_{dif}	Stress exponent		1	
E_{dif}	Activation energy	$\mathrm{kJ\,mol^{-1}}$	375	
V_{dif}	Activation volume	$\mathrm{m^3\,mol^{-1}}$	6×10^{-6}	
	Dislocation creep			
A_{dis}	Pre-exponential factor	$\mathrm{MPa^{-n}\,s^{-1}}$	1.1×10^5	
m	Grain size exponent		3	
n_{dis}	Stress exponent		3.5	
E_{dis}	Activation energy	$\mathrm{kJ\,mol^{-1}}$	530	
V_{dis}	Activation volume	$\mathrm{m^3\,mol^{-1}}$	13×10^{-6}	
	Serpentinization[d]			
s	Serpentinization degree		0 - 1.0	
S	Serpentinization rate	$\mathrm{s^{-1}}$		
S_0	Reaction rate scaling factor	$\mathrm{s^{-1}}$	3×10^{-13}	
a	Normalized reaction rate parameters		808.3	
b	—"—	K	3640	
c	—"—	K	8759	
T_{s0}	Max. temperature of reaction	K	623.6	
ρ'_{ol}	Olivine mass per rock volume	$\mathrm{kg\,m^{-3}}$		
H_{serp}	Exothermic heat of reaction	$\mathrm{J\,m^{-3}\,s^{-1}}$		
Q_{serp}	Heat release per kg of olivine	$\mathrm{kJ\,kg^{-1}}$	290	
	Grain size evolution[e]			
r	Grain size	µm	1 - 10^4, initial: 1900	
f_{H_2O}	Water fugacity	Pa	600 H/10^6 Si	
K_g	Growth rate constant	$\mathrm{m^p\,s^{-1}}$	3	
p	Grain growth exponent		3.2	
E_{GG}	Activation energy	$\mathrm{kJ\,mol^{-1}}$	620	
V_{GG}	Activation volume	$\mathrm{m^3\,mol^{-1}}$	5×10^{-6}	
λ	Damage partitioning factor		0.01	
γ	Grain boundary energy	$\mathrm{J\,m^2}$	1	
Ψ	Dislocation creep work rate	$\mathrm{Pa\,s^{-1}}$		
H_{vd}	Heat from viscous dissipation	$\mathrm{J\,m^{-3}\,s^{-1}}$		

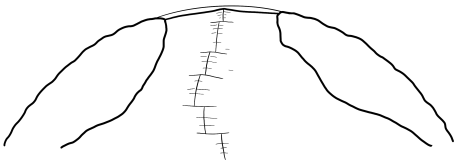

Table 4.1: Continued

Parameter	Description	Unit	Value
	Hydrothermal cooling		
Nu	Effective Nusselt number		
Nu_0	Reference Nusselt number		6.4 - 10.8
θ	Temperature-dependent taper		
β	Smoothing factor		0.75[f]
P_{ht}	Scaling pressure hydrothermal activity	MPa	330
P_{sf}	Seafloor hydrostatic pressure (axial valley)	MPa	101
K_{FZ}	Fault zone cooling factor		
W	Deformation measure ($\tau_{II} \cdot \varepsilon_{II} \cdot \dot{\varepsilon}_{II}$)	$\mathrm{J\,s^{-1}\,m^{-3}}$	
W_1, W_2	Deformation thresholds	$10^{-6}\,\mathrm{J\,s^{-1}\,m^{-3}}$	4, 1000
F_{max}	Exponent of max. cooling		0 - 2.5
	Magmatic intrusions[g]		
M	Intrusion volume flux / brittle lithosphere flux		0 - 0.12
T_{sol}	Solidus temperature	°C	1000
T_{liq}	Liquidus temperature	°C	1200
H_{lat}	Latent heat of crystallization	$\mathrm{J\,m^{-3}\,s^{-1}}$	
Q_{lat}	Heat release per kg of melt	$\mathrm{kJ\,kg^{-1}}$	335
B_{melt}	Melt factor in creep viscosities		
ξ	Melt fraction		0 - 1.0
k	Melt exponent in creep viscosities		35[a]

[a] Olivine properties from Andrés-Martínez et al. (2019); Hirth and Kohlstedt (2003)
[b] Bickert et al. (2020); Osako et al. (2010)
[c] Brackets contain values at full strain softening.
[d] Iyer et al. (2010); Malvoisin et al. (2012); Rüpke and Hasenclever (2017)
[e] Ruh et al. (2022); Speciale et al. (2020)
[f] Gregg et al. (2009)
[g] Fan et al. (2021)

network (cf. Section 4.2.2.3) and magmatic sill emplacement (cf. Section 4.2.4) are disregarded in this incompressible formulation.

The conservation equation of heat is solved to obtain the temperature T:

$$\rho C_p \frac{DT}{Dt} = \frac{\partial}{\partial x_i}\left(\kappa \frac{\partial T}{\partial x_i}\right) + H_{vd} + H_{serp} + H_{lat}, \tag{4.4}$$

where C_p is the specific heat capacity and κ is the thermal conductivity. H-terms represent the heat sources and sinks introduced in the next sections, i.e. viscous dissipation H_{vd}, exothermic heat of serpentinization H_{serp} and latent heat of crystallization H_{lat}. Radiogenic heat production is neglected in this study, since for the case of amagmatic spreading investigated here, we assume the lithosphere will mainly consist of mantle rocks with a low concentration of radioactive elements.

4.2.2 Rheology

4.2.2.1 Visco-Elasto-Plastic behavior

On geological time scales, the mechanical deformation of lithosphere and upper mantle rocks occurs through three different mechanisms: reversible elastic deformation, irreversible viscous flow and irreversible plastic deformation simulating brittle failure. All three mechanisms act at strongly variable quantitative proportions depending mainly on the ambient temperature-pressure conditions and stresses. A numerical model for lithosphere dynamics has to be able

to resolve these processes, and different theoretical descriptions of visco-elasto-plastic rheology have been suggested (e.g., Andrés-Martínez et al., 2019; Gerya, 2019; Kaus, 2010; Lavier & Buck, 2002). In line with these studies we follow the approach by Moresi et al. (2003) and assume elastic, viscous and plastic (superscripts e, v and p, resp.) deformation processes to be active simultaneously so that the respective strain rates are additive. This allows to adopt an additive decomposition of the total deviatoric strain rate, $\dot{\varepsilon}_{ij}$:

$$\dot{\varepsilon}_{ij} = \dot{\varepsilon}^{v}_{ij} + \dot{\varepsilon}^{e}_{ij} + \dot{\varepsilon}^{p}_{ij} \tag{4.5}$$

$$= \frac{\tau_{ij}}{2\eta_v} + \frac{\dot{\tau}_{ij}}{2G} + \dot{\lambda}\frac{\partial Q}{\partial \tau_{ij}}, \tag{4.6}$$

where η_v is the effective viscous creep viscosity, G is the elastic shear modulus, $\dot{\lambda}$ is the plastic multiplier and Q is the plastic flow potential. The stress-strain rate relation is based on the visco-elastic Maxwell-model:

$$\tau_{ij} = \eta_{eff}\left(2\dot{\varepsilon}_{ij} + \frac{\hat{\tau}_{ij}}{G\Delta t}\right), \tag{4.7}$$

where η_{eff} is an effective visco-elasto-plastic viscosity (discussed below), $\hat{\tau}_{ij}$ are the Jaumann-rotated old deviatoric stresses (for a detailed description see de Montserrat et al., 2019, and references therein), and Δt is the model time step. The second term on the right side represents the elastic deformation memory.

Viscous deformation includes diffusion (subscript *dif*) and dislocation creep (subscript *dis*) and we assume both creep mechanisms to be simultaneously active. The effective creep viscosity η_v is thus given by

$$\eta_v = \left(\frac{1}{\eta_{dif}} + \frac{1}{\eta_{dis}}\right)^{-1} . \tag{4.8}$$

All rocks are assumed to be isotropic, which allows use of a scalar measure for the strain rate magnitude in the dislocation creep law. Following Gerya (2019) we use the second invariant of the viscous strain rate tensor, $\dot{\varepsilon}_{II,v} = \sqrt{\frac{1}{2}\,\dot{\varepsilon}_{ij,v}\cdot\dot{\varepsilon}_{ij,v}}$, to describe the non-Newtonian behavior of dislocation creep. Diffusion and dislocation creep viscosities are defined as

$$\eta_{dif} = \frac{1}{3}\left(A_{dif}\cdot B_{melt}\cdot r^{-m}\right)^{-\frac{1}{n_{dif}}} \exp\left(\frac{E_{dif}+PV_{dif}}{n_{dif}RT}\right) \tag{4.9}$$

$$\eta_{dis} = \frac{1}{2^{\frac{n_{dis}-1}{n_{dis}}}\,3^{\frac{n_{dis}+1}{2n_{dis}}}}\left(A_{dis}\cdot B_{melt}\right)^{-\frac{1}{n_{dis}}}\left(\dot{\varepsilon}_{II,v}\right)^{\frac{1}{n_{dis}}-1}\exp\left(\frac{E_{dis}+PV_{dis}}{n_{dis}RT}\right) . \tag{4.10}$$

The pre-exponential factor A, grain size d, grain size exponent m, activation energy E and activation volume V depend on rock type and creep mechanism. The factors in front of A result from scaling triaxial and uniaxial experiment parameters (Gerya, 2019). Mantle peridotite forms the largest fraction of lithosphere at amagmatic ridges, and olivine is the most abundant and weakest mineral of this rock type. We therefore use a dry olivine rheology in our model (Hirth & Kohlstedt, 2003). B_{melt} incorporates the effect of partial melts in intrusion regions on the rock's viscosity (see Section 4.2.4).

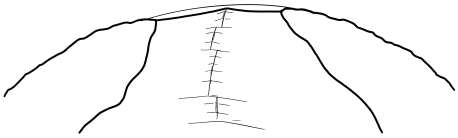

To include the plastic deformation into the viscous formulation we adopt the Prandtl-Reuss flow rule which, upon yielding, reduces the rock's stress state to the yield stress. The standard plasticity formulation is known to cause a mesh resolution-dependent shear band width of ∼3 elements (Lavier et al., 2000). To reduce this unwanted numerical effect we implemented a viscoplastic regularization following Duretz et al. (2021). This allows the model to build up overstress to a certain level controlled by the viscoplastic viscosity η_{vp}. We implemented a yield criterion τ_{yield} similar to a Drucker-Prager criterion, however, we use the local lithostatic pressure P_{ls} instead of the total pressure P from Eq. (4.2). We prefer this so-called "depth-dependent von Mises" criterion over the Drucker-Prager criterion because the latter is known to potentially cause numerical convergence problems (Spiegelman et al., 2016). The resulting yield function is given by

$$F = \tau_{II} - \tau_{yield} - \dot{\lambda}\eta_{vp} = \tau_{II} - C \cdot \cos\Phi - \sin\Phi \cdot P_{ls} - \dot{\lambda}\eta_{vp}, \tag{4.11}$$

with C and Φ being the cohesive strength and the friction angle, respectively. The rock's stress state is quantified using the second invariant of the deviatoric stress tensor τ_{II}.

In summary, the effective viscosity including the effect of plastic yielding can be expressed by

$$\eta_{eff} = \begin{cases} \left(\frac{1}{\eta_v} + \frac{1}{G\Delta t}\right)^{-1}, & \text{if } \tau_{II} < \tau_{yield}. \\ \frac{\tau_{yield} + \dot{\lambda}\eta_{vp}}{2\dot{\varepsilon}_{II}}, & \text{if } \tau_{II} \geq \tau_{yield}. \end{cases} \tag{4.12}$$

Using Eqs. (4.8) - (4.11) with the parameters of the dry olivine rheology and a geothermal gradient of $0.05\,^{\circ}\mathrm{C\,m^{-1}}$, we find that the transition from elastic-brittle to ductile behavior occurs at ∼750 °C at a depth of ∼15 km. This is in agreement with the temperature assumed for the lower end of the seismogenic zone at (ultra-)slow spreading ridges (Grevemeyer et al., 2019) and we refer to the $T_{bd} = 750\,^{\circ}\mathrm{C}$ isotherm from here on as the base of the brittle lithosphere. For numerical stability reasons, viscosity is limited between 10^{18} and $10^{23}\,\mathrm{Pa\,s}$.

4.2.2.2 Strain weakening

Strain weakening of fractured rocks is a critical process that needs to be considered in numerical models for lithosphere faulting. It parametrizes the weakening effects of pore fluids, gouge materials and mineral transformations in regions of strong plastic deformation, i.e. shear zones. Strain weakening should thus scale with the deformation that a rock has experienced. It is incorporated in our model by reducing rock cohesion by $\frac{\Delta C}{C_0} = 0.9$ over the range of accumulated plastic strain $\varepsilon_{II,p}$ from 0 to $\varepsilon_{p,sw} = 1.0$:

$$C = C_0 \cdot \left(1 - \min\left\{1, \frac{\varepsilon_{II,p}}{\varepsilon_{p,sw}}\right\} \cdot \frac{\Delta C}{C_0}\right) \tag{4.13}$$

To calculate plastic strain accumulated in yielding regions, the plastic strain rate, which corresponds to the total strain rate minus the visco-elastic strain rate, is integrated over time, following

$$\varepsilon_{II,p}(t + \Delta t) = \varepsilon_{II,p}(t) + \dot{\varepsilon}_{II,p}(t) \cdot \Delta t. \tag{4.14}$$

4.2.2.3 Serpentinization

To investigate the lithosphere-scale influence of the reaction of olivine and water to form serpentine at temperatures below 350 °C, we adopt the temperature-dependent kinetic rate used by Rüpke and Hasenclever (2017):

$$S(T) = S_0 \cdot a \cdot \exp\left(-\frac{b}{T}\right) \cdot \left[1 - \exp\left(-c\left(\frac{1}{T} - \frac{1}{T_{s0}}\right)\right)\right], \tag{4.15}$$

with $S_0 = 3 \times 10^{-13}\,\mathrm{s}^{-1}$ (Rüpke & Hasenclever, 2017) and $a = 808.3$, $b = 3640\,\mathrm{K}$, $T_{s0} = 623.6\,\mathrm{K}$, and $c = 8759\,\mathrm{K}$ (Malvoisin et al., 2012). Note that we do not incorporate grain size effects on the kinetic rate (Malvoisin et al., 2012). This rate describes the relative change of olivine mass per rock volume ρ'_{ol}, thus allows to calculate the serpentinization degree s of the rock by

$$\frac{\partial \rho'_{ol}}{\partial t} = -S(T)\rho'_{ol} \tag{4.16}$$

$$s = 1 - \frac{\rho'_{ol}}{\rho}. \tag{4.17}$$

Furthermore, this representation directly allows to calculate the exothermic heat released during the reaction (Iyer et al., 2010) by:

$$H_{serp} = -Q_{serp}\frac{\partial \rho'_{ol}}{\partial t}, \tag{4.18}$$

where Q_{serp} is the heat produced per unit mass of olivine of $2.9 \times 10^5\,\mathrm{J\,kg^{-1}}$ (value for forsterite from Iyer et al., 2010).

Since we do not explicitly resolve the dynamics of hydrothermal fluid flow through a porous medium, we follow the approach of Bickert et al. (2020) to asses the availability of water for the reaction. The product of stress and accumulated strain, representing the volumetric work done to the rock by deformation, is used as a proxy for the formation of a fracture network giving water access to the rock. The threshold for this work, above which temperature-controlled serpentinization is activated, is set to $10^8\,\mathrm{J\,m^{-3}}$.

Serpentine properties are listed in Table 4.1 and are used to derive effective rock properties by calculating the volumetric mean between olivine and serpentine properties using the serpentinization degree (cf. Eq. 4.3). Mechanical weakening due to serpentinization is incorporated by reducing cohesion and friction angle (Escartín et al., 1997b). The occurrence of serpentine in the oceanic spreading context is limited to shallow and cold regions. We therefore refrain from adjusting the viscous flow law parameters for serpentine, as serpentinized regions are expected to deform predominantly elasto-plastically.

4.2.2.4 Dynamic Grain Size Evolution

Grain size reduction occurs through dynamic recrystallization at sufficiently high applied stresses and results in a decrease of the diffusion creep viscosity (Eq. 4.9). We adopt the dynamic grain size evolution model by Ruh et al. (2022), which is based on the palaeo-

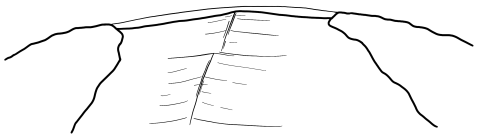

wattmeter (Austin & Evans, 2007):

$$\frac{Dr}{Dt} = \frac{K_g f_{\mathrm{H_2O}} \exp\left(-\frac{E_G + PV_G}{RT}\right)}{p r^{p-1}} - \frac{\lambda r^2}{\gamma \pi} \Psi \tag{4.19}$$

Eq. (4.19) describes the change of grain size r under the influence of grain growth driven by surface energy (first term) and grain size reduction through dynamic recrystallization (second term). K_g is the growth rate constant, $f_{\mathrm{H_2O}}$ is the water fugacity, E_G and V_G are activation energy and volume, respectively, and p is the growth exponent. γ is the grain boundary energy, the geometrical factor π results from the assumption of spherical grains. $\Psi = \tau_{ij}\dot{\varepsilon}_{ij,dis}$ is the mechanical work rate from dislocation creep, of which the portion λ goes into grain size reduction. This reduces the heat from viscous dissipation, which takes the form of

$$H_{vd} = \tau_{ij}\dot{\varepsilon}_{ij} - \Psi\lambda. \tag{4.20}$$

Experimentally derived model parameters are from Speciale et al. (2020) and listed in Table 4.1. For numerical stability we limit the grain size from 1 µm to 10 mm consistent with observations (e.g., Bickert et al., 2021).

4.2.3 Hydrothermal Cooling

To incorporate the large-scale cooling effect of fluid circulation, we implemented an enhanced thermal conductivity. The enhancement factor is commonly referred to as the Nusselt number Nu in this context – not to confuse with its classical definition – as it up-scales conductive heat transfer to account for the missing cooling effect from the advection of hydrothermal fluids (e.g., Gregg et al., 2009; Phipps Morgan et al., 1987; Theissen-Krah et al., 2011). Here we adapt the approach of Gregg et al. (2009), in which thermal conductivity additionally depends on temperature and depth. We have modified this formulation by using lithostatic pressure instead of depth and applying a linear taper of the conductivity-scaling across the brittle-ductile transition between 600 °C and 750 °C. The latter avoids the temperature dependence in the exponential term and reduces non-linear feedbacks. Thus, we obtain:

$$\kappa = \kappa_0 \cdot \mathrm{Nu} \tag{4.21a}$$

$$\text{with} \quad \mathrm{Nu} = 1 + \theta\,(\mathrm{Nu}_0 - 1) \exp\left(\beta\left(1 - \frac{P_{ls}}{P_{ht}}\right)\right) \cdot K_{FZ}, \tag{4.21b}$$

$$\text{and} \quad \theta = \max\left\{0,\ \min\left\{1,\ 1 - \frac{T - 600\,^\circ\mathrm{C}}{750\,^\circ\mathrm{C} - 600\,^\circ\mathrm{C}}\right\}\right\}. \tag{4.21c}$$

κ_0 is a rock type-dependent reference conductivity, Nu_0 is a reference Nusselt number, θ is the temperature-dependent taper, $\beta = 0.75$ a smoothing factor, and $P_{ht} = 330$ MPa the scaling lithostatic pressure for hydrothermal activity. For a flat topography, P_{ht} corresponds to 10 km depth. Since our models always form an axial valley and lithostatic pressure laterally balances at relatively shallow depths, this value corresponds to approximately 6 km depth below the ridge axis, which is a typical assumption for the maximum depth of vigorous hydrothermal convection (e.g., Gregg et al., 2009).

Motivated by the approach of Lavier and Buck (2002), who enhance cooling around active faults, we have incorporated the factor K_{FZ} into Eq. (4.21b). We use this factor to account for enhanced hydrothermal fluid circulation in damaged regions, i.e. fault zones, where highly permeable pathways are likely to form. K_{FZ} is a function of the product $W = \tau_{II} \cdot \varepsilon_{II,p} \cdot \dot{\varepsilon}_{II}$ of the second invariants of stress τ, accumulated plastic strain ε_p and strain rate $\dot{\varepsilon}$. K_{FZ} follows a logarithmic increase between the activation threshold of $W_1 = 4 \cdot 10^{-6}\,\mathrm{Js^{-1}m^{-3}}$ and the upper limit of $W_2 = 10^{-3}\,\mathrm{Js^{-1}m^{-3}}$:

$$K_{FZ} = \begin{cases} 1 & , \text{ if } W < W_1 \\ \left(\frac{W}{W_1}\right)^{\frac{F_{max}}{log_{10}(W_2/W_1)}} & , \text{ if } W_1 \leq W \leq W_2 \\ 10^{F_{max}} & , \text{ if } W_2 < W \end{cases} \tag{4.22}$$

Analogously to the activation of serpentinization, K_{FZ} parametrizes the formation of a connected fracture network ($\tau \cdot \varepsilon_p$) but additionally favors active fault zones ($\dot{\varepsilon}$), where processes clogging the tectonically opened pore space, such as mineral precipitation from hydrothermal fluids, mineral transformations in the rock and consolidation of fractured rocks, have not yet closed the fracture network again. The activation threshold W_1 is derived from the serpentinization threshold of $10^8\,\mathrm{Nm^{-3}}$ and a typical fault zone strain rate of $4 \cdot 10^{-14}\,\mathrm{s^{-1}}$, while the upper limit W_2 has been defined empirically to have maximum cooling in the center of the most active shear zone. F_{max} is the exponent of maximum cooling intensity, which we vary in our parameter study to test the influence of hydrothermal fault zone cooling.

4.2.4 Magmatic Intrusions

Magmatic intrusions are periodically emplaced as sills of variable size and periodicity. Based on the strategy by Fan et al. (2021) and consistent with thermal models by Chen et al. (2022), emplacement is assumed to occur instantaneously below the shallowest point of the 1000 °C isotherm, representing the basaltic solidus T_{sol}. This corresponds to a mean depth of about 18 km below seafloor, however, the exact positions of individual intrusions depend on the model dynamics. The emplacement temperature is a basaltic liquidus temperature T_{liq} of 1200°C. Upon cooling, latent heat of crystallization is assumed to be evenly released between liquidus and solidus temperature:

$$H_{lat} = -\rho \frac{Q_{lat}}{T_{liq} - T_{sol}} \frac{DT}{Dt} \qquad \text{for} \qquad T_{liq} \geq T \geq T_{sol}, \tag{4.23}$$

where ρ is the density, $\frac{DT}{Dt}$ is the total derivative of temperature with respect to time, and Q_{lat}=335 kJ kg^{-1} is the latent heat per kilogram of melt. Numerically, this is implemented by increasing the specific heat capacity in intrusion regions between liquidus and solidus temperatures (C_p in Eq. 4.4). To account for the effect of partial melts on the viscosity of crystallizing intrusions, we adopt the exponential formulation by Hirth and Kohlstedt (2003) and multiply an additional factor B_{melt} to the pre-exponential flow law parameters (A_{dis}, A_{dif} in Eqs. 4.9 and 4.10). For simplicity, we do not track melt content, but assume melt fraction ξ to be a linear function from 0 to 1 between solidus and liquidus temperature. This

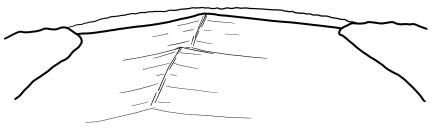

yields

$$B_{melt} = \exp(k\xi) = \begin{cases} 1, & \text{if } T < T_{sol} \\ \exp\left(k \cdot \frac{T - T_{sol}}{T_{liq} - T_{sol}}\right), & \text{if } T_{sol} \leq T \leq T_{liq} \\ \exp(k), & \text{if } T_{liq} < T \end{cases} \tag{4.24}$$

We use a moderate pre-exponential factor $k = 35$ so that the intrusion viscosity remains at the lower cut-off viscosity of 10^{18} Pa s until intrusions have crystallized to about 25 %. From then on, viscosity increases until complete crystallization. For simplicity we do not consider rheological differences between solidified basaltic intrusions and other lithospheric rocks so that any rheological effect of intrusions vanishes once they have cooled below the solidus temperature. Further mechanical aspects of intrusions such as volume changes and related effects on the stress field are not considered here as they require a compressible mechanical model (de Montserrat et al., 2019).

4.2.5 Code Structure

We use the 2-D Galerkin finite element method (FEM) with unstructured triangular elements to solve the system of equations in a Lagrangian reference frame (i.e. the mesh is advected according to the calculated deformation). All meshes are generated using the mesh generator *Triangle* by Shewchuk (2002). Mechanical and thermal parts of the model are solved sequentially over every time step. The mechanical solver uses Crouzeix-Raviart elements with continuous quadratic order shape functions to approximate the deformation field and linear, discontinuous shape functions to approximate the pressure. We employ the so-called penalty method (Donea & Huerta, 2003, and references therein) to derive an incompressible deformation field by iteratively solving Eqs. (4.1) and (4.2).

Next, we solve for heat diffusion and heat sources using a fully-implicit FEM with quadratic order (6-node) triangles. The converged flow field is then converted to a displacement field using the current time step to advect the nodes of the finite element mesh. This step accounts for advective heat transport. Last, the second-order variables such as accumulated strain, serpentinization degree, grain size, lithostatic pressure and rock properties are calculated for the new configuration.

Between two time steps, mesh quality is checked to decide whether or not a remesh procedure is necessary. If so, a new mesh is created that preserves the high resolution regions near the ridge axis and that is adaptively refined along the active fault zones and in regions where intrusions are emplaced. To save computation time, these high resolution mesh regions are coarsened again once the intrusion temperature falls below the solidus temperature. After a remesh, all important variables are transferred from the old to the new mesh by interpolation using the finite element shape functions. The transfer of variables only stored at integration points requires an intermediate mapping step from integration points to nodes before interpolating to the location of integration points in the new mesh (see Fig. 3 in de Montserrat et al., 2019).

The time step size dynamically adjusts to the model dynamics, e.g., flow field and temperature changes, between 0.5 and 5 kyr. Upon intrusion emplacement, the thermal solver

sub-iterates with time steps down to 100 yr in order to properly resolve the heat transfer from the intrusion to its surroundings where high temperature gradients exist. The model is written in MATLAB (ver. R2020a, www.mathworks.com) and uses a vectorized element assembly for an improved performance as suggested by Dabrowski et al. (2008). In addition we make use of the libraries SuiteSparse (Davis & Hager, 2009) and MUTILS (Krotkiewski & Dabrowski, 2010). Data visualizations are done using MATLAB and Tecpot 360 EX (ver. 2021 R1, www.tecplot.com).

4.2.6 Model Setup

The model setup is illustrated in Fig. 4.1. The model domain is 200×80 km, discretized with a triangular finite element mesh and variable mesh resolution. The mean vertex node spacing in the region of the axial lithosphere is 375 m and increases to up to 1500 m toward the bottom boundary. Additionally, the mesh is adaptively refined along actively deforming regions during each remesh procedure with a node spacing of 250 m in the fault zones. The model has a free surface (Andrés-Martínez et al., 2015) with $z = 0$ km corresponding to a water depth of 4650 m and constant mantle inflow along the bottom boundary that balances the lateral extension of 7 mm yr^{-1} on both sides. Spreading rate and water depth represent the amagmatic segments of the SWIR at 62°E to 65°E (Cannat et al., 2008, 2006). To stabilize the initial model phase, we trigger the first fault by imposing a linear profile of accumulated strain (Fig. 4.1).

The initial temperature field is based on Bickert et al. (2020), however, we assume a slightly thinner axial brittle lithosphere of 15 km in agreement with recently reported data (Chen et al., 2023). The geometry of the initial temperature field has been adjusted accordingly, see Fig. 4.1. At the domain top and bottom, isothermal boundary conditions are set to 4 °C and 1400 °C respectively. The lateral domain boundaries are insulating.

For our parameter study, we use one configuration without magmatic input and five

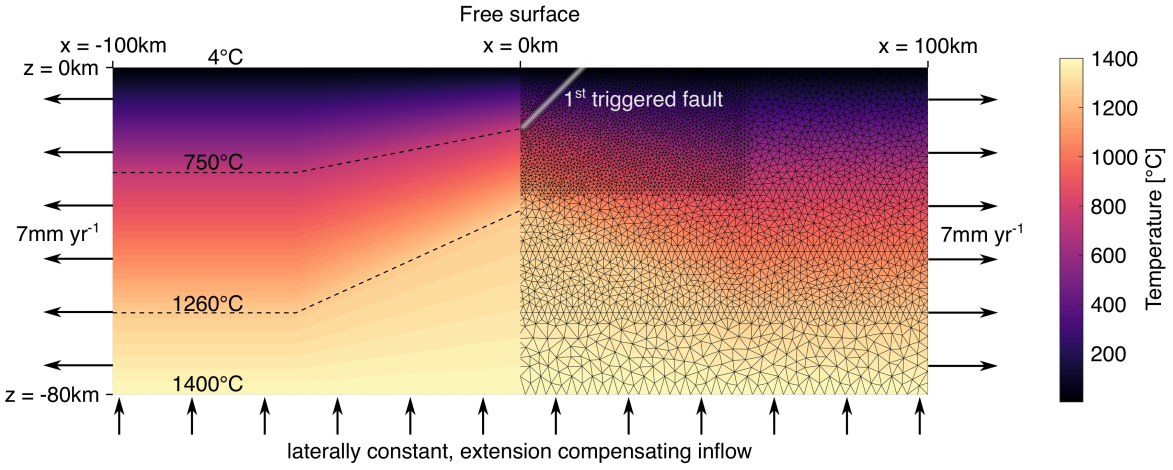

Figure 4.1. Initial temperature field, finite element mesh and mechanical boundary conditions. The geometry of the temperature field is controlled by the axial depth to the 750 °C and 1260 °C isotherms (brittle-ductile transition at 15 km and lithosphere-asthenosphere boundary 35 km, respectively), the off-axis depth of the 1260 °C isotherm of 60 km, and the width of the axial thermal structure of 55 km.

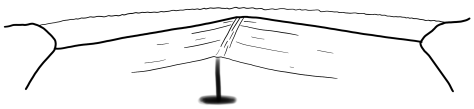

configurations with intrusion geometries and periodicities ranging from 0.14×1.4 km sized sills every 40 kyr to 0.5×5 km sized sills every 100 kyr (Fan et al., 2021). The ratio of intrusion volume flux (average over time) to brittle lithosphere flux (15 km×14 km/Myr) serves as a proxy for the fraction of lithosphere extension that is potentially compensated by magma input through dikes, commonly referred to as the M-factor (Buck et al., 2005). Assuming that the melt budget provided by the intrusions could go into diking, the above intrusion scenarios correspond to equivalent hypothetical values of M between 0.02 and 0.12. Note, however, that spreading in our models is always amagmatic and the actual M-factor in all calculations is zero because neither the volume flux of intrusions nor diking are considered. To investigate the effect of hydrothermal cooling, we vary the magnitude of enhanced hydrothermal fault zone cooling using six values of F_{max} ranging from 0 to 2.5. In each setup, Nu_0 in Eq. (4.21b) is adjusted to F_{max} and M and takes values between 6.4 and 10.2 to obtain a similar average axial brittle lithosphere thickness for all setups. The exact model parameters for each setup can be found in Appendix A. For all experiments, we set the maximum simulation time to 40 Myr.

4.3 Results

Lithosphere deformation is controlled by several feedback mechanisms between thermal and rheological sub-processes. In our model calculations we observe various faulting modes that are illustrated in Fig. 4.2. We distinguish between the formation of individual faults (e.g., a detachment of opposite polarity or an accommodating footwall fault) and the fault sequence (e.g., successive parallel faults or flip-flop). To facilitate a comparison between our model calculations and the ones by Bickert et al. (2020) – despite using different numerical techniques and parametrizations of key processes – we first investigate a setup that is very similar to theirs. To do so we analyse the faulting dynamics of a model with imposed temperature structure, where the initial temperature field is modified only by the vertical movement of the domain top representing seafloor relief. We analyse the faulting dynamics of this model in Section 4.3.1.

In Section 4.3.2 we present the fully-coupled models with a dynamically evolving temperature field. We first show one calculation without any hydrothermal cooling (Section 4.3.2.1) to emphasize the importance of this additional cooling mechanism for reproducing the observed lithosphere thickness. Afterwards we present the different faulting modes observed in the parameter study.

4.3.1 Model with Imposed Temperature Structure

Tests with this simplified thermal model show particular sensitivity to weakening parameters and the prescribed thermal structure, similar to the findings of Bickert et al. (2020). We observe a very stable and uniform sequence of flip-flop faults (Figs. 4.3 and 4.4). The shown faulting sequence starts at 11.1 Myr, after nine flip-flop detachment faults have already formed in the same manner. Each detachment starts as a high angle normal fault (Fig. 4.3 a). With increasing vertical displacement, the footwall rolls back under its own weight. Thereby it experiences large flexure, indicated by the formation of a region with increased strain rate

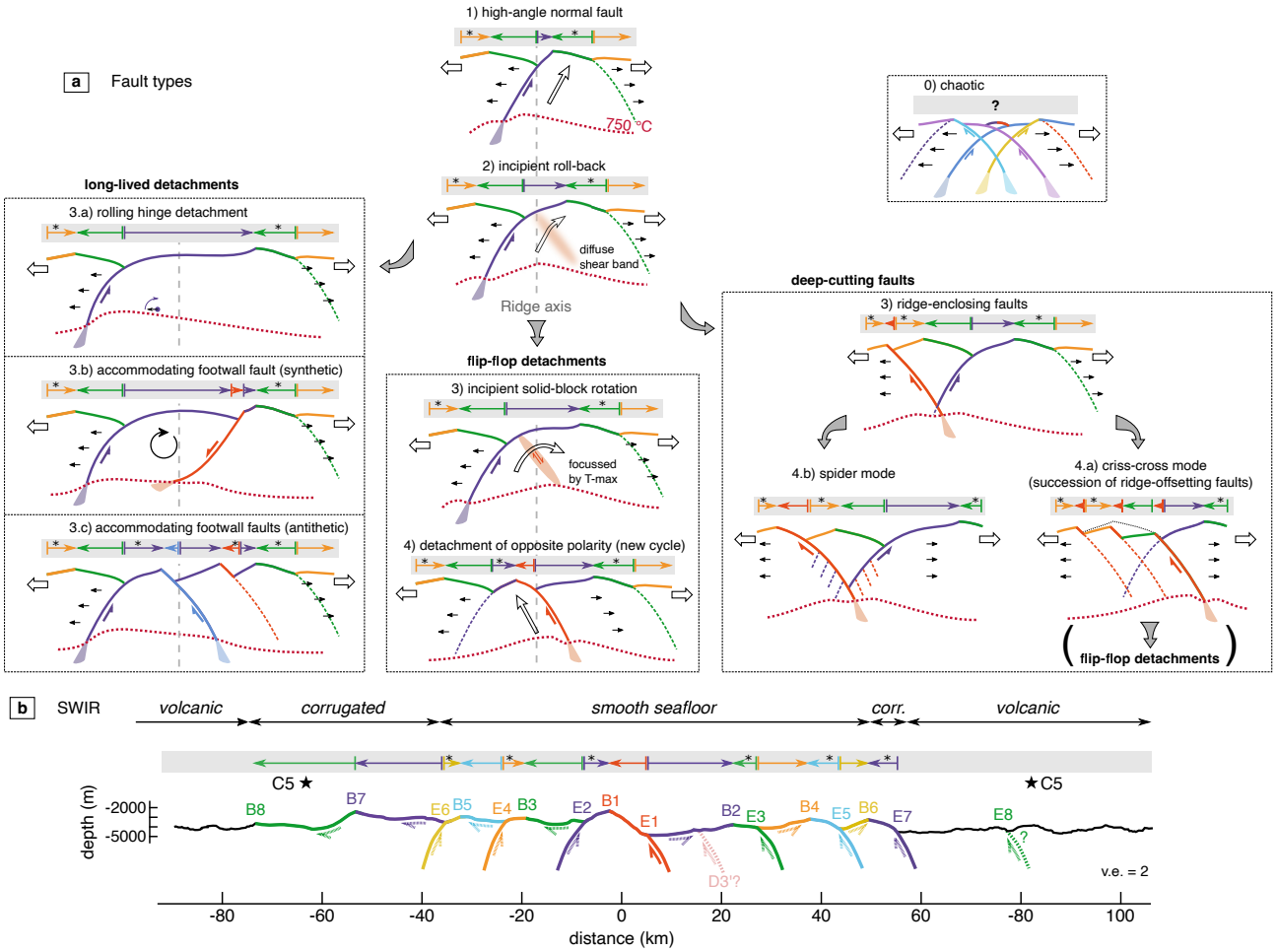

Figure 4.2. **a**: Sketches illustrating the different faulting modes observed in our simulations. The numbering indicates the order of the sequences. Colored arrows on top indicate direction of increasing age of the respective seafloor section. Abnormal age gradients (increasing age towards ridge axis) are indicated by an asterisk. In the chaotic mode, seafloor structures are frequently dismantled by the underlying faults, making a classification practically impossible. **b**: Interpretation of fault zones and seafloor relief of the eastern amagmatic corridor of the SWIR by Cannat, Sauter, et al. (2019) (D3' from Corbalán et al., 2021); vertical exaggeration 2:1; B - Breakaway, E - Emergence, #1 is the currently active detachment, C5 - magnetic anomaly #5. Modified after Cannat, Sauter, et al. (2019).

pointing from the central footwall to the emergence of detachment D10 (Fig. 4.3 b), consistent with the dynamics suggested by Reston and McDermott (2011). Since the temperature field evolves with the seafloor relief, the upward movement of the footwall results in a shallow temperature maximum in the central footwall close to the centre of the incipient solid-block rotation. The resulting rheological weakening focuses flexural strain (Fig. 4.3 c) and acts as a trigger for the new fault D11 with a polarity opposite to its predecessor D10, in agreement with the assumption that a new fault cuts the hinge of its predecessors footwall (Reston, 2018). Eventually, a shear-localizing feedback loop between deformation and grain size reduction/serpentinization is activated. This leads to the formation of a new fault accounting for a major portion of extension and the cycle starts over again (D11 in Fig. 4.3 d).

The stability of the flip-flop cycles are shown in Fig. 4.4. We find that successive strain rate increase and focusing occur simultaneously with grain size reduction prior to the "activation"

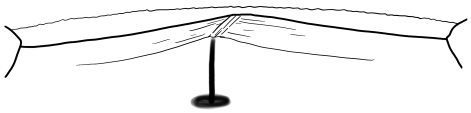

of the new fault zone, which from then on accommodates a major part of the deformation (dashed vertical lines in the left panels of Fig. 4.4). For evaluating each fault's lifetime we take the time span between the activation of one detachment to the next. Thus, the mean fault duration is also obtained by dividing the total duration of a faulting sequence by the number of faults, allowing for comparison with the SWIR data by Cannat, Sauter, et al. (2019). The results of this simulation are in perfect agreement with the data from the SWIR.

The strain rate of each fault peaks at around $3 \cdot 10^{-13}\,\mathrm{s}^{-1}$, while fault zone width and minimum grain size converge to 1 km and 1.5 µm, respectively, in agreement with seismic and petrological data (Bickert et al., 2021, 2020; Momoh et al., 2020).

Besides the similarities between our simulation, SWIR observations and the classical flip-flop mechanism (Reston, 2018; Sauter et al., 2013), we also see some differences. From the theoretical model, we would expect the new fault to cut its predecessors exhumed shear plane a few kilometres away from its emergence. Also, with the formation of the new fault, the predecessor should successively fade out as it reaches the colder and thicker off-axis lithosphere. Instead, new faults in our simulations often cut the shear plane around the emergence, and the preceding fault remains active and continues to exhume mantle material to the seafloor. The two simultaneously active faults enclose a central horst with predominantly vertical motion, until it tilts towards the older fault and initiates the mechanism discussed above. Slip on the old detachment ends with the formation of the second next fault with same polarity (D9 becomes inactive when D11 forms; see Fig. 4.3 d). Interestingly, this faulting sequence can also explain the segments of abnormal seafloor age pattern at the SWIR (Cannat, Sauter, et al., 2019). To observe more classical flip-flop detachments with more pronounced roll-back, a stronger reorientation of the fault zone from initially straight to curved would be required. Tests have shown that a lower yield stress, i.e. lower friction angle and/or cohesion, or an increase of η_{vp} in the visco-plastic regularization lead to faster yielding and wider fault zones, both allowing for more efficient fault zone reorientation and roll-back.

Our model with imposed temperature structure generally confirms the conclusion of Bickert et al. (2020) – despite the differences in modeling techniques and parametrizations – that grain size reduction allows for strain focusing in the deep lithosphere at the root of the incipient detachment fault, which in turn facilitates flip-flop faulting. An important prerequisite for triggering a new fault of opposite polarity is, however, a higher temperature in the footwall relative to the colder active fault zone(s) (cf. Figs. 4.2 a and 4.3 b). In the next sections we investigate how such a thermal structure can dynamically evolve through the interplay of tectonic, magmatic and hydrothermal processes.

4.3.2 Models with Dynamic Thermal Evolution

We conducted 36 simulations with a dynamically evolving temperature field to test the effects of hydrothermal cooling – widespread plus enhanced to a certain level within and around active fault zones (see Eq. 4.21b) – and magmatic input in form of sill intrusions that can be converted into a hypothetical M-factor. In all model simulations, the mean axial brittle lithosphere thickness, defined as the minimum depth of the 750 °C isotherm below the seafloor, is in the range of 15.1 ± 1.0 km, which matches observations and facilitates a good comparison

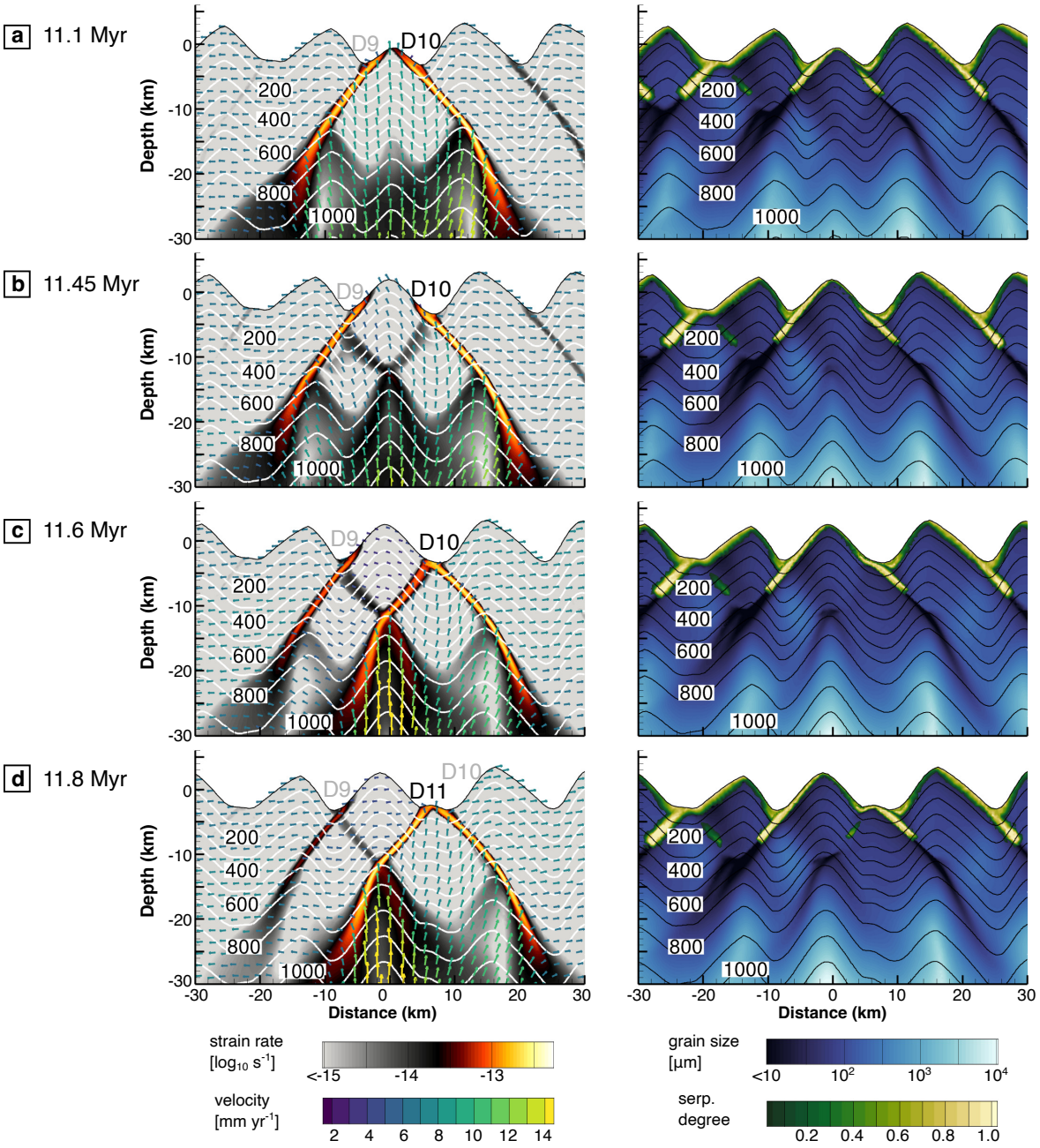

Figure 4.3. Central model region displaying flip-flop dynamics in the model with imposed temperature structure. Left: strain rate and white isotherms, vector colours show advection velocity. Fault numbering as in Fig. 4.4. Right: Grain size in µm (blue to white) overlain by serpentinization degree (green to yellow) and black isotherms. The same graphical framework is used for all related figures. The full sequence can be seen in Movie S4.1.

of the different model calculations. These simulations are labelled using an index of 1 to 36 to refer to them later in the summarizing parameter space plot (Fig. 4.11 below). Additionally, we show simulation 0 in the next section, which has no magmatic input and no hydrothermal cooling at all. Over the following sections we will present the different faulting modes observed in our simulations.

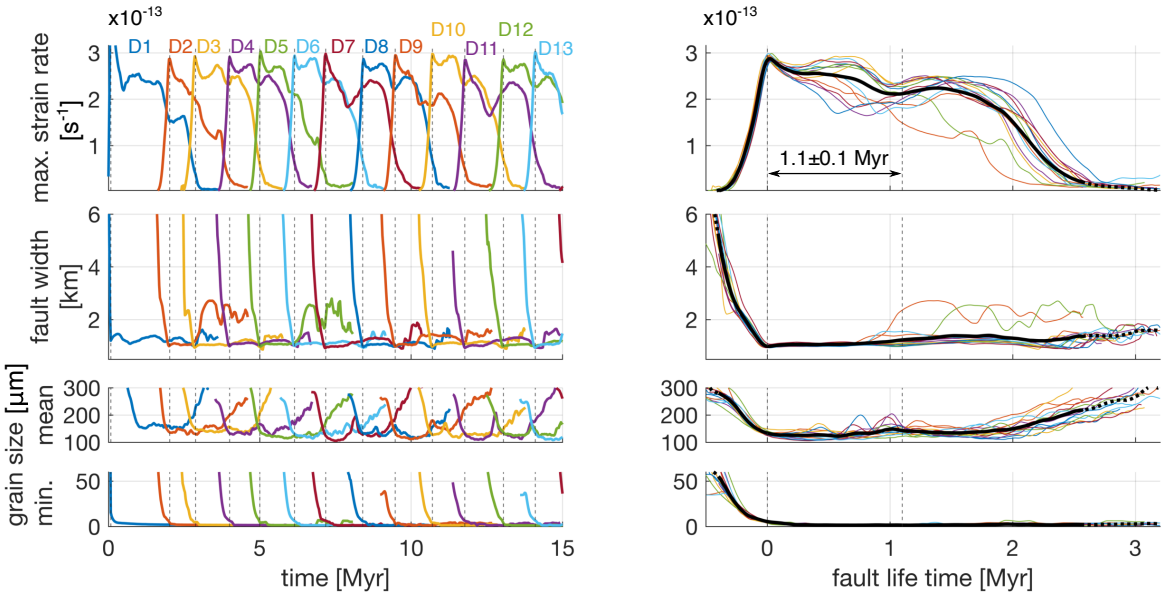

Figure 4.4. Fault zone analysis of the model with imposed temperature structure showing the evolution of strain rate, fault width and grain size. Strain rate and fault width are evaluated in the brittle lithosphere, grain size at the detachment root around the brittle-ductile transition between 500 °C and 1000 °C. Left panel: Time series of subsequent faults. Dashed vertical lines indicate the activation of a new detachment. Right panel: Same data for all detachments in the simulation but as a function of their life time, i.e. shifted so that their point of activation (vertical lines in the left panel) match. The second vertical line indicates the onset of the following detachment, giving a mean fault period duration of 1.1 ± 0.1 Myr (SWIR: 1.1 ± 0.3 Myr; Cannat, Sauter, et al., 2019).

4.3.2.1 Miniature Flip-Flop (No Hydrothermal Cooling)

Without the additional cooling effect of hydrothermal circulation (Nu = 1), the upwelling hot mantle reduces brittle lithosphere thickness (defined by the 750 °C isotherm) to less than 4 km (Fig. 4.5). This result is incompatible with microseismicity data indicating a thickness of around 15 km (Chen et al., 2023; Grevemeyer et al., 2019). Also, the seafloor topography is much smoother than observed at the SWIR. We show this calculation to emphasize the importance of hydrothermal cooling not only at predominantly magmatic fast- and intermediate spreading ridges but also at amagmatic slow- and ultraslow ridges. Interestingly, the faulting pattern is very similar to that of the model with imposed temperature structure and could be

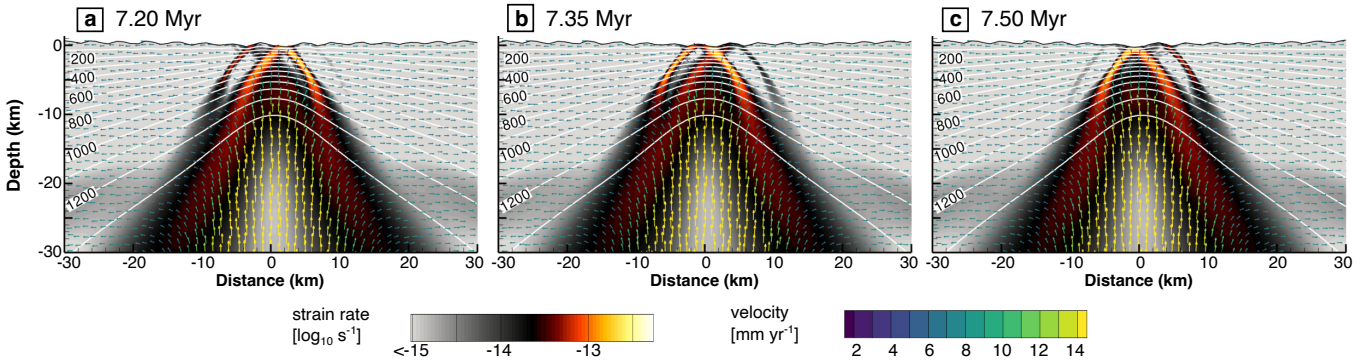

Figure 4.5. Sequence showing a model without any hydrothermal cooling (Nu = 1) and no magmatic input. The full sequence can be seen in Movie S4.2.

considered a miniature version of flip-flop faulting. However, such a thin lithosphere is typical for much faster spreading ridges or for sections of slow spreading ridges with a significantly increased melt budget. We therefore consider this setup to be unrealistic for an amagmatic slow-spreading ridge.

4.3.2.2 Long-Lived Detachment Mode

Each of the simulations of the parameter study shows several faulting modes (cf. Fig. 4.2). There is no calculation that maintains a single faulting mode throughout the 40 Myr simulation time. However, certain faulting modes clearly dominate depending on the intensity of fault zone cooling and magmatic input. Note that all calculations include a wide-spread background hydrothermal cooling to achieve a realistic lithosphere thickness.

We first focus on simulation 1 (Fig. 4.6 a + b), which has neither enhanced cooling of fault zones nor magmatic input (M = 0, $F_{max} = 0$, i.e. $K_{FZ} = 1$ in Eq. 4.21b). With increasing displacement on the fault plane, hot mantle material is pulled up with the footwall. The advective velocity and thus the pull-up is largest close to the active fault zone resulting in a temperature maximum at this position (Fig. 4.6 a) – similar to the findings of Behn and Ito (2008). With ongoing fault activity, the temperature maximum then moves together with the fault zone towards the hanging wall side (Fig. 4.6 b). Thereby, the fault remains in a hot, weak environment instead of migrating into thicker, stronger lithosphere. This generally allows the fault to stay active significantly longer than a typical flip-flop detachment and leads to a *long-lived detachment* that may be accompanied by accommodating footwall faults.

For most simulations with low hydrothermal fault zone cooling and low magmatic input, we observe a behavior similar to that of simulation 1. Long-lived detachment faults

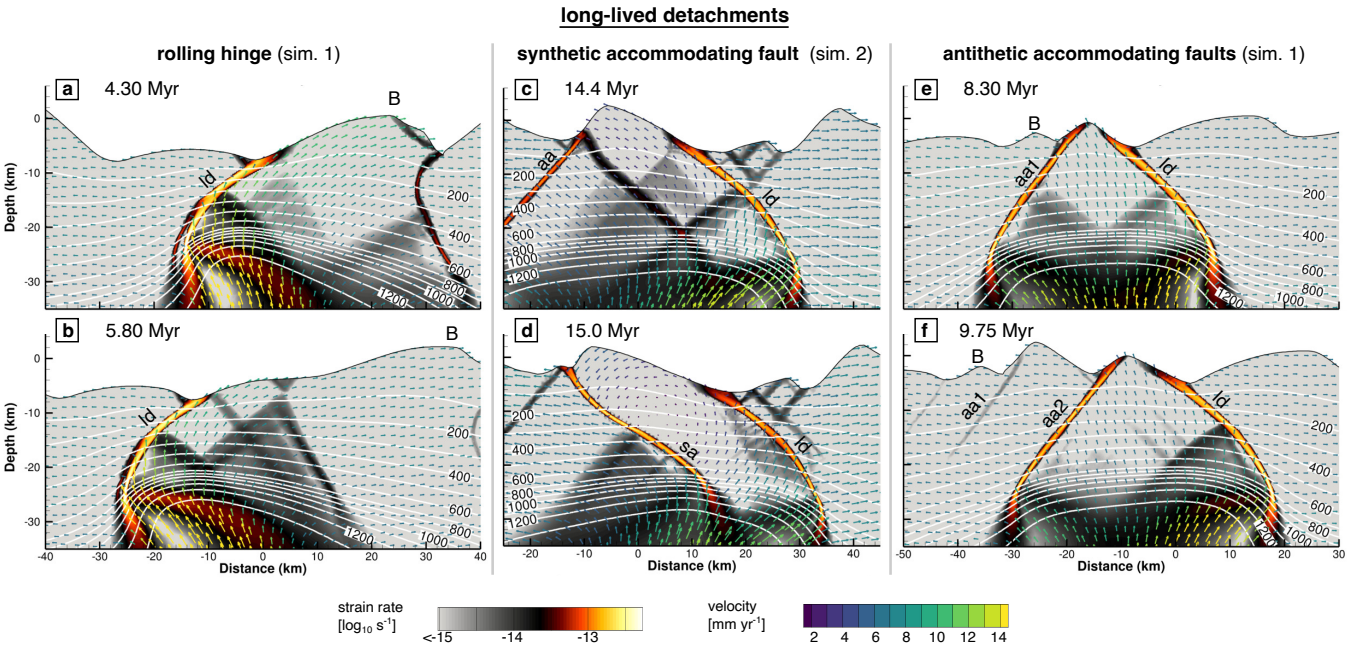

Figure 4.6. Sequences illustrating the different types of long-lived detachments observed in the simulations. Labels: B - breakaway of the long-lived detachment; ld - long-lived detachment; sa - synthetic accommodating fault; aa - antithetic accommodating fault. The full sequences can be seen in Movies S4.3 (a,b,e,f), and S4.4 (c,d).

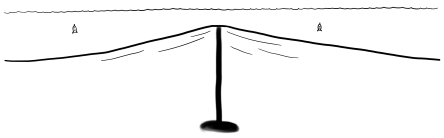

and their accommodating faults are the dominant faulting mode. We observe three variations of long-lived detachments: 1) *rolling-hinge detachments*, 2) detachments with *synthetic accommodating footwall faults*, and 3) detachments with *antithetic accommodating footwall faults*. The different modes are illustrated by sketches in Fig. 4.2 a and by snapshots from two different simulations in Fig. 4.6.

Rolling-hinge detachments (Fig. 4.6 a + b) are characterized by a rotation of the footwall that transitions into a horizontal plate motion further off-axis (Buck, 1988; Lavier et al., 1999). This goes along with stretching and shearing in the footwall, but the emerging shear bands do not become focused enough to form a new fault zone (Fig. 4.6 a). At the seafloor, a very smooth and kilometre-long shear plane is exhumed.

Synthetic accommodating faults are secondary faults of the same orientation as the detachment but opposite curvature in the upper part (Fig. 4.6 c + d). Similar faults have been observed by Lavier et al. (2000) and Sandiford et al. (2021). In-between this fault-pair, a closed solid-block rotation with very little shear deformation begins. The accommodating fault either fades out after some time or realigns its curvature and may become the major active detachment fault itself.

Antithetic accommodating faults (Fig. 4.6 e + f) cut the footwall of the active detachment with opposite polarity. The general deformation in the footwall remains dominated by the curved long-lived detachment. After producing significant relief, but before experiencing major roll-back, the accommodating fault fades out instead of becoming a full-grown detachment. We find that one long-lived detachment fault can cause and survive multiple antithetic accommodating faults. Interestingly, the resulting fault zone pattern and seafloor topography closely resembles that of flip-flop faulting.

4.3.2.3 Detachments with Opposite Polarity

One characteristic of flip-flop faulting is the alternating polarity of successive detachments, each of which accommodates a significant amount of extension. A sequence of such detachments with alternating polarity is thus required for considering a simulation to exhibit flip-flop faulting.

Figs. 4.7 and 4.8 show a temporal evolution from simulation 28 ($M = 0.1$, $F_{max} = 1.5$), which is an example for such a sequence and shares many characteristics discussed above for the model with imposed temperature structure. With increasing displacement on the detachment fault, the footwall experiences roll-back (Fig. 4.7 a + b left column). At the same time, the increased cooling of the active fault zone(s) shifts the isotherms around the detachment to slightly greater depth (Fig. 4.7 a + b right column). This cooling effect increases the temperature difference between active fault zone and footwall and thereby pushes the temperature maximum further into the footwall. The emplacement of intrusions (size: 4000×400 m every 80 kyr) near the temperature maximum further weakens the footwall, which eventually allows for enough focusing of flexural strain to initiate the feedback loop between grain size reduction and strain rate increase (Fig. 4.7 b + c). After the new detachment fault of opposite polarity has formed (Fig. 4.7 c), heat is extracted from its root by (in our case parametrized) hydrothermal circulation. The heat extraction causes the temperature maximum again to

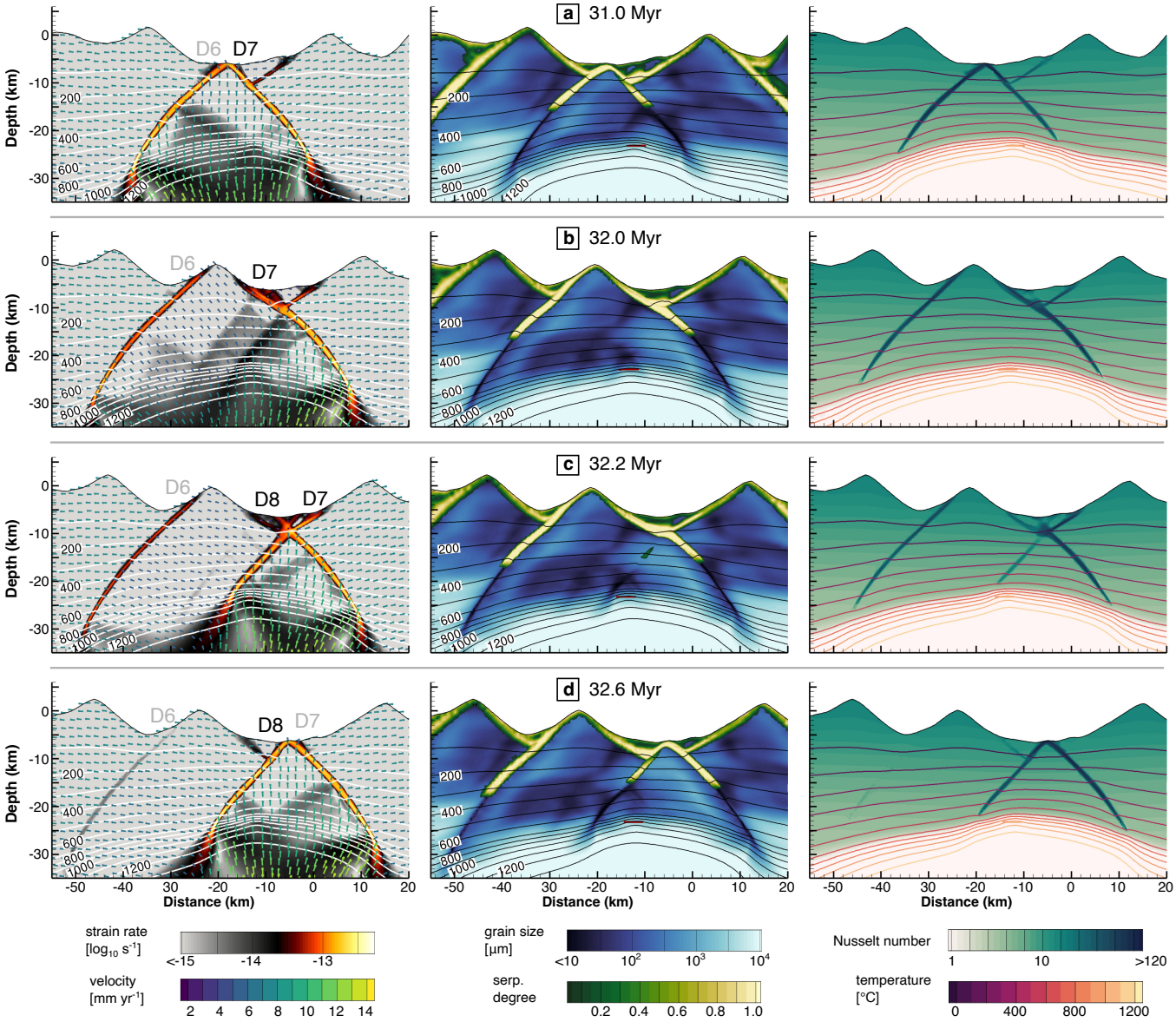

Figure 4.7. Flip-flop sequence from simulation 28 including hydrothermal fault zone cooling and magmatic intrusions (M = 0.095, $F_{max} = 1.5$). First and second column: see Fig. 4.3. Third column: Nusselt number on a logarithmic scale, maximum value $\mathrm{Nu}_{max} \approx 200$. Intrusions are marked in red in the central panels and by temperature in the right panels. The full sequence can be seen in Movie S4.5.

move into the footwall of the new detachment (Fig. 4.7 d) and the next cycle begins.

In the model with a dynamic thermal evolution, footwall roll-back is more pronounced and takes longer compared to that with an imposed temperature structure. This is reflected in a smoother seafloor relief and longer fault life times. The stronger roll-back is possibly related to slightly wider fault zones. Compared to the model with imposed thermal structure (Fig. 4.4), the strain rate of individual faults (Fig. 4.8) does not drop as significantly at the activation of the next detachment, indicating a different partitioning of the total deformation between the active detachments. Furthermore, within the dynamic thermal model flip-flop sequences are shorter and faulting is generally more diverse including cross-cutting faults and more variable fault dips and life times.

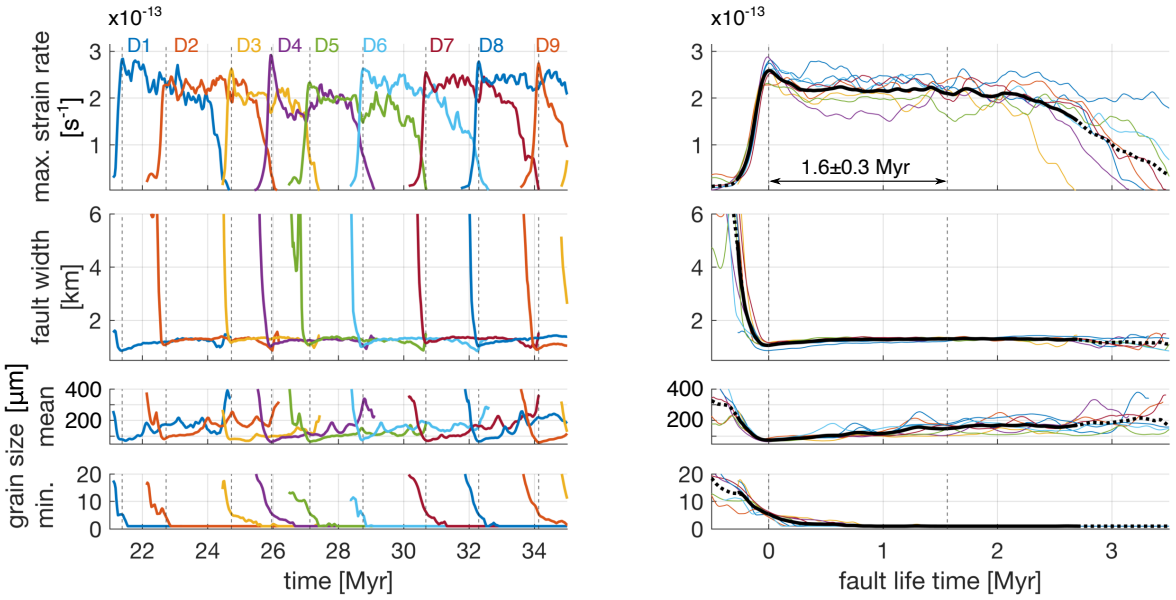

Figure 4.8. Fault zone analysis of a flip-flop sequence from simulation 28 including hydrothermal fault zone cooling and magmatic intrusions (M = 0.095, F_{max} = 1.5). Analysis strategy as described for Fig. 4.4.

While single detachments of opposite polarity are initiated at lower hydrothermal fault zone cooling, it requires $F_{max} \geq 1.5$ to achieve stable sequences of alternating polarity in the absence of intrusions (simulation 4). A similar trend is observed in simulations without enhanced cooling of fault zones, where a magmatic input equivalent to M = 0.095 (simulation 25) or more is required to achieve such stable sequences. Combinations of both, moderately enhanced fault zone cooling and moderate magmatic input, also reveal stable sequences of alternating polarity. This indicates that a combination of hydrothermal activity in fault zones and magmatic sill intrusions below the footwall may favor flip-flop faulting.

4.3.2.4 Deep-Cutting Faults: Criss-Cross and Spider Modes

Another type of faults that we observe in many simulations are *deep-cutting faults*. The name refers to the case where a new fault of opposite polarity cuts its predecessor several kilometers below the seafloor. The two faults then form an X-shape that encloses a large central block with significant surface relief (Fig. 4.9). After the formation of such a deep-cutting fault pair, we observe two different faulting pattern evolutions.

The first mode is what Bickert et al. (2020) have named *spider mode*, where both deep-cutting faults remain active almost symmetrically. For geometrical reasons, this configuration requires an alternating activity of the faults below the crossing point, which temporarily induces strain and weak regions in both footwalls. These regions of accumulated strains migrate upwards and form the 'spider legs' faintly visible in the strain rate plots (Fig. 4.9 b + c). While magmatic intrusions are not necessarily required to activate spider mode, they support and stabilize this mode by weakening the region below the intersection of the two faults. Spider mode typically ends after some million years when one fault becomes dominant due to an emerging asymmetry.

Criss-cross mode is a new mode identified in our simulations. It represents the second option for the evolution of deep-cutting faults, in which the two faults migrate through the central block by slicing it in several discrete steps. Each step is a short-lived normal fault that offsets a part of the central block (Fig. 4.9 e). The name *criss-cross* refers to the alternating, almost perpendicular normal faults that cut-off sections of the central block. The number of dissecting normal faults during the criss-cross phase varies, and so does the impact on the enclosed surface relief. Criss-cross mode ends when the intersection point of the two deep-cutting faults reaches the seafloor allowing them to separate and migrate off-axis in opposite directions, similar to "detachments of opposite polarity".

We find criss-cross faults to become more frequent with stronger fault zone cooling. At increased F_{max} (Eq. 4.21b), new faults tend to form at a higher frequency. Thus, there is less time for shifting the temperature maximum away from the root of a fault into its

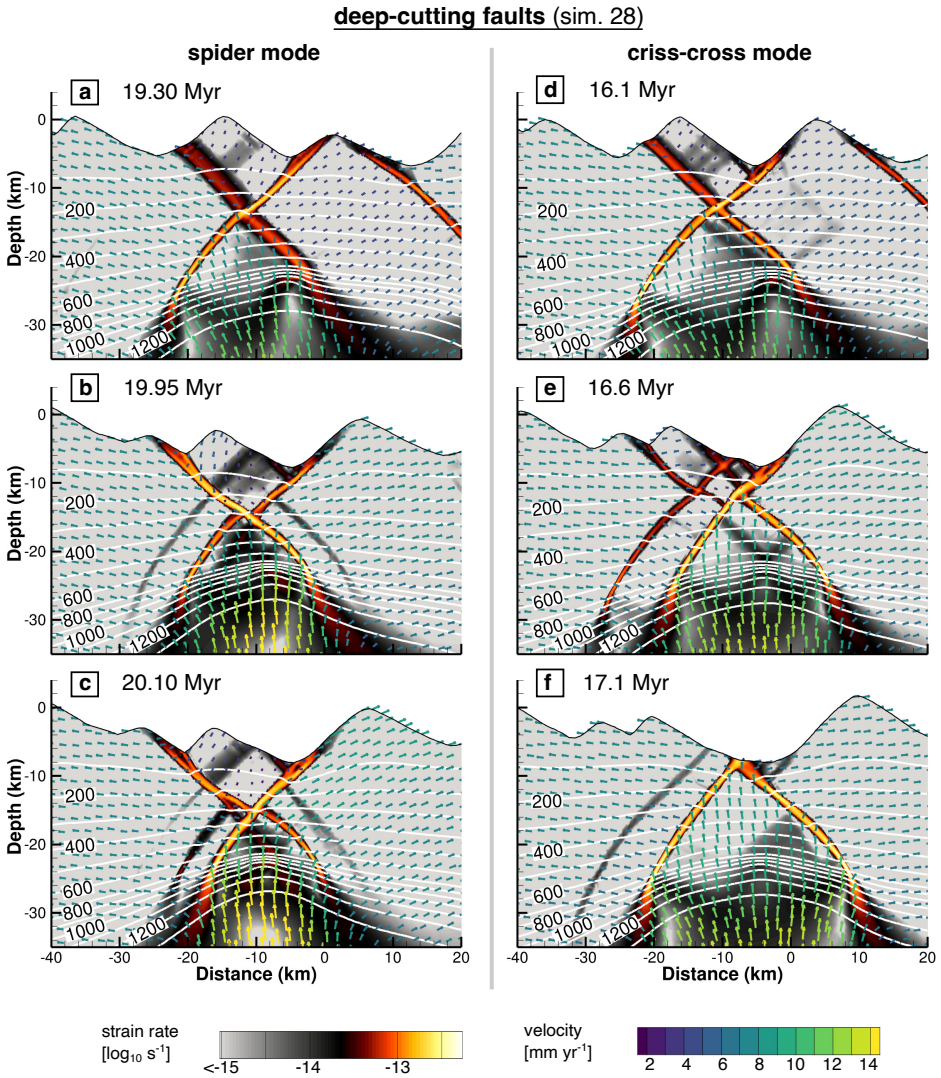

Figure 4.9. Exemplary sequences from simulation 28 showing two different modes of deep-cutting faults. **a - c**: spider mode: both deep-cutting faults remain symmetrically active. The 'spider legs' are visible in c in the low strain rate regions on the side of the central block. They are even better visible in the grain size evolution in the corresponding Movie S4.5 showing the full sequence. **d - f**: criss-cross mode: deep-cutting faults repeatedly cut the enclosed block and offset the surface relief.

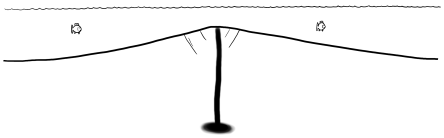

footwall, and the next fault is more likely to form as a deep-cutting fault close to the root of its predecessor. The more spontaneous fault initiation also facilitates the formation of the sequence of dissecting normal faults.

4.3.2.5 Chaotic Faulting Patterns

At the largest values of F_{max} that we tested, fault formation becomes mostly chaotic. New faults form at high frequency, can be scattered around the axial region and possess variable fault dip and curvature. In this mode, more than two faults may be active simultaneously and accommodate comparable portions of total extension. Since each fault is repeatedly dissected by new faults, the surface relief is continuously reworked, which renders an interpretation of seafloor topography rather complicated. An exemplary sequence from simulation 24 ($M = 0.07$, $F_{max} = 2.5$) displaying this *chaotic mode* is shown in Fig. 4.10. Simulations featuring this mode do not resemble any observations from amagamatic ridges and we therefore consider this setup to be unrealistic.

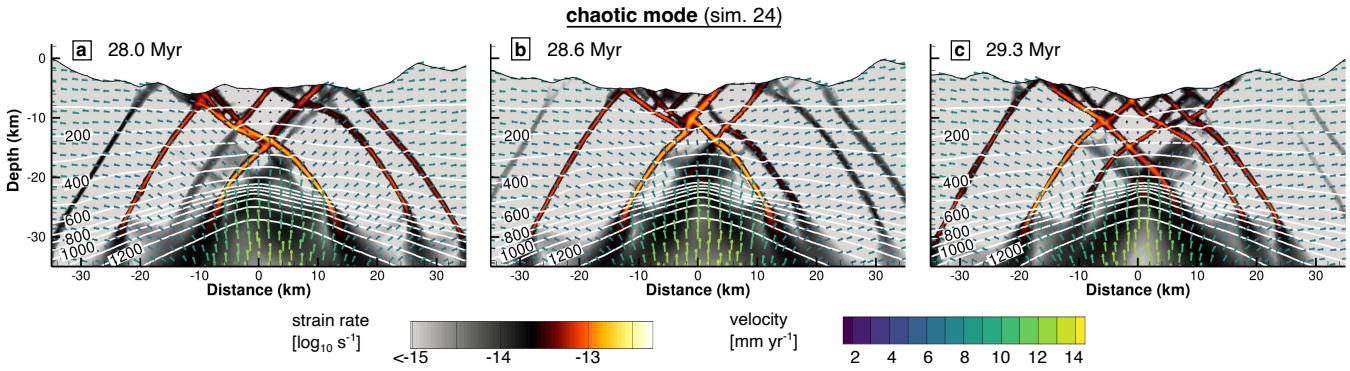

Figure 4.10. Exemplary sequences from simulation 24 showing the chaotic faulting mode. The full sequence can be seen in Movie S4.6.

4.3.2.6 Faulting Mode Summary

The faulting modes resulting from varying fault zone cooling and magmatic input are summarized in Fig. 4.11 and we observe several trends. The occurrence of long-lived detachments and their accommodating faults is mainly limited to simulations with relatively low fault zone cooling ($F_{max} \leq 1$), while criss-cross mode evolving from deep-cutting faults mainly occurs for $F_{max} \geq 1$. Chaotic mode is limited to the largest values of $F_{max} \geq 2.0$. Spider mode is observed almost equally over the whole range of F_{max} that we tested, however it occurs more frequently with increasing M. Consequently, the number of observed long-lived detachments and criss-cross faults slightly decreases with increasing M. Detachments of opposite polarity are the most abundant faulting mode in our simulations with $F_{max} \leq 2.0$.

Over the next sections, we will discuss the mechanisms that produce flip-flop detachment faulting in our model and evaluate different fault sequences from our results in the scope of observations from the SWIR.

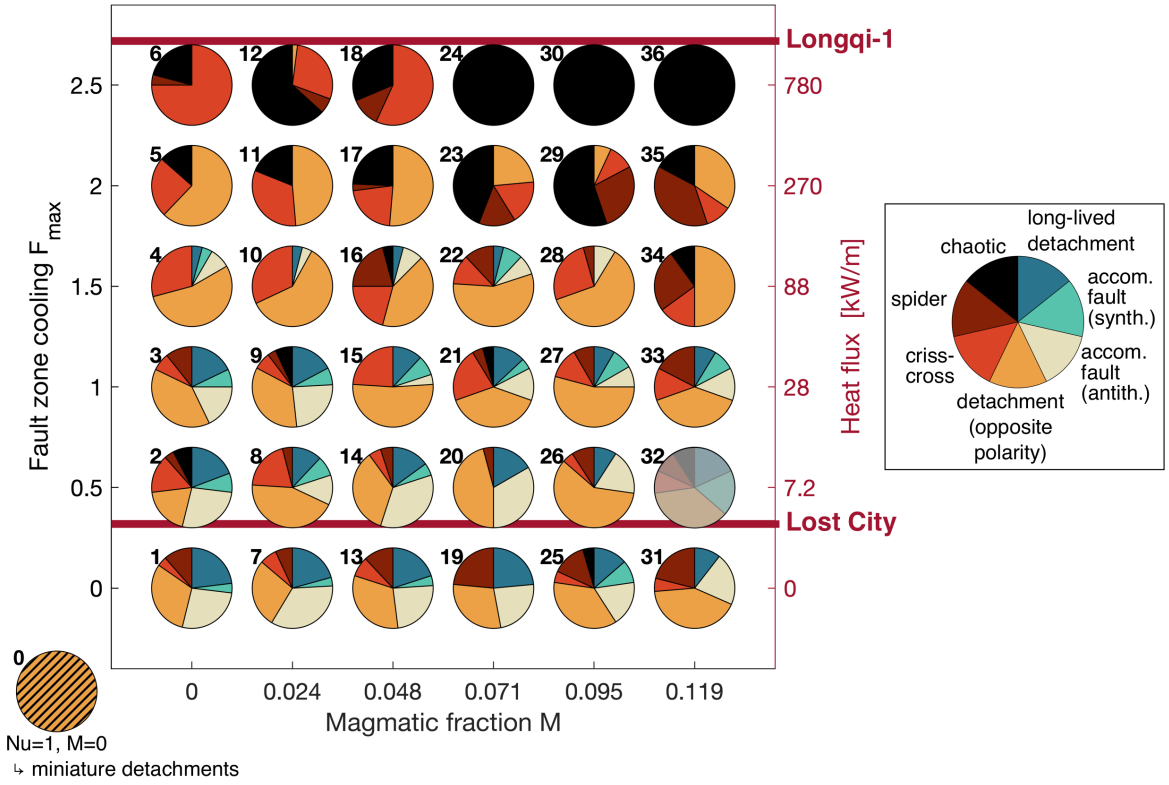

Figure 4.11. Parameter space plot showing all 36 simulations of the parameter study as a function of magmatic input fraction (controlled by intrusion size and periodicity) and magnitude of fault zone cooling. Additionally, simulation 0 without any hydrothermal cooling and magmatic intrusions is shown. Pie diagrams show the different faulting modes identified in each simulation. Fig. A.2 in Appendix A breaks down the pie diagrams to the percentages of each mode during the 40 Myr model time. Since faults can form as one type and evolve to a different type, e.g., synthetic accommodating faults to long-lived detachments, the total number of types per pie diagram generally adds up to more than the total number of faults per simulation. Simulation 32 is blurred because faulting takes place close to the domain boundary, i.e. outside of the central well-resolved mesh region, and the simulation is therefore disregarded. Descriptions of the faulting modes are found in the text as is the conversion from F_{max} to hydrothermal heat flux values at the fault zone. Literature values for the total heat output of Lost City (40 kW) and Longqi-1 (250 MW) vent fields are taken from Lowell (2017) and Tao et al. (2020), respectively, and are divided by their fault zone parallel extent.

4.4 Discussion

4.4.1 Thermal Structure of the Footwall

Our simulations demonstrate that a crucial prerequisite for sequences of alternating detachments that constitute flip-flop faulting is a temperature maximum in the central footwall. In the model with an imposed temperature structure this automatically evolves as the footwall is uplifted. In the fully-coupled model with a dynamic thermal evolution, footwall uplift together with hydrothermal fault zone cooling yields a similar thermal structure that is reinforced by magmatic intrusions. To assess the influence of fault zone cooling and magmatic sill intrusions on the temperature field and thus faulting pattern more systematically, we reduce the number of non-linear feedbacks in the fully-coupled model. This is done by taking the deformation field from simulation 28 and combining it with different parameter combinations

of F_{max} and M to compute alternative temperature evolutions. In Fig. 4.12 we compare the temperature field of simulation 28 with those evolving with the same magmatic input but no enhanced fault zone cooling (setup of simulation 25), same fault zone cooling but zero magmatic input (setup of simulation 4) and without either of the two processes being active (setup of simulation 1). We will analyse the temperature changes relative to the temperature field evolving without intrusions and enhanced fault zone cooling.

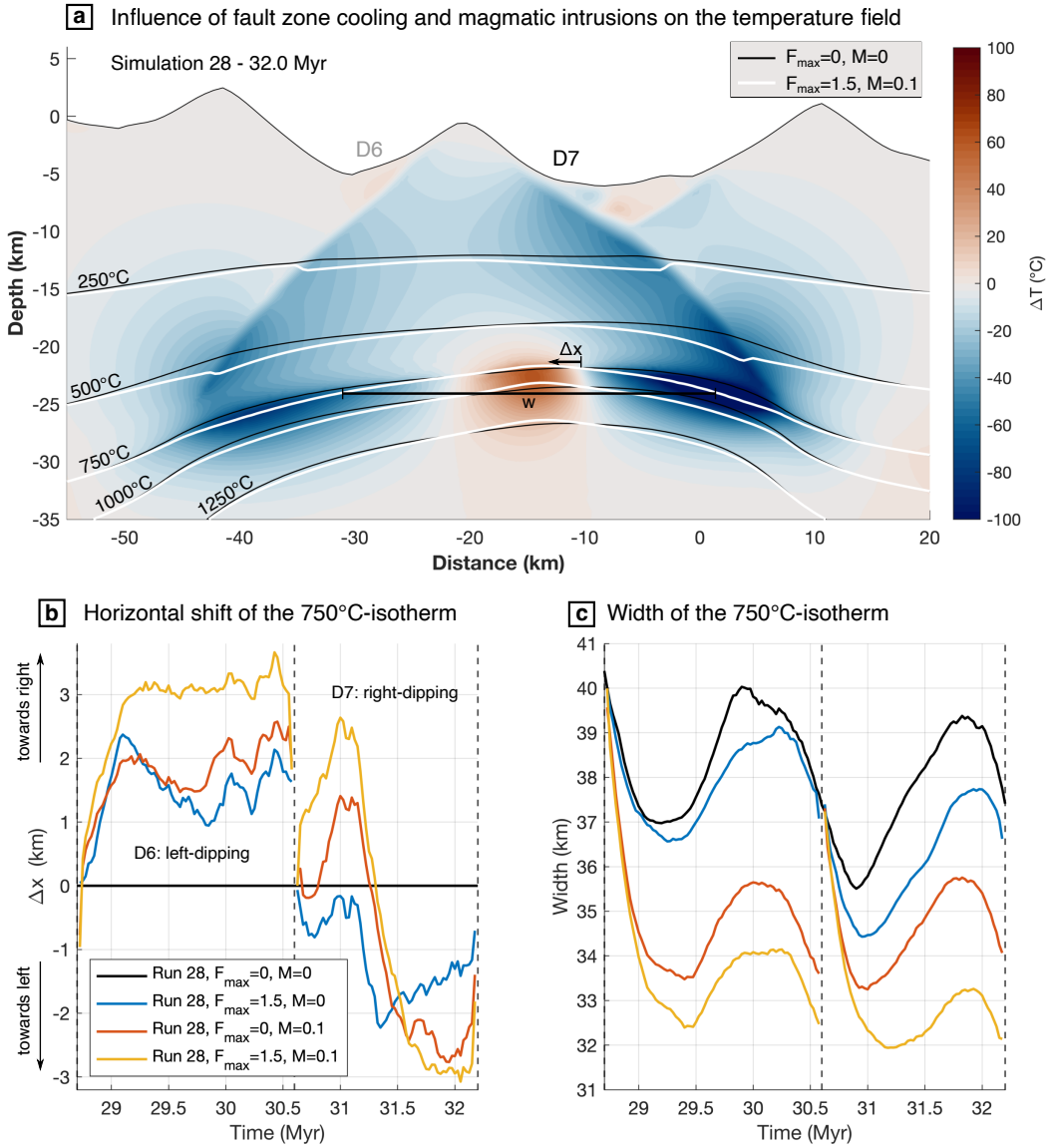

Figure 4.12. Analysis of the influence of different parameter combinations on the temperature field using the deformation from simulation 28. **a:** Temperature difference between simulation 28 and its evolution when setting $F_{max} = 0$ and $M = 0$ (same snapshot and fault numbers as in Fig. 4.7 b). White isotherms are from simulation 28, black ones are for $F_{max} = 0$ and $M = 0$. The horizontal bars illustrate the meaning of the parameters plotted in b and c. **b:** Horizontal shift of the shallowest point of the 750 °C-isotherm compared to the setup with $F_{max} = 0$ and $M = 0$. Dashed vertical black lines indicate the formation of a new fault. Note that the temperature field is reset at 30.6 Myr when the new fault forms to facilitate this comparison. **c:** Width of the 750 °C-isotherm compared to the setup with $F_{max} = 0$ and $M = 0$. The width is calculated as the geometric mean between five slices at 1 km to 5 km below the shallowest point of the isotherm.

Fig. 4.12 a shows how the parametrized hydrothermal activity efficiently cools the currently active D7 and, to a lesser extent, the preceding fault zone D6. This shifts the temperature maximum at the brittle-ductile transition away from the active fault zone up to 3 km into the central footwall (Fig. 4.12 b). The emplacement of intrusions near the temperature maximum reinforces (Fig. 4.12 a) and narrows this high-temperature region by about 6 km (Fig. 4.12 c). Note that the cooler regions below the active faults result from stronger background cooling of the brittle lithosphere (i.e. larger Nu_0), which is adjusted to the extra heat input from the intrusions to reproduce the observed lithosphere thickness (see Fig. A.1).

The effects of these temperature variations on the faulting mode can be best understood by translating the temperature field in the deep brittle lithosphere and below to a modified viscosity and thus strength structure. Reduced temperature in the deeper fault zone corresponds to a viscosity increase, making the fault zone less efficient after a period of slip and cooling. Magmatic intrusions on the other side cause increased temperatures in the footwall below the brittle lithosphere, serving as a weak spot to focus flexural deformation. This combination of reducing the active fault zone efficiency and providing a weak spot in a geometrically favorable position is what triggers the next detachment of opposite polarity. The repetition of this cycle leads to the flip-flop faulting sequence (Reston, 2018; Sauter et al., 2013).

4.4.2 Model Assumptions

4.4.2.1 Hydrothermal Cooling of Active Fault Zones

As a first step towards a hydro-thermo-mechanical model that resolves porous flow within a visco-elasto-plastic deforming lithosphere, we have parametrized the heat transport by hydrothermal fluids taking into account the deformation state of the rock. To relate the magnitude of hydrothermal cooling predicted by our model to natural systems, we convert the enhanced thermal conductivity and resulting temperature gradients to an equivalent hydrothermal power output at a hypothetical fault-related vent site. To facilitate a comparison between all model calculations shown in Fig. 4.11, we aim for a relation that only depends on the factor F_{max}, by which we enhance the cooling effect of fault zones. Doing so allows to place a second axis of hypothetical hydrothermal heat fluxes on the right side of Fig. 4.11. From our simulations we evaluate representative values for a fault-related seafloor temperature gradient of $0.05\,^{\circ}\mathrm{C\,m^{-1}}$, and a fault zone width, over which an enhanced heat flux from the lithosphere into the ocean occurs, of 2 km. As fault zone thermal conductivity we take the conductivity of serpentinized mantle at the seafloor reduced by the background cooling. Using Eqs.(4.21b) and (4.22) we obtain a fault zone thermal conductivity of

$$\kappa_{FZ} = \kappa_{0,serp}\,(\mathrm{Nu}_0 - 1)\exp\left(\beta\left(1 - \frac{P_{sf}}{P_{ht}}\right)\right)\cdot\left(10^{F_{max}} - 1\right). \tag{4.25}$$

The value of Nu_0 for each value of F_{max} is taken from the simulation at $\mathrm{M} = 0$. Seafloor hydrostatic pressure P_{sf} is evaluated in the axial valley. Multiplication of temperature gradient, fault zone width, and fault zone conductivity κ_{FZ} provides an estimate for the total power output of the hypothetical vent fields. Although the resulting estimates should be viewed with

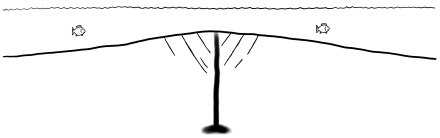

caution because of the uncertainties involved, they allow at least for an order-of-magnitude comparison with vent field observations. Fault related heat fluxes predicted by our model (axis on the right-hand-side of Fig. 4.11) span a plausible range from the low-temperature Lost City Hydrothermal Field located on a core complex off-axis the Mid-Atlantic Ridge (Lowell, 2017) to the high-temperature Longqi-1 Vent Field located on the hanging wall of a detachment fault in a magmatic section of the SWIR (Tao et al., 2020).

The hydrothermal site that is most relevant for the flip-flop dominated section of the SWIR investigated here is the recently discovered Old City hydrothermal field (Cannat, Agrinier, et al., 2019) located on the exposed fault surface of the currently active detachment in the amagmatic segment. Total heat flux estimates or venting temperature data are still missing, however, the vent field has a larger spatial extent than Lost City (Cannat, Agrinier, et al., 2019) and an estimated comparable venting temperature of <100 °C (Fan et al., 2021). We therefore suppose that values of F_{max} much larger than 1.5 seem unlikely, because they would correspond to heat fluxes of more than twenty times that of Lost City. However, venting temperatures of > 335 °C of the inactive Tianzuo hydrothermal field inferred from geochemical data (Ding et al., 2021) could point towards higher heat fluxes. More data on those and other, presumably existing (Baker et al., 2004) yet undiscovered vent fields in similar tectonic settings, is needed to constrain representative numerical models. Note that our model cannot account for the limited life time of individual vent fields (Humphris & Cann, 2000) but parametrizes the time-averaged cooling effect of all hydrothermal activity.

An open question is, to which depth hydrothermal circulation can efficiently cool the lithosphere. The maximum depth of hydrothermal fluid flow is mainly controlled by the subsurface permeability structure, which is a difficult to assess quantity and suggested values for oceanic lithosphere span orders of magnitude (e.g., Andersen et al., 2015; Barreyre et al., 2018; Hasenclever et al., 2014; Marjanović et al., 2019). Models and data generally suggest a decrease of permeability with depth (e.g., Kuang & Jiao, 2014, and references therein), which would inhibit hydrothermal heat extraction at depths greater than a few kilometres. At temperatures above 600 °C to 800 °C, pore space is assumed to be thermally closed to vigorous fluid flow (Hirth et al., 1998). Fan et al. (2021) argue that under certain circumstances thermal cracking can extend the reach of hydrothermal convection down to 10 km depth. Tao et al. (2020) model fluid circulation in the brittle lithosphere over a thickness of 13 km if permeability increase in the fractured fault zone is sufficient. Observation of hydrothermally altered minerals at this and comparable tectonic settings indicate that at least a limited amount of fluids reaches down to the brittle-ductile transition, even in the presence of an extremely thick lithosphere (Bickert et al., 2023; Patterson et al., 2021; Vieira Duarte et al., 2020). However, these observations may represent the limit of maximum fluid penetration depth, while active hydrothermal convection and cooling may be efficient only at shallower depth.

Our model accounts for the discussed effects by having a pressure-dependent scaling of thermal conductivity leading to a decrease with depth in agreement with previous studies (e.g., Gregg et al., 2009), a fading influence across the brittle-ductile transition and a significant increase of the hydrothermal cooling effect around actively deforming fault zones. The incorporated depth-dependence is, however, possibly underestimated compared to scaling lengths

given by Kuang and Jiao (2014). Note that the cooling effect incorporated by the Nusselt number parametrization spatially integrates the effect of fluid flow and may thus reach deeper than active hydrothermal circulation. To answer more in-depth questions about the role of active fault zones on hydrothermal circulation pathways – including potential feedbacks with magmatism and faulting – will require to resolve porous flow of hydrothermal fluids in the model instead of parametrizing its cooling effect.

While certainly affected by our model limitations, including its 2-D nature (discussed below), our results nonetheless indicate that enhanced cooling of active fault zones is a key process controlling the tectonic mode of a magma-poor ridge section. Simulations in which the tectonic state has no influence on the parametrized hydrothermal cooling ($F_{max} = 0$) produce only limited flip-flop faulting, while simulations with a too strong enhancement of fault zone cooling do not produce flip-flop faulting at all.

4.4.2.2 Magmatic Sill Intrusions - Model vs. Data

In this study we have varied sill sizes as well as emplacement frequencies such that the magmatic input fraction corresponds to a reasonable range of M-values lower than 0.12. This can be considered almost amagmatic, and limited amounts of melt are in agreement with observations (Paquet et al., 2016; Sauter et al., 2013). Intrusions in our model facilitate flip-flop faulting through direct (rheological) and indirect (thermal) weakening. We hypothesize that further mechanical aspects which we have not considered in our model, such as additional stresses resulting from volumetric effects of intrusion emplacement and cooling or melt migration along faults could increase the influence of intrusions and affect the faulting types summarized in Fig. 4.11. Moreover, we cannot speculate on the dominant faulting modes at greater M-values, where volumetric effects become critical and diking is essential to explain the transition to the more magmatic faulting mode of corrugated detachments.

When designing our model, our intention was to put as few constrains on the dynamic evolution as possible. We therefore decided to not prescribe the location of intrusions but to choose realistic criteria for where ascending melts might gather to form a sill. We assume that melts migrate up to the shallowest position of the basaltic solidus temperature, which most often is located in the footwall below the active fault. While variable emplacement depths could affect our results, our chosen method is consistent with the predictions of the numerical study by Chen et al. (2022) on the thermal regime of magma-poor segments. After emplacement, cooling intrusions are transported upward where they are cut and sheared by subsequent faults. This cycle is in agreement with recent seismic data (Momoh et al., 2020): Stacked sills in the deep lithosphere can potentially explain a cluster of sub-horizontal seismic reflectors between 9.3 km and 13 km depth, while sheared intrusions could intensify the seismic signature of the detachment faults, which are identified by a series of dipping reflectors.

4.4.2.3 3-D Effects of the Ridge Axis

Both amagmatic corridors of the 62°E to 65°E segment of the SWIR are enclosed by more magmatic sections characterized by axial volcanism and symmetric normal faulting. This segmentation presumably results from strong along-axis focusing of melts (Cannat et al.,

2003). The more magmatic sections do most likely serve as thermal and mechanical anchors for the evolution of their magma-poor neighboring segments. We presume this to be the main factor missing in our 2-D model, which cannot account for along-ridge variations in magma supply or faulting patterns. Coupling between an amagmatic segment sandwiched between magmatic sections could prevent long-lived detachment faults from shifting tectonic activity several tens of kilometres from the initial position at the ridge axis. Fault life times would consequently be shorter and faulting patterns more stable.

However, being able to reproduce a stable flip-flop faulting mode in a dynamic thermo-mechanical 2-D model without prescribing the ridge axis position lets us speculate that the interplay of hydrothermal cooling (enhanced in fault zones) and the heat input plus weakening effect of sill intrusions are key mechanisms that facilitate flip-flop faulting.

4.4.3 Tectonic Significance of Observed Faulting Modes

We performed a three-step analysis on each of the simulations. First, we picked the onset time of every fault zone and categorized it (Fig. 4.11). In the second step, we identified fault sequences of at least 4 consecutive faults that fall in one of the two categories "apparent flip-flop" and "true flip-flop" (Fig. 4.13 a + b). As "apparent flip-flop" we categorize faults that produce off-axis dipping fault zones and relatively regular spaced ridges, since these are the main features used to identify flip-flop detachments from observational data. For the category "true flip-flop" we additionally evaluate if the faulting mechanism resembles the flip-flop mechanism described in the previous sections. Faulting sequences are mostly terminated by a long-lived detachment or a deep-cutting fault/ spider mode phase. As a last step of our analyses, we calculate the mean fault duration during the faulting sequences (Fig. 4.13 c).

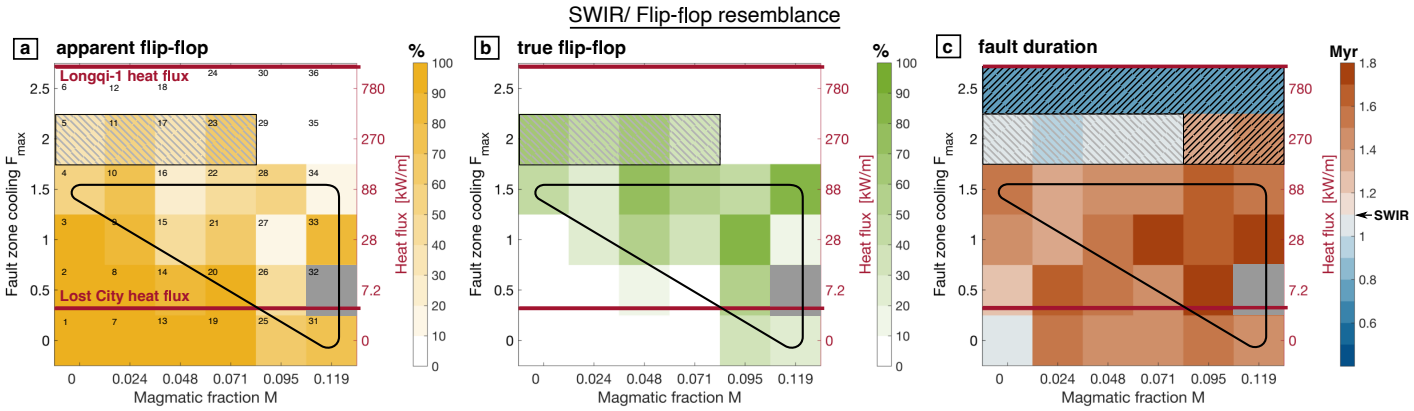

Figure 4.13. Parameter space plot showing the analysis of faulting sequences. All three plots use the framework described for Fig. 4.11, numbers in a are the numerical identifiers of each simulation. Triangular outlined region marks the parameter range producing stable true flip-flop faulting. Gray hatched region at $F_{max} = 2.0$ is excluded from further analyses, see Section 4.4.3.2. **a**: Proportion of faults within identified fault sequences that reproduce bathymetric and subsurface features without displaying classical flip-flop mechanics. **b**: Proportion of faults within identified fault sequences that, additionally to the conditions for a, reproduce the flip-flop mechanism. **c**: Mean fault duration of faults within identified fault sequences. The black hatched region gives mean general fault duration for simulations without SWIR/flip-flop resembling faulting sequences.

4.4.3.1 Fault Life Time

Before we discuss the relevance of the different fault sequences, we will first have a look at the observed fault life times during these sequences. Fig. 4.13 c shows that the mean fault duration of simulations with $F_{max} \leq 1.5$, including the presented flip-flop sequence from simulation 28, is about 1.6 Myr thus ∼0.5 Myr longer than estimated for the SWIR. This is presumably due to the missing 3-D effects of the ridge axis providing external triggers for the formation of new on-axis faults. Another potential reason is the chosen rheology with relatively high yield stress promoting well defined and stable fault zones.

Fault duration slightly increases with an increase of M. Before fault zone cooling can significantly shift the temperature maximum and thus intrusion emplacement into the footwall, intrusions are emplaced close to the root of the new fault zone, stabilizing and prolonging its initial phase. This mechanism is evident in Fig. 4.12 b, where in the first phase of D7 the temperature maximum is shifted towards the fault zone instead of into the footwall, if intrusions are considered (red and yellow lines).

Increasing F_{max} to 2.0 results in a clear drop in the mean flip-flop fault duration. Simulation 5 for example displays sequences of rather uniform flip-flop faulting with a mean fault duration of 1.0 Myr (see Movie S4.7). However, we cannot verify the role of a footwall temperature maximum as a trigger for the new faults in these simulations, as it does not coincide as clearly with the evolving shear band that develops into the next detachment of opposite polarity. We rather believe that instead the feedback loop between rheology, deformation and cooling that allows for a more spontaneous fault initiation explains the increased fault frequency. These feedbacks, however, occur very localized within the fault zone and to be able to properly address it, we would require to resolve hydrothermal flow inside the fault zone and to include effects of fluid-rock-interaction on rheology. Consequently, we see $F_{max} = 2.0$ as the point, where the concept of our parametrization breaks down and we therefore hatched the corresponding region in the parameter space plots in Fig. 4.13.

4.4.3.2 True Flip-Flop Faulting

From Fig. 4.13 b it can be inferred that the activation of flip-flop faulting mechanism is not simply caused by the absence of melt input but seems to result from a sensitive interplay of thermal, tectonic and magmatic processes. The relevant parameter range that best reproduces the conditions necessary for a stable flip-flop faulting mode in line with the commonly accepted interpretation of SWIR observations is identified by the green band in Fig. 4.13 b.

A feature that we observe in many flip-flop producing simulations are antithetic faults in the hanging wall of the active detachment (Fig. 4.7 a, b + d). These are highly consistent with microseismicity data (Chen et al., 2023). In our simulations, they often help to focus the footwall deformation resulting in the next fault of opposite polarity (Fig. 4.7 b + c). This could indicate that new faults indeed form around the emergence of their predecessor as predicted by our simulations. While we know of no evidence for still ongoing deformation along the preceding fault zone, i.e. D2 in Fig. 4.2 b, we could imagine that activity alternates between the two faults on a time scale not resolved by existing observations instead of both being continuously active.

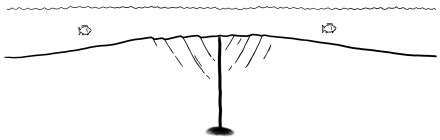

Flip-flop faulting has originally been proposed for the magma-poor rifted West Iberia margin (Reston & McDermott, 2011) and is also observed at another segment of the SWIR (51.5°E to 53.5°E; C. Liu et al., 2020). However, at virtually amagmatic segments along other ultraslow-spreading ridges like the Gakkel or the Knipovich Ridge this distinct faulting pattern has not been observed yet (Meier et al., 2021; Michael et al., 2003). If flip-flop faulting is indeed absent at these settings, this mode may represent a special case that depends on the specific regional conditions – e.g., thermal structure, stress field or the characteristics of neighboring magmatic segments – rather than being the normal state for ridges at this spreading rate and melt supply. This is further supported by the high sensitivity of stable flip-flop faulting to the imposed temperature field and rheology that we observed in tests for the simulation presented in Section 4.3.1. It could explain, why smooth seafloor areas are not observed more frequently.

Note that the parameter range yielding realistic results possibly goes beyond the simulations displaying the longest and most uniform flip-flop sequences, which is supported by both models and data. Reston and McDermott (2011) suggest alternating polarities to be dominant, but do not preclude successive detachments of the same polarity. Flip-flop sequences observed at mid-ocean ridges are of limited duration: eastern corridor of the 62°E to 65°E segment: 11 Myr (Sauter et al., 2013); 51.5°E to 53.5°E segment: ∼7 Myr (Fig. 7 in C. Liu et al., 2020). They also show considerable variability: The western magma-poor corridor of the 62°E to 65°E segment of the SWIR appears to have a lower magmatic budget and more symmetric ridges than the eastern corridor, indicating at least a variable periodicity of the faulting sequence (Sauter et al., 2013). More symmetrical ridges in our simulations often reflect horst-like flip-flop detachments (especially in simulations with imposed thermal structure, Fig. 4.3). Ridges with steeper outward- than inward-facing slopes as observed in the eastern corridor, are indicative of more intensive footwall rollback, or of another faulting mode (see next section). For a more in-depth analyses of the surface relief, surface processes such as erosion and mass wasting would need to be considered. Without, our experiments generally produce stronger relief than observed.

4.4.3.3 "Apparent Flip-Flop" Modes

We now consider sequences featuring other modes besides true flip-flop faulting that are also compatible with some of the most important observations. These modes are antithetic accommodating faults in the wake of long-lived detachments (Fig. 4.6 e + f) and criss-cross faults succeeding a deep-cutting fault. The latter ones are only classified as apparent flip-flop if they offset the enclosed ridge only slightly before they separate at the surface and continue just as regular flip-flop detachments (e.g., Fig. 4.9 d - f). There are some arguments in favor of considering these modes as potential alternative interpretation of the SWIR observations, especially since they occur over a wide and realistic parameter range as Fig 4.13 a shows. Both modes produce a series of off-axis, outward dipping inactive faults and pronounced, more or less regularly spaced ridges. Furthermore, they are generally able to produce an abnormal seafloor age pattern (see arrows indicating seafloor age in Fig. 4.2): antithetic accommodating faults as they are passively transported towards their hanging wall side after becoming inactive, and deep-cutting faults like regular flip-flop faults, depending on where

they finally cut their predecessors exhumed shear plane. However, this is mainly a conceptual notion, because seafloor age with distance from the SWIR axis is, to our knowledge, mostly inferred from sampling breakaway and fault emergence locations and interpreting these within the conceptual kinematics of flip-flop faulting.

Even though high-resolution magnetic profiles exist for this region (Bronner et al., 2014), only one magnetic anomaly can be confidently traced to the amagmatic corridors (C5 in Fig. 4.2 b) due to the extensive serpentinization and very low contribution of magmatic rocks. These data indicate long-term symmetric spreading compatible with flip-flop mode as well as antithetic accommodating (cf. a L-r-r-R-l-l sequence, where uppercase letters stand for long-lived detachments and lowercase letters for accommodating faults) and deep-cutting faulting modes. We are not aware of other data such as high-resolution petrological profiles that would rule out one or the other faulting mode. Moreover, some of the interpreted fault zones are still under debate. For example, D3' interpreted by Corbalán et al. (2021) from seismic velocities has significantly smaller relief than the other detachments and could well be attributed to one of our alternative two modes. Also, both modes can produce asymmetric ridges in agreement with the bathymetry from the eastern magma-poor corridor of the 62°E to 65°E segment of the SWIR.

Including these possible alternative interpretations provides a much broader fit of our simulations to observations than constraining the results to perfectly uniform flip-flop detachment faulting. We thus hypothesize that while pure flip-flop mode may indeed represent a special case, a mix of the three modes discussed here provides a more robust explanation for magma-poor spreading in a very thick brittle lithosphere. This sheds new light on existing data and emphasizes the need for more densely sampled profile data, such as seafloor age measurements and hypocentre locations of microseismicity, also at other settings potentially hosting flip-flop detachment faulting.

4.5 Conclusions

Numerical experiments with an imposed temperature structure (Bickert et al., 2020) have demonstrated the key role of a temperature maximum in the central footwall of a detachment for focusing strain to trigger a new on-axis fault of opposite polarity. Using a dynamic thermo-mechanical model that accounts for the key mechanisms grain size evolution, serpentinization, enhanced hydrothermal cooling of fault zones, and the influence of periodic sill intrusions at the base of the lithosphere, we have further explored the evolving faulting modes. Results of experiments in which we systematically varied magnitudes of magmatic input and hydrothermal cooling show that:

- Fault zone cooling increases the temperature difference between the active fault and its surroundings. It thereby shifts the temperature maximum caused by the upwelling mantle material into the footwall.
- Intrusion emplacement reinforces this temperature maximum and assists strain focusing through thermal and rheological weakening.
- Stable flip-flop faulting that is controlled by the large-scale temperature field is limited

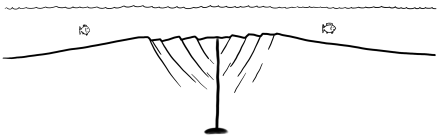

to simulations with a fault-related long-term average heat flux about twenty times that of the Lost City Hydrothermal Field. Generally, flip-flop faulting is observed at reduced magnitudes of hydrothermal fault zone cooling and magmatic sill intrusions if both processes act together.

- Two other faulting modes, antithetic accommodating footwall faults and criss-cross faults, offer an alternative interpretation of the current data base.

Our results indicate that the combination of weak magmatism at the base of the lithosphere and fault zone related hydrothermal activity can explain the thermal structure of the lithosphere and consequently the faulting mode of magma-poor mid-ocean ridges like the 62°E to 65°E segment of the SWIR, which might be more diverse than previously thought.

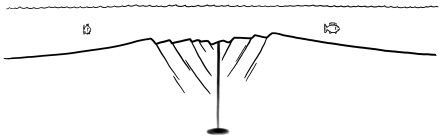

Chapter 5

Massive Sulfide Deposition at the 13°30'N Oceanic Core Complex: Lessons Learned from Coupled Hydro-Thermo-Mechanical Modeling

Arne Glink, Jörg Hasenclever, Lars Rüpke, Matthias Hort, and Sven Petersen

Key Points

- We model the tectono-magmatic evolution of the 13°30'N OCC as well as hydrothermal circulation and sulfide deposition
- Combined effects of topography, fault permeability, transient shallow heat sources and hydrothermal plume interactions control fluid flow
- Modeled 2-D fluid mass flow rates indicate strong 3-D hydrothermal flow focusing across an OCC

Author Contributions:

As the first author of the manuscript and primary contributor to the DFG project proposal, I led the core aspects of this study, including its design, execution, and manuscript drafting. **Jörg Hasenclever** was the main supervisor of the PhD project, making significant contributions across all 14 roles specified in the CRediT taxonomy (National Information Standards Organization, 2022), as detailed at the beginning of Chapter 4. As co-supervisors of the PhD project, **Lars Rüpke** and **Matthias Hort** provided *Supervision* and in their role as head of the working groups in Hamburg and Kiel, respectively, they provided *Resources*. Furthermore, they supported the *Funding Acquisition* and *Project Administration* through feedback on the project proposal and by serving as applicants, and contributed in the *Conceptualization* of the study through frequent discussions and feedback. As an expert for numerical modeling of marine tectonic, magmatic and hydrothermal systems, **Lars Rüpke** also provided feedback and support in *Methodology* and *Software*. **Sven Petersen** has contributed his geological expertise in the *Conceptualization* by helping to sharpen the research question and to identify a suitable case study. All co-authors contributed in the *Review and Editing* of the initial manuscript.

This study has been published in 2025 under the same title in *Geochemistry, Geophysics, Geosystems*, Volume 26, Issue 6 (doi: 10.1029/2024GC012144).

Abstract

Young oceanic lithosphere created at mid-ocean spreading centers is subject to complex magmatic, tectonic and hydrothermal processes, especially in regions of widespread detachment faulting. This study focuses on the oceanic core complex at the Mid Atlantic Ridge at 13°30'N. The OCC hosts the active Semenov-2 vent field and four inactive fields, including the exceptionally large Semenov-4 sulfide deposit (∼10 Mt), which is located near the emergence of a detachment fault. To study the relationship between tectonic detachment faulting and fluid circulation we couple models for mechanical deformation and hydrothermal fluid flow. Our aim is to identify the role of the detachment in controlling location and size of sulfide deposition. First, we develop a baseline model for the tectono-magmatic evolution of the OCC using a data-based sequence for magnitude and position of axial magmatic diking. The resulting history of tectonic deformation provides a dynamic framework for modeling hydrothermal flow through the porous rock, incorporating regions of active faulting and seafloor topography evolution. We then examine the impact of various fault zone permeability structures and heat sources on hydrothermal sulfide deposition. Our results show that a combination of a topographic influence, anisotropic permeability along the fault zone, transient shallow heat sources and plume interactions can efficiently reorganize the hydrothermal system. Increasing horizontal distance between heat source and vent field, however, significantly reduces hydrothermal plume stability. Modeled mass flow rates suggest that vent fields like Semenov-4 and TAG result from the focusing of fluid flow across the entire along-axis extent of the detachment structure.

Plain Language Summary

Mid-ocean ridges are boundaries where tectonic plates move apart and new seafloor forms. In these regions, the Earth's outer layer is thinner, allowing heat from the mantle to drive hydrothermal circulation. Hot fluids travel through the porous rock, where they dissolve minerals, which then settle on the seafloor as ore deposits when the fluids are released into the ocean and cool. These deposits have both scientific and economic importance. At slow-spreading ridges, large and long-lived tectonic faults called detachment faults are common, and many massive ore deposits form near them. This study explores how these faults form and how they influence hydrothermal fluid flow and ore deposition using computer models. We first model the tectonic and magmatic history of a specific detachment fault at 13°30'N at the slow-spreading Mid-Atlantic Ridge. Then, we examine the channeling of fluids along the detachment fault, the influence of different heat sources, and the impact of seafloor topography. Our results suggest that a combination of these factors is needed to focus fluid flow over the large area controlled by the detachment (about 10 km by 10 km) to create the massive ore deposits observed in nature.

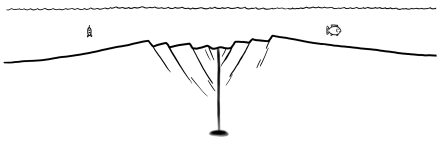

5.1 Introduction

Slow-spreading mid-ocean ridges like the Mid-Atlantic Ridge generally exhibit a more complex and diverse formation history than their fast-spreading counterparts. Due to reduced melt budget, part of the lithospheric extension cannot be accommodated by the accretion of a magmatic crust but is taken up by lithosphere-scale faults (Behn & Ito, 2008; Buck et al., 2005; Tucholke et al., 2008). Tectonic faults are assumed to act as permeable pathways to hydrothermal fluids circulating through the crust, and, together with more scattered magmatic heat sources, may shift hydrothermal venting away from the magmatic spreading axis (e.g., Andersen et al., 2015; deMartin et al., 2007; McCaig et al., 2007). This process is most evident for long-lived oceanic detachment faults controlling ∼40 % of the MAR between 12 °N and 35 °N (Howell et al., 2019, and references therein).

Detachments form during periods of reduced melt supply to the ridge axis and accommodate around half of the extension. While detachments initiate as high-angle normal faults, they rotate to shallower angles of 20 - 30 ° with increasing displacement and exhume lower crust and mantle rocks to the seafloor (e.g., Smith et al., 2006). Phases of very low melt supply are associated with increased asymmetry and migration of the fault across the original ridge axis. This can result in the injection of magma into the central footwall due to the propagation of adjacent ridge segments, leading to the termination of the detachment (MacLeod et al., 2009).

The domed and corrugated detachment shear planes are known as oceanic core complexes, and both foot- and hangingwall of detachments are frequently associated with a range of different types of hydrothermal activity (see review by Früh-Green et al., 2022). While hydrothermal venting occurs at various temperatures below ∼400 °C, only high-temperature fluids (>300 °C) are able to transport metals leached from the crust to the seafloor, where they are deposited and form massive ore deposits (e.g., Hannington et al., 2011). These deposits are of biological and economical interest but are also key to assess past hydrothermal activity. From seafloor observations of active and inactive vent fields, different modes of detachment-related hydrothermal activity have been identified. Here, we follow the classification by McCaig et al. (2007):

TAG-type:

> High-temperature venting in the hanging wall next to the emergence of the detachment, driven either by an axial heat source tapped by the permeable detachment or by shallow intrusions directly below the vent field (e.g., TAG, deMartin et al., 2007; Logatchev-1, Petersen et al., 2009; Semenov-4, Pertsev et al., 2012; Longqi-1, Tao et al., 2020).

Rainbow-type:

> High-temperature venting on top of the OCC driven by magmatic intrusions into the footwall and facilitated by secondary faults (e.g., Irinoskoye, Semenov-1,2,3,5, Pertsev et al., 2012; Von Damm, Connelly et al., 2012; Rainbow, Andreani et al., 2014).

Lost City-type:

> Low-temperature venting on top of the OCC, driven by residual mantle heat, late-stage cooling of mafic intrusions (Evans et al., 2024), serpentinization and/or thermal cracking of deep hot rocks (e.g., Lost City, Früh-Green et al., 2003; Old City, Lecoeuvre et al., 2021.

Further differentiation can be done based on vent fluid chemistry (e.g., Früh-Green et al., 2022). Our study focuses on the relationship between tectonic deformation, magmatic heat sources and hydrothermal circulation pathways. Under this focus, TAG-type vent fields are of special interest. The hypothesis of permeable fault zones tapping a distant heat source has been repeatedly invoked (Andersen et al., 2015; McCaig et al., 2007; Tao et al., 2020) and is supported by hydrothermally altered rocks exhumed along the detachment shear plane (Verlaguet et al., 2021) and by the spatial correlation between vent fields and faults (McCaig et al., 2007). In contrast, Guo et al. (2023) argue that the ability of the fault zone to guide hot upflow over long distances is limited. Instead, they suggest that hydrothermal activity is more likely driven by a shallow magmatic heat source directly below the observed vent field location, consistent with observations at TAG (deMartin et al., 2007; Graber et al., 2020; Zhao et al., 2013). Similarly, shallow intrusions have been reported below Rainbow (Dunn et al., 2017; Evans et al., 2024; Jian et al., 2024). The ongoing discussion makes it particularly relevant to test the limits of the different hypotheses.

Additionally, tectonically controlled vent fields are generally rather long-lived due to persistent host rock structures and reduced magmatic overprinting (German et al., 2016). This explains why numerous large vent fields along slow-spreading ridges are located off-axis and produce exceptionally large massive sulfide deposits (German et al., 2016). In particular, TAG-like hydrothermal activity yields some of the largest known sulfide deposits (Semenov: 9-40 Mt, TAG (incl. inactive mounds): 2.7(29) Mt; Cherkashev et al., 2013; Graber et al., 2020; Hannington et al., 2010). Thus, identifying general mechanisms responsible for the formation of large seafloor massive sulfides (SMS) around the emergence of detachment faults could help understanding their role within the detachment life cycle and support the search for comparable deposits.

Detachment faulting at slow-spreading ridges has been in the focus of numerous studies using numerical modeling over the past 20 years. A key parameter in those models is the magmatically accommodated fraction of plate separation, commonly referred to as the M-factor. It is implemented as a volumetric fraction of the opening rate supplied as melt to an axial diking region (e.g., Behn & Ito, 2008; Buck et al., 2005; Howell et al., 2019; Tucholke et al., 2008). These models mainly focus on the rock mechanics and show that detachment faults form at around M=0.5, while larger values lead to periodic normal faulting and lower values lead to faults that migrate across the ridge axis and become dissected. On the other hand, numerical studies on hydrothermal activity either focus on the thermal state of the ridge (Chen et al., 2022; Fan et al., 2021; Theissen-Krah et al., 2016) or on the influence of permeable, geometrically prescribed fault zones on flow patterns (Andersen et al., 2015, 2017; Guo et al., 2023; Tao et al., 2017). However, no study so far has coupled the complex evolution of an OCC and the associated hydrothermal fluid flow patterns, which is necessary

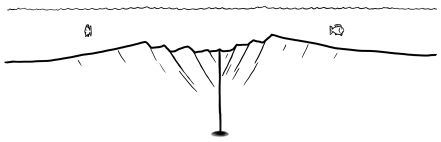

to answer the previously raised questions.

For this study, we take the well-studied OCC at the MAR at 13°30'N as a reference case and use a numerical model to study the formation of the core complex and the associated hydrothermal activity. The OCC hosting the Semenov vent fields is suspected to be at the end of its detachment life cycle (MacLeod et al., 2009). To reconstruct the complete evolution of the OCC, we first set up a thermo-mechanical model featuring a diking region that varies in strength and position. In a second step, we use the output of that model as the transient framework for a hydrothermal flow model which allows us to consider the rock-mechanical and topography effects of the evolving OCC and detachment geometry on the fluid flow field.

5.2 Geological Setting: 13°30'N OCC & Semenov Vent Fields

Several core complexes have been identified in the 13°N segment of the MAR north of the Marathon Fracture Zone, both at the ridge axis and some tens of kilometers away (Fig. 5.1 A). While most of them are relict, the 13°20'N OCC shows clear signs of activity and the 13°30'N OCC is presumably in its terminating stage (Escartín et al., 2017; Mallows & Searle, 2012; Parnell-Turner et al., 2020). Originally identified from bathymetric data by Smith et al. (2006, 2008), the 13°30'N OCC has since then been extensively studied using (micro-)bathymetry and video imagery (Fig. 5.1 A + B; Escartín et al., 2017; MacLeod et al., 2009; Mallows & Searle, 2012; Searle et al., 2019; Smith et al., 2006), drilling and seafloor sampling (Escartín et al., 2017; MacLeod et al., 2009; Pertsev et al., 2012), multibeam sonar (Fig. 5.1 C; MacLeod et al., 2009; Mallows & Searle, 2012), magnetic and gravity data (Mallows & Searle, 2012; Searle et al., 2019; Smith et al., 2008), microseismicity (Fig. 5.1 D; Parnell-Turner et al., 2020), and seismic imaging (Fig. 5.1 D; Peirce et al., 2023, 2019, 2020; Simão et al., 2020).

The corrugated surface of the detachment extends 8 km along the spreading direction (Fig. 5.1 B, E). Several tectonic ridges can be identified in the chaotic terrain west of the corrugated surface (Fig. 5.1 B). Although the exact position of the breakaway cannot be pinpointed with absolute certainty, the total heave of the detachment fault is around 14 km. While the domed, wedge-shaped part of the fault surface with higher reflectivity (Fig. 5.1 B, C) only extends about 4 km along-axis, the detachment is interpreted to have a full along-axis extent of ∼12 km.

The exhumed shear plane west of the emergence has a slope of ∼10 °, its subsurface continuation has an estimated dip of 25 ° (Fig. 5.1 D; Simão et al., 2020). A cluster of micro-earthquakes 4 km to 7 km east of the emergence at 7 km to 12 km depth below seafloor can be interpreted as the shear zone of the detachment, indicating a substantial steepening of the fault zone with depth (Fig. 5.1 D; Parnell-Turner et al., 2020).

Fault rocks are mainly hydrothermally altered peridotites (serpentinized and talc-replaced) and sporadic gabbros from mantle and lower crust, respectively (Escartín et al., 2017; MacLeod et al., 2009; Pertsev et al., 2012). The OCC also features some recent volcanic overprinting (Escartín et al., 2017; Pertsev et al., 2012). Some of these basalts are found in the projection of a ridge segment north of the OCC that is shifted to the west in a non-transform offset (Pertsev et al., 2012). This ridge segment seems to propagate southward into the OCC,

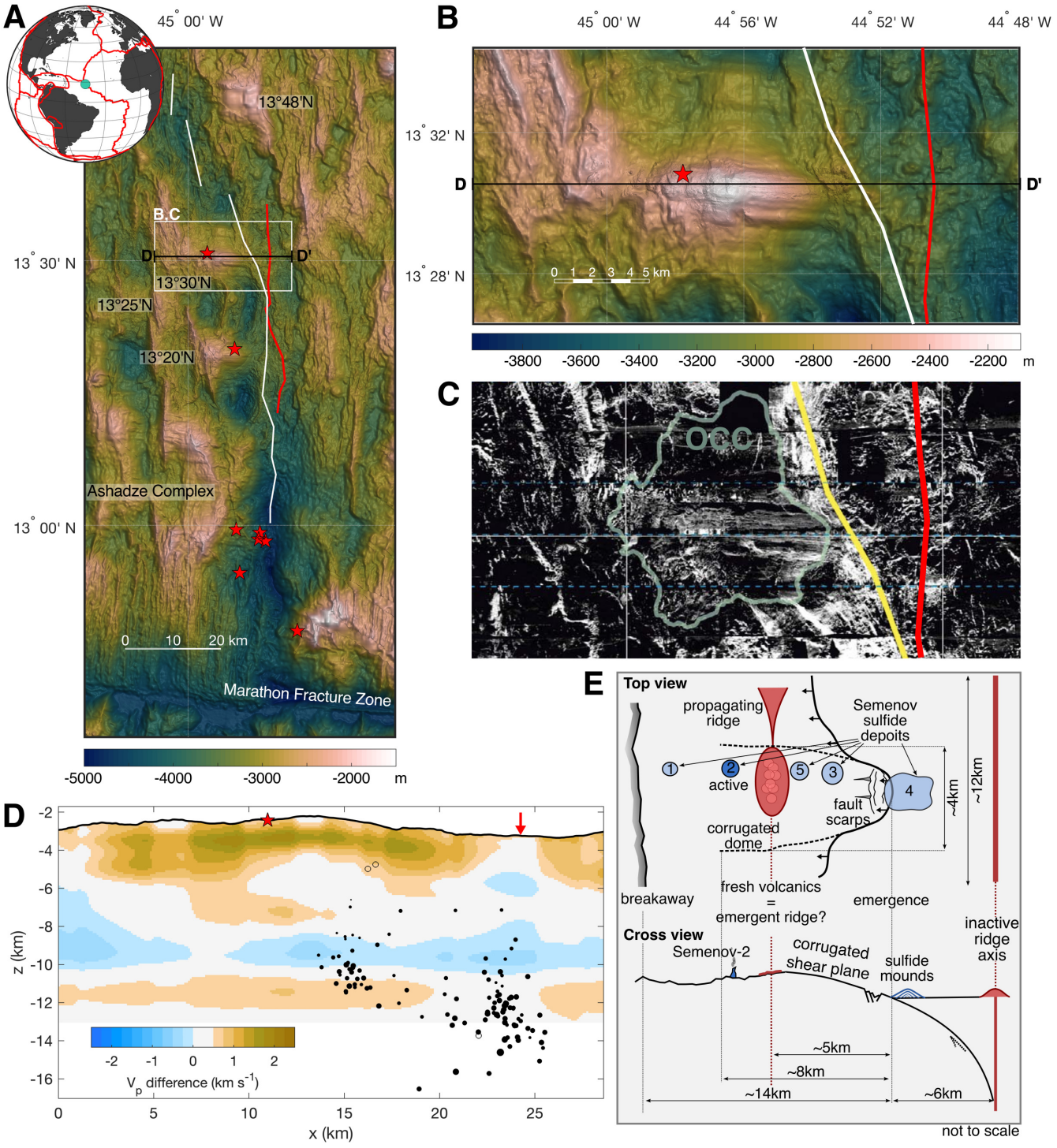

Figure 5.1. **A**: Bathymetry of the MAR ridge segment hosting the 13°30'N OCC (Escartín et al., 2017; Ryan et al., 2009). Positions of OCCs indicated by their names, red stars indicate active vent fields (Beaulieu & Szafranski, 2020). Lines indicate the position of the ridge axis, white (yellow in C) from Mallows and Searle (2012), red from Simão et al. (2020). White box shows the outline of the zoom in B and C, black line indicates the position of the cross section shown in D. **B**: Zoom on the bathymetry of the 13°30'N OCC. **C**: TOBI side scan sonar section showing seafloor reflectivity. OCC outline in turquoise. From Mallows and Searle (2012). **D:** Cross section showing difference in P-wave velocity compared to a reference profile from Simão et al. (2020). Overlain by microseismic events within 1.5 km of the profile as black dots scaled with magnitude (empty circle: no magnitude information), from Sohn et al. (2020). Red arrow indicates the position of the ridges axis from Simão et al. (2020). **E**: Geological sketches and distribution of the hydrothermal fields associated with the 13°30'N OCC.

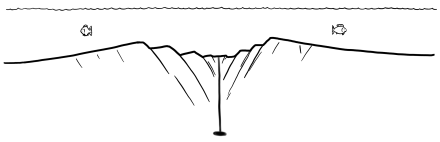

causing intrusions into the footwall and leading to the termination of the fault. Further evidence that the detachment is in its final stage is the low seismicity compared to the 13°20'N OCC (Parnell-Turner et al., 2020), the cutting of the eastern OCC tip by newer faults, the thicker sedimentary cover (Mallows & Searle, 2012), and the absence of a rubble moat on the emergence (Escartín et al., 2017).

Multibeam backscatter data shows that the broad neovolcanic zone to the north and south of the core complex vanishes opposite to the OCC (Fig. 5.1 C; MacLeod et al., 2009; Mallows & Searle, 2012). Low backscatter intensity of the faulted and sediment-covered volcanic seafloor opposite to the OCC indicates very reduced magmatic activity during detachment faulting and makes the definition of the spreading axis difficult. While Mallows and Searle (2012) interpret a structure with increased reflectivity directly in front of the emergence as the spreading axis (Fig. 5.1 C), Simão et al. (2020) assume the axis position further to the east based on reduced P-wave velocity (Fig. 5.1 D). We follow the second model as this position is in agreement with the maximum crustal thickness derived from gravity data (Mallows & Searle, 2012) and matches the position of the detachment root inferred from microseismicity (Fig. 5.1 D; Parnell-Turner et al., 2020).

The core complex hosts five sulfide deposits, called Semenov-1 to -5 (alternatively: Semyenov), with Semenov-2 being the only active site hosting several white smokers with maximum venting temperature of 317 °C (Fig. 5.1 E; Escartín et al., 2017). Four deposits (1,-2,-3, and -5), presumably related to Rainbow-type venting, are relatively small and located on top of the OCC, potentially aligned along a spreading-parallel fault structure on the exhumed shear plane (Pertsev et al., 2012). Their duration inferred from age date limits ranges between 8 kyr and 76 kyr and their timing shows no clear correlation with distance from the ridge axis (Kuznetsov et al., 2011). Data from other OCCs suggest that venting is driven by gabbroic intrusions into the core complex and fluid circulation is independent of the detachment fault zone (Dunn et al., 2017; Jian et al., 2024; Verlaguet et al., 2021). In contrast, Semenov-4 is located on the hanging wall wedge directly next to the emergence. TAG-type venting resulted in sulfide mineralization covering an area of ca. 1600×2700 m (Cherkashev et al., 2013), including the mounds identified in high-resolution bathymetry (Escartín et al., 2017; Murton et al., 2022). The dredged and drilled fault rocks show various clear signs of hydrothermal alteration, indicative of fluid flow through the actively deforming, permeable fault zone. Focused high-temperature venting required for the deposition of Semenov-4 indicates that the fluid circulation responsible for the alteration of the fault plane was rooted significantly deeper than the 2 km infered for the 13°20'N OCC (Verlaguet et al., 2021). The total deposited mass of the cluster estimated from seafloor area ranges from 9 Mt (Hannington et al., 2010) to up to 40 Mt (Cherkashev et al., 2013), ranking Semenov among the largest known submarine ore deposits. Deposition at Semenov-4 started around 124 kyr ago and lasted at least 122 kyr (Kuznetsov et al., 2011). The available age measurements do not provide sufficient information to determine whether the activity was continuous or intermittent (Jamieson et al., 2023).

In the following section, we will set up a thermo-mechanical model to reconstruct the OCC at 13°30'N based on its first order characteristics: Numerical models demonstrate that asymmetric detachment faulting generally initiates during phases of reduced melt supply

(Behn & Ito, 2008; Buck et al., 2005; Tucholke et al., 2008). Seafloor observations show no recent magmatic activity at the ridge axis (MacLeod et al., 2009; Mallows & Searle, 2012). An adjacent ridge segment projects onto the OCC from the north and is associated with recent magmatic activity, and presumably diking (Escartín et al., 2017; MacLeod et al., 2009). Deformation along the detachment shear plane is about to stall (Escartín et al., 2017; Parnell-Turner et al., 2020), fault heave indicates a total duration of around 1 Myr, depending on the degree of asymmetry (Escartín et al., 2017; MacLeod et al., 2009). NNW/SSE-oriented fault scarps at the OCC tip and footwall seismicity indicate the dissection of the footwall by recent faulting (Fig. 5.1 B, D, E; Escartín et al., 2017).

5.3 13°30'N OCC: Thermo-Mechanical Baseline Model

For this study we use an updated version of our 2-D visco-elasto-plastic thermo-mechanical model `M2TRI_vep` (Hasenclever, 2010; Hasenclever & Glink, 2025). Details on the numerical model including model parameters can be found in Chapter 4 and in Appendix B.1. We implemented topography diffusion (Andrés-Martínez et al., 2019; Kaufman et al., 1991) and added the volume (Schierjott et al., 2023) and heat effects (Behn & Ito, 2008) of diking at the ridge axis. Diking in this model represents the time-averaged effects of individual magmatic events. The dike region is represented by a vertical column spanning the brittle lithosphere, where a prescribed fraction M of the volume opened by extension is added via a dilation term in the mass conservation. A correction term on the strain rate in the momentum conservation ensures purely horizontal opening of the dike region. We assume instantaneous emplacement of melt and consider the associated heat from cooling to ambient temperatures and from crystallization.

Magnitude and position of the dike region are prescribed as time-dependent sequences (Fig. 5.2 B), based on the life cycle of the 13°30'N OCC. Previous studies (e.g., Behn & Ito, 2008; Buck et al., 2005; Tucholke et al., 2008) show that asymmetric accretion, i.e. detachment faulting, generally emerges in this type of numerical model when diking accounts for around 50 % of the extension. We therefore set up an initial diking region at the center of the domain with M=0.5 (Fig. 5.2 A). This represents the currently magmatically inactive ridge axis east of the OCC. After footwall rotation and exhumation of the OCC have established, diking rate is linearly reduced to 0 between 400 kyr and 450 kyr, marking the low-magmatic mature phase of the detachment (MacLeod et al., 2009; Mallows & Searle, 2012). Following 200 kyr of amagmatic spreading, the dike region is shifted 10 km into the footwall of the detachment, where diking builds up between 650 kyr and 730 kyr until it accounts for 80 % of the extension. This new diking region represents the adjacent ridge segment propagating southward into the OCC. The ridge jump distance of 10 km is estimated from the position of the low-velocity zones in Fig. 5.1 D, the projection of the adjacent ridge segment in Fig. 5.1 A, and seafloor evidence of old and recent magmatic activity (Escartín et al., 2017; Pertsev et al., 2012). Sonar and bathymetry data indicate a reduction of asymmetry to the north (Fig. 11 in Mallows & Searle, 2012), justifying M=0.8, which is the typical value favoring normal faulting in numerical models (e.g., Behn & Ito, 2008; Buck et al., 2005).

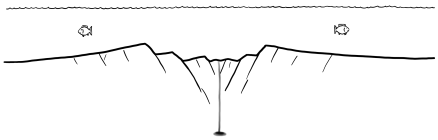

5.3.1 Thermo-Mechanical Model Setup

The model setup is illustrated in Fig. 5.2. The thermo-mechanical baseline model including the initial temperature field and imposed rheology is adapted from the one used by Behn and Ito (2008) to make our results comparable to previous studies using a similar setup. The model employs a homogeneous visco-elasto-plastic dry diabase rheology (Mackwell et al., 1998). Viscous behavior is controlled by non-Newtonian temperature- and strain rate-dependent creep, elastic deformation is controlled by a shear modulus of 10 GPa and plastic yielding follows a stress-dependent yield criterion (see Appendix B.1). Strain weakening linearly reduces cohesion from initially 44 MPa to 4 MPa and friction angle from 30 ° to 20 ° over a critical plastic strain of 0.2. Strain heals over a characteristic time scale of 30 kyr. Plastic parameters, strain weakening and healing are largely based on Behn and Ito (2008) and fall in the range used by similar studies (Howell et al., 2019; Sandiford et al., 2021; Tucholke et al., 2008).

Imposed constant lateral extension of 12 mm yr^{-1} and water depth at z=0 km of 3000 m represent the Mid-Atlantic Ridge at 13°30'N. Extension is compensated by constant inflow through the bottom boundary (Fig. 5.2 A).

We define an axial porous region, where in the second step of our study hydrothermal fluid flow will be modeled within the framework of our baseline model. In the thermo-mechanical model, the presence of pore fluids is considered by applying a volumetric average between rock and fluid properties and pore fluid pressure reduces the effective pressure in the yield criterion. The effect of hydrothermal cooling is parametrized through an increase of the thermal conductivity:

$$\kappa = \kappa_0 \cdot (1 + (\mathrm{Nu} - 1) \cdot \theta_{\mathrm{lin}}(x, z, T)) \tag{5.1}$$

κ_0 is the thermal conductivity of the host rock, Nu = 8 is the maximum increase, and θ_{lin} is a linear taper to account for the porosity/ permeability closure from (a) clogging and consolidation of older off-axis rocks, (b) increasing lithostatic pressure at depth, and (c) the transition to ductile rock behavior at high temperatures. Taper intervals are (a) 7 km to 10 km distance x from the spreading axis, (b) 6 km to 7 km depth z, and (c) temperature T of 500 °C to 700 °C. On the detachment side of the ridge axis, the porous region widens with the half spreading rate to include the OCC and account for proven hydrothermal activity inside the footwall. Over the taper intervals, parametrized cooling decays linearly and porosity is reduced from 5 % to effectively 0 %, also shutting down the effect of pore fluid pressure.

5.3.2 Modeled Detachment Cycle

The model evolution is illustrated in Fig. 5.3 A - E. We trigger the formation of a right-dipping (east-dipping) fault from the initially symmetric shear bands by initiating an asymmetry in the accumulated plastic strain at the surface (Fig. 5.2 A). As long as diking occurs at its original position and compensates for 50 % of the extension, the right-dipping fault roots at the base of the dike region (Fig. 5.3 A + B). With increasing displacement, the initially high-angle normal fault (∼50 °) evolves into a detachment by rotating to shallower angles at the top and it continuously exhumes material to the seafloor to form the core complex. Once

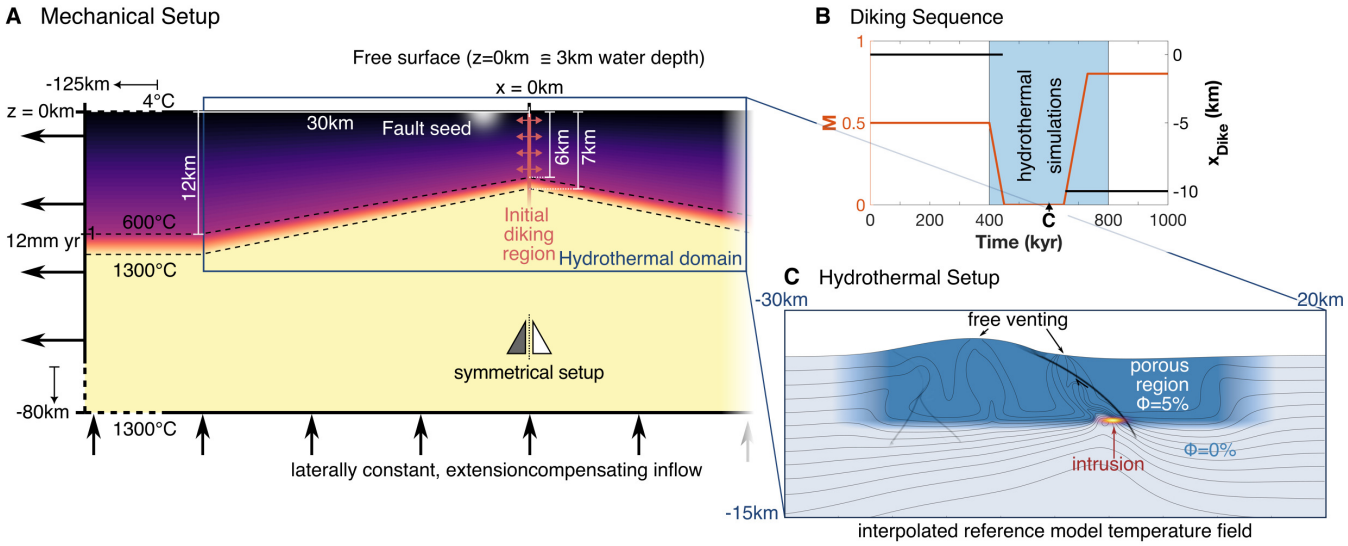

Figure 5.2. **A**: Setup including the initial temperature field indicated by colors and boundary conditions of the thermo-mechanical reference model. Lateral boundaries are insulating. The setup is symmetric except for the fault seed. **B**: Dike sequence described by the magmatically accommodated portion of extension M and the position of the dike region x_{dike}. Blue box indicates the time interval of hydrothermal simulations. **C**: Hydrothermal model domain and setup. Porosity ϕ in white to blue, isotherms in black at increments of 100 °C, snapshot from the reference hydrothermal simulation at 600 kyr. Lateral boundaries are insulating.

diking vanishes after 400 ky (∼4.3 km heave), the detachment starts to migrate across the original spreading axis and the lower part of the fault steepens as it cools (Fig. 5.3 B + C). At the same time, a branching fault forms at the transition between the rotating footwall and the horizontal far-field plate motion (cf. Sandiford et al., 2021). After the new, prescribed dike region emerges in the footwall, the detachment fault slowly fades out and its activity ultimately ceases at ∼800 kyr (∼14.2 km heave; Fig. 5.3 D). Shortly after, new normal faults form around the diking region and dissect the footwall (Fig. 5.3 E).

We interpret the model configuration between 700 and 800 kyr to represent the current state of the 13°30'N OCC as described in Section 5.2. Fig. 5.3 F demonstrates the fit between our model result and the data. The modeled detachment fault lies close to the edge of the larger microseismicity cluster, consistent with the expectation that most of the deformation of a detachment takes place in the fault zone and the footwall, while the hanging wall is almost stagnant. The position of the original magmatic dike region lies in the low velocity zone identified by Simão et al. (2020). The incipient normal fault in the footwall can explain the offset at the tip of the OCC and roughly matches with the second cluster of microseismicity. Height and shape of the model seafloor relief closely align with observations, which is crucial for the subsequent hydrothermal simulations which are sensitive to bathymetry (Bani-Hassan et al., 2012).

5.4 Hydrothermal Flow Model

To study hydrothermal circulation patterns evolving around an oceanic detachment fault, we coupled the output of our thermo-mechanical model to a Darcy flow model based on Hasenclever et al. (2014). Further details on the numerical model including model parameters can

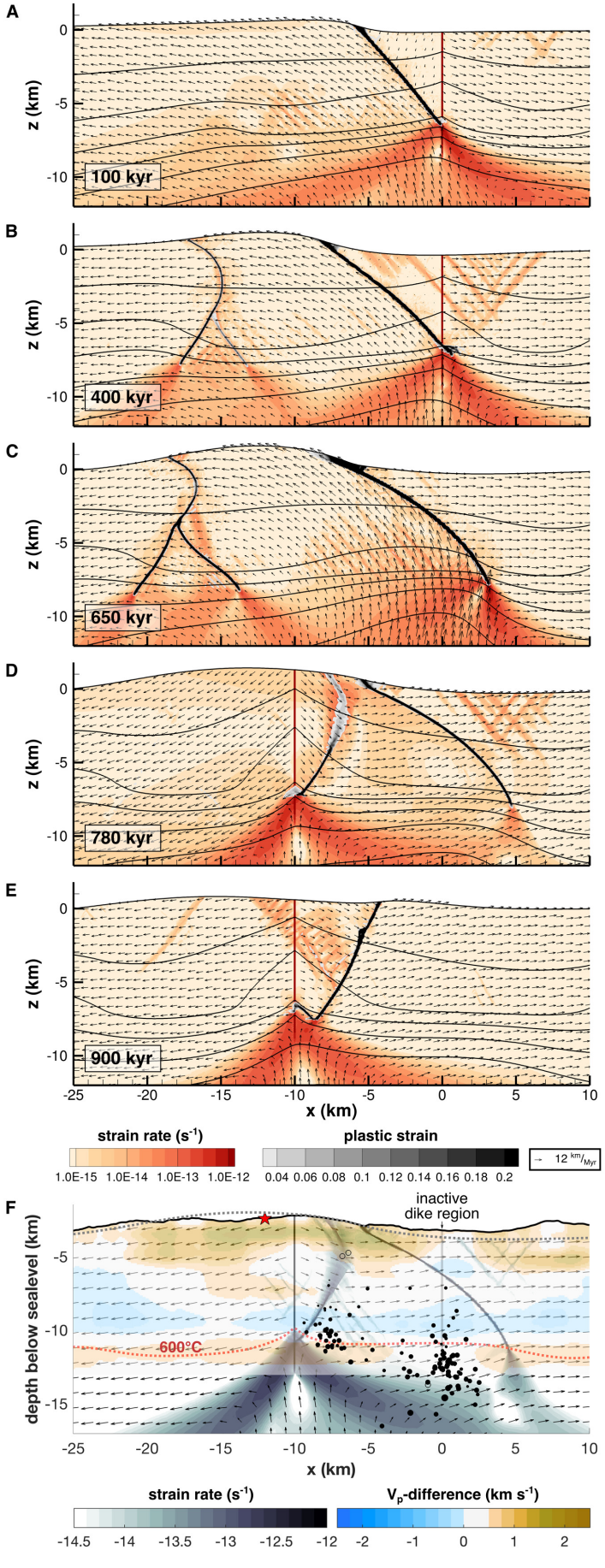

Figure 5.3. **A** - **E**: Snapshots of the reference thermo-mechanical simulation. Orange colors depict the second invariant of the full strain rate, overlain by accumulated plastic strain in gray. Thick black lines are faults, where the plastic strain colormap saturates. Isotherms have 200 °C-increments, vectors show the solid advection velocity. The full model evolution can be seen in Movie S5.1.
F: Model solution after 780 kyr compared to microseismicity and P-wave velocity difference as in Fig. 5.1 D. Dotted black line is the model topography, red star indicates the position of Semenov-2 at the seafloor, dotted red line is the model brittle-ductile transition at 600 °C.

be found in Appendix B.2. The coupling in this study is one-way: The history of tectono-magmatic deformation including mantle upwelling, diking, footwall rotation, localized plastic strain and evolving seafloor relief is mapped to the hydrothermal domain that resolves hydrothermal circulation in the axial region including the OCC with a finer finite element mesh. Model geometry and mechanical variable fields are continuously updated during hydrothermal simulations. All hydrothermal simulations start at 400 kyr with the shutdown of diking and run until 800 kyr.

5.4.1 Setup

The hydrothermal domain and boundary conditions are illustrated in Fig. 5.2 C. Porosity and permeability inside the porous region have constant values of 5 % and $1.3 \times 10^{-15}\,\mathrm{m}^2$, based on previous studies (e.g., Andersen et al., 2017; Chen et al., 2022), and are reduced to effectively 0 % (linearly) and $10^{-19}\,\mathrm{m}^2$ (logarithmically) outside. To reduce boundary effects on the evolving flow patterns we widen the porous region compared to the detachment model by modifying the taper limits for x and T to 10 km to 16 km and 600 °C to 800 °C, respectively. At the bottom of the hydrothermal domain, we set the interpolated temperature field from the thermo-mechanical simulation as boundary condition, lateral boundaries are insulating and the top boundary allows for free in- and outflow.

High-temperature venting generally requires a magmatic driving force. We set up a Gaussian-shaped heat source at 6 km depth in the footwall next to the detachment root to represent the time-averaged heat from repeated emplacement of magmatic intrusions. Melts at this position could either be related to decompression melting in the uplifting footwall or stem from residual magmatic activity in the original diking region, which lies inside the footwall after the rightward (eastward) migration of the detachment in the amagmatic phase (Fig. 5.3 C, D + F). The prescribed intrusion position is also consistent with the output of our detachment model: Emplacement depth approximately corresponds to the base of the diking region defined by the axial lithosphere thickness, the horizontal position matches the maximum vertical temperature gradient at the base of the brittle-ductile-transition, which is where melts will likely accumulate. Additionally, the intrusion position matches previous studies on detachment-related fluid flow (Andersen et al., 2015, 2017; Tao et al., 2020), making our results more comparable to existing research. The dimensions of the Gaussian function in x- and z-direction are 1000 m and 250 m, respectively. At M=0.5, our modeled dike region supplies approximately $12\,\mathrm{kW\,m^{-1}}$ to the ridge axis by cooling and crystallization of melt, based on the parameters listed in Table B.1. This matches the lower limit of magmatic heat fluxes tested by Andersen et al. (2017). Throughout the hydrothermal simulations, we assume that an equivalent amount of melt is trapped below the detachment during the period without diking. Thus, intrusion-related heat flux compensates for the reduction in magmatic heat from diking. Consequently, the intrusion heat scales inversely with M, giving

$$H_{intr} = \max\{0,\ 2 \cdot (0.5 - \mathrm{M})\} \cdot 12\,\mathrm{kW\,m^{-1}} \tag{5.2}$$

for the Gaussian-shaped heat source at the detachment root.

5.4.2 Reference Hydrothermal Simulation

In our reference hydrothermal simulation (Fig. 5.4), we impose constant permeability in the porous region and a single deep heat source. In this simulation, no additional effects of the detachment fault apart from solid advection are included. Figs. 5.4 A to D show snapshots from that simulation, Fig. 5.4 E shows the temporal evolution of seafloor topography, fault emergence and variations in venting temperature and location.

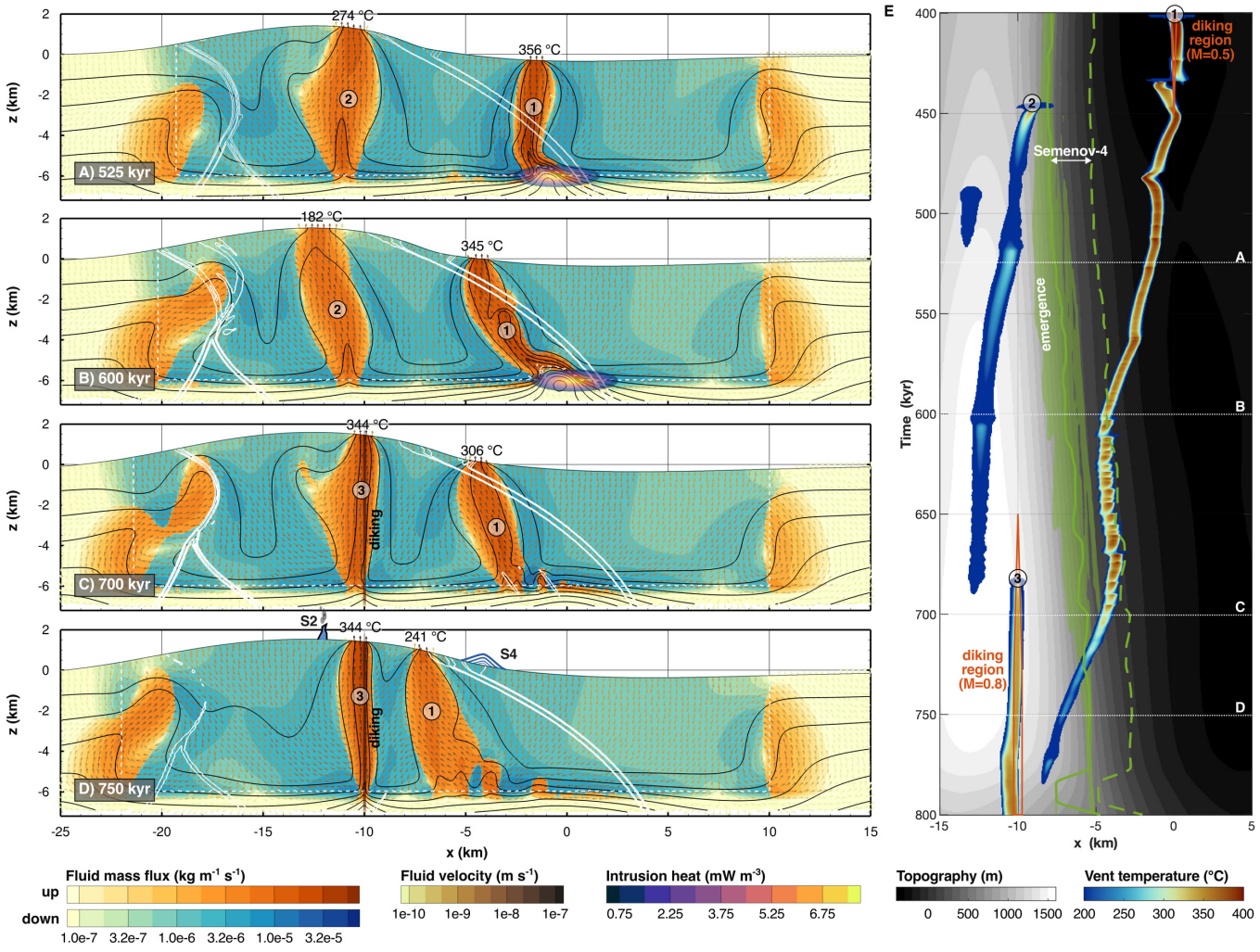

Figure 5.4. **A** - **D**: Snapshots of the reference hydrothermal simulation. Fluid mass flux in blue for downward flow and in red for upward flow. Intrusion heat is depicted by the transparent purple to yellow patch. Black isotherms have 100 °C-increments, vectors show fluid advection velocity. White isolines depict plastic strain at 10 %, 50 % and full strain weakening in the thermo-mechanical model, dashed white line indicates the inner boundary of the porous region. The porous region widens to the left with time as described in Section 5.3.1. Numbers in circles are plume indices used in the text and in **E**. In **C** and **D**, the transparent red line indicates the new diking region at x = −10 km. In **D**, we added the positions of Semenov-2 and 4 for reference. The snapshots show the full lateral extent of the hydrothermal domain, demonstrating that model domain and porous region are wide enough to minimize boundary effects. Subsequent snapshots focus on the central region of interest. The full model evolution can be seen in Movie S5.2. **E**: Temporal evolution of venting temperature and position overlying seafloor topography. The emergence area is depicted by full strain weakening (green transparent area), and maximum strain rate (green line), the outer edge of the Semenov-4 deposits is indicated by the dashed green line 2.6 km right of the emergence. The jump at around 780 kyr is associated with the formation of the footwall cutting normal fault (Fig. 5.3 D). Red lines indicate dike regions, the width represents the M value. White dotted horizontal lines depict the time of the snapshots.

Initially, an axial plume driven by a combination of intrusion and dike heat evolves (plume #1). It is first guided along the fading dike, later realigns itself and rises subvertically above the intrusion (Fig. 5.4 A). Venting temperatures are consistently higher than 300 °C (Fig. 5.4 E). The plume repeatedly absorbs minor upflows that emerge in its proximity. At 450 kyr (after 50 kyr simulation time), a weaker second plume evolves in the rotating footwall block next to the topographic maximum (plume #2). It is driven by residual mantle heat alone and results in venting temperatures mostly below 250 °C (Fig. 5.4 E).

After diking at the original ridge axis has stopped, venting of plume #1 in the hanging wall gradually shifts along the steadily rising seafloor topography, moving toward the elevated core complex between 450 kyr and 600 kyr (Fig. 5.4 A, B+E). This behavior is typical of submarine environments, since the fluid pressure at a given depth is lower inside the warm rock than it is in the cold seawater (Bani-Hassan et al., 2012). As a consequence, the plume rises diagonally while it also detaches further to the left of the intrusion region instead of at its center (Fig. 5.4 B). The greater the horizontal distance between heat source and venting position, the colder and less stable the plume becomes due to entrainment of colder surrounding fluids. This is reflected in the flow pattern (Fig. 5.4 B) and the increasing oscillation of the venting temperature (Fig. 5.4 E). Redirection of plume #1 towards the OCC is potentially supported by interaction with plume #2. The two plumes share the space in-between for recharge flow, which creates a negative non-hydrostatic pressure and thus attraction between the two plumes.

Deflection of the intrusion-driven plume reaches its maximum at around 600 kyr. Between 600 kyr and 700 kyr, the venting position remains relatively stable within the right half of the Semenov-4 region marked by the green lines in Fig 5.4 E. This presumably marks the maximum possible distance between heat source at depth and venting at the seafloor, and significant oscillations in venting temperature can be observed during this interval (Fig. 5.4 E). At 650 kyr, the new dike region, representing the propagation of the adjacent ridge segment, emerges within the footwall. As the new dike region develops, the heat contribution from the intrusion is progressively reduced following Eq. (5.2). Consequently, the plume's origin shifts leftward, moving away from the waning intrusion region and into the footwall (Fig. 5.4 C). At the same time, plume #2 in the footwall realigns and intensifies along the new dike region that cuts the OCC close to the topographic maximum as indicated by seafloor observations. After the intrusion heat reaches zero at 700 kyr, plume #1 migrates further uphill, crosses the emergence (Fig. 5.4 E), and ultimately merges with the footwall plume (now #3).

The simulation demonstrates that the topographic effect of an OCC on fluid flow alone can lead to significant redirection of hydrothermal fluids from the root of the detachment fault towards the emergence. Moreover, the time interval when high-temperature venting of plume #1 occurs in the Semenov-4 region between 600 kyr and 725 kyr (Fig. 5.4 B, C+E) matches the minimum duration of the Semenov-4 vent field of 122 kyr very well. Additionally, duration and position of the high-temperature footwall plume #3 match well those of the other four Semenov deposits, if we assume that transient variations of heat source position and hydrothermal pathways not resolved by our model distribute the mass flux over the OCC.

This reference simulation already demonstrates an excellent fit to the observations. In this

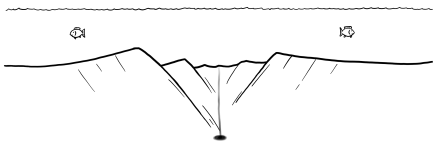

case, however, the detachment influences the hydrothermal system only indirectly through its impact on the heat source position and the evolving topography. Consequently, venting in the Semenov-4 region is a result of this specific geometrical configuration. To strengthen our findings, we will now investigate whether incorporating a more permeable fault zone or partitioning intrusion heat between deep and shallow levels can further facilitate the redirection and locking of hydrothermal plumes to that position.

5.4.3 Fault Zone Permeability

5.4.3.1 Permeability Model

Natural fault zones are characterized by an intensely sheared fault core and a surrounding damage zone of more distributed deformation (Choi et al., 2016). The competing mechanisms of strain weakening and strain healing in our detachment model, however, result in a relatively sharp transition from high to low strain at the fault rim. Here, we mimic the integrated effect of opening of permeable pathways along tectonic faults by scaling the permeability k of our hydrothermal model with the accumulated plastic strain $\varepsilon_{II,p}$:

$$k = k_0 \cdot \left(1 + (a-1) \cdot \min\left\{1, \frac{\varepsilon_{II,p}}{\varepsilon_{sw}}\right\}\right) \cdot \theta_{\log}(x, z, T) \tag{5.3}$$

where k_0 is the constant background permeability, $\varepsilon_{sw} = 0.2$ is the plastic strain of maximum strain weakening in the mechanical model, a is the maximum fault zone permeability increase at $\varepsilon_{II,p} \geq \varepsilon_{sw}$, and $\theta_{\log}$ is the logarithmic taper at the boundary of the porous region that depends on distance to the ridge axis, depth, and ambient temperature (cf. Eq. 5.1 and Section 5.4.1). We explore two endmember fault rock scenarios, (1) homogeneously ground fault rock represented by an isotropic permeability increase, and (2) a network of perfectly aligned fractures represented by an anisotropic permeability increase in the direction of slip.

The first approach is the most straightforward implementation also used by other studies (Andersen et al., 2015; Tao et al., 2020). Fluids inside the fault zone can easily move in any direction, also facilitating them to enter and leave the fault. Based on geological evidence (Caine et al., 1996; Walker et al., 2013), however, we suggest an anisotropic high-permeability fault zone to be a better representation of nature. In this case, the fault represents a channel, along which fluids can travel fast, while flow normal to the direction of slip remains at background intensity. For the implementation of anisotropy see Appendix B.2.

The fault zone width of the detachment model defined by the plastic strain is 270 m on average (Fig. B.1). Without regularization (e.g., Duretz et al., 2021), fault width is controlled by the model discretization. We resolve faults at 75 m, which is not based on geological evidence, but balances computational efficiency with consistency in fault zone width across previous studies (Andersen et al., 2015; Tao et al., 2020). We test permeability factors a of 2, 5 and 10, matching the range proposed by Andersen et al. (2017) for this fault width.

5.4.3.2 Results

In the isotropic case, the effect of a twofold permeability inside the fault zone is marginal (Fig. 5.5 A + B). Venting reaches the Semenov-4 region about 10 kyr earlier (Fig. 5.5 B) and

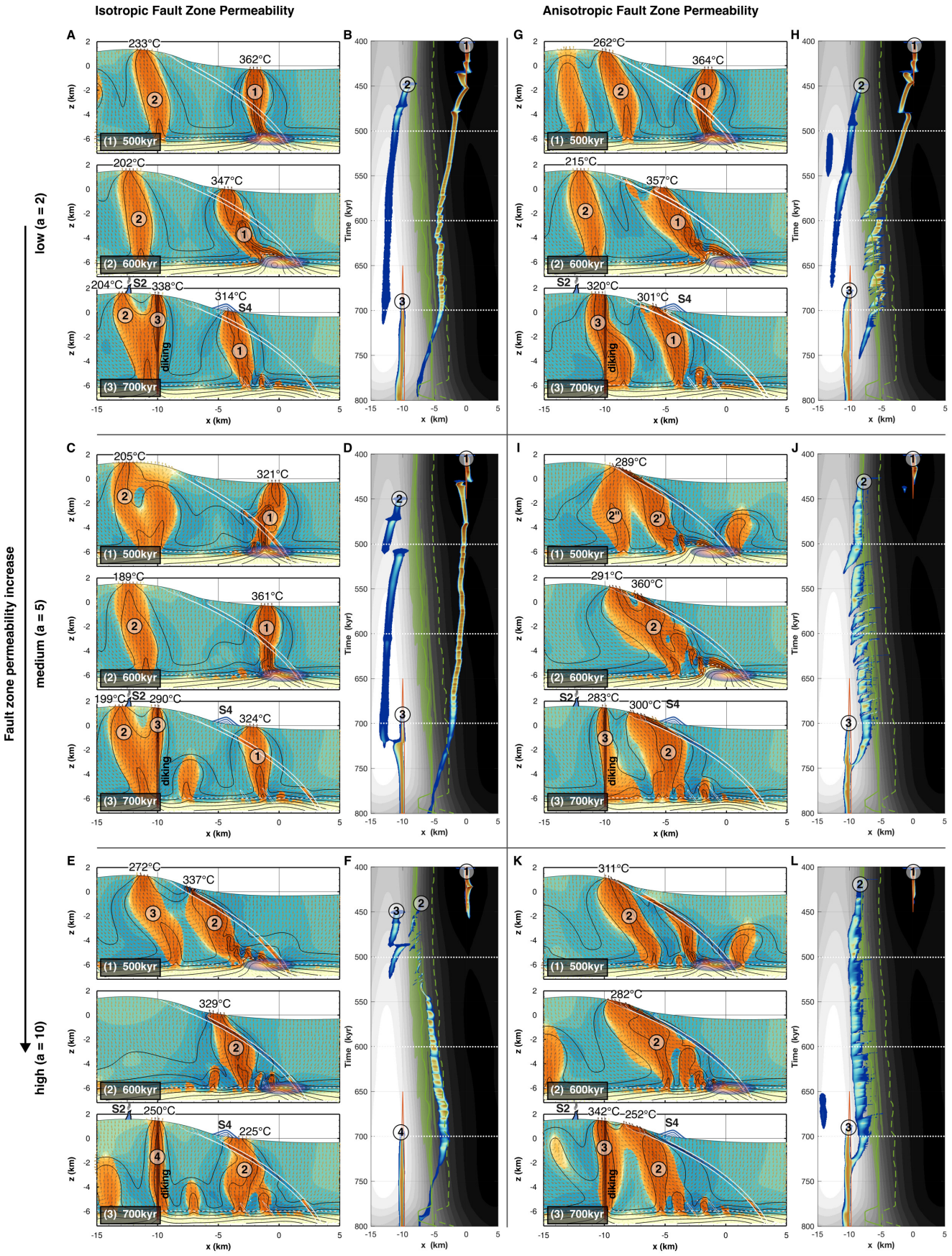

Figure 5.5. Fluid mass flux snapshots and vent properties for the simulations with different fault zone permeabilities. Color scales and framework as in Fig. 5.4. The full simulations can be seen in Movies S5.3 - S5.8.

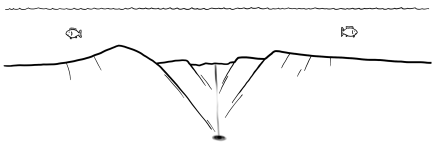

mass flux locally increases by a factor 1.5 (Fig. 5.5 A), which could indicate a slight redirection of the plume along the fault. However, neither the duration of venting inside the Semenov-4 region changes significantly, nor does the stable venting position get closer to the emergence (Fig. 5.5 B).

For an isotropic permeability increase of 5, the fault zone tends to be primarily used for recharge (Fig. 5.5 C). We speculate that this can be explained by maximizing transport efficiency through homogenizing flow resistance along the fluid path: Cold water with intrinsically higher dynamic viscosity uses the permeable fault, while hot and buoyant fluids with much lower viscosity vertically rise through the less permeable rock. Recharge along shallower parts of the fault shifts the venting position to the right, so that no high-temperature venting occurs in the Semenov-4 region (Fig. 5.5 D).

For a factor of 10, strongly increased fluid flux along the fault zone, both down- and upward, leads to more dynamic variations of the flow field (Fig. 5.5 E + F). The hot upflow dominating the mid-depths is blocked by cold fluids entering the emergence zone (Fig. 5.5 E). This prevents hot fluids from migrating further to the left following the fault zone and the topography. This results in venting over the whole width of the Semenov-4 region between 440 kyr and 750 kyr (Fig. 5.5 F). Fig. 5.5 F shows that venting temperatures in the Semenov-4 region are slightly lower than in the reference simulation due to the increased fault permeability (Driesner, 2010). Nevertheless, high-temperature venting is broadly present from 550 to 700 kyr, yielding a robust fit with observations. It is important to emphasize that we are dealing with a highly dynamic model, particularly if permeability is high, and single simulations can be strongly influenced by non-linear feedbacks between the competing mechanisms. In some test calculations with a_{iso}=10 but other parameter choices, for example, we observed a similar behavior as for $a_{\mathrm{iso}} = 5$, where cold recharge is dominant along the fault shifting venting into the hanging wall.

Anisotropic fault zone permeability generally guides hot upflow more persistently along the fault zone as it promotes this flow direction (Fig. 5.5 G, I+K). After the fluids heated by the intrusion start to rise along the permeable fault, mixing with cold ambient fluids is reduced, since fluid transport perpendicular to the direction of maximum permeability is less efficient. As a consequence, high-temperature venting reaches the Semenov-4 region already at 550 kyr in the simulation with a twofold, anisotropic fault permeability (Fig. 5.5 G + H). It continues until 700 kyr, mostly in the left half of the Semenov-4 region and even on the OCC. The large horizontal distance between heat source and venting position further reduces plume stability and in turn increases oscillations in vent temperature and position.

Factors of 5 and 10 (Fig. 5.5 I-L) reinforce these effects, leading to venting exclusively on the exhumed shear plane left of the Semenov-4 region. Figs. 5.5 H, J and L also demonstrate the reduction in venting temperature with increasing fault zone permeability. Venting in the simulations with factors of 5 and 10 is largely too cold for significant sulfide deposition, which is not in agreement with natural observations. In both cases, the strongly bent plume merges with upflows in the footwall, resulting in a single, unsteady plume until the opening of the new dike region (Fig. 5.5 J+L).

5.4.4 Influence of a Shallow Heat Source

The detachment footwall is in a complex stress state (Sandiford et al., 2021) and experiences constant deformation, possibly allowing limited amounts of melt to rise to shallower depths through cracks and fissures. The presence of shallow magmatic bodies within the footwall is consistent with seismic observations and vent fluid chemistry at the Rainbow vent field (Dunn et al., 2017; Evans et al., 2024; Jian et al., 2024). This idea supports the hypothesis that TAG-like venting is driven by a shallow heat source below the vent field (e.g., Guo et al., 2023). In the second part our parameter study, we therefore test the influence of variable partitioning of the total intrusion heat from Eq. (5.2) between the main, deep heat source and a second, shallower heat source. This additional intrusion region is placed at 3 km depth in the footwall next to the fault zone with the same dimensions as the deep source. The total heat is partitioned between the deep and the shallower intrusion at different ratios between 0 and 1. Note that these heat sources again represent the time-averaged effect of repeated intrusions rather than emplacement and cooling of a single magmatic body.

We would expect an initially vertical plume, driven by the deep intrusion, to be attracted by the shallower intrusion when bypassing. However, the plume already crosses the shallow intrusion region for most of the intrusion duration due to the topographic redirection. Therefore, no significant change from the reference simulation is apparent for the simulations with up to $\frac{1}{4}$ of the total heat emplaced at a shallower level (Fig. 5.6 A - D). At this point, we can only speculate that the shallow intrusion heat stabilizes the plume redirection, but we will add more evidence to that idea in the Discussion.

If half of the heat goes into the shallow intrusion, the plume is less anchored at the deep intrusion, but detaches at its left edge (Fig. 5.6 E), allowing the venting to move faster and further (Fig. 5.6 F). That way, it vents over the whole Semenov-4 region between ∼520 kyr and 680 kyr, but also merges earlier with the central footwall plume. The venting region in this simulation is slightly wider and colder (Fig. 5.6 F).

Venting in the Semenov-4 region is further stabilized if we assume a shallow intrusion alone (Fig. 5.6 G + H). Plume #2 collects mantle heat from a wide range, crosses the shallow intrusion and rises subvertically towards the Semenov-4 region (Fig. 5.6 G), where high-temperature venting occurs for 260 kyr between 460 kyr and 720 kyr (Fig. 5.6 H). This is not surprising since the strong and relatively shallow heat source represents a fix-point for the hydrothermal circulation and limits the topography effect.

5.5 Discussion

5.5.1 Reconstructing the Tectonic History at MAR 13°30'N

We successfully reconstruct the first order geometrical features of the OCC at the MAR 13°30'N by prescribing a simple, data-based sequence for the magnitude and position of magmatic diking in a thermo-mechanical model. Initiated by an axial dike that accommodates 50 % of plate divergence, the detachment matures during an amagmatic phase and is finally terminated by a new region of magmatic diking in its footwall, leading to the dissection of the OCC by normal faults. This confirms the detachment life cycle model by MacLeod et al.

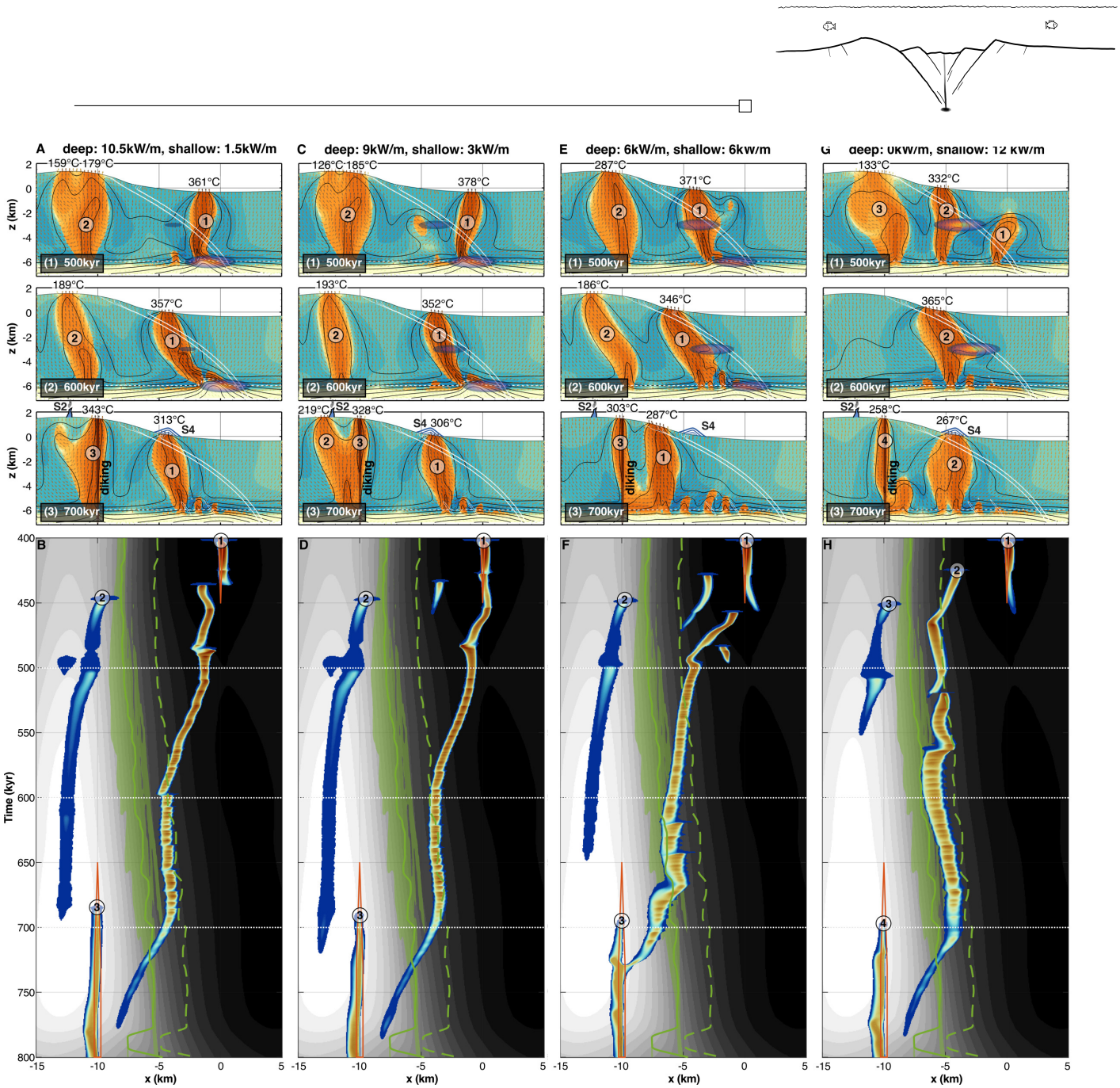

Figure 5.6. Fluid mass flux snapshots and vent properties for the simulations with different partitioning of the intrusion heat but uniform permeability. Color scales and framework as in Fig. 5.4. The full simulations can be seen in Movies S5.9 - S5.12.

(2009) and the data based conclusion that the southward propagation of the adjacent ridge segment into the OCC heralds its terminating stage (Escartín et al., 2017; Mallows & Searle, 2012; Parnell-Turner et al., 2020).

Note that the thermo-mechanical simulation featured here (Fig. 5.3) is the best fit model from a series of tests not shown in this study. As demonstrated by previous studies, the strongest influences on the tectonic model are the plastic parameters including strain weakening intensity and the initial thermal structure (e.g., Behn & Ito, 2008; Bickert et al., 2020; Sandiford et al., 2021). Varying these parameters can result in shallower fault dips, a more symmetrical initial phase with a second antithetic fault on the opposite side of the ridge, stronger accommodating faulting in the footwall, and/or more chaotic fault sequences. We cannot rule out influences of these processes occurring in nature, however, our reference sim-

ulation represents the most straightforward possible model for the development of the OCC.

The prescribed diking sequence is not the only possible representation of the seafloor observations. Previous studies have shown that detachment faults can form within an M-value range of 0.3 to 0.6 (Behn & Ito, 2008; Buck et al., 2005; Tucholke et al., 2008). During the mature phase, some residual magmatic activity below M=0.3 at the former magmatic spreading axis cannot be ruled out. Models indicate that normal faulting occurs between M=0.6 – 0.9 (Behn & Ito, 2008; Buck et al., 2005), suggesting a potential range for the emerging diking region within the footwall. However, the prescribed diking sequence has minor influence on the general model behaviour, as long as it stays within this observational framework. It mainly controls the timing and thus fault configuration at the transition between the different phases, while the qualitative evolution of the model remains very similar.

The only apparent inconsistency in the comparison with the data is that the fault zone does not curve enough to cross the microseismic cluster at depth. We could not achieve a better fit with our model and suggest this discrepancy may stem from the natural system's more complex rheology – such as variations between basaltic crust, gabbroic intrusions, and mantle rocks – or, alternatively, that the microseismicity arises not from faulting but from internal footwall deformation or melt intrusion. The latter could also explain the extension of the cluster to depths greater than our brittle-ductile transition. If the fault dips in fact steeper than our model suggests, this could potentially accommodate hot upflow of fluids more efficiently (Andersen et al., 2015, 2017) and would reduce the horizontal distance between the heat source and the emergence. Both possible explanations would facilitate TAG-like venting at the emergence of the detachment.

5.5.2 Detachment-Related SMS Accumulation at Semenov-4

We have already pointed out the very good fit between our reference hydrothermal simulation illustrated in Fig. 5.4 and observations. To further evaluate this, we will now convert our modeled fluid mass flow rates to deposited mass and compare to the data. We adopt the approach and parameters from Andersen et al. (2017) and use a deposition efficiency of 5 % and a total H_2S-SiO_2-metal concentration of 730 ppm, independent of fluid temperature. Only high-temperature fluids are able to transport metals and contribute to sulfide deposition (Hannington et al., 2011). We observe high-temperature venting in the Semenov-4 region between 600 kyr and 700 kyr (Fig. 5.4 E) and we will therefore focus on this interval. First, we assume a circular vent field and calculate 3-D deposited mass by integrating the 2-D surface profiles over two semi-circles around the heat flux maximum. If we only include fluids that vent with at least 350 °C, the predicted deposited mass is 0.2 Mt and increases to 0.9 Mt if also fluids with T>300 °C are considered to transport significant amounts of metal. This is at least one order of magnitude too low compared to Semenov-4 with ≥9 Mt, even when accounting for the possibility of more efficient deposition or higher metal concentrations in the fluid prior to venting, compared to those measured during venting.

Next, we assume the integrated flux of a line vent field in along-axis direction and calculate the extent required to explain the average deposition rate of at least 73.8 t yr^{-1} at Semenov-4. The predicted deposition rate per kilometer ridge axis is 6.4 t yr^{-1} to 17.7 t yr^{-1}

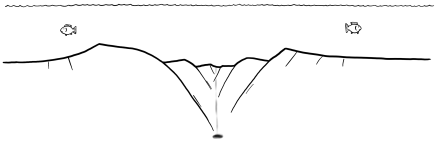

if we only consider fluids hotter than 350 °C and 300 °C, respectively. This requires an extent of the hydrothermal system of 4 km to 12 km to match Semenov-4, corresponding to the along-axis extent of the domed part of the OCC or even the full detachment structure. The estimated along-axis extent falls in the range of heat extraction distances estimated for TAG (2 - 10 km, German & Lin, 2004), the Piccard Hydrothermal Field at the Mid Cayman Rise (3.6 – 5.4 km, Kinsey & German, 2013), and Rainbow (≥24 km, German & Lin, 2004), and is also in agreement with the plume spacing in our model. It indicates strong focusing of fluid flow, presumably by an interplay of the mechanisms reviewed below.

5.5.3 Plume Redirection Mechanisms

5.5.3.1 Topographic Effect

The dominant effect on hydrothermal circulation in our reference simulation appears to be seafloor topography. Hydrothermal flow is driven by intrusion heat at the root of the detachment, while venting follows the gradually rising seafloor relief towards the emergence until the plume stability limit is reached. The geometrical configuration resulting from our thermomechanical detachment model and reasonable assumptions about heat source strength and position give rise to a very good fit of our reference simulation to the characteristics of the Semenov vent fields.

However, we suspect that the already good fit masks further important effects in our parameter study on fault zone permeability and shallow heat sources that could help to explain TAG-like sulfide deposits also in a wider range of configurations. To circumvent this and isolate different effects, we set up a simplified test case shown in Fig. 5.7 A. The circular solid velocity field represents the motion of the footwall relative to the hanging wall at around 700 kyr. Fault width is 270 m as in our detachment model. At the bottom, we set a heat flux boundary condition to compensate for the missing basal heat input from the mantle. Model parameters including intrusion properties are the same as in the previous hydrothermal simulations. Simulations are run for 300 kyr. Fig. 5.7 B shows the model result of the simplified reference simulation with constant permeability and a single deep intrusion. Since our test case has a flat topography away from the artificial OCC, the plume remains vertical, meaning that any deviation in venting position will be a direct result of the additional mechanisms.

5.5.3.2 Permeable Fault Zone

Figs. 5.7 C - H confirm our findings on the effect of fault zone permeability. For an isotropic permeability increase, i.e. assuming homogeneously fractured fault rocks, recharge and discharge compete inside the fault zone and only the strongest permeability increase leads to a significant shift of the venting position of 4 km towards the emergence. In contrast, anisotropic permeability increase in the fault, i.e. assuming perfectly aligned fractures in the direction of slip, results in a strong focusing of hot fluids along the fault by reducing mixing with cold ambient fluids and shifts venting even onto the OCC.

The 2-D nature of our model likely contributes to the along-fault separation of recharge and discharge sections. In a 3-D scenario, large areas of the fault plane could accommodate

recharge, while discharge would be concentrated near the along-axis position of the heat source, as shown by Guo et al. (2023). This is also consistent with the conclusion of Chapter 4 that detachment faults as a whole cause local cooling of the lithosphere. In general, strong horizontal redirection of fluids through a permeable fault zone lengthens the fluid pathway, increasing the time available for heat loss to surrounding colder fluids. Additionally, lower permeability causes the fluids to rise earlier, accumulating less basal heat. Together, these factors reduce vent temperatures (Fig. 5.8 A), which in turn decreases the capacity for metal transport. Therefore, we question whether this process alone can account for TAG-like venting associated with large SMS.

5.5.3.3 Shallow Intrusions

Fig. 5.7 J demonstrates an effect hidden in the previous simulation. Emplacing $\frac{1}{4}$ of the total intrusion heat, i.e. $3\,\mathrm{kW\,m^{-1}}$, at a shallow level is sufficient to significantly redirect the hydrothermal plume by 2.5 km. Heating of the fluids by the shallow intrusion region creates a suction driving diagonal upflow from the deep intrusion region so that the evolving plume efficiently collects and discharges the heat from both regions.

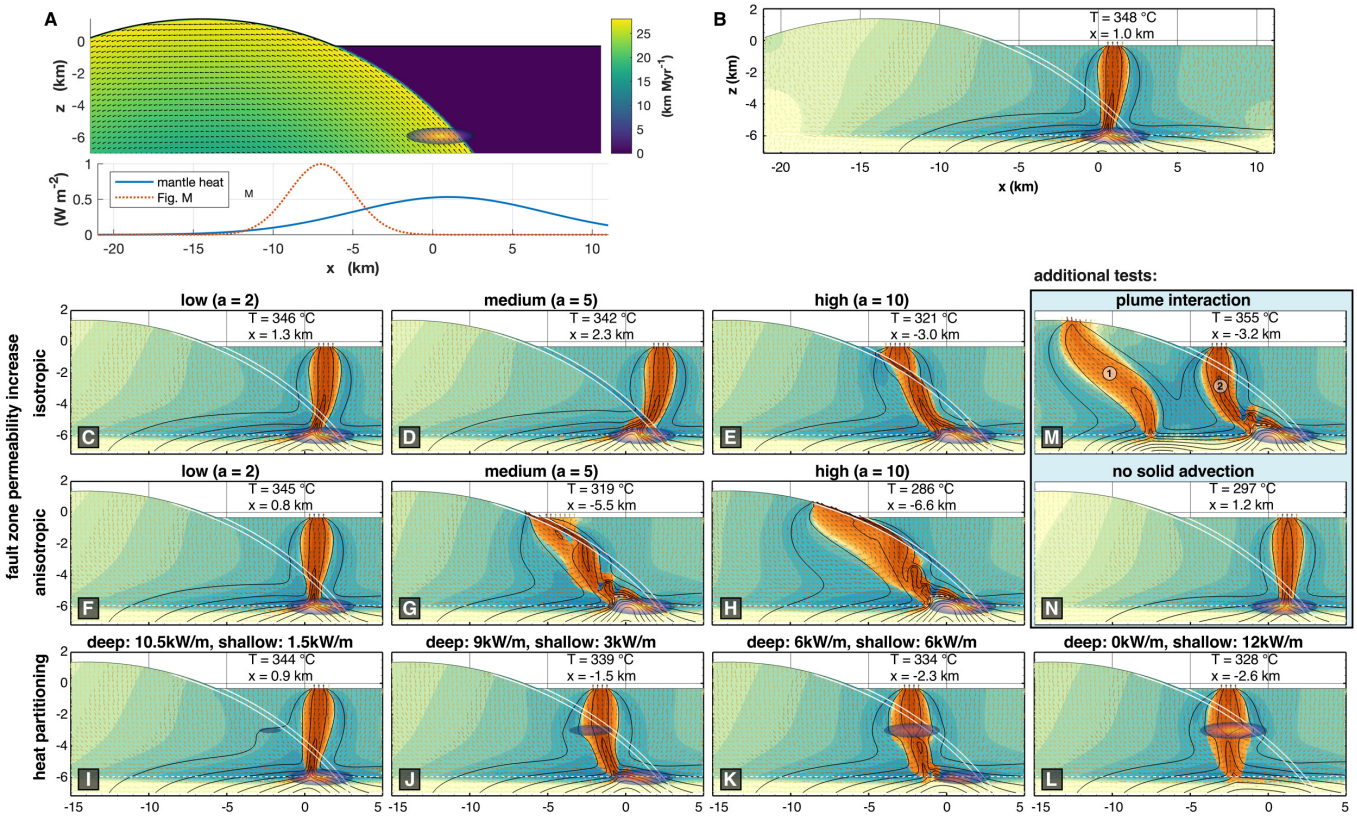

Figure 5.7. **A**: Simplified test setup to demonstrate plume redirection mechanisms. The solid advection including the dome is described by a rotation with $28\,\mathrm{km\,Myr^{-1}}$ at a radius of 21.3 km around [-14, -20] km, the rest of the top boundary is at a depth of -0.3 km (water depth 3300 m). The domain is initiated at 4 °C, the Gausssian heat flux boundary condition at the bottom shown by the line plot has a magnitude of $8\,\mathrm{kW\,m^{-1}}$ and a width of 6 km around x = 1 km. The dotted line depicts the additional heat source to trigger a second plume for the simulation shown in panel **M** (magnitude: $5\,\mathrm{kW\,m^{-1}}$, width: 2 km, x = -7 km). **B - N**: Fluid mass flux snapshots after 300 kyr. Color scales and framework as in previous figures. The full simulations can be seen in Movies S5.13 - S5.25.

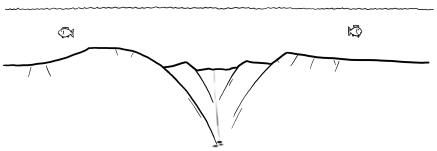

We expect shallow intrusions to be of limited duration, controlled by transient fractures and magmatic activity. We therefore analyze the plume behavior after switching the model back to a single deep heat source (Fig. 5.8 B). It shows that the plume does not retreat towards its undisturbed vent position. Instead, the diagonal plume creates a hot channel in the host rock making it more efficient to use this hot, deflected pathway (Fig. 5.7 J) rather than the straight vertical pathway through cold host rock. We have confirmed this idea in tests with a flat topography and a moving heat source. Thus, a shallow intrusion region of limited size, active over a limited duration, can cause significant and long-lasting redirection of hydrothermal activity, even after it has cooled to ambient temperatures, and at the same time remain undetected in seismic data. Note that we do not consider stresses and rheological differences associated with intrusions. These might, on the one hand, further control fluid outflow through evolving fractures, but on the other hand act as a low-permeability barrier reducing deeper hydration of the OCC (Jian et al., 2024). The continued heating of the plume visible in Fig. 5.8 B likely suggests that the model has not yet reached a steady state at 300 kyr, whereas the slowed migration of the venting position beyond 300 kyr may indicate that the plume is already close enough to the OCC to be influenced by its topography.

The simplified setup again demonstrates that a strong shallow heat source controls the venting position most effectively (Fig. 5.7 L). Seismic methods do not show extensive shallow melt regions (Peirce et al., 2023; Simão et al., 2020). However, continuous intrusion regions in our model represent the time-averaged effects of repeated intrusions that are not necessarily captured by a single seismic snapshot. Furthermore, recent volcanic rocks not covered by sediments have been found in the graben formed by the fault scarps at the tip of the OCC (Escartín et al., 2017). Therefore, the available data do not rule out the scenario of a single shallow intrusion region.

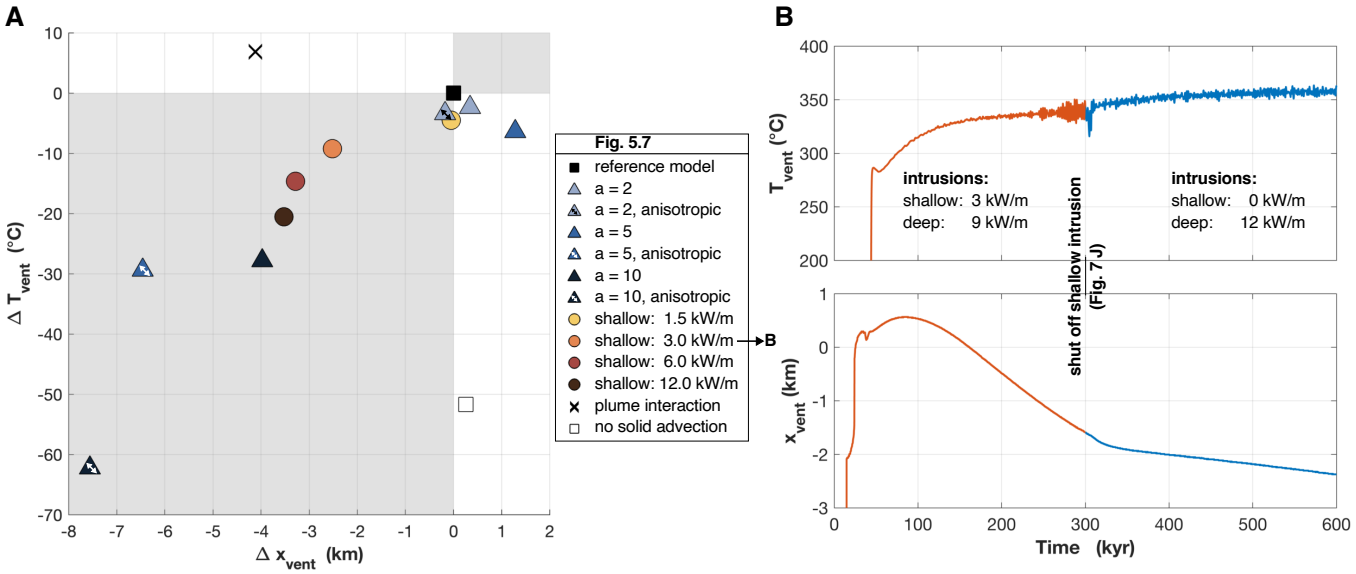

Figure 5.8. **A**: Deviation of venting temperature ΔT_{vent} and position Δx_{vent} in the different simulations with the simplified setup (Fig. 5.7) compared to the reference simulation (Fig. 5.7 B). Gray boxes highlight the different quadrants around the origin. **B**: Evolution of the venting temperature and position in the simulation with a shallow intrusion of 3 kW m^{-1} before and after switching the shallow intrusion region off. x_{vent} refers to the x-axis in Fig. 5.7.

5.5.3.4 Plume Interaction

We now want to demonstrate and discuss the interaction between two hydrothermal plumes mentioned in Section 5.4.2. We trigger a second, weaker plume by adding an additional heat source below the footwall (Fig. 5.7 M). The recharge flow in-between the two plumes causes a low pore pressure region and attraction between the two plumes. This competes with the topographic effect on plume #1 and causes plume #1 to pull plume #2 to the left as it migrates up the topography. In the full-sized, more dynamic simulations, the magnitude of the pull effect depends on position and strength of the secondary footwall plume.

At 13°30'N, Semenov-1,-2,-3, and -5 vent fields are seafloor expressions of hydrothermal plumes that have potentially interacted with the hydrothermal system below the simultaneously active Semenov-4. In 3-D, the effect might be less pronounced as recharge can come from the third dimension and does not necessarily occupy the space between plumes. Semenov-1,-2,-3, and -5 vent fields are aligned in E-W-direction along a spreading-parallel steepening of slope of the high-resolution AUV bathymetry (Fig. 5.1 B; Escartín et al., 2017). Pertsev et al. (2012) interpret this to be the surface expression of a spreading-parallel tectonic structure, which could reduce the along-axis influence.

5.5.3.5 Footwall Rotation

We also used our simplified setup to test the effect of solid advection on fluid flow, which is a unique feature of our coupled model. Our test shows that footwall rotation results in a leftward shift of only 200 m (Fig. 5.7 B) compared to a simulation without solid advection (Fig. 5.7 N). The effect is small, since heat transport through advection of hydrothermal fluids is around 10 to 100 times faster than solid advection and thermal diffusion. The additional advective heat transport from mantle upwelling results in 51 °C hotter venting.

5.5.3.6 Summary of Redirection Mechanisms

Hydrothermal venting at the 13°30'N OCC on the Mid-Atlantic Ridge is aligned close to the spine, i.e. the shallowest along-axis part of the detachment. This suggests a strong role of both, topography and the subsurface continuation of the fault zone (Parnell-Turner et al., 2020) for focusing fluid flow towards the domed part of the OCC. Based on our 2-D modeling results, shallow magmatic intrusions of limited duration and extent could further focus the large-scale hydrothermal system below the detachment. Additional support potentially comes from the interaction between plumes. Once a hydrothermal plume has been redirected, the percolated host rock forms a hot channel that facilitates efficient fluid flow. This leads to prolonged venting at a certain position without the need for plume redirection mechanisms to be permanently active.

Fig. 5.8 A demonstrates that any deviation of the hydrothermal plume from its reference state leads to a reduction in venting temperature (excluding the last two simulations with modified heat input). A clear correlation is observed between the displacement of the venting position in either direction and the vent temperature. This underscores that, in nature, sulfide deposition at the seafloor requires an interplay between the permeability structure and heat source(s) that sustains high-temperature venting.

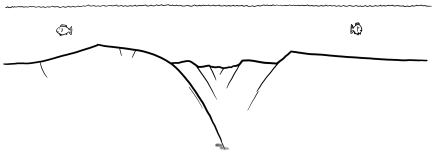

Note that circulation patterns in our model tend to be relatively inert. While the model effectively captures the long-term evolution within a framework of continuous deformation and heat supply, it may not fully account for intermittent, short-term activity, such as that documented through drilling at TAG (Humphris et al., 1995). We propose that episodic large-flux venting – in case it represents the dominant mode of hydrothermal activity – likely requires stronger and more localized increases in permeability and heat input than those modeled here. Nevertheless, intermediate phases of seawater influx along the shallow fault zone, as indicated by the mineralization of fault rocks (Martin et al., 2024), align with oscillations in vent fluxes reproduced by our model. These are primarily driven by plume instability caused by horizontal fluid transport, especially when applying an anisotropic fault zone permeability (Fig. 5.5 G - L). This alternating activity highlights the complex and ambiguous role of the fault zone and may serve as an indicator of transient shallow magmatic activity that periodically refuels hot upflow toward the vent field.

5.5.3.7 Generalization of the Proposed Mechanisms

Our study is specifically designed to reconstruct the 13°30'N OCC and the Semenov vent fields, with a particular focus on Semenov-4. The mechanisms discussed here, however, are of fundamental nature and are likely to be broadly applicable to detachment-related, TAG-like hydrothermal venting. The elevated seafloor relief characteristic to OCCs inherently exerts the topographic effect on the underlying hydrothermal system. Furthermore, all OCCs are formed by large-scale tectonic detachment faults. Although the exact permeability structure remains ambiguous, fault zone permeability is likely increased and anisotropic in the direction of slip. This facilitates circulation of fluids within the fault plane, and it limits mixing of the hot, rising fluids with cold ambient water.

Footwall magmatism, repeatedly recorded at different core complexes (e.g., Blackman et al., 2019; Dunn et al., 2017; Harding et al., 2017; Haughton et al., 2019; Jian et al., 2024), presumably focuses background circulation within the footwall and secondary faults. We have proven that intrusions of limited spatial and temporal extent are very efficient in reorganizing the hydrothermal system. We propose that this is an important aspect to understanding the formation of the large deposits associated to TAG-like venting. This leads to the question, what mechanisms trap these melts below the fault zone. Possible explanations are (1) a petrological barrier due to the contrast between footwall and hanging wall rocks, (2) clogging of the pore space surrounding the fault due to precipitation of hydrothermal minerals like serpentine or anhydrite (Andreani et al., 2007; Lowell & Yao, 2002), (3) migration of melts through the fault itself. These ideas in turn again point at the uncertainties about the permeability structure of the fault, which can have significant influence on fluid circulation pathways as demonstrated by our study.

Further research on the permeability structure of active detachment faults and their influence on melt migration in the footwall will help to complete the picture of detachment-related SMS accumulation drawn by our study. A better understanding of the factors controlling their formation will support the search for further large SMS by narrowing the search area for other methods such as sediment geochemistry (Liao et al., 2024) or machine learning approaches (Haroon et al., 2023).

5.6 Conclusion

We couple the output of a thermo-mechanical model that reconstructs the tectono-magmatic history of the oceanic core complex at the Mid-Atlantic Ridge at 13°30'N to a hydrothermal flow model to investigate factors controlling the position and amount of sulfides deposited at the seafloor. In a suitable configuration between fault zone, evolving seafloor relief and heat source, the topographic effect of the core complex alone can explain high-temperature venting close to the emergence of the detachment fault, where the largest deposits are found in nature. In combination with further controls on the flow field, we can explain long-term venting at this position over a wider range of configurations.

1. An anisotropic permeability increase along the fault zone is more efficient in guiding hot upflow through the fault than an isotropic increase due to reduced entrainment of cold ambient water.
2. A small shallow heat source can efficiently focus the hydrothermal system driven by deep larger heat sources.
3. Hydrothermal flow locally heats the host rock, causing stable flow paths along these hot channels and reducing the need for continuously acting focusing mechanisms.

Our results challenge the idea that a localized hydrothermal plume is redirected from an axial heat source by the fault zone alone. On the one hand, extensive horizontal fluid transport destabilizes the plume and reduces vent temperature and metal transport potential. On the other hand, measured mass accumulation rate indicates focusing of fluid flow over the along-axis extent of the core complex. We suggest that large seafloor massive sulfides are more likely associated with reorganization and focusing of the entire hydrothermal system by a combination of the mechanisms discussed in this paper.

Testing our ideas with a 3-D porous flow model, either by following our coupling approach and using a suitable thermo-mechanical model or by extrapolating our simplified setup will most likely give valuable additional insight on the role of fault zones, heat source distribution, and plume interactions.

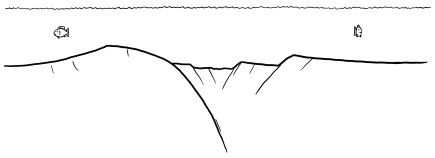

Chapter 6

Synthesis of Modeling Results & Implications

6.1 Methodological Advances

Before connecting the threads from our two studies, I will review the main code developments that facilitated this research. The numerical geodynamic model `M2TRI_vep`, employed in the studies presented in this thesis, builds on on the 2-D mantle convection model `M3TRI` developed by Hasenclever (2010). Successive extensions include a free surface algorithm (Andrés-Martínez et al., 2015), visco-elastic deformation (Hasenclever et al., 2017) and plastic deformation (Andrés-Martínez, 2016).

With the support of Jörg Hasenclever, I developed a model aimed at facilitating and advancing simulations of a wide range of mid-ocean ridge processes. We debugged and refined existing modules, implemented additional physical processes, and incorporated advanced numerical methods. Additionally, we designed setups to reconstruct the evolution of specific case studies, such as smooth seafloor areas between 62°E and 65°E on the SWIR, and the OCC at 13°30'N on the MAR.

While many of these contributions are discussed in the model descriptions in previous chapters, others represent subtle improvements that enhance code performance and output quality. Below is a summary of the major code enhancements we accomplished. Unless otherwise noted, I was the primary developer, with Jörg Hasenclever providing support through existing code, feedback, and testing.

Plasticity: Debugging of strain weakening, implementation of strain rate decomposition, plastic strain accumulation, strain healing (e.g., Behn & Ito, 2008; Kaus, 2010; Olive & Escartín, 2016), and visco-plastic regularization (Duretz et al., 2021).

Serpentinization: Implementation of the thermal and rheological effects of the reaction, controlled by a temperature-dependent kinetic rate (based on a function from Rüpke & Hasenclever, 2017) and access of rock to water for the reaction, parametrized by a volumetric work threshold (Bickert et al., 2020).

Dynamic grain size evolution: Implementation for mantle olivine following Ruh et al. (2022), based on the palaeo-wattmeter by Austin and Evans (2007), using experimental parameters by Speciale et al. (2020).

Hydrothermal cooling: Implementation of an advanced parametrization through increasing thermal conductivity (Gregg et al., 2009; Phipps Morgan et al., 1987; Theissen-Krah et al., 2011) and incorporating localized fault zone cooling controlled by rock deformation work.

Hydrothermal fluid flow: Coupling of the thermo-mechanical model evolution to a

porous flow model based on Hasenclever et al. (2014), allowing to consider rock-mechanical and topography effects.

Magmatic intrusions: Implementation in the form of (1) the thermal and rheological effects of periodic sill intrusions, or (2) continuous intrusion heat, together with different emplacement position strategies, such as the shallowest point of the melting region or the root of a detachment.

Magmatic diking: Implementation of the volume and heat effects of an axial diking region, allowing to study effects of the M-factor, based on Behn and Ito (2008) and Schierjott et al. (2023).

Surface processes: Incorporation of the module for surface sedimentation and erosion developed by Andrés-Martínez et al. (2019).

Numerical methods:

Dynamic mesh refinement controlled by model evolution to better resolve regions of interest. Simulations presented here, e.g., use strain rate or plastic strain to refine fault zones.

Remeshing procedure:

- Improved mapping of variables stored at integration points, e.g., plastic strain, serpentinization, and grain size, during the remeshing procedure. A mixed linear-quadratic scheme balances numerical diffusion against overshooting values during the intermediate mapping step to element nodes of the old mesh.
- Improved surface topography tracking

All modules are written in MATLAB, include detailed documentation, and are part of the latest version of the publicly available `M2TRI_vep 2.0` (Hasenclever & Glink, 2025). Additionally, all functions to perform the analyses of model results presented in this dissertation, as well as a library to make use of publicly available, perceptually uniform colormaps (e.g., Crameri, 2021), are included. The full code development history is documented in a git repository, access can be granted upon reasonable request. As part of this project, we generated the first open access version of the code. For the open access publication, I developed a new, cleaner code structure that will hopefully help new users to get started with the code more easily and facilitates adding modules in future code versions.

6.2 Insights from Numerical Models: Detachment Faulting and Hydrothermalism

In the previous chapters, we introduced different methods for coupling tectonic, magmatic and hydrothermal processes associated with oceanic spreading and detachment faulting. Notably, we implemented two distinct approaches to model hydrothermal activity. In Chapter 4, we parametrized the hydrothermal cooling effect by enhancing thermal conductivity, particularly along fault zones, to study flip-flop detachment faulting at the magma-poor segments of the ultraslow-spreading Southwest Indian Ridge. In Chapter 5, we explicitly modeled hy-

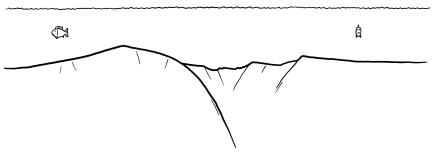

drothermal circulation within the faulted lithosphere at the oceanic core complex at the Mid Atlantic Ridge at 13°30'N. In this chapter, I will compare the influences on the temperature field of these two approaches and their respective fields of application. I will further discuss the implications for the tectonic evolution and finally integrate the findings into a broader understanding of the processes shaping detachment-dominated mid-ocean ridges.

6.2.1 Comparative Analysis of Hydrothermal Modeling Approaches

We have demonstrated in two studies that our approach of post-processing the mechanical output of a detachment model with different (hydro)thermal models is an efficient strategy to systematically compare different processes and parameters within a controlled framework (see Fig. 4.12 and Section 5.4). Here, I will apply each of the two hydrothermal modeling approaches to the respective other setting, effects on the temperature fields are illustrated in Fig. 6.1.

The parameterized approach (Fig. 6.1 A + C) offers a significant advantage in computational costs, making it particularly suitable for modeling long-term tectonic evolution, such as the reconstruction of the 11 Myr-long flip-flop sequence at the SWIR. For instance, the simulation depicted in Fig. 6.1 A can be completed within one to two days, whereas a fully-coupled hydrothermal-tectonic simulation over the same timespan would likely require at least a month to run using the current code version and hardware. However, the parameterized approach does not provide insights into hydrothermal circulation pathways within the lithosphere or the potential locations of high-temperature venting. Such details can only be resolved using computationally more expensive, explicit hydrothermal flow models (Fig. 6.1 B + D).

We know that at mid-ocean ridges, heat input from the mantle is dissipated by hydrothermal activity in the brittle lithosphere (e.g., Phipps Morgan et al., 1987; Theissen-Krah et al., 2011). Both modeling approaches reproduce this balance, and the sub-seafloor permeability structure (represented by the thermal conductivity scaling factor Nu in the parametrized approach) has been adjusted in our studies to reconstruct different axial lithosphere thicknesses at the two settings. This is essential for evaluating lithosphere strength and thus faulting. However, assumptions on the subsurface permeability structure also have implications for the vertical and lateral extent of hydrothermal activity in the model and thus on the thermal structure of the brittle-ductile transition and off-axis plate thickening.

In our study of flip-flop faulting at the SWIR, we account for a decrease in the cooling effect with depth and taper it around the brittle-ductile transition, without imposing explicit depth or off-axis limits. Figs. 6.1 A + C demonstrate that this results in a significantly deeper-reaching impact of hydrothermal circulation and faster off-axis plate thickening compared to strictly confining hydrothermal activity to the brittle lithosphere above 6 km depth around the axial region, as implemented in our model of the OCC at 13°30'N MAR (Fig. 6.1 B + D). Both permeability models rely on valid assumptions that are discussed in Sections 4.4.2.1 and 5.3.1. Models allowing for similarly deep hydrothermal circulation as our SWIR simulations are supported by studies such as Tao et al. (2020). However, data-based permeability models, such as those by Kuang and Jiao (2014), suggest a faster reduction in permeability with depth, especially outside active fault zones. In general, constraining subsurface permeability

structures remains challenging and includes significant uncertainties, as discussed in greater detail later.

Comparison between different modeling approaches is further complicated by the uncertainty of how conductivity scaling translates to the vigor of an equivalent hydrothermal system. Ongoing work on analytical scaling laws between permeability and Nu by Jean-Arthur Olive, Jie Chen and Antoine Demont (personal communication) will potentially allow to evaluate and compare parameter choices between parametrized and resolved hydrothermal simulations. A first quantitative assessment can be done by comparing the power output of

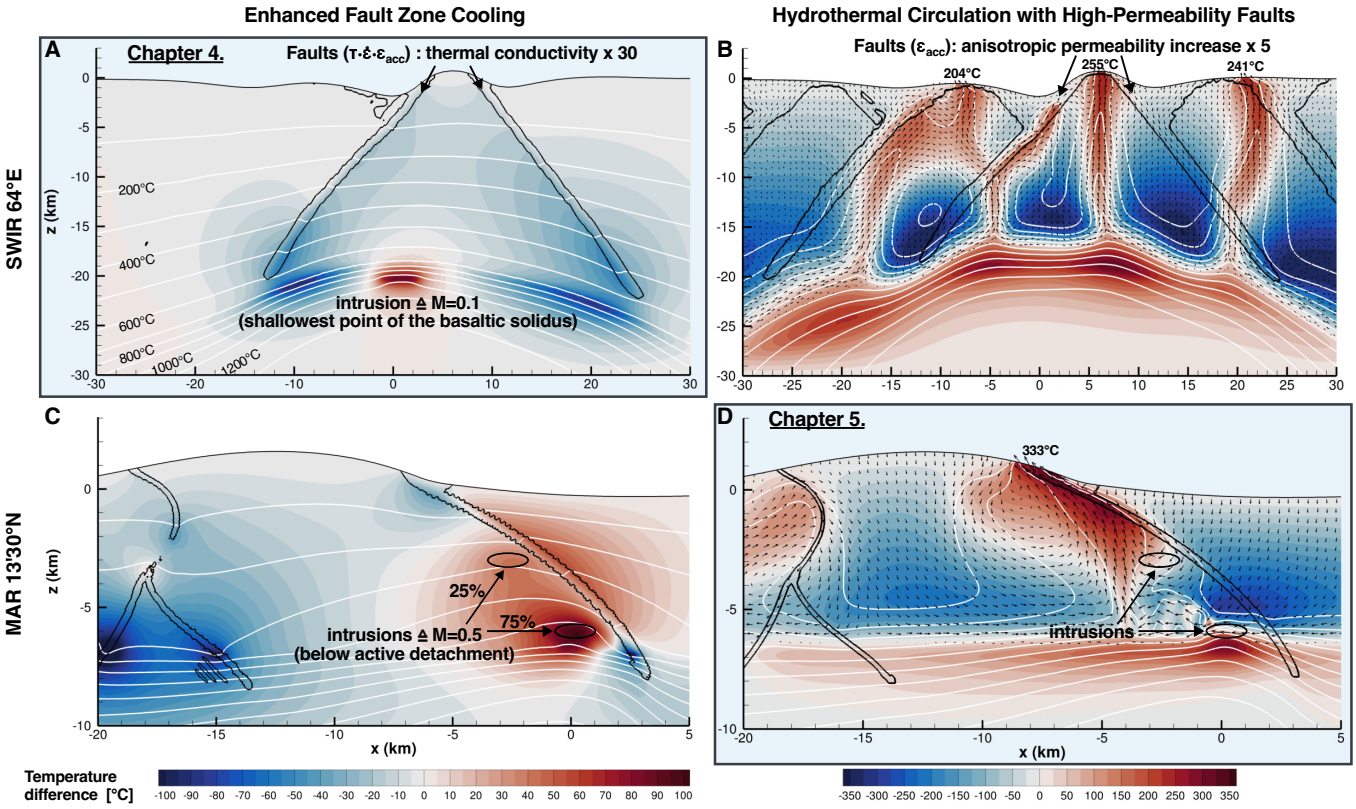

Figure 6.1. Comparison of two approaches to modeling the effects of hydrothermal activity and magmatic intrusions on the lithosphere temperature field, applied to the two case studies presented in this thesis. Left column (**A** + **C**): Parametrized hydrothermal cooling, enhanced along active fault zones, identified from a deformation work threshold, i.e. the product of stress τ, strain rate $\dot{\varepsilon}$, and accumulated plastic strain ε_{acc}. Right column (**B** + **D**): Porous flow simulations including high-permeability fault zones, identified by accumulated plastic strain. Top row (**A** + **B**): Setup representing smooth seafloor generating flip-flop detachment faulting at the SWIR between 62°E and 65°E. Intrusions representing a melt budget equivalent to M=0.1 are emplaced below the shallowest point of the 1000 °C-isotherm. Bottom row (**C** + **D**): Setup representing the OCC at the MAR at 13°30'N. Intrusions are emplaced at 3 km and 6 km depth in the footwall next to the detachment. Setups presented here showcase parameter combinations identified to yield a good fit in our studies. Fault zones are characterized by a thermal conductivity increase by a factor of $10^{1.5}$ an an anisotropic permeability increase by a factor of 5, respectively. While the permeability factor of 5 slightly exceeds the best-fit model discussed in the previous chapter, it is intentionally selected to better illustrate the effects of a permeable fault. For further details on the setups, see Appendix C. The parametrized hydrothermal model produces localized cooling along fault zones and a distinct temperature gradient between the cooler footwall and warmer hanging wall. The effect's strength depend on fault zone width and thermal conductivity increase. In contrast, the porous flow model features broad regions of cold downflow and more localized hot upflow zones, leading to stronger temperature variations. The distribution of hot and cold regions, as well as the role of fault zones, varies depending on topography, heat sources, and the permeability field.

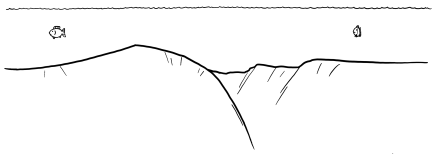

venting at the seafloor. In Section 4.4.2.1, we estimated a fault-related hydrothermal heat flux of $44\,\mathrm{W\,m^{-2}}$ for the same parameter combination as in Fig. 6.1 A, matching observed vent field heat outputs between the low-temperature Lost City and the high-temperature Longqi-1 vent fields. This compares reasonably well with the average maximum vent field heat flux of $30\,\mathrm{W\,m^{-2}}$ and medium venting temperatures between 200 °C and 260 °C in the porous flow simulation in Fig. 6.1 B, further validating our models.

Qualitatively, the main difference between the parametrized and resolved hydrothermal simulations is that the parametrization captures the time and space integrated effects of hydrothermal activity in contrast to actual fluid pathways. In turn, snapshots of the 2-D hydrothermal flow field do not necessarily show the long-term impact of the fault zone as hot or cold regions at first glance, complicating the direct comparison of the temperature fields resulting from the different models. Nevertheless, hydrothermal cooling of footwall and fault zone observed in the parametrized simulations (Fig. 6.1 A + C) is in agreement with conclusions from our hydrothermal flow simulations in Chapter 5: Dynamics of the 2-D flow field, estimated 3-D deposited mass and comparison to related numerical and geological evidence (e.g., Cherkashev et al., 2013; Guo et al., 2023; Martin et al., 2024) let us conclude that the 3-D detachment fault plane significantly assists in focussing footwall circulation and thus cooling with large-scale cold downflow and localized hot upflow.

6.2.2 Implications for Detachment Faulting

By integrating our findings with previous research summarized in Chapter 2, we can now draw a more comprehensive picture of oceanic detachment faulting and the associated hydro-tectono-magmatic feedbacks (Fig. 6.2). Below, statements supported by findings from Chapter 4 are denoted by superscript [4], and those from Chapter 5 by [5].

Detachment footwalls hosts large-scale hydrothermal convection cells driven by heat from upwelling mantle material and serpentinization. These processes result in low-temperature background hydrothermal activity and Type-3 / Lost City-type venting[5].

Magmatic activity within the detachment footwall intensifies fluid circulation, leading to higher vent temperatures[5]. Additionally, fluid venting may be shifted some kilometers away from the main magmatic heat source by the influence of shallow melts[5], possibly rising through secondary faults within the stressed footwall. Depending on the location of magmatic activity, this results either in TAG- or Rainbow-type venting[5]: Intrusions below the fault plane are more likely to result in Type-1 fluids that vent in the hanging wall. In contrast, if intrusions are emplaced further in the footwall, it is more likely that the elevated topography of the exhumed footwall will cause the hot fluids to redirect and vent Rainbow-like on the exhumed shear plane with Type-2 fluids.

The subsurface shear plane of the detachment fault itself acts as a permeable conduit, focusing part of the hydrothermal convection[5]. While this can support TAG-type venting, redirection of fluid flow away from the driving heat source is limited and reduces venting temperature. Therefore, Type-2 / Rainbow-type venting on the OCC is most likely not associated with circulation through the detachment fault zone[5].

The reason, why TAG-like deposits tend to be larger than Rainbow-like deposits is pre-

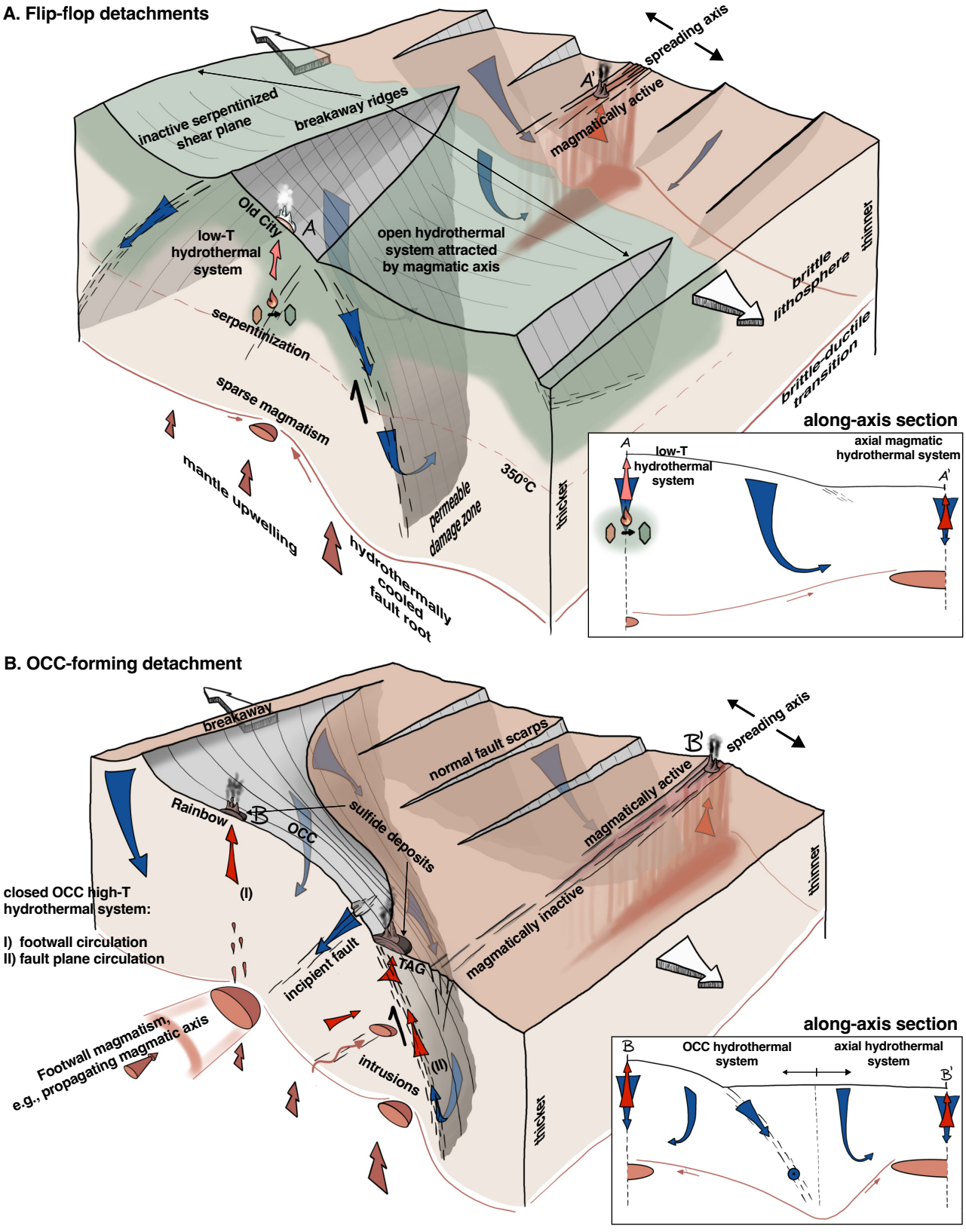

Figure 6.2. 3-D sketches of (**A**) flip-flop and (**B**) OCC forming detachments illustrating the diverse interplay of tectonic, hydrothermal, and magmatic processes, derived from a synthesis of our model results (not to scale). Sketches focus on active processes, geological information is illustrated in more detail in Fig. 2.2. Inset boxes depict along-axis sections crossing the exhumed fault plane, from detachment-dominated to magmatic areas.

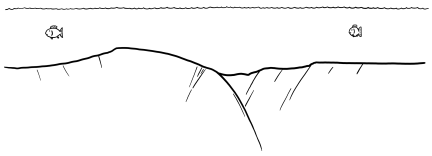

sumably because of a more stable configuration between the close-by long-lived detachment fault and the driving heat source. Maximum mantle upwelling and the original, yet potentially temporarily inactive magmatic spreading axis provide continuous heat, leading to long-term activity at the same location[5]. Furthermore, fluid pathways can stabilize themselves by creating hot channels in the host rock that facilitate efficient fluid flow[5]. Thus, transient controls such as magmatic intrusions can have a long-term impact on circulation patterns.

The location of magmatic activity – and consequently the type of hydrothermal activity – is controlled by tectonic deformation, thermal structure and along axis-variability[4,5]. Hydrothermal activity, which alters the footwall thermal structure, can thus affect the position of potential melt accumulation[4]. If fluids primarily cool the fault plane, melts extracted from the hot mantle rising beneath the detachment may accumulate further into the footwall, away from the detachment[4]. This effect may be particularly prominent at magma-poor flip-flop segments, such as at the SWIR, where the sparse magmatism reacts more passively to the lithosphere structure. At the right position and sufficient intensity, footwall magmatism eventually terminates detachment activity by triggering new faults that dissect the footwall[4,5]. This feedback applies even in magma-poor settings, where magmatic heat may be insufficient to sustain high-temperature venting[4].

At domed OCCs, detachments likely exhibit a concave-downward along-axis shape (Parnell-Turner et al., 2020), consistent with their seafloor morphology. Circulation within the fault plane therefore potentially focuses localized hot upflow in along-axis direction toward shallower parts of the fault zone. Anisotropy of the increased fault zone permeability within the shear plane limits mixing with ambient fluids[5]. This could confine footwall hydrothermal activity beneath the fault and insulate against neighboring ridge segments, further focusing fluid flow (see along-axis section in Fig. 6.2 B).

In contrast, the large ridges formed by flip-flop detachments at magma-poor segments indicate more elongated fault zones (Cannat, Sauter, et al., 2019; Cannat et al., 2006), which may prevent this along-axis hydrothermal confinement. Instead, circulation within the footwall and fault zone may remain open in along-axis direction, with hot upflow attracted to neighboring, magmatically robust segments (see along-axis section in Fig. 6.2 A). In the very thick lithosphere of flip-flop segments, migration of sparse melt to shallow depths is mostly inhibited, further reducing the potential for focusing high-temperature fluids. Consequently, high-temperature venting during magma-poor flip-flop detachment faulting, such as that inferred at the inactive Tianzu hydrothermal field (Ding et al., 2021) is likely an exception[5].

6.3 Limitations of Numerical Models: Parameter Uncertainties

The value that (numerical) models can contribute to our understanding of natural processes is closely tied to the number and quality of independent observational constraints on the model. In our simulations, three parameters have proven particularly influential on model outcomes: the structure of the brittle-ductile transition, the strain weakening parameters, and the permeability. This section revisits how these parameters affect model results, evaluates how well they are currently constrained, and explores potential improvements for future modeling efforts.

The **brittle-ductile transition** fundamentally governs lithospheric strength, influencing the initiation, evolution, and longevity of faults. Its structure has therefore been essential in both our studies and the focus of numerous earlier investigations (e.g., Bickert et al., 2020; Ito & Behn, 2008; Olive & Escartín, 2016). A thicker lithosphere, for example, supports less footwall rotation, faster off-axis lithosphere thickening results in increased faulting frequency, and magmatic footwall thinning can determine where new faults emerge. Additionally, the brittle-ductile transition represents the maximum depth for hydrothermal fluid penetration, thereby shaping hydrothermal circulation pathways. The primary constraint on brittle lithosphere thickness comes from microseismicity (e.g., Grevemeyer et al., 2019; Parnell-Turner et al., 2020), which limits our knowledge to seismically active regions that may be subject to temporal fluctuations not resolved by the seismic campaigns. Further insight can come from seismic velocity data, which is mostly used to estimate crustal thickness, but low-velocity regions can also indicate melt intrusions. However, 3-D seismic velocity models and reflection seismic surveys are restricted to a few well-studied areas (e.g., Dunn et al., 2017; Jian et al., 2024; Momoh et al., 2020; Simão et al., 2020), leaving much of the internal structure of OCCs and smooth seafloor ridges poorly resolved. Expanded (micro)seismic studies of additional detachment systems could refine our understanding of how hydrothermal cooling influences brittle deformation depths or of the conditions under which footwall magmatism thins the lithosphere.

Mechanical models are particularly sensitive to the **plastic parameters** and those used to implement strain weakening, that is the degree of friction angle reduction and cohesion loss, and the critical plastic strain over which these changes occur. These parameters control fault initiation, structural evolution, and termination, as demonstrated in multiple studies (e.g., Demont et al., 2024; Lavier et al., 2000; Sandiford et al., 2021) and verified in our own test simulations. Even though laboratory experiments provide estimates of plastic parameters for specific rock types (e.g., compilations by Escartín et al., 1997b; Handin, 1966; Karakul & Ulusay, 2024), their prescribed values and the extent and rate of weakening vary significantly between numerical studies. This variability potentially arises because (1) different experimental methods can yield different parameter values (Karakul & Ulusay, 2024), (2) scaling laboratory experiments on samples to geological stress-strain rate conditions of rock masses is challenging (e.g., Villeneuve & Heap, 2021), and (3) strain weakening is often used to parametrize a variable number of additional processes such as grain size reduction, hydrothermal alteration, and fault rock comminution. Parameter choices often lack detailed justification, making cross-study comparisons difficult. Numerical models of faulting would greatly benefit from a comprehensive, widely accepted catalog of the plastic parameters for common rock types (e.g., mantle peridotite, gabbro, basalt, serpentine), including both intact and weakened values for cohesion and friction angle, as well as characteristic weakening rates. Additionally, weakening could be based on descriptions of exposed fault zone structures, such as those provided by Escartín et al. (2017) for domed OCCs or the recent work by Mahato and Cannat (2025) on flip-flop detachments. Moreover, systematic investigations of the influence of different strength contrasts between fault zones and the brittle lithosphere in numerical models would provide valuable insights. Antoine Demont has made important contributions to this topic in the course of his doctoral project (Demont et al., 2024).

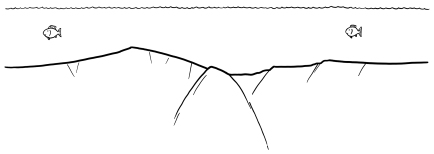

The **permeability structure** plays a critical role in determining the temperature field and hydrothermal circulation patterns, as reviewed in the previous section. Direct measurements are mostly constrained to the upper magmatic crust (e.g., Pruis & Johnson, 2002), and the three main uncertainties that influence porosity and permeability models are: How these properties change with age (or off-axis distance), how they vary with depth, and how they are modified by deformation within the fault zone. On the one hand, systematic investigations of different permeability structures in a simplified OCC model setup such as that demonstrated in Chapter 5 could help to evaluate the influence of these uncertainties on model results. On the other hand, methods to reduce uncertainties could include measuring the phase lag of detachment-related hydrothermal venting caused by tidal forcing, as demonstrated by Barreyre et al. (2018) for different axial vent fields, and converting seismic velocity data into porosity and permeability structures, as demonstrated by Marjanović et al. (2019) for the East Pacific Rise at 9°50'N. A more ambitious but potentially highly insightful approach would involve drilling a series of boreholes across an active OCC to directly measure variations in permeability and other properties.

6.4 Interdisciplinary Applications

Numerical models depend on being well-constrained by interdisciplinary datasets. Conversely, these models provide a critical link between seafloor observations – such as topography, rock composition, and hydrothermal deposits – and the underlying sub-seafloor processes. For instance, understanding how tectonic structures govern hydrothermal circulation and consequently the formation of seafloor ore deposits can aid in identifying new hydrothermal vent fields and sulfide deposits, thereby facilitating interdisciplinary research. Hydrothermal fluids are recognized as essential nutrient sources for the global ocean (Preiner et al., 2020), and vent fields continue to provide fundamental insights into diverse microbial communities, potentially shedding light on the origins of life itself (Früh-Green et al., 2022, and references therein). Seafloor massive sulfides also hold potential as future mining resources (Bang & Trellevik, 2022; Hannington et al., 2011), however, mining efforts must be approached with caution, ensuring comprehensive understanding of the bio-geo-chemical systems involved and the potential consequences of a human interference (Drazen et al., 2020).

In a broader sense, a more nuanced understanding of mid-ocean ridge processes and their role in shaping Earth will facilitate the interpretation of new data collected by international research initiatives, including research cruises and seafloor observatories. The recently deployed *EMSO-Mohn* observatory at the ultraslow-spreading Mohn's Ridge promises fascinating insights into venting dynamics of an ultramafic-hosted hydrothermal system. This will gain additional value from an analysis of potential sub-seafloor hydrothermal pathways based on numerical modeling. The *Seabed 2030* initiative aims to achieve a complete map of the seafloor by 2030. Using models to understand how different spreading modes and faulting patterns express at the seafloor will facilitate automatic feature identification and classification, as demonstrated by C. Liu et al. (2020).

Our approach of computing realistic fault patterns and stress fields and subsequently applying them to hydrothermal models has potential applications beyond mid-ocean ridge

settings. For example, it could inform studies of igneous sill intrusions in sedimentary basins (Galerne & Hasenclever, 2019; Rabbel et al., 2023) or practical implementations such as carbon capture and storage (CCS) and geothermal energy projects. CCS initiatives require robust evaluations of the integrity and longevity of potential host rock formations before and during CO_2 injection to reduce induced seismicity and prevent fresh water contamination (Kelemen et al., 2019, and references therein). In geothermal energy and lithium production, such as in the Rhine Graben, pre-existing fault structures significantly influence fluid dynamics and resource recovery (e.g., Goldberg et al., 2023).

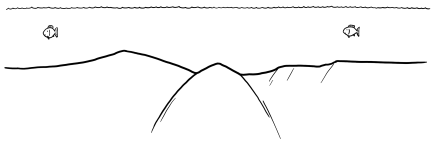

Chapter 7

Future Directions

Research on mid-ocean ridges remains a highly multidisciplinary field with numerous open questions, even when we focus on detachment-dominated ridges only. This outlook highlights potential future directions where integrating and advancing our models and methods alongside recent and ongoing research could produce synergies to take the next step in understanding these complex systems.

7.1 3-D Effects

Throughout this work, we have highlighted potential 3-D effects that may influence the results of our 2-D models. In the context of thermo-mechanical simulations, the along-axis variability of melt distribution and the location of the magmatic spreading axis is particularly relevant. At the SWIR, magma-poor, flip-flop-dominated corridors are bounded by magmatically robust segments that may act as thermal and mechanical anchors, stabilizing faulting patterns. Adapting our SWIR model setup to an existing open access 3-D geodynamic code, such as ASPECT (Bangerth et al., 2024) or LaMEM (Popov & Kaus, 2024), could verify this hypothesis. Specifically, the along-axis variability of melt supply could be introduced by prescribing variations in the magmatic fraction M, as done by Howell et al. (2019), or by considering melt extraction from the mantle and migration toward segment centers. Within our modeling framework for the 13°30'N OCC, validating our reconstruction of the detachment life cycle by including 3-D ridge axis propagation would be of particular interest.

Our 2-D hydrothermal flow simulations raised three key questions about their potential 3-D behavior: (1) How would the fault zone circulation pattern evolve when fluid recharge and discharge no longer compete within a 2-D channel? (2) How do extrapolated mass deposition rates align with actual 3-D venting? (3) To what extent does along-axis recharge reduce attraction between hydrothermal plumes? All three questions can be approached using a 3-D extension of our simplified 2-D OCC setup, illustrated in Fig. 7.1. A 3-D hydrothermal model is available, e.g., from Hasenclever et al. (2014).

7.2 Magmatism

Two key aspects of the hydro-tectono-magmatic network remain underexplored in our studies, as illustrated in Fig. 7.2: magmatism and the feedbacks of fluid-flow on faulting, particularly fluid-rock interactions. In our models, we employ data-driven assumptions about the location and volume of melt, simplifying the intricate processes of melt generation, migration, and emplacement that are central to mid-ocean ridge dynamics (Olive, 2023, and references therein). To address these gaps, a mantle melting module, such as the one available from Hasenclever

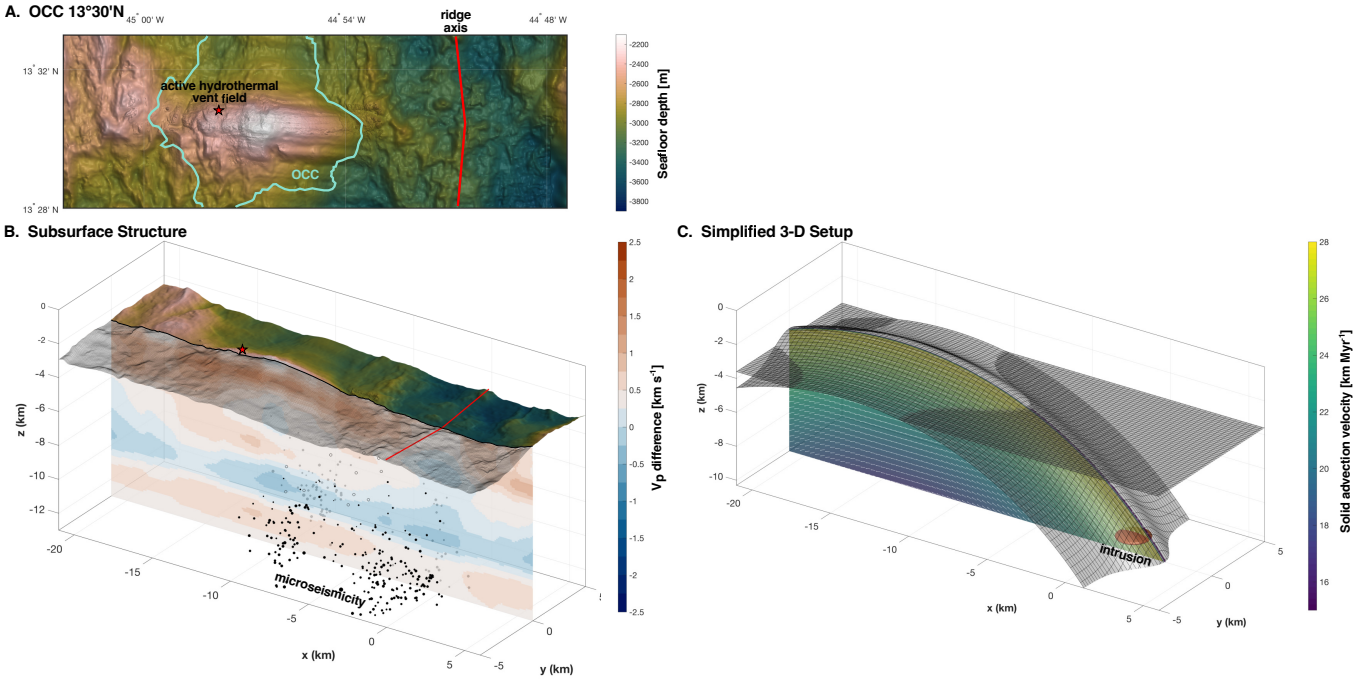

Figure 7.1. A + B: Bathymetry, P-wave velocity difference and microseismicity of the OCC at the MAR at 13°30'N as in Fig. 5.1 (data from Beaulieu & Szafranski, 2020; Escartín et al., 2017; Ryan et al., 2009; Simão et al., 2020; Sohn et al., 2020). Turquoise line in A marks the outline of the OCC following Mallows and Searle (2012). **C:** Exemplary 3-D extension of the simplified OCC model setup demonstrated in Fig. 5.7. The "seafloor" shape of the artificial OCC approximates the shape of the real OCC in A by modulating the radius of the circular deformation field with a Gaussian bell curve in along-axis direction. This translates into a concave-downward along-axis shape of the subsurface fault zone (cf. Parnell-Turner et al., 2020) with potentially interesting effects on the hydrothermal circulation pattern. The spindle-shaped radial deformation field around the rotation axis at $[x = -14, z = -20]$ km allows to consider solid deformation without having to adjust the model geometry.

et al. (2017), could be integrated into our model. Stresses associated with melt emplacement could also be considered using the compressible formulation from de Montserrat et al. (2019), which is already part of an unreleased version of our model `M2TRI_vep`. Even without explicitly modeling two-phase flow of melt and rock, incorporating these features would enable us to explore two critical questions that arise from our studies: (1) How much melt is generated in our models, how does this compare to the amount of melts incorporated by periodic intrusions and diking, and what constraints does this place on along-axis melt transport? (2) Do the stresses induced by melt emplacement and subsequent cooling significantly reduce the amount of melt required to trigger a new fault in the footwall of a waning detachment?

7.3 Fluid-Rock Interactions

In Chapter 5, we examined the effects of a one-way coupling between the mechanical detachment model and hydrothermal flow. The next logical step is to investigate the feedbacks of fluid circulation on mechanical evolution (cf. Fig. 7.2). Therefore, Fig. 7.3 presents the results of a fully-coupled simulation using the framework for the OCC at 13°30'N MAR from Chapter 5. Technical details on the setup and coupling are provided in Appendix C.3. The key difference from the previous study is that now the influence of fluid flow on rock rheology through temperature and pore fluid pressure is considered.

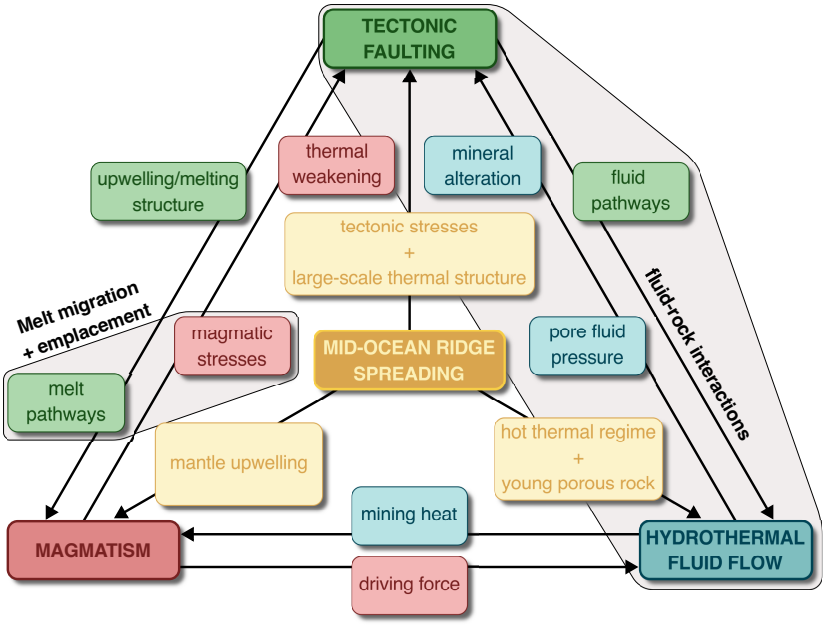

Figure 7.2. Parts of the hydro-tectono-magmatic network that remain underexplored by the two studies included in this dissertation.

The detachment evolution in this coupled model closely resembles that of the reference simulation with parametrized hydrothermal cooling in Fig. 5.3. The most striking difference is the second, antithetic fault that is temporarily active on the other side of the spreading axis between 550 kyr and 650 kyr (Fig. 7.3 D + E). However, neither the subsequent evolution of the OCC, nor the hydrothermal circulation pattern are significantly affected. Moreover, this and further differences, such as the slightly shallower fault dip, greater seafloor relief, and hydrothermal pathways, fall within the variability range of purely mechanical or hydrothermal test simulations. These results confirm the consistency of the mechanical and hydrothermal models from Chapter 5, despite one-way coupling.

The impact of hydrothermal circulation on mechanical evolution is limited in this model because it primarily impacts the temperature field within the porous region. Rock deformation, however, is only sensitive to temperature in the viscous domain, which is only slightly influenced by fluid flow, with more significant effects arising from intrusion emplacement (cf. Fig 6.1 D). This highlights once more the importance of constraining subsurface permeability structure and penetration depth, as discussed in Section 6.3. Improved constraints on these parameters are likely to yield greater insights than increasing model complexity alone.

Hydrothermal convection-induced variations in pore fluid pressure also have minor impact on mechanical evolution. In the simulation without porous flow, we assume hydrostatic pore fluid pressure based on temperature and pressure-dependent fluid properties (see Appendix B.1.2). Differences in pore fluid pressure due to flow-induced density variations are less than 10 %, resulting in negligible effects on the brittle yield criterion.

The results in Fig. 7.3 represent an initial step toward a fully-coupled hydro-thermo-mechanical detachment model, which will require further testing and validation. The strong consistency with our one-way coupled simulations is already a promising indicator of the

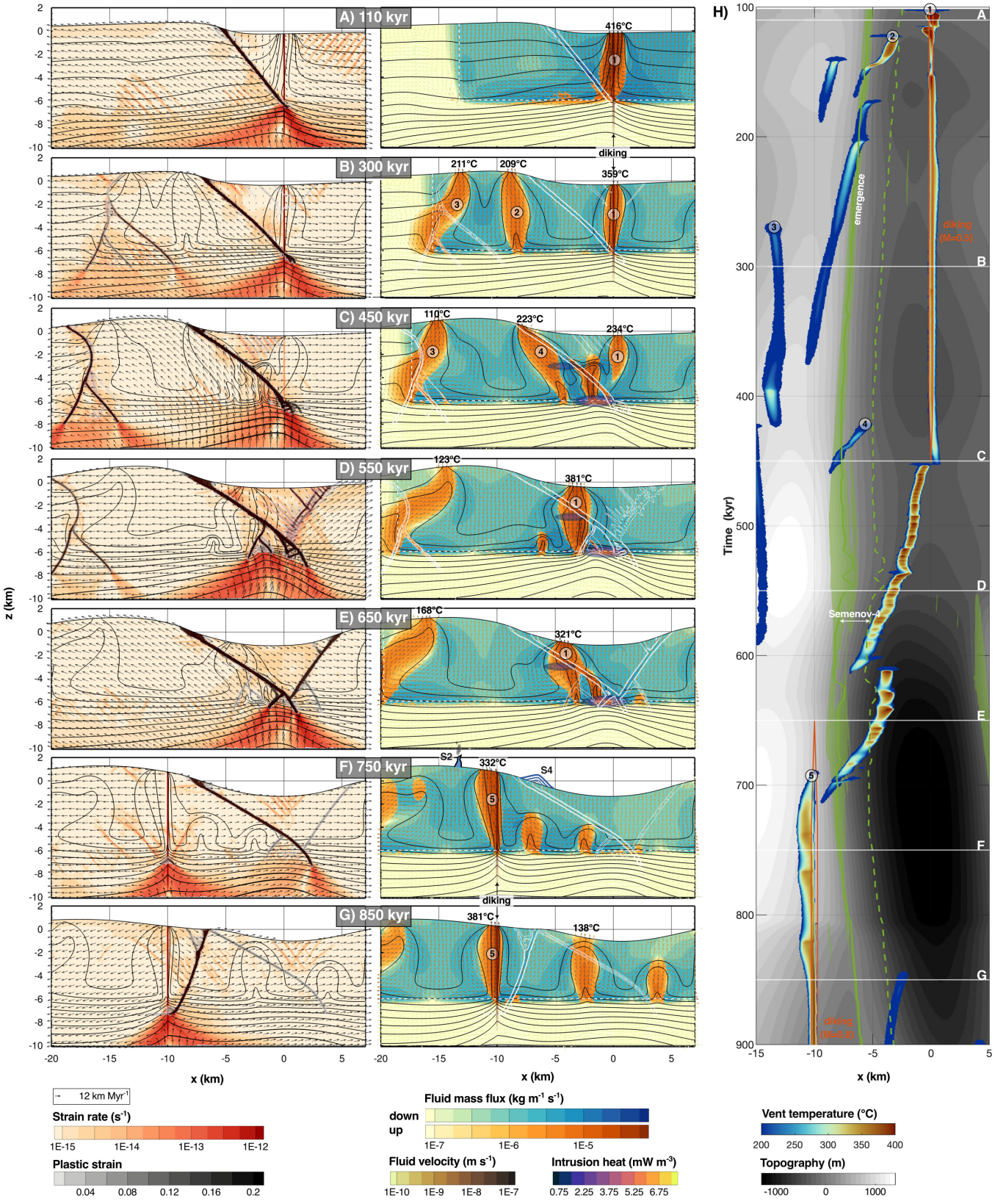

Figure 7.3. Solid deformation, temperature, fluid mass flux and seafloor properties of a fully-coupled hydro-thermo-mechanical simulation. Graphical frameworks and modeling setup of the OCC at 13°30'N MAR from Chapter 5. Intrusions and fault zone permeability employ the best-fit parameter combination from the one-way coupled simulations: intrusion heat is split at the ratio 1-3 between 3 km and 6 km depth, fault zones have a twofold anisotropic permeability compared to the background. The full simulation can be seen in Movie S7.1, for technical details see Appendix C.3.

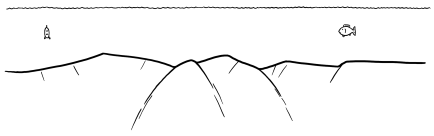

model's robustness. The list of feedbacks to explore with such a coupled model is long: Incorporating poro-elasticity, where porosity evolves dynamically with the stress field and pore fluid pressure (e.g., Keller et al., 2013), could lead to pore space opening along faults, drawing in surrounding fluids (Mezri et al., 2015) and thereby enhancing the role of faults in fluid circulation. This could also increase and localize variations in pore fluid pressure, potentially leading to hydrofracturing, or fluid-assisted rock failure, further altering permeability and fault evolution. A fully-coupled model would also facilitate advanced simulations of rock alteration processes, such as serpentinization, by accounting for fluid availability and consumption during reactions, as well as fracturing and permeability/ porosity effects due to volume changes and mineral precipitation (e.g., Iyer et al., 2010).

As we incorporate these additional processes, it is crucial to build our understanding incrementally, starting with simple feedbacks and consistently validating models against observations. This approach will provide more sustainable insights than pursuing overly complex models prematurely. As emphasized in my introductory statement on numerical modeling, the most complex models should be seen as proofs of concept, useful only after the mechanisms involved have been studied individually to untangle the intricacies of the system. My work has taken important steps in this direction, paving the path for further exploration.

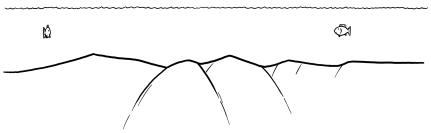

Appendix A

Supporting Information for Chapter 4

A.1 Additional Information for the Parameter Study

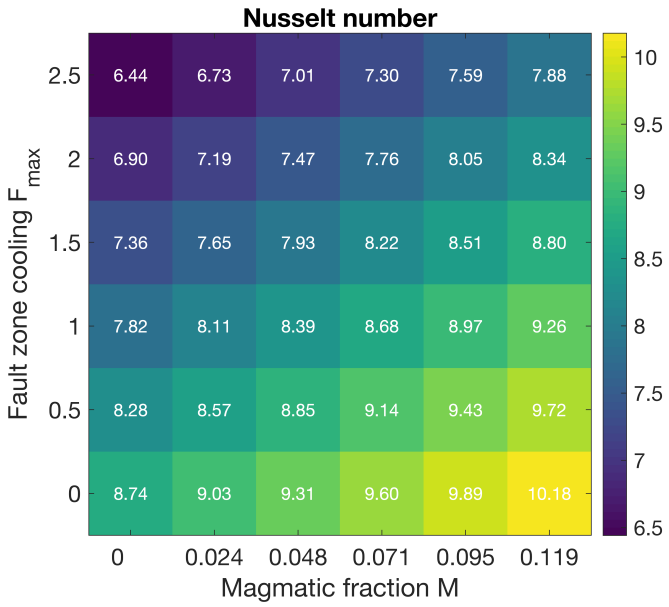

Figure A.1. Values of Nu_0 used for the different simulations of the parameter study. Nu_0 has been adjusted with F_{max} and M to reproduce observed brittle lithosphere thickness.

Table A.1. Geometry and emplacement period of magmatic sills used in the experiments and the equivalent M-factor.

Width × height (km)	$1000\sqrt{2} \times 100\sqrt{2}$	2000×200	3000×300	4000×400	5000×500
Emplacement every ... kyr	40	40	60	80	100
M-factor	0.024	0.048	0.071	0.095	0.119

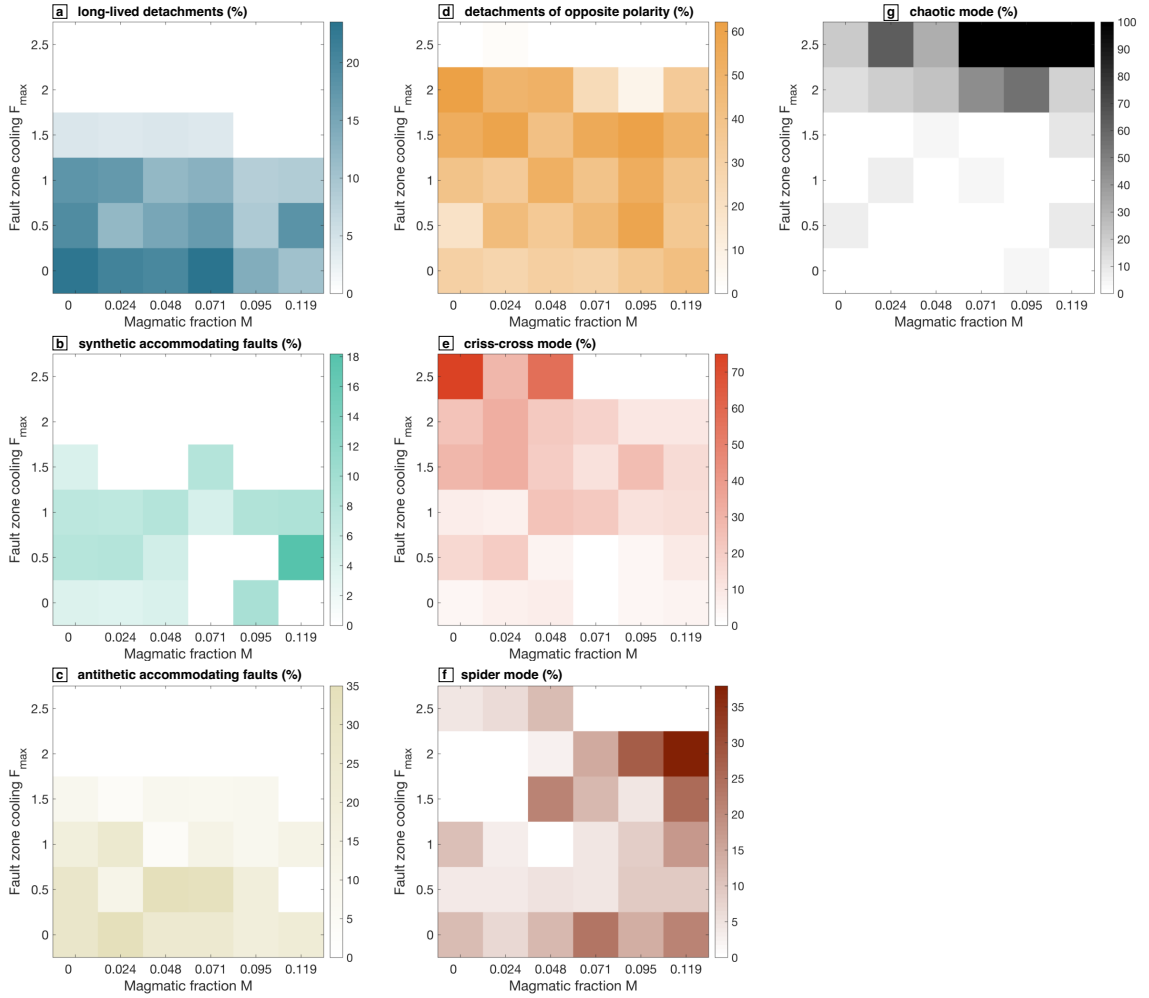

Figure A.2. Fig. 4.11 broke down to the percentages of each faulting mode.

A.2 Movie Descriptions

Simulation movies are found online at https://doi.org/10.25592/uhhfdm.16721.

Movie S4.1. - `GlinkHasenclever2024-ms01-steadyT-ff.mp4`

Flip-flop detachment faulting (imposed temperature field):

Zoom into the central model region displaying flip-flop dynamics in the model with imposed temperature field. Left: strain rate and white isotherms. Vectors represent the advection velocity. Right: Grain size in µm (blue) overlain by serpentinization degree (green to yellow) and black isotherms.

Movie S4.2. - `GlinkHasenclever2024-ms02-noIntr-noNu-Run0.mp4`

Miniature flip-flop faulting in a simulation without hydrothermal cooling:

Sequence from simulation 0 (numbering as in Fig. 4.11) without hydrothermal cooling or intrusion emplacement ($\mathrm{Nu} = 1$, $\mathrm{M} = 0$) showing faulting in a very thin brittle lithosphere. Same graphical framework as in Movie S4.1.

Movie S4.3. - `GlinkHasenclever2024-ms03-longDet-Run1.mp4`

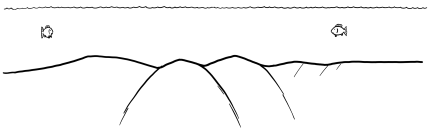

Long-lived detachments and antithetic accommodating faults:

Sequence from simulation 1 without fault zone cooling or intrusion emplacement ($M = 0$, $F_{max} = 0$) showing the evolution of the two long-lived detachment faults and their accommodating faults illustrated in Fig. 4.6 a,b,e+f. Note that the spin-up phase of 2.7 Myr featuring spider mode faults is excluded from the classification in Fig. 4.11, since it is mainly controlled by the initial configuration and similar for most of the simulations. Same graphical framework as in Movie S4.1.

Movie S4.4. - `GlinkHasenclever2024-ms04-longDet-synAcc-Run2.mp4`

Long-lived detachment and synthetic accommodating fault:

Sequence from simulation 2 ($M = 0$, $F_{max} = 0.5$) showing the evolution of a long-lived detachment fault and its synthetic accommodating fault illustrated in Fig. 4.6 c + d. Same graphical framework as in Movie S4.1.

Movie S4.5. - `GlinkHasenclever2024-ms05-ff-dc-Run28.mp4`

Flip-flop sequence and deep-cutting modes:

Sequence from simulation 28 ($M = 0.095$, $F_{max} = 1.5$) showing the flip-flop sequence illustrated in Fig. 4.7 and the evolution of two deep-cutting faults to criss-cross mode and spider mode as illustrated in Fig. 4.9. Left and central panel as in Movie S4.1, right panel shows the Nusselt number on a logarithmic scale, overlain by yellow to purple isotherms. Intrusions are marked in red in the central panels and by temperature in the right panels.

Movie S4.6. - `GlinkHasenclever2024-ms06-chaotic-Run24.mp4`

Chaotic faulting mode:

Sequence from simulation 24 ($M = 0.071$, $F_{max} = 2.5$) showing chaotic faulting illustrated in Fig. 4.10. Same graphical framework as in Movie S4.5.

Movie S4.7. - `GlinkHasenclever2024-ms07-FFnoTmax-Run5.mp4`

Flip-flop faulting in high-F_{max} simulation:

Flip-flop sequence from simulation 5 ($M = 0$, $F_{max} = 2.0$). Flip-flop faulting in high-F_{max} simulations cannot be attributed to the mechanism described in Section 4.4.1 "Thermal Structure of the Footwall" anymore, since the footwall temperature maximum lies between the old and the evolving new fault instead of triggering the new fault at its root. Same graphical framework as in Movie S4.5.

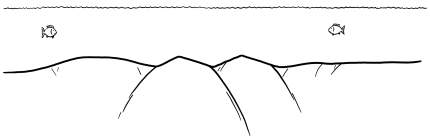

Appendix B

Supporting Information for Chapter 5

B.1 Thermo-Mechanical Model Description

A detailed model description of our thermo-mechanical model including further references can be found in Chapter A. Here, we provide a brief overview of the constitutive equations with a focus on features introduced in this study. Thermo-mechanical variables and parameters are listed in Table B.1.

B.1.1 Mechanical Conservative Equations

We solve the conservation equations for mass, Eq. (B.1), and momentum (Stokes flow), Eq. (B.2), for an incompressible medium using the Boussinesq approximation. The solution variables are displacement velocity components u_i and total pressure P:

$$\frac{\partial u_i}{\partial x_i} = 0, \tag{B.1}$$

$$\frac{\partial \tau_{ij}}{\partial x_j} - \frac{\partial P}{\partial x_i} + \rho g_i = 0, \quad \text{with} \quad \rho = \rho_0 \left(1 - \alpha\right) T, \tag{B.2}$$

where x_i are the spatial coordinates, τ_{ij} are the deviatoric stresses, ρ is the density and g_i are the components of the gravitational acceleration. Reference density ρ_0 is defined at the reference temperature of 0 °C and α is the thermal expansion coefficient.

B.1.2 Rheology

Viscous, elastic and plastic (subscripts e, v, and p, respectively) deformation processes are assumed to be additive, the stress-strain rate relation is based on the visco-elastic Maxwell-model:

$$\tau_{ij} = \eta_{eff} \left(2\dot{\varepsilon}_{ij} + \frac{\hat{\tau}_{ij}}{G\Delta t} \right), \tag{B.3}$$

where $\dot{\varepsilon}_{ij}$ are the deviatoric strain rates, $\hat{\tau}_{ij}$ are the Jaumann-rotated old deviatoric stresses, and Δt is the model time step. The effective viscosity η_{eff} including the effect of plastic yielding can be expressed by

$$\eta_{eff} = \begin{cases} \left(\frac{1}{\eta_v} + \frac{1}{G\Delta t} \right)^{-1}, & \text{if} \tau_{II} < \tau_{yield}. \\ \frac{\tau_{yield}}{2\dot{\varepsilon}_{II}}, & \text{if} \tau_{II} \geq \tau_{yield}. \end{cases} \tag{B.4}$$

We assume an isotropic medium and use the second invariant defined by $\chi_{II} = \sqrt{\frac{1}{2}\ \chi_{ij} \cdot \chi_{ij}}$

Table B.1. Description and values of model parameters and variables used for the thermo-mechanical detachment model.

Parameter	Description	Unit	Value
g_i	Gravitational acceleration	$\mathrm{m\,s^{-2}}$	[0, 0, -9.81]
P	Total pressure	Pa	
R	Gas constant	$\mathrm{J\,kg^{-1}\,mol^{-1}}$	8.314472
t	Time	s	
Δt	Time step	kyr	0.5 - 5
T	Temperature	°C	
u_i	Advection velocity	$\mathrm{m\,s^{-1}}$	
U_{x0}	Full spreading rate	$\mathrm{km\,Myr^{-1}}$	24
x_i	Spatial coordinates	m	
$\dot{\varepsilon}_{ij}$	Deviatoric strain rate	$\mathrm{s^{-1}}$	
$\dot{\epsilon}_{ij}$	Full strain rate	$\mathrm{s^{-1}}$	
$\varepsilon_{II,p}$	Accumulated plastic strain		
ε_{sw}	Plastic strain of full strain weakening		0.2
η	Viscosity	Pa s	$10^{18} - 10^{24}$
τ_{heal}	Strain healing time scale	kyr	30
τ_{ij}	Deviatoric stresses	Pa	
τ_{yield}	Yield stress	Pa	
	Thermo-mechanical rock properties[a]		
C	Cohesion	MPa	44(4)
C_p	Specific heat capacity	$\mathrm{J\,kg^{-1}\,K^{-1}}$	1000
G	Shear modulus	GPa	10
H_{rad}	Radiogenic heat production rate	$\mathrm{W\,m^{-3}}$	0.25×10^{-6}
α	Thermal expansion coefficient	$\mathrm{K^{-1}}$	3×10^{-5}
κ_0	Thermal conductivity	$\mathrm{W\,m^{-1}\,K^{-1}}$	2.5
ρ_0	Reference density	$\mathrm{kg\,m^{-3}}$	3300
Φ	Friction angle	°	30(10)
	Dry diabase creep law[b]		
A	Pre-exponential factor	$\mathrm{MPa^{-n}\,s^{-1}}$	100
n	Stress exponent		4.7
E	Activation energy	$\mathrm{kJ\,mol^{-1}}$	485
	Surface processes[c]		
K_s	Submarine diffusion coefficient	$\mathrm{m^2\,yr}$	100
λ_s	Submarine diffusion coefficient decay	$\mathrm{m^{-1}}$	5×10^{-4}
h_w	Local depth below sealevel	m	
z_{top}	Vertical position of top nodes	m	
	Conservation of heat		
H_{shear}	Shear heating rate	$\mathrm{W\,m^{-3}}$	
H_{dike}	Magmatic heat from diking	$\mathrm{W\,m^{-3}}$	
Nu	Nusselt number		8
θ	x-, z- and T-dependent porous region taper		[0, 1]
	Diking		
$\dot{\psi}$	Dilation rate from diking	$\mathrm{s^{-1}}$	
w	Width of dike region	m	130
T_{liq}	Magma liquidus	°C	1200
T_{sol}	Magma solidus	°C	1000
Q_{lat}	Latent heat per kilogram of melt	$\mathrm{kJ\,kg^{-1}}$	335

[a] Properties based on Behn and Ito (2008), values of pure rock before considering fluid volume
[b] Mackwell et al. (1998)
[c] Kaufman et al. (1991)

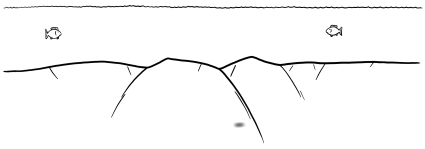

as a scalar measure of tensor variables χ_{ij}. Elastic deformation is controlled by the shear modulus G, non-Newtonian creep viscosity η_v is defined by

$$\eta_v = \frac{1}{2^{\frac{n-1}{n}} 3^{\frac{n+1}{2n}}} A^{-\frac{1}{n}} \left(\dot{\varepsilon}_{II,v}\right)^{\frac{1}{n}-1} \exp\left(\frac{E}{nRT}\right) . \tag{B.5}$$

Upon yielding, the effective stress is reduced to the yield stress τ_{yield} defined by a Drucker-Prager criterion using the full dynamic pressure P reduced by pore fluid pressure P_f:

$$\tau_{yield} = C \cdot \cos\Phi + \sin\Phi \cdot (P - P_\mathrm{f}) , \tag{B.6}$$

with C and Φ being the cohesive strength and the friction angle, respectively. An equilibrium pore fluid pressure field is computed at every time step based on Eq. (B.18) (next section). Using the parameter values from Table B.1 and a geothermal gradient of $0.1\,^\circ\mathrm{C\,m^{-1}}$, we find that the transition from elastic-brittle to ductile behavior of the intact rock occurs at 600-700 °C at a depth of 6-7 km.

Strain weakening is incorporated in our model by linearly reducing rock cohesion and friction angle by factors of 0.9 and 2/3, respectively, over the range of accumulated plastic strain $\varepsilon_{II,p}$ from 0 to 0.2. The accumulated plastic strain is computed by integration of the plastic strain rate over time. Plastically deformed rock is able to heal over a characteristic time span of $\tau_{heal} = 30\,\mathrm{kyr}$:

$$\varepsilon_{II,p}(t + \Delta t) = \left(\varepsilon_{II,p}(t) + \dot{\varepsilon}_{II,p}(t) \cdot \Delta t\right) \cdot \left(1 - \frac{\Delta t}{\tau_{heal}}\right) . \tag{B.7}$$

B.1.3 Surface Processes

Surface processes, i.e. submarine sediment transport and mass wasting, are implemented as described in Andrés-Martínez et al. (2019) based on the diffusion equation by Kaufman et al. (1991):

$$\frac{\partial z_{top}}{\partial t} = \frac{\partial}{\partial x}\left(K_s \cdot \exp\left(-\lambda_s h_w\right) \frac{\partial z_{top}}{\partial x}\right) . \tag{B.8}$$

Diffusivity decays exponentially with local depth below sealevel h_w. K_s is the diffusivity at sealevel, λ_s is the decay coefficient. In every advection step, we solve the 1-D diffusion equation and adjust the position of the top nodes z_{top}.

B.1.4 Conservation of Heat

The conservation equation of heat is solved to obtain the temperature T:

$$\rho C_p \frac{DT}{Dt} = \frac{\partial}{\partial x_i}\left(\kappa \frac{\partial T}{\partial x_i}\right) + H_{shear} + H_{dike} + H_{rad}, \tag{B.9}$$

where C_p is the specific heat capacity and κ is the thermal conductivity. H-terms represent the heat sources and sinks, i.e. visco-plastic shear heat $H_{shear} = \tau_{II} * \dot{\varepsilon}_{II,vp}$, heat from cooling and crystallization of diking melts H_{dike}, and radiogenic heat production H_{rad}. In the thermo-mechanical simulation, the effect of hydrothermal cooling is parametrized through an increase

of the thermal conductivity:

$$\kappa = \kappa_0 \cdot (1 + (\mathrm{Nu} - 1) \cdot \theta_{\mathrm{lin}}(x, z, T)) \tag{B.10}$$

κ_0 is the thermal conductivity of the host rock, Nu = 8 is the increase within the axial prorous region defined by the taper θ, which accounts for porosity/ permeability closure (see Section 5.3.1 of the main text for further explanations and taper limits). In the porous region, we take the volumetric average between rock (subscript r) and fluid (subscript f) properties based on porosity ϕ. $C_{p,\mathrm{f}}$, α_{f}, κ_{f} and ρ_{f} are pressure- and temperature-dependent and evaluated from look-up tables created from the IAPS-84 equation of state. Other properties listed in Table B.1 are 0 for the fluid phase.

B.1.5 Diking

Diking is implemented by adding a dilation term $\dot{\psi}$ to the conservation of mass (volume) inside a prescribed dike region. Added volume scales with the full plate spreading velocity U_{x0}, the magmatically accommodated fraction of spreading M and the width w of the dike region:

$$\dot{\psi} = \mathrm{M}\frac{U_{x0}}{w} \tag{B.11}$$

We assume purely horizontal opening of the dike region, which is ensured by adding a correction term on the strain rate in the momentum conservation based on

$$\dot{\varepsilon}_{ij} = \dot{\varepsilon}_{ij,vep} + \dot{\varepsilon}_{ij,dike} \tag{B.12}$$

$$\dot{\varepsilon}_{ij,dike} = \dot{\epsilon}_{ij,dike} - \frac{1}{3}\mathrm{tr}\left(\dot{\epsilon}_{dike}\right)\delta_{ij} \tag{B.13}$$

$$\begin{bmatrix} \dot{\varepsilon}_{xx} & \dot{\varepsilon}_{xz} \\ \dot{\varepsilon}_{zx} & \dot{\varepsilon}_{zz} \end{bmatrix}_{dike} = \begin{bmatrix} \dot{\psi} & 0 \\ 0 & 0 \end{bmatrix} - \frac{1}{3}\begin{bmatrix} \dot{\psi} & 0 \\ 0 & \dot{\psi} \end{bmatrix} = \begin{bmatrix} \frac{2}{3}\dot{\psi} & 0 \\ 0 & -\frac{1}{3}\dot{\psi} \end{bmatrix} = \dot{\psi}D_{ij}. \tag{B.14}$$

$\dot{\epsilon}_{ij}$ is the full strain rate tensor, the tensor representation of $\dot{\epsilon}_{ij,dike}$ in Eq. (B.14) contains the assumption of horizontal dike opening. The final term is added to the strain rate in Eq. (B.3), which results in an additional term on the right-hand side of Eq. (B.2) during matrix assembly. This strategy is similar to the implementation of diking by Schierjott et al. (2023). Note that this approach does not consider stress build-up and release associated with the formation of individual dikes but models their time integrated volume effect. We therefore do not allow diking to influence rheology by removing the effect of the dilation term from the flow field when converting it to stresses and strain rates.

We assume instantaneous emplacement of melt and consider the heat from cooling from liquidus to ambient temperature and crystallization heat based on Behn and Ito (2008):

$$H_{dike} = \begin{cases} 0 & \text{, for} \quad T \geq T_{liq} \\ \dot{\psi}\rho_{\mathrm{r}}\left(C_{p,\mathrm{r}}\left(T_{liq} - T\right) + Q_{lat}\frac{T_{liq}-T}{T_{liq}-T_{sol}}\right) - \rho_{\mathrm{r}}\frac{Q_{lat}}{T_{liq}-T_{sol}}\frac{DT}{Dt} & \text{, for} \quad T_{liq} \geq T \geq T_{sol} \\ \dot{\psi}\rho_{\mathrm{r}}\left(C_{p,\mathrm{r}}\left(T_{liq} - T\right) + Q_{lat}\right) & \text{, for} \quad T_{sol} \geq T \end{cases} \tag{B.15}$$

The partially molten case assumes crystal fraction to increase linearly with decreasing temperature from liquidus (T_{liq}) to solidus (T_{sol}). Q_{lat} is the latent heat per kilogram of melt. The term featuring the material derivative of the temperature is implemented by increasing the specific heat capacity in Eq. (B.9) inside the dike region.

The dike region has the width of one element and is defined by a column of vertically aligned elements spanning the brittle lithosphere between the seafloor and the 600 °C-isotherm. To account for the gradual brittle-ductile transition and to reduce artifacts, we add a 3 km deep region to the bottom of the dike over which the dilation term is linearly reduced to zero.

B.1.6 Discretization

The model domain is 250×80 km, discretized with an unstructured finite element mesh using 7-node Crouzeix-Raviart triangular elements. Active fault zones as well as the dike region are resolved at 75 m, the axial region at 150 m, and resolution further coarsens towards the lateral (250 m) and bottom boundaries (1000 m). The model time step dynamically adjusts to solid advection velocity and temperature changes and ranges between 500 and 5000 years. At each time step, Eqs. (B.1) and (B.2) are solved and used to update the non-linear rheology model in successive Picard iterations until their residual falls below a prescribed threshold or the maximum number of 40 iterations is reached.

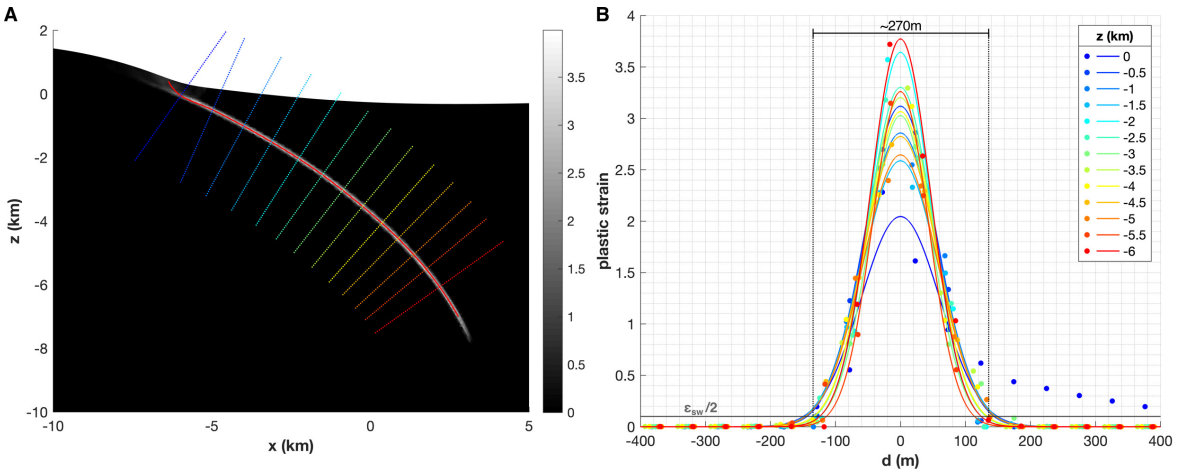

Figure B.1. Illustration of the fault width analysis. **A:** Plastic strain at 650 kyr. Red line is the center of the fault zone, dotted lines are the locations of the rectangular profiles shown in **B**. Points are interpolated strain values along the profiles, lines are fitted Gaussian curves. We define the fault width from the mean width of the 50 % strain weakening region of fitted Gaussian curves.

B.2 Hydrothermal Model Description

B.2.1 Porous Flow Constitutive Equations

We model flow of supercritical pure water through a deforming porous medium. Fluid mass transport is described by Darcy's law:

$$v_i = -\frac{k}{\eta_\mathrm{f}}\left(\frac{\partial P_\mathrm{f}}{\partial x_i} - \rho_\mathrm{f} g_i\right), \tag{B.16}$$

with v being Darcy velocity and k is permeability. Subscript f denotes fluid properties. Hydrothermal variables and parameters are listed in Table B.2. Our permeability model is described in Sections 5.4.1 and 5.4.3.1 of the main text. Fluid mass balance is given by

$$\frac{\partial \phi \rho_\mathrm{f}}{\partial t} = -\frac{\partial}{\partial x_i}\left(v_i \rho_\mathrm{f}\right), \tag{B.17}$$

where ϕ is rock porosity. Substituting Eq. (B.16) into Eq. (B.17) and considering the fluid's thermal expansivity α_f and compressibility β_f yields

$$\phi\left(\beta_\mathrm{f}\frac{\partial P_f}{\partial t} - \alpha_\mathrm{f}\frac{\partial T}{\partial t}\right) + \rho_\mathrm{f}\frac{\partial \phi}{\partial t} = \frac{\partial}{\partial x_i}\left(\rho_\mathrm{f}\frac{k}{\eta_\mathrm{f}}\left(\frac{\partial P_\mathrm{f}}{\partial x_i} - \rho_\mathrm{f} g_i\right)\right). \tag{B.18}$$

Porosity changes $\frac{\partial \phi}{\partial t}$ only arise from changes of the porous region (lateral widening, thermal closure at the bottom). We solve Eq. (B.18) for the pore fluid pressure, which can subsequently be used to calculate fluid velocity using Eq. (B.16).

The conservation of heat described by Eq. (B.9) is modified to account for effects related to hydrothermal convection:

$$\rho C_p \frac{DT}{Dt} = \frac{\partial}{\partial x_i}\left(\kappa\frac{\partial T}{\partial x_i}\right) + \sum_{\text{Eq.(B.9)}} H + \rho_\mathrm{f} C_{p,\mathrm{f}}\, v_i \frac{\partial T}{\partial x_i} + \frac{\eta_\mathrm{f}}{k_{II}}|v|^2 + \phi\left(\frac{\partial \ln \rho_\mathrm{f}}{\partial \ln T}\right)_P \frac{DP_\mathrm{f}}{Dt} + H_{intr} \tag{B.19}$$

Additional terms are, from left to right, (1) heat advection by fluid flow, (2) heat generation by internal friction of the fluid, (3) the pressure–volume work of the fluid and (4) heat from magmatic intrusions. Both, H_{dike} and H_{intr}, represent magmatic heat, but while H_{dike} explicitly considers cooling and crystallization of melts, H_{intr} is a prescribed heat flux as introduced in Section 5.4.1 of the main text.

B.2.2 Anisotropic Permeability

As introduced in the main text, the permeability field in our model is described by the relation

$$k = k_0 \cdot \left(1 + (a-1)\cdot \min\left\{1, \frac{\varepsilon_{acc}}{\varepsilon_{sw}}\right\}\right) \cdot \theta_{\log}(x,z,T) = k_0 \cdot f(\varepsilon_{acc}) \cdot \theta_{\log}(x,z,T). \tag{B.20}$$

For this study, we implemented local anisotropy of the permeability field into our model. In addition to its magnitude from Eq. (B.20), anisotropic permeability is defined by the angle φ of the most permeable direction measured clockwise from the x-axis, making permeability a

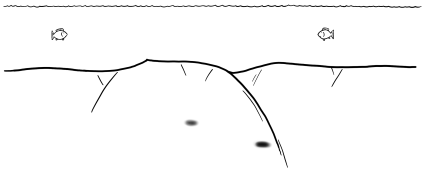

Table B.2. Description and values of model parameters and variables used for the hydrothermal flow model.

Parameter	Description	Unit	Value
a	Fault zone permeability factor		[1, 2, 5, 10]
H_{intr}	Magmatic heat from intrusions	$\mathrm{W\,m^{-3}}$	see main text Section 5.4.1
k	Permeability	$\mathrm{m^2}$	1.3×10^{-15} [a]
v_i	Darcy velocity	$\mathrm{m\,s^{-1}}$	
v_{z0}	Velocity buffer of venting b.c.	$\mathrm{m\,s^{-1}}$	10^{-9}
ϕ	Porosity	%	5 [a]
	Fluid properties[b]		
$C_{p,\mathrm{f}}$	Specific heat capacity	$\mathrm{J\,kg^{-1}\,K^{-1}}$	P-T-dependent look-up table
α_f	Thermal expansion coefficient	$\mathrm{K^{-1}}$	– " –
β_f	Compressibility	$\mathrm{Pa^{-1}}$	– " –
κ_f	Thermal conductivity	$\mathrm{W\,m^{-1}\,K^{-1}}$	– " –
η_f	Viscosity	$\mathrm{Pa^{-1}}$	– " –
ρ_f	Density	$\mathrm{kg\,m^{-3}}$	– " –

[a] Background values of the porous region
[b] IAPS-84 equation of state of pure water

tensor field:

$$\mathbf{k_0} = k_0 \cdot \theta_{\log}(x, z, T) \cdot \begin{bmatrix} \sqrt{2f(\varepsilon_{acc})^2 - 1} & 0 \\ 0 & 1 \end{bmatrix} \tag{B.21}$$

$$\mathbf{R} = \begin{bmatrix} \cos\varphi & -\sin\varphi \\ \sin\varphi & \cos\varphi \end{bmatrix} \tag{B.22}$$

$$\mathbf{k} = \mathbf{R}' * \mathbf{k_0} * \mathbf{R} \tag{B.23}$$

The second invariant of the anisotropic permeability tensor reduces the above formulation to Eq. (B.20) so that the magnitude of fault zone enhancement is comparable between the isotropic and the anisotropic case for the same value of a.

In the anisotropic case, Darcy's law becomes

$$v_x = -\frac{1}{\eta_\mathrm{f}} \left(k_{xx} \frac{\partial P_\mathrm{f}}{\partial x} + k_{xz} \left(\frac{\partial P_\mathrm{f}}{\partial z} - \rho_\mathrm{f} g \right) \right) \tag{B.24}$$

$$v_z = -\frac{1}{\eta_\mathrm{f}} \left(k_{zx} \frac{\partial P_\mathrm{f}}{\partial x} + k_{zz} \left(\frac{\partial P_\mathrm{f}}{\partial z} - \rho_\mathrm{f} g \right) \right) \tag{B.25}$$

We determine the local slip angle at each node by fitting a line to all nodes within a 200 m radius weighted by their respective plastic strain.

B.2.3 Modified Free Venting Condition

The classical free venting condition applied in most porous flow models is composed of a fixed temperature at regions of fluid inflow (seawater temperature of 4 °C for submarine systems), and zero vertical temperature gradient at regions of outflow. This is mainly designed to represent large energy fluxes associated with focused high-temperature venting, but tests have shown that it can lead to excessive extension of slow-venting regions. To reduce this effect,

we incorporate a buffer region defined by a vertical Darcy velocity range $v_{z0} = 10^{-9}\,\mathrm{m\,s^{-1}}$, over which the temperature of in- and outflowing fluids mix based on their velocity:

$$v_z \leq -v_{z0}: \qquad T_{bc} = T_{top} = 4\,^{\circ}\mathrm{C} \tag{B.26}$$

$$-v_{z0} < v_z < +v_{z0}: \qquad T_{bc} = T_{top} + (T - T_{top})\frac{v_z + v_{z0}}{2v_{z0}} \tag{B.27}$$

$$+v_{z0} \leq v_z: \qquad \frac{dT}{dz} = 0. \tag{B.28}$$

B.2.4 Discretization

The hydrothermal model domain covers the x-range from -30 km to 20 km and extends to a depth of 15 km. It is discretized with an unstructured finite element mesh using linear 3-node triangular elements. Faults are resolved at 40 m so that flow along the detachment is resolved by ∼8 elements. The axial region and the footwall are resolved at 80 m, and resolution coarsens to 200 m at the lateral boundaries and 400 m in the impermeable lower region. The model time step dynamically adjusts to fluid advection velocity and temperature changes and is fixed between 0.2 and 200 years, but is about 4 years most of the model time.

B.2.5 List of Hydrothermal Simulations

Table B.3. Parameter values and movie names of the hydrothermal simulations in the detachment model framework.

Movie	**a**	**Anisotropy**	**Intrusion heat [kw m^{-1}]**		**File name**
			$z = -6$ km	$z = -3$ km	
S5.2	1		12		`Glink2025-ms02-HT-RefRun.mp4`
S5.3	2		12		`Glink2025-ms03-HT-a2-iso.mp4`
S5.4	5		12		`Glink2025-ms04-HT-a5-iso.mp4`
S5.5	10		12		`Glink2025-ms05-HT-a10-iso.mp4`
S5.6	2	✓	12		`Glink2025-ms06-HT-a2-aniso.mp4`
S5.7	5	✓	12		`Glink2025-ms07-HT-a5-aniso.mp4`
S5.8	10	✓	12		`Glink2025-ms08-HT-a10-aniso.mp4`
S5.9	1		10.5	1.5	`Glink2025-ms09-HT-shallow1-5kW.mp4`
S5.10	1		9	3	`Glink2025-ms10-HT-shallow3kW.mp4`
S5.11	1		6	6	`Glink2025-ms11-HT-shallow6kW.mp4`
S5.12	1		0	12	`Glink2025-ms12-HT-shallow12kW.mp4`

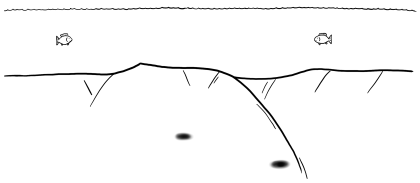

Table B.4. Parameters values and movie names of the hydrothermal simulations in the simplified framework.

Movie	a	Aniso.	Intrusion heat [$\mathrm{kw\,m^{-1}}$]		Notes	File name
			$z = -6\,\mathrm{km}$	$z = -3\,\mathrm{km}$		
S5.13	1		12			`Glink2025-ms13-HT-simpleOCC-RefRun.mp4`
S5.14	2		12			`Glink2025-ms14-HT-simpleOCC-a2-iso.mp4`
S5.15	5		12			`Glink2025-ms15-HT-simpleOCC-a5-iso.mp4`
S5.16	10		12			`Glink2025-ms16-HT-simpleOCC-a10-iso.mp4`
S5.17	2	✓	12			`Glink2025-ms17-HT-simpleOCC-a2-aniso.mp4`
S5.18	5	✓	12			`Glink2025-ms18-HT-simpleOCC-a5-aniso.mp4`
S5.19	10	✓	12			`Glink2025-ms19-HT-simpleOCC-a10-aniso.mp4`
S5.20	1		10.5	1.5		`Glink2025-ms20-HT-simpleOCC-shallow1-5kW.mp4`
S5.21	1		9	3	+300 kyr with deep intrusion only	`Glink2025-ms21-HT-simpleOCC-shallow3kW.mp4`
S5.22	1		6	6		`Glink2025-ms22-HT-simpleOCC-shallow6kW.mp4`
S5.23	1		0	12		`Glink2025-ms23-HT-simpleOCC-shallow12kW.mp4`
S5.24	1		12		2nd plume	`Glink2025-ms24-HT-simpleOCC-2ndPlume.mp4`
S5.25	1		12		No solid advection	`Glink2025-ms25-HT-simpleOCC-Usolid0.mp4`

B.2.6 Movie Description

Simulation movies are found online at https://doi.org/10.25592/uhhfdm.16721. Movies show the evolution of the hydrothermal models using the same framework as figures in Chapter 5. Fluid mass flux in blue for downward flow and in red for upward flow. Black isotherms have 100 °C-increments, transparent patches show intrusion heat, vectors show the fluid advection velocity. White isolines depict plastic strain at 10 %, 50 % and full weakening, dashed white line indicates the inner boundary of the porous region. The porous region widens to the left with time as described in Section 5.3.1 of the main text. The line plot on top depicts venting temperature. A list of file names is found in Tables B.3 and B.4.

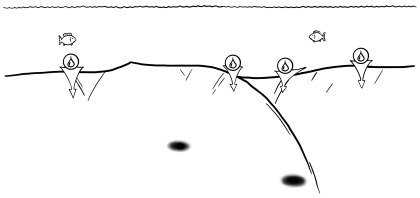

Appendix C

Model Descriptions for Chapters 6 & 7

C.1 SWIR 64°E Simulations

The mechanical model used for the simulations shown in Fig. 6.1 A + B is an updated version of the one described in Section 4.2. For simplicity, I used the imposed temperature field as described in Section 4.3.1. Additionally, this simulation features surface diffusion (cf. Section B.1.3) to achieve a more realistic seafloor relief essential for the porous flow simulations. The yield criterion uses the full dynamic pressure (Drucker-Prager criterion) for more realistic fault dips, however, this increases the non-linearity of the model. Therefore, friction angle softening of $\frac{1}{3}$ is used in addition to cohesion loss and plastic strain heals over a characteristic time scale of 100 kyr to increase fault stability. For further investigation of detachment faulting at the SWIR, I suggest to use this updated modeling setup. In the thermal post-processing illustrated in Fig. 6.1 A + B, strain healing is however disregarded, because the resulting accumulated plastic strain and width of the fault zone, and in consequence the hydrothermal cooling effect would be inconsistent with the results presented in Chapter 4.

While the mechanical model has been run with an imposed temperature field, Figs. 6.1 A + B show the temperature difference compared to a conductive temperature field without enhanced fault zone cooling (cf. simulation 1 in Chapter 4: $F_{max} = 0$, M = 0). Parameterized cooling represented by Nu exponentially decreases with depth as discussed in Section 4.2.3. Fig. 6.1 A showing the effect of periodic intrusions and enhanced fault zone cooling (cf. simulation 28: $F_{max} = 1.5$, M = 0.1) over one detachment cycle between 18.8 Myr and 19.5 Myr is equivalent to Fig. 4.12. Fig. 6.1 B shows the result of a porous flow simulation over the same time interval. The background permeability, like Nu, decreases exponentially from the surface value of $1.3 \times 10^{-15}\,\mathrm{m}^2$ over the same characteristic depth of 10 km. It only has a temperature cut-off between 600 °C and 800 °C, but no depth or off-axis limits. Fault zone permeability is anisotropic and increased by a factor of 5 in the direction of slip. Intrusion parameters are similar to the parametrized simulation. All other parameters and settings of the hydrothermal simulation are similar to the model presented in Chapter 5 and Appendix B.2.

C.2 MAR 13°30'N Simulations

The simulations shown in Figs. 6.1 C + D use the thermo-mechanical baseline model of the OCC at the MAR at 13°30'N presented in Section 5.3.2 for the mechanical evolution and the reference temperature field. Fig. 6.1 C shows the effect of enhanced fault zone cooling with $F_{max} = 1.5$, while the background cooling is the same as in the baseline model with Nu = 8 constant over the porous region. Because of the significantly different fault zone parameters compared to the SWIR model, I adjusted the work thresholds over which the enhancement

is applied to 10^{-8} and $10^{-6}\,\mathrm{J\,s^{-1}\,m^{-3}}$. Note, that these values are not motivated by observations but to demonstrate the qualitative difference between the two approaches. Fig. 6.1 D illustrates the temperature effect in a simulation with a fivefold, anisotropic fault zone permeability. In both simulations, the total intrusion heat of $12\,\mathrm{kW\,m^{-1}}$ is split, $3\,\mathrm{kW\,m^{-1}}$ are emplaced at 3 km depth next to the detachment, $9\,\mathrm{kW\,m^{-1}}$ are emplaced at 6 km depth

C.3 Fully Coupled Simulation

The mechanical and the hydrothermal models alone are the same as those described in Appendix B. Coupling is realized by replacing the thermal diffusion solver in the thermo-mechanical simulations with the hydrothermal model. Over the duration of a mechanical time step, hydrothermal computations are performed using smaller time steps with lengths determined by temperature changes and flow velocities.

The hydrothermal domain corresponds to the central, high-resolution region of the full modeling domain, in this simulation at $-28 \leq x \leq 14\,\mathrm{km}$ and $z \geq -10\,\mathrm{km}$. The finite element mesh in that region basically remains the same for both models, but the quadratic 6-node elements used for thermal diffusion (same as the 7-node Crouzeix-Raviart mechanical elements without the central bubble node) are divided into four linear 3-node elements for hydrothermal flow computations.

Instead of refining faults, the resolution in the whole central model region is set to 75 m to achieve adequate resolution of hydrothermal flow within the porous region. Faults in this coupled model are less resolved compared to the hydrothermal post-processing simulations in Chapter 5, where both mesh resolutions can be chosen completely independent. In the fully-coupled model, however, independent meshes would require mapping between them in every hydrothermal time step, when diffusion over the whole domain is computed. This repeated mapping between two meshes of significantly different resolution would lead to numerical diffusion. Therefore, improving fault resolution in the coupled would require either a higher fault resolution in the mechanical model or further splitting elements. The first approach would reduce comparability to previous results since no regularization is used, the latter would necessitate implementing a scheme to manage hanging nodes at the edges of the refined hydrothermal domain. For this proof-of-concept simulation, the current resolution is sufficient.

As described before, thermal diffusion is computed across the entire thermo-mechanical domain within the hydrothermal sub-iterations. Since the models share the same nodes, no mapping is necessary. At the end of the hydrothermal sub-iterations, variables are stored, either to be used in the mechanical computations, such as temperature, pore fluid pressure and fluid properties, or to be used at the beginning of the next hydrothermal sub-iterations.

The simulation illustrated in Fig. 7.3 uses the best fit parameter combination from Chapter 5 with a twofold anisotropic fault zone permeability increase and intrusion heat split to $3\,\mathrm{kW\,m^{-1}}$ at 3 km depth and $9\,\mathrm{kW\,m^{-1}}$ at 6 km depth. The off-axis taper of the porous region is applied to the hanging wall (right side) between 8 km and 12 km. In the footwall (left side), the taper initially spans 12 km to 16 km and shifts leftward at the half-spreading rate of $12\,\mathrm{km\,Myr^{-1}}$. All other model parameters remain unchanged.

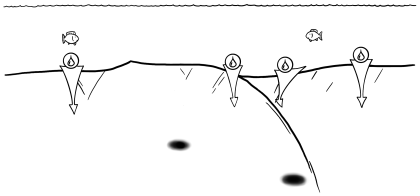

To initialize the simulation, a 100 kyr conductive spin-up phase without hydrothermal computations is used. This approach ensures the formation of a single, well-defined fault at the ridge axis and provides a basis for comparing subsequent fault evolution. Since the initial, undisturbed model state is somewhat artificial anyway, this does not compromise the model's validity.

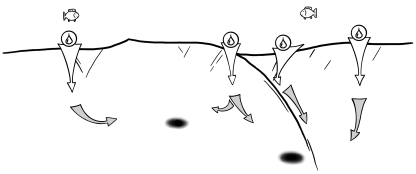

References

Andersen, C., Rüpke, L., Hasenclever, J., Grevemeyer, I., & Petersen, S. (2015). Fault geometry and permeability contrast control vent temperatures at the Logatchev 1 hydrothermal field, Mid-Atlantic Ridge. *Geology*, *43*(1), 51–54. doi: 10.1130/g36113.1

Andersen, C., Theissen-Krah, S., Hannington, M., Rüpke, L., & Petersen, S. (2017). Faulting and off-axis submarine massive sulfide accumulation at slow spreading mid-ocean ridges: A numerical modeling perspective. *Geochemistry, Geophysics, Geosystems*, *18*(6), 2305–2320. doi: 10.1002/2017gc006880

Andreani, M., Escartin, J., Delacour, A., Ildefonse, B., Godard, M., Dyment, J., ... Fouquet, Y. (2014). Tectonic structure, lithology, and hydrothermal signature of the Rainbow massif (Mid-Atlantic Ridge 36°14'N). *Geochemistry, Geophysics, Geosystems*, *15*(9), 3543–3571. doi: 10.1002/2014gc005269

Andreani, M., Mével, C., Boullier, A., & Escartín, J. (2007). Dynamic control on serpentine crystallization in veins: Constraints on hydration processes in oceanic peridotites. *Geochemistry, Geophysics, Geosystems*, *8*(2). doi: 10.1029/2006gc001373

Andrés-Martínez, M. (2016). *Rifted margin architecture and the interplay between mantle, crustal and surface processes from geodynamic numerical experiments.* (Doctoral Thesis, Royal Holloway, University of London).

Andrés-Martínez, M., Phipps Morgan, J., Pérez-Gussinyé, M., & Rüpke, L. (2015). A new free-surface stabilization algorithm for geodynamical modelling: Theory and numerical tests. *Physics of the Earth and Planetary Interiors*, *246*, 41–51. doi: 10.1016/j.pepi.2015.07.003

Andrés-Martínez, M., Pérez-Gussinyé, M., Armitage, J., & Phipps Morgan, J. (2019). Thermomechanical Implications of Sediment Transport for the Architecture and Evolution of Continental Rifts and Margins. *Tectonics*, *38*(2), 641–665. doi: 10.1029/2018tc005346

Austin, N. J., & Evans, B. (2007). Paleowattmeters: A scaling relation for dynamically recrystallized grain size. *Geology*, *35*(4), 343–346. doi: 10.1130/g23244a.1

Baines, A. G., Cheadle, M. J., John, B. E., & Schwartz, J. J. (2008). The rate of oceanic detachment faulting at Atlantis Bank, SW Indian Ridge. *Earth and Planetary Science Letters*, *273*(1-2), 105–114. doi: 10.1016/j.epsl.2008.06.013

Baker, E. T., Edmonds, H. N., Michael, P. J., Bach, W., Dick, H. J. B., Snow, J. E., ... Langmuir, C. H. (2004). Hydrothermal venting in magma deserts: The ultraslow-spreading Gakkel and Southwest Indian Ridges. *Geochemistry, Geophysics, Geosystems*, *5*(8). doi: 10.1029/2004gc000712

Baker, E. T., Resing, J. A., Haymon, R. M., Tunnicliffe, V., Lavelle, J. W., Martinez, F., ... Nakamura, K. (2016). How many vent fields? New estimates of vent field populations on ocean ridges from precise mapping of hydrothermal discharge locations. *Earth and Planetary Science Letters*, *449*, 186–196.

Bang, R. N., & Trellevik, L.-K. L. (2022). Perspectives on exploration and extraction of seafloor massive sulfide deposits in Norwegian waters. *Mineral Economics*, 1–49. doi: 10.1007/s13563-022-00346-y

Bangerth, W., Dannberg, J., Fraters, M., Gassmoeller, R., Glerum, A., Heister, T., ... Naliboff, J. (2024). *ASPECT: Advanced Solver for Planetary Evolution, Convection, and Tectonics, User Manual.* (Software) doi: 10.6084/m9.figshare.4865333

Bani-Hassan, N., Iyer, K., Rüpke, L. H., & Borgia, A. (2012). Controls of bathymetric relief on hydrothermal fluid flow at mid-ocean ridges. *Geochemistry, Geophysics, Geosystems*, *13*(5). doi: 10.1029/2012GC004041

Barreyre, T., Olive, J.-A., Crone, T. J., & Sohn, R. A. (2018). Depth-Dependent Permeability and Heat Output at Basalt-Hosted Hydrothermal Systems Across Mid-Ocean Ridge Spreading Rates. *Geochemistry, Geophysics, Geosystems*, *19*(4), 1259–1281. doi: 10.1002/2017gc007152

Beaulieu, S., & Szafranski, K. (2020). InterRidge Global Database of Active Submarine Hydrothermal Vent Fields, Version 3.4. Retrieved 2024-09-18, from `http://vents-data.interridge.org` (Database)

Behn, M. D., & Ito, G. (2008). Magmatic and tectonic extension at mid-ocean ridges: 1. Controls on fault characteristics. *Geochemistry, Geophysics, Geosystems*, *9*(8). doi: 10.1029/2008gc001965

Bickert, M., Cannat, M., & Brunelli, D. (2023). Hydrous fluids down to the semi-brittle root zone of detachment faults in nearly amagmatic ultra-slow spreading ridges. *Lithos*, *442-443*, 107084. doi: 10.1016/j.lithos.2023.107084

Bickert, M., Cannat, M., Tommasi, A., Jammes, S., & Lavier, L. (2021). Strain localization in the root of detachment faults at a melt-starved mid-ocean ridge: a microstructural study of abyssal peridotites from the Southwest Indian Ridge. *Geochemistry, Geophysics, Geosystems*, *22*(5), e2020GC009434. doi: 10.1029/2020GC009434

Bickert, M., Lavier, L., & Cannat, M. (2020). How do detachment faults form at ultraslow mid-ocean ridges in a thick axial lithosphere? *Earth and Planetary Science Letters*, *533*, 116048. doi: 10.1016/j.epsl.2019.116048

Bird, P. (2003). An updated digital model of plate boundaries. *Geochemistry, Geophysics, Geosystems*, *4*(3). doi: 10.1029/2001gc000252

Blackman, D. K., Abe, N., Carlson, R. L., Guerin, G., Ildefonse, B., & Kumpf, A. (2019). Seismic properties of gabbroic sections in oceanic core complexes: constraints from seafloor drilling. *Marine Geophysical Research*, *40*(4), 557–569. doi: 10.1007/s11001-019-09385-7

Boschi, C., Früh-Green, G. L., Delacour, A., Karson, J. A., & Kelley, D. S. (2006). Mass transfer and fluid flow during detachment faulting and development of an oceanic core complex, Atlantis Massif (MAR 30°N). *Geochemistry, Geophysics, Geosystems*, *7*(1). doi: 10.1029/2005GC001074

Bronner, A., Sauter, D., Munschy, M., Carlut, J., Searle, R. C., Cannat, M., & Manatschal, G. (2014). Magnetic signature of large exhumed mantle domains of the Southwest Indian Ridge – results from a deep-tow geophysical survey over 0 to 11 Ma old seafloor. *Solid Earth*, *5*(1), 339–354. doi: 10.5194/se-5-339-2014

Buck, W. R. (1988). Flexural rotation of normal faults. *Tectonics*, *7*(5), 959–973. doi: 10.1029/tc007i005p00959

Buck, W. R., Lavier, L., & Poliakov, A. (2005). Modes of faulting at mid-ocean ridges. *Nature*, *434*, 719–723. doi: 10.1038/nature03358

Caine, J. S., Evans, J. P., & Forster, C. B. (1996). Fault zone architecture and permeability structure. *Geology*, *24*(11), 1025–1028. doi: 10.1130/0091-7613(1996)024<1025:fzaaps>2.3.co;2

Canales, J. P., Singh, S. C., Detrick, R. S., Carbotte, S. M., Harding, A., Kent, G. M., ... Nedimović, M. R. (2006). Seismic evidence for variations in axial magma chamber properties along the southern Juan de Fuca Ridge. *Earth and Planetary Science Letters*, *246*(3), 353–366. doi: 10.1016/j.epsl.2006.04.032

Cannat, M., Agrinier, P., Martinez, I., Brovarone, A. V., Lecoeuvre, A., Corre, M., ... Roumejon, S. (2019). A forest of carbonate-brucite chimneys at the Southwest Indian ridge: the ultramafic-hosted Old City hydrothermal field. *Goldschmidt Abstracts*, *2019*, 463.

Cannat, M., Mevel, C., Maia, M., Deplus, C., Durand, C., Gente, P., ... Reynolds, J. (1995). Thin crust, ultramafic exposures, and rugged faulting patterns at the Mid-Atlantic

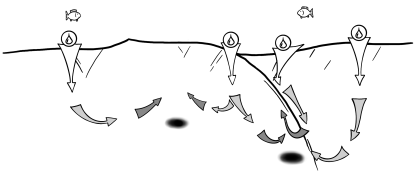

Ridge (22°–24°N). *Geology*, *23*(1), 49–52. doi: 10.1130/0091-7613(1995)023<0049:tcuear>2.3.co;2

Cannat, M., Rommevaux-Jestin, C., & Fujimoto, H. (2003). Melt supply variations to a magma-poor ultra-slow spreading ridge (Southwest Indian Ridge 61° to 69°E). *Geochemistry, Geophysics, Geosystems*, *4*(8). doi: 10.1029/2002gc000480

Cannat, M., Sauter, D., Bezos, A., Meyzen, C., Humler, E., & Rigoleur, M. L. (2008). Spreading rate, spreading obliquity, and melt supply at the ultraslow spreading Southwest Indian Ridge. *Geochemistry, Geophysics, Geosystems*, *9*(4). doi: 10.1029/2007gc001676

Cannat, M., Sauter, D., Lavier, L., Bickert, M., Momoh, E., & Leroy, S. (2019). On spreading modes and magma supply at slow and ultraslow mid-ocean ridges. *Earth and Planetary Science Letters*, *519*, 223–233. doi: 10.1016/j.epsl.2019.05.012

Cannat, M., Sauter, D., Mendel, V., Ruellan, E., Okino, K., Escartín, J., ... Baala, M. (2006). Modes of seafloor generation at a melt-poor ultraslow-spreading ridge. *Geology*, *34*(7), 605–608. doi: 10.1130/g22486.1

Carbotte, S. M., Marjanović, M., Arnulf, A. F., Nedimović, M. R., Canales, J. P., & Arnoux, G. M. (2021). Stacked Magma Lenses Beneath Mid-Ocean Ridges: Insights From New Seismic Observations and Synthesis With Prior Geophysical and Geologic Findings. *Journal of Geophysical Research: Solid Earth*, *126*(4). doi: 10.1029/2020jb021434

Charlou, J., Donval, J., Fouquet, Y., Jean-Baptiste, P., & Holm, N. (2002). Geochemistry of high H2 and CH4 vent fluids issuing from ultramafic rocks at the Rainbow hydrothermal field (36°14'N, MAR). *Chemical Geology*, *191*(4), 345–359. doi: 10.1016/s0009-2541(02)00134-1

Chen, J., Cannat, M., Tao, C., Sauter, D., & Munschy, M. (2021). 780 Thousand Years of Upper-Crustal Construction at a Melt-Rich Segment of the Ultraslow Spreading Southwest Indian Ridge 50°28'E. *Journal of Geophysical Research: Solid Earth*, *126*(10), e2021JB022152. doi: 10.1029/2021jb022152

Chen, J., Crawford, W. C., & Cannat, M. (2023). Microseismicity and lithosphere thickness at a nearly-amagmatic oceanic detachment fault system. *Nature Communications*, *14*(1), 430. doi: 10.1038/s41467-023-36169-w

Chen, J., Olive, J.-A., & Cannat, M. (2022). Thermal Regime of Slow and Ultraslow Spreading Ridges Controlled by Melt Supply and Modes of Emplacement. *Journal of Geophysical Research: Solid Earth*, *127*(4), e2021JB023715. doi: 10.1029/2021JB023715

Cherkashev, G. A., Ivanov, V. N., Bel'tenev, V. I., Lazareva, L. I., Rozhdestvenskaya, I. I., Samovarov, M. L., ... Kuznetsov, V. Y. (2013). Massive sulfide ores of the northern equatorial Mid-Atlantic Ridge. *Oceanology*, *53*(5), 607–619. doi: 10.1134/s0001437013050032

Chiba, H., Masuda, H., Lee, S., & Fujioka, K. (2001). Chemistry of hydrothermal fluids at the TAG Active Mound, MAR 26°N, in 1998. *Geophysical Research Letters*, *28*(15), 2919–2922. doi: 10.1029/2000gl012645

Choi, J.-H., Edwards, P., Ko, K., & Kim, Y.-S. (2016). Definition and classification of fault damage zones: A review and a new methodological approach. *Earth-Science Reviews*, *152*, 70–87. doi: 10.1016/j.earscirev.2015.11.006

Connelly, D. P., Copley, J. T., Murton, B. J., Stansfield, K., Tyler, P. A., German, C. R., ... Wilcox, S. (2012). Hydrothermal vent fields and chemosynthetic biota on the world's deepest seafloor spreading centre. *Nature Communications*, *3*(1), 620. doi: 10.1038/ncomms1636

Corbalán, A., Nedimović, M. R., Louden, K. E., Cannat, M., Grevemeyer, I., Watremez, L., & Leroy, S. (2021). Seismic Velocity Structure Along and Across the Ultraslow-Spreading Southwest Indian Ridge at 64°30'E Showcases Flipping Detachment Faults. *Journal of Geophysical Research: Solid Earth*, *126*(10), e2021JB022177. doi: 10.1029/

2021jb022177

Corliss, J. B., Dymond, J., Gordon, L. I., Edmond, J. M., Herzen, R. P. v., Ballard, R. D., ... Andel, T. H. v. (1979). Submarine Thermal Springs on the Galapagos Rift. *Science*, *203*(4385), 1073–1083. doi: 10.1126/science.203.4385.1073

Coumou, D., Driesner, T., Geiger, S., Paluszny, A., & Heinrich, C. A. (2009). High-resolution three-dimensional simulations of mid-ocean ridge hydrothermal systems. *Journal of Geophysical Research: Solid Earth*, *114*(B7). doi: 10.1029/2008JB006121

Cowie, P. A., Scholz, C. H., Edwards, M., & Malinverno, A. (1993). Fault strain and seismic coupling on mid-ocean ridges. *Journal of Geophysical Research: Solid Earth*, *98*(B10), 17911–17920. doi: 10.1029/93JB01567

Crameri, F. (2021). *Scientific colour maps (7.0.1).* Zenodo. (Software) doi: 10.5281/zenodo.5501399

Dabrowski, M., Krotkiewski, M., & Schmid, D. W. (2008). MILAMIN: MATLAB-based finite element method solver for large problems. *Geochemistry, Geophysics, Geosystems*, *9*(4). doi: 10.1029/2007gc001719

Davis, T. A., & Hager, W. W. (2009). Dynamic Supernodes in Sparse Cholesky Update/Downdate and Triangular Solves. *ACM Transactions on Mathematical Software*, *35*(4). doi: 10.1145/1462173.1462176

deMartin, B. J., Sohn, R. A., Canales, J. P., & Humphris, S. E. (2007). Kinematics and geometry of active detachment faulting beneath the Trans-Atlantic Geotraverse (TAG) hydrothermal field on the Mid-Atlantic Ridge. *Geology*, *35*(8), 711–714. doi: 10.1130/g23718a.1

Demont, A., Cannat, M., & Olive, J.-A. (2024). *Modes of detachment faulting at slow and ultraslow mid-oceanic ridges.* EGU General Assembly 2024, Vienna, Austria, 14–19 Apr 2024. EGU24-15593. doi: 10.5194/egusphere-egu24-15593

de Montserrat, A., Phipps Morgan, J., & Hasenclever, J. (2019). LaCoDe: A Lagrangian two-dimensional thermo-mechanical code for large-strain compressible visco-elastic geodynamical modeling. *Tectonophysics*, *767*, 228173. doi: 10.1016/j.tecto.2019.228173

Detrick, R. S., Buhl, P., Vera, E., Mutter, J., Orcutt, J., Madsen, J., & Brocher, T. (1987). Multi-channel seismic imaging of a crustal magma chamber along the East Pacific Rise. *Nature*, *326*(6108), 35–41. doi: 10.1038/326035a0

Ding, T., Tao, C., Dias, A. A., Liang, J., Chen, J., Wu, B., ... Huang, H. (2021). Sulfur isotopic compositions of sulfides along the Southwest Indian Ridge: implications for mineralization in ultramafic rocks. *Mineralium Deposita*, *56*(5), 991–1006. doi: 10.1007/s00126-020-01025-0

Donea, J., & Huerta, A. (2003). *Finite Element Methods for Flow Problems.* John Wiley & Sons. doi: 10.1002/0470013826

Drazen, J. C., Smith, C. R., Gjerde, K. M., Haddock, S. H. D., Carter, G. S., Choy, C. A., ... Yamamoto, H. (2020). Midwater ecosystems must be considered when evaluating environmental risks of deep-sea mining. *Proceedings of the National Academy of Sciences*, *117*(30), 17455–17460. doi: 10.1073/pnas.2011914117

Driesner, T. (2010). The interplay of permeability and fluid properties as a first order control of heat transport, venting temperatures and venting salinities at mid-ocean ridge hydrothermal systems. *Geofluids*, *10*(1-2), 132–141. doi: 10.1111/j.1468-8123.2009.00273.x

Dunn, R. A. (2015). 1.13 - Crust and Lithospheric Structure - Seismic Structure of Mid-Ocean Ridges. In G. Schubert (Ed.), *Treatise on Geophysics* (2nd ed., p. 419-451). Oxford: Elsevier. doi: 10.1016/B978-0-444-53802-4.00011-7

Dunn, R. A., Arai, R., Eason, D. E., Canales, J. P., & Sohn, R. A. (2017). Three-Dimensional Seismic Structure of the Mid-Atlantic Ridge: An Investigation of Tectonic, Magmatic,

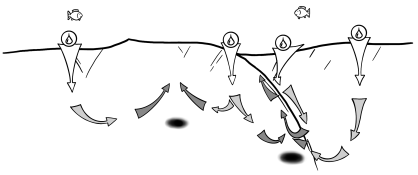

and Hydrothermal Processes in the Rainbow Area. *Journal of Geophysical Research: Solid Earth*, *122*(12), 9580 – 9602. doi: 10.1002/2017jb015051

Duretz, T., Borst, R. d., & Yamato, P. (2021). Modeling Lithospheric Deformation Using a Compressible Visco-Elasto-Viscoplastic Rheology and the Effective Viscosity Approach. *Geochemistry, Geophysics, Geosystems*, *22*(8), e2021GC009675. doi: 10.1029/2021gc009675

Elderfield, H., & Schultz, A. (1996). Mid-Ocean Ridge Hydrothermal Fluxes and the Chemical Composition of the Ocean. *Annual Review of Earth and Planetary Sciences*, *24*(1), 191–224. doi: 10.1146/annurev.earth.24.1.191

EMSO-Azores. (n.d.). Ifremer & CNRS. Retrieved 2025-01-22, from `https://www.emso-fr.org/Azores`

EMSO-Mohn. (n.d.). University of Bergen. Retrieved 2025-01-22, from `https://emso.eu/observatories-node/nordic-seas/`

Escartín, J., Andreani, M., Hirth, G., & Evans, B. (2008). Relationships between the microstructural evolution and the rheology of talc at elevated pressures and temperatures. *Earth and Planetary Science Letters*, *268*(3-4), 463–475. doi: 10.1016/j.epsl.2008.02.004

Escartín, J., & Canales, J. P. (2011). Detachments in Oceanic Lithosphere: Deformation, Magmatism, Fluid Flow, and Ecosystems. *Eos, Transactions American Geophysical Union*, *92*(4), 31–31. doi: 10.1029/2011EO040003

Escartín, J., Cowie, P. A., Searle, R. C., Allerton, S., Mitchell, N. C., MacLeod, C. J., & Slootweg, A. P. (1999). Quantifying tectonic strain and magmatic accretion at a slow spreading ridge segment, Mid-Atlantic Ridge, 29°N. *Journal of Geophysical Research: Solid Earth*, *104*(B5), 10421–10437. doi: 10.1029/1998JB900097

Escartín, J., Hirth, G., & Evans, B. (1997a). Effects of serpentinization on the lithospheric strength and the style of normal faulting at slow-spreading ridges. *Earth and Planetary Science Letters*, *151*(3), 181–189. doi: 10.1016/S0012-821X(97)81847-X

Escartín, J., Hirth, G., & Evans, B. (1997b). Nondilatant brittle deformation of serpentinites: Implications for Mohr-Coulomb theory and the strength of faults. *Journal of Geophysical Research: Solid Earth*, *102*(B2), 2897–2913. doi: 10.1029/96JB02792

Escartín, J., Mével, C., MacLeod, C. J., & McCaig, A. M. (2003). Constraints on deformation conditions and the origin of oceanic detachments: The Mid-Atlantic Ridge core complex at 15°45'N. *Geochemistry, Geophysics, Geosystems*, *4*(8). doi: 10.1029/2002GC000472

Escartín, J., Mével, C., Petersen, S., Bonnemains, D., Cannat, M., Andreani, M., ... Garcia, R. (2017). Tectonic structure, evolution, and the nature of oceanic core complexes and their detachment fault zones (13°20'N and 13°30'N, Mid Atlantic Ridge). *Geochemistry, Geophysics, Geosystems*, *18*(4), 1451–1482. doi: 10.1002/2016gc006775

Escartín, J., & Olive, J.-A. (2022). 8.31 - Mid-Ocean Ridges and Their Geomorphological Features. In J. J. F. Shroder (Ed.), *Treatise on Geomorphology* (2nd ed., p. 847-881). Oxford: Academic Press. doi: 10.1016/B978-0-12-818234-5.00193-0

Escartín, J., Smith, D. K., Cann, J., Schouten, H., Langmuir, C. H., & Escrig, S. (2008). Central role of detachment faults in accretion of slow-spreading oceanic lithosphere. *Nature*, *455*(7214), 790–794. doi: 10.1038/nature07333

Escartín, J., Soule, S. A., Fornari, D. J., Tivey, M. A., Schouten, H., & Perfit, M. R. (2007). Interplay between faults and lava flows in construction of the upper oceanic crust: The East Pacific Rise crest 9°25'–9°58'N. *Geochemistry, Geophysics, Geosystems*, *8*(6). doi: 10.1029/2006GC001399

Evans, G. N., Charin, S., Seyfried, W. E., & Zheng, X.-Y. (2024). The Role of Mafic Intrusions in Producing Alkaline Vent Fluids at the Lost City Hydrothermal Field: Evidence from Stable Potassium Isotopes. *Geochimica et Cosmochimica Acta*, *386*,

84–95. doi: 10.1016/j.gca.2024.08.030

Fan, Q., Olive, J.-A., & Cannat, M. (2021). Thermo-Mechanical State of Ultraslow-Spreading Ridges With a Transient Magma Supply. *Journal of Geophysical Research: Solid Earth*, *126*(4), e2020JB020557. doi: 10.1029/2020JB020557

Fontaine, F. J., Olive, J.-A., Cannat, M., Escartín, J., & Perol, T. (2011). Hydrothermally-induced melt lens cooling and segmentation along the axis of fast- and intermediate-spreading centers. *Geophysical Research Letters*, *38*(14). doi: 10.1029/2011gl047798

Fornari, D., Damm, K. V., Bryce, J., Cowen, J., Ferrini, V., Fundis, A., ... White, S. (2012). The East Pacific Rise Between 9°N and 10°N: Twenty-Five Years of Integrated, Multidisciplinary Oceanic Spreading Center Studies. *Oceanography*, *25*(1), 18–43. doi: 10.5670/oceanog.2012.02

Früh-Green, G. L., Connolly, J. A., Plas, A., Kelley, D. S., & Grobéty, B. (2004). Serpentinization of Oceanic Peridotites: Implications for Geochemical Cycles and Biological Activity. In W. Wilcock, E. Delong, D. Kelley, J. Baross, & S. C. Cary (Eds.), *The Subseafloor Biosphere at Mid-Ocean Ridges* (pp. 119–136). American Geophysical Union (AGU). doi: 10.1029/144GM08

Früh-Green, G. L., Kelley, D. S., Bernasconi, S. M., Karson, J. A., Ludwig, K. A., Butterfield, D. A., ... Proskurowski, G. (2003). 30,000 Years of Hydrothermal Activity at the Lost City Vent Field. *Science*, *301*(5632), 495–498. doi: 10.1126/science.1085582

Früh-Green, G. L., Kelley, D. S., Lilley, M. D., Cannat, M., Chavagnac, V., & Baross, J. A. (2022). Diversity of magmatism, hydrothermal processes and microbial interactions at mid-ocean ridges. *Nature Reviews Earth & Environment*, *3*(12), 852–871. doi: 10.1038/s43017-022-00364-y

Galerne, C. Y., & Hasenclever, J. (2019). Distinct Degassing Pulses During Magma Invasion in the Stratified Karoo Basin—New Insights From Hydrothermal Fluid Flow Modeling. *Geochemistry, Geophysics, Geosystems*, *20*(6), 2955–2984. doi: 10.1029/2018GC008120

Gass, I. G. (1968). Is the Troodos Massif of Cyprus a Fragment of Mesozoic Ocean Floor? *Nature*, *220*(5162), 39–42. doi: 10.1038/220039a0

German, C. R., & Lin, J. (2004). The Thermal Structure of the Oceanic Crust, Ridge-Spreading and Hydrothermal Circulation: How Well do we Understand their Inter-Connections? In C. R. German, J. Lin, & L. Parson (Eds.), *Mid-ocean ridges* (pp. 1–18). American Geophysical Union (AGU). doi: 10.1029/148GM01

German, C. R., Petersen, S., & Hannington, M. D. (2016). Hydrothermal exploration of mid-ocean ridges: Where might the largest sulfide deposits be forming? *Chemical Geology*, *420*, 114–126. doi: 10.1016/j.chemgeo.2015.11.006

Gerya, T. (2019). *Introduction to Numerical Geodynamic Modelling* (2nd ed.). Cambridge University Press. doi: 10.1017/9781316534243

Glink, A. (2020). *The thermal influence of hydrothermal fluid flow on tectonic faulting at ultraslow-spreading mid-ocean ridges.* (Master Thesis, University of Hamburg).

Glink, A., & Hasenclever, J. (2024). How Hydrothermal Cooling and Magmatic Sill Intrusions Control Flip-Flop Faulting at Ultraslow-Spreading Mid-Ocean Ridges. *Geochemistry, Geophysics, Geosystems*, *25*(2), e2023GC011331. doi: 10.1029/2023gc011331

Glink, A., Hasenclever, J., Rüpke, L., Hort, M., & Petersen, S. (2025). Massive Sulfide Deposition at the 13°30'N Oceanic Core Complex: Lessons Learned from Coupled Hydro-Thermo-Mechanical Modeling. *Geochemistry, Geophysics, Geosystems*. (under review)

Goldberg, V., Dashti, A., Egert, R., Benny, B., Kohl, T., & Nitschke, F. (2023). Challenges and Opportunities for Lithium Extraction from Geothermal Systems in Germany—Part 3: The Return of the Extraction Brine. *Energies*, *16*(16), 5899. doi: 10.3390/en16165899

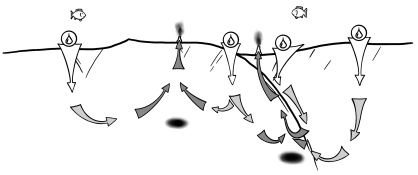

Graber, S., Petersen, S., Yeo, I., Szitkar, F., Klischies, M., Jamieson, J., ... Stobbs, I. (2020). Structural Control, Evolution, and Accumulation Rates of Massive Sulfides in the TAG Hydrothermal Field. *Geochemistry, Geophysics, Geosystems*, *21*(9). doi: 10.1029/2020gc009185

Gregg, P. M., Behn, M. D., Lin, J., & Grove, T. L. (2009). Melt generation, crystallization, and extraction beneath segmented oceanic transform faults. *Journal of Geophysical Research: Solid Earth*, *114*(B11). doi: 10.1029/2008jb006100

Grevemeyer, I., Hayman, N. W., Lange, D., Peirce, C., Papenberg, C., Avendonk, H. J. V., ... Dannowski, A. (2019). Constraining the maximum depth of brittle deformation at slow- and ultraslow-spreading ridges using microseismicity. *Geology*, *47*(11), 1069–1073. doi: 10.1130/g46577.1

Guo, Z., Rüpke, L., Petersen, S., German, C. R., Ildefonse, B., Hasenclever, J., ... Tao, C. (2023). Detachment-parallel recharge can explain high discharge fluxes at the TAG hydrothermal field. *Earth and Planetary Science Letters*, *617*, 118245. doi: 10.1016/j.epsl.2023.118245

Handin, J. (1966). Section 11: Strength and Ductility. In S. P. J. Clark (Ed.), *Handbook of Physical Constants* (pp. 223–290). Geological Society of America. doi: 10.1130/MEM97-p223

Hannington, M. D., Jamieson, J., Monecke, T., & Petersen, S. (2010). Modern sea-floor massive sulfides and base metal resources: Toward an estimate of global sea-floor massive sulfide potential. In R. J. Goldfarb, E. E. Marsh, & T. Monecke (Eds.), *The challenge of finding new mineral resources: Global metallogeny, innovative exploration, and new discoveries.* (Vol. 2, pp. 317–338). Littleton, Colorado: Society of Economic Geologists. doi: 10.5382/SP.15.2.001

Hannington, M. D., Jamieson, J., Monecke, T., Petersen, S., & Beaulieu, S. (2011). The abundance of seafloor massive sulfide deposits. *Geology*, *39*(12), 1155–1158. doi: 10.1130/g32468.1

Harding, J. L., Avendonk, H. J. V., Hayman, N. W., Grevemeyer, I., Peirce, C., & Dannowski, A. (2017). Magmatic-tectonic conditions for hydrothermal venting on an ultraslow-spread oceanic core complex. *Geology*, *45*(9), 839–842. doi: 10.1130/g39045.1

Haroon, A., Paasche, H., Graber, S., Petersen, S., Attias, E., Jegen, M., ... Klischies, M. (2023). Automated Seafloor Massive Sulfide Detection Through Integrated Image Segmentation and Geophysical Data Analysis: Revisiting the TAG Hydrothermal Field. *Geochemistry, Geophysics, Geosystems*, *24*(12). doi: 10.1029/2023gc011250

Hasenclever, J. (2010). *Modeling Mantle Flow and Melting Processes at Mid-Ocean Ridges and Subduction Zones — Development and Application of Numerical Models.* (Doctoral Thesis, University of Hamburg).

Hasenclever, J., & Glink, A. (2024). *M2TRI_vep 1.1.* (Software) doi: 10.25592/uhhfdm.14130

Hasenclever, J., & Glink, A. (2025). *M2TRI_vep 2.0.* (Software) doi: 10.25592/uhhfdm.16176

Hasenclever, J., Knorr, G., Rüpke, L. H., Kohler, P., Phipps Morgan, J., Garofalo, K., ... Hall, I. R. (2017). Sea level fall during glaciation stabilized atmospheric CO2 by enhanced volcanic degassing. *Nature Communications*, *8*(1), 15867. doi: 10.1038/ncomms15867

Hasenclever, J., Theissen-Krah, S., Rüpke, L., Phipps Morgan, J., Iyer, K., Petersen, S., & Devey, C. (2014). Hybrid shallow on-axis and deep off-axis hydrothermal circulation at fast-spreading ridges. *Nature*, *508*, 508–12. doi: 10.1038/nature13174

Haughton, G. A., Hayman, N. W., Searle, R. C., Bas, T. L., & Murton, B. J. (2019). Volcanic-Tectonic Structure of the Mount Dent Oceanic Core Complex in the Ultraslow Mid-Cayman Spreading Center Determined From Detailed Seafloor Investigation. *Geochemistry, Geophysics, Geosystems*, *20*(3), 1298–1318. doi: 10.1029/2018gc008032

Hayman, N. W., Grindlay, N. R., Perfit, M. R., Mann, P., Leroy, S., & de Lépinay, B. M.

(2011). Oceanic core complex development at the ultraslow spreading Mid-Cayman Spreading Center. *Geochemistry, Geophysics, Geosystems*, *12*(3). doi: 10.1029/2010gc003240

Hirth, G., Escartín, J., & Lin, J. (1998). The Rheology of the Lower Oceanic Crust: Implications for Lithospheric Deformation at Mid-Ocean Ridges. In W. R. Buck, P. T. Delaney, J. A. Karson, & Y. Lagabrielle (Eds.), *Faulting and Magmatism at Mid-Ocean Ridges* (p. 291-303). American Geophysical Union (AGU). doi: 10.1029/GM106p0291

Hirth, G., & Kohlstedt, D. (2003). Rheology of the Upper Mantle and the Mantle Wedge: A View from the Experimentalists. In J. Eiler (Ed.), *Inside the Subduction Factory* (pp. 83–105). American Geophysical Union (AGU). doi: 10.1029/138GM06

Howell, S. M., Olive, J.-A., Ito, G., Behn, M. D., Escartín, J., & Kaus, B. (2019). Seafloor expression of oceanic detachment faulting reflects gradients in mid-ocean ridge magma supply. *Earth and Planetary Science Letters*, *516*, 176–189.

Huang, P. Y., & Solomon, S. C. (1988). Centroid Depths of Mid-Ocean Ridge Earthquakes: Dependence on Spreading Rate. *Journal of Geophysical Research: Solid Earth*, *93*(B11), 13445–13477. doi: 10.1029/jb093ib11p13445

Humphris, S. E., & Cann, J. R. (2000). Constraints on the energy and chemical balances of the modern TAG and ancient Cyprus seafloor sulfide deposits. *Journal of Geophysical Research: Solid Earth*, *105*(B12), 28477-28488. doi: 10.1029/2000JB900289

Humphris, S. E., Herzig, P. M., Miller, D. J., Alt, J. C., Becker, K., Brown, D., ... Zhao, X. (1995). The internal structure of an active sea-floor massive sulphide deposit. *Nature*, *377*(6551), 713–716. doi: 10.1038/377713a0

Ito, G., & Behn, M. D. (2008). Magmatic and tectonic extension at mid-ocean ridges: 2. Origin of axial morphology. *Geochemistry, Geophysics, Geosystems*, *9*(9). doi: 10.1029/2008gc001970

Iyer, K., Rüpke, L. H., & Phipps Morgan, J. (2010). Feedbacks between mantle hydration and hydrothermal convection at ocean spreading centers. *Earth and Planetary Science Letters*, *296*(1), 34–44. doi: 10.1016/j.epsl.2010.04.037

Jamieson, J. W., Galley, C., McNeil, N., & Mora, D. S. (2023). Evaluating episodicity of high-temperature venting within seafloor hydrothermal vent fields. *Earth and Planetary Science Letters*, *606*, 118051. doi: 10.1016/j.epsl.2023.118051

Jian, H., Canales, J. P., Dunn, R., & Nedimović, M. R. (2024). Hydrothermal flow and serpentinization in oceanic core complexes controlled by mafic intrusions. *Nature Geoscience*, *17*(6), 566–571. doi: 10.1038/s41561-024-01444-y

Jian, H., Chen, Y. J., Singh, S. C., Li, J., Zhao, M., Ruan, A., & Qiu, X. (2017). Seismic structure and magmatic construction of crust at the ultraslow-spreading Southwest Indian Ridge at 50°28'E. *Journal of Geophysical Research: Solid Earth*, *122*(1), 18–42. doi: 10.1002/2016jb013377

Karakul, H., & Ulusay, R. (2024). An alternative method for predicting internal friction angle of rock materials. *Environmental Earth Sciences*, *83*(10), 306. doi: 10.1007/s12665-024-11606-1

Kaufman, P., Grotzinger, J. P., & McCormick, D. S. (1991). Depth-dependent diffusion algorithm for simulation of sedimentation in shallow marine depositional systems. *Bulletin - Kansas Geological Survey*, *233*, 489–508.

Kaus, B. J. (2010). Factors that control the angle of shear bands in geodynamic numerical models of brittle deformation. *Tectonophysics*, *484*(1), 36–47. doi: 10.1016/j.tecto.2009.08.042

Kelemen, P., Benson, S. M., Pilorgé, H., Psarras, P., & Wilcox, J. (2019). An Overview of the Status and Challenges of CO2 Storage in Minerals and Geological Formations. *Frontiers in Climate*, *1*, 9. doi: 10.3389/fclim.2019.00009

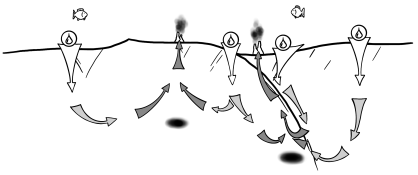

Keller, T., May, D. A., & Kaus, B. J. P. (2013). Numerical modelling of magma dynamics coupled to tectonic deformation of lithosphere and crust. *Geophysical Journal International*, *195*(3), 1406–1442. doi: 10.1093/gji/ggt306

Kelley, D. S., & Shank, T. M. (2010). Hydrothermal Systems: a Decade of Discovery in Slow Spreading Environments. In *Diversity Of Hydrothermal Systems On Slow Spreading Ocean Ridges* (p. 369-407). American Geophysical Union (AGU). doi: https://doi.org/10.1029/2010GM000945

Kinsey, J. C., & German, C. R. (2013). Sustained volcanically-hosted venting at ultraslow ridges: Piccard Hydrothermal Field, Mid-Cayman Rise. *Earth and Planetary Science Letters*, *380*, 162–168. doi: 10.1016/j.epsl.2013.08.001

Klein, F., & Le Roux, V. (2020). Quantifying the volume increase and chemical exchange during serpentinization. *Geology*, *48*(6), 552–556. doi: 10.1130/g47289.1

Krotkiewski, M., & Dabrowski, M. (2010). Parallel Symmetric Sparse Matrix-Vector Product on Scalar Multi-Core CPUs. *Parallel Computing*, *36*(4), 181–198. doi: 10.1016/j.parco.2010.02.003

Kuang, X., & Jiao, J. J. (2014). An integrated permeability-depth model for Earth's crust. *Geophysical Research Letters*, *41*(21), 7539–7545. doi: 10.1002/2014gl061999

Kuo, B.-Y., & Forsyth, D. W. (1988). Gravity anomalies of the ridge-transform system in the South Atlantic between 31 and 34.5° S: Upwelling centers and variations in crustal thickness. *Marine Geophysical Researches*, *10*(3-4), 205–232. doi: 10.1007/bf00310065

Kuznetsov, V., Maksimov, F., Zheleznov, A., Cherkashov, G., Bel'Tenev, V., & Lazareva, L. (2011). 230Th/U chronology of ore formation within the Semyenov hydrothermal district (13°31'N) at the Mid-Atlantic Ridge. *Geochronometria*, *38*(1), 72–76. doi: 10.2478/s13386-011-0001-1

Lavier, L. L., & Buck, W. R. (2002). Half graben versus large-offset low-angle normal fault: Importance of keeping cool during normal faulting. *Journal of Geophysical Research: Solid Earth*, *107*(B6), ETG 8–1-ETG 8-13. doi: 10.1029/2001jb000513

Lavier, L. L., Buck, W. R., & Poliakov, A. N. B. (1999). Self-consistent rolling-hinge model for the evolution of large-offset low-angle normal faults. *Geology*, *27*(12), 1127–1130. doi: 10.1130/0091-7613(1999)027<1127:scrhmf>2.3.co;2

Lavier, L. L., Buck, W. R., & Poliakov, A. N. B. (2000). Factors controlling normal fault offset in an ideal brittle layer. *Journal of Geophysical Research: Solid Earth*, *105*(B10), 23431–23442. doi: 10.1029/2000jb900108

Lecoeuvre, A., Ménez, B., Cannat, M., Chavagnac, V., & Gérard, E. (2021). Microbial ecology of the newly discovered serpentinite-hosted Old City hydrothermal field (southwest Indian ridge). *The ISME Journal*, *15*(3), 818–832. doi: 10.1038/s41396-020-00816-7

Liao, S., Tao, C., Dias, A. A., Liu, J., Su, X., Lv, S., ... Yang, X. (2024). Sediment geochemistry reveals abundant off-axis hydrothermal fields on the ultraslow-spreading Southwest Indian Ridge. *Earth and Planetary Science Letters*, *643*, 118916. doi: 10.1016/j.epsl.2024.118916

Lin, J., & Phipps Morgan, J. (1992). The spreading rate dependence of three-dimensional mid-ocean ridge gravity structure. *Geophysical Research Letters*, *19*(1), 13–16. doi: 10.1029/91gl03041

Lister, C. R. B. (1974). On the Penetration of Water into Hot Rock. *Geophysical Journal International*, *39*(3), 465-509. doi: 10.1111/j.1365-246X.1974.tb05468.x

Liu, C., Li, J., Tao, C., Fan, Q., Song, J., Luo, Y., & Feng, B. (2020). Variations in faulting style of the Southwest Indian Ridge (46°–53.5°E): Implications for crustal accretion process at ultraslow-spreading ridges. *Tectonophysics*, *790*, 228552. doi: 10.1016/j.tecto.2020.228552

Liu, Z., & Buck, W. R. (2020). Global Trends of Axial Relief and Faulting at Plate Spreading

Centers Imply Discrete Magmatic Events. *Journal of Geophysical Research: Solid Earth*, *125*(8), e2020JB019465. doi: 10.1029/2020jb019465

Lowell, R. P. (2017). A fault-driven circulation model for the Lost City Hydrothermal Field. *Geophysical Research Letters*, *44*(6), 2703–2709. doi: 10.1002/2016gl072326

Lowell, R. P., Farough, A., Hoover, J., & Cummings, K. (2013). Characteristics of magma-driven hydrothermal systems at oceanic spreading centers. *Geochemistry, Geophysics, Geosystems*, *14*(6), 1756–1770. doi: 10.1002/ggge.20109

Lowell, R. P., & Rona, P. A. (2002). Seafloor hydrothermal systems driven by the serpentinization of peridotite. *Geophysical Research Letters*, *29*(11), 26–1-26-4. doi: 10.1029/2001gl014411

Lowell, R. P., & Yao, Y. (2002). Anhydrite precipitation and the extent of hydrothermal recharge zones at ocean ridge crests. *Journal of Geophysical Research: Solid Earth*, *107*(B9), EPM 2–1-EPM 2-9. doi: 10.1029/2001jb001289

Macdonald, K. C., Fox, P. J., Alexander, R. T., Pockalny, R., & Gente, P. (1996). Volcanic growth faults and the origin of Pacific abyssal hills. *Nature*, *380*(6570), 125–129. doi: 10.1038/380125a0

Mackwell, S. J., Zimmerman, M. E., & Kohlstedt, D. L. (1998). High-temperature deformation of dry diabase with application to tectonics on Venus. *Journal of Geophysical Research: Solid Earth*, *103*(B1), 975–984. doi: 10.1029/97jb02671

MacLeod, C., Searle, R., Murton, B., Casey, J., Mallows, C., Unsworth, S., ... Harris, M. (2009). Life cycle of oceanic core complexes. *Earth and Planetary Science Letters*, *287*(3), 333–344. doi: 10.1016/j.epsl.2009.08.016

Mahato, S., & Cannat, M. (2025). Footwall Geology and Deformation at Flip-Flop Mid-Ocean Ridge Detachment Faults: 64°35'E Southwest Indian Ridge (SWIR). *Geochemistry, Geophysics, Geosystems*, *26*(1), e2024GC011769. doi: 10.1029/2024GC011769

Mallows, C., & Searle, R. C. (2012). A geophysical study of oceanic core complexes and surrounding terrain, Mid-Atlantic Ridge 13°N–14°N. *Geochemistry, Geophysics, Geosystems*, *13*(6). doi: 10.1029/2012GC004075

Malvoisin, B., Brunet, F., Carlut, J., Rouméjon, S., & Cannat, M. (2012). Serpentinization of oceanic peridotites: 2. Kinetics and processes of San Carlos olivine hydrothermal alteration. *Journal of Geophysical Research: Solid Earth*, *117*(B4). doi: 10.1029/2011JB008612

Marjanović, M., Barreyre, T., Fontaine, F. J., & Escartín, J. (2019). Investigating Fine-Scale Permeability Structure and Its Control on Hydrothermal Activity Along a Fast-Spreading Ridge (the East Pacific Rise, 9°43'–53'N) Using Seismic Velocity, Poroelastic Response, and Numerical Modeling. *Geophysical Research Letters*, *46*(21), 11799–11810. doi: 10.1029/2019GL084040

Marjanović, M., Carbotte, S. M., Carton, H., Nedimović, M. R., Mutter, J. C., & Canales, J. P. (2014). A multi-sill magma plumbing system beneath the axis of the East Pacific Rise. *Nature Geoscience*, *7*(11), 825–829. doi: 10.1038/ngeo2272

Marjanović, M., Carbotte, S. M., Carton, H. D., Nedimović, M. R., Canales, J. P., & Mutter, J. C. (2018). Crustal Magmatic System Beneath the East Pacific Rise (8°20' to 10°10'N): Implications for Tectonomagmatic Segmentation and Crustal Melt Transport at Fast-Spreading Ridges. *Geochemistry, Geophysics, Geosystems*, *19*(11), 4584–4611. doi: 10.1029/2018gc007590

Martin, A. J., Jamieson, J. W., Petersen, S., Fayek, M., & Escartin, J. (2024). Fluid Flow, Mineralization and Deformation in an Oceanic Detachment Fault: Microtextural, Geochemical and Isotopic Evidence From Pyrite at 13°30'N on the Mid-Atlantic Ridge. *Geochemistry, Geophysics, Geosystems*, *25*(1). doi: 10.1029/2023gc011033

Maury, M. F. (1860). *The physical geography of the sea.* Thomas Nelson and Sons, London.

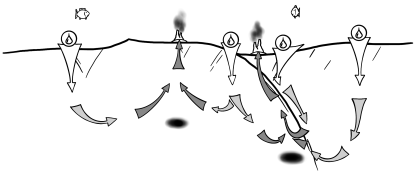

McCaig, A. M., Cliff, R. A., Escartín, J., Fallick, A. E., & MacLeod, C. J. (2007). Oceanic detachment faults focus very large volumes of black smoker fluids. *Geology*, *35*(10), 935–938. doi: 10.1130/g23657a.1

Meier, M., Schlindwein, V., Scholz, J.-R., Geils, J., Schmidt-Aursch, M. C., Krüger, F., ... Janik, T. (2021). Segment-Scale Seismicity of the Ultraslow Spreading Knipovich Ridge. *Geochemistry, Geophysics, Geosystems*, *22*(2), e2020GC009375. doi: 10.1029/2020gc009375

Mezri, L., García-Pintado, J., Pérez-Gussinyé, M., Liu, Z., Bach, W., & Cannat, M. (2024). Tectonic controls on melt production and crustal architecture during magma-poor seafloor spreading. *Earth and Planetary Science Letters*, *628*, 118569. doi: 10.1016/j.epsl.2024.118569

Mezri, L., Pourhiet, L. L., Wolf, S., & Burov, E. (2015). New parametric implementation of metamorphic reactions limited by water content, impact on exhumation along detachment faults. *Lithos*, *236-237*, 287–298. doi: 10.1016/j.lithos.2015.08.021

Michael, J., Langmuir, C. H., Dick, H. J. B., Snow, J. E., Goldstein, S. L., Graham, D. W., ... Edmonds, H. N. (2003). Magmatic and amagmatic seafloor generation at the ultraslow-spreading Gakkel ridge, Arctic Ocean. *Nature*, *423*(6943), 956–961. doi: 10.1038/nature01704

Momoh, E., Cannat, M., & Leroy, S. (2020). Internal Structure of the Oceanic Lithosphere at a Melt-Starved Ultraslow-Spreading Mid-Ocean Ridge: Insights From 2-D Seismic Data. *Geochemistry, Geophysics, Geosystems*, *21*(2), e2019GC008540. doi: 10.1029/2019gc008540

Momoh, E., Cannat, M., Watremez, L., Leroy, S., & Singh, S. C. (2017). Quasi-3-D Seismic Reflection Imaging and Wide-Angle Velocity Structure of Nearly Amagmatic Oceanic Lithosphere at the Ultraslow-Spreading Southwest Indian Ridge. *Journal of Geophysical Research: Solid Earth*, *122*(12), 9511–9533. doi: 10.1002/2017jb014754

Moresi, L., Dufour, F., & Mühlhaus, H.-B. (2003). A Lagrangian integration point finite element method for large deformation modeling of viscoelastic geomaterials. *Journal of Computational Physics*, *184*(2), 476–497. doi: 10.1016/s0021-9991(02)00031-1

Mottl, M. J. (2003). Partitioning of energy and mass fluxes between mid-ocean ridge axes and flanks at high and low temperature. In P.E.Halbach, V. Tunnicliffe, & J. Hein (Eds.), *Energy and mass transfer in marine hydrothermal systems* (pp. 271–286). Berlin: Dahlem University Press.

Murton, B., MacLeod, C. J., Lusty, P., Jamieson, J., Lichtschlag, A., Yeo, I., ... Figueroa, A. (2022). *Expedition JC224 Project ULTRA Cruise #1.* National Oceanography Center, Southampton. (Cruise Report)

National Information Standards Organization. (2022). *CRediT, Contributor Roles Taxonomy.* doi: 10.3789/ansi.niso.z39.104-2022

Ocean Networks Canada. (n.d.). University of Victoria. Retrieved 2025-01-22, from `https://www.oceannetworks.ca`

Ocean Observatories Initiative Regional Cabled Array. (n.d.). National Science Foundation & University of Washington. Retrieved 2025-01-22, from `https://interactiveoceans.washington.edu/about/regional-cabled-array/`

Olive, J.-A. (2023). Chapter 20 - Mid-Ocean Ridges: Geodynamics Written in the Seafloor. In J. C. Duarte (Ed.), *Dynamics of Plate Tectonics and Mantle Convection* (pp. 483–510). Elsevier. doi: 10.1016/b978-0-323-85733-8.00018-4

Olive, J.-A., Behn, M. D., & Tucholke, B. E. (2010). The structure of oceanic core complexes controlled by the depth distribution of magma emplacement. *Nature Geoscience*, *3*(7), 491–495. doi: 10.1038/ngeo888

Olive, J.-A., & Dublanchet, P. (2020). Controls on the magmatic fraction of extension at

mid-ocean ridges. *Earth and Planetary Science Letters*, *549*, 116541. doi: 10.1016/j.epsl.2020.116541

Olive, J.-A., & Escartín, J. (2016). Dependence of seismic coupling on normal fault style along the Northern Mid-Atlantic Ridge. *Geochemistry, Geophysics, Geosystems*, *17*(10), 4128–4152. doi: 10.1002/2016GC006460

Osako, M., Yoneda, A., & Ito, E. (2010). Thermal diffusivity, thermal conductivity and heat capacity of serpentine (antigorite) under high pressure. *Physics of the Earth and Planetary Interiors*, *183*(1), 229–233. doi: 10.1016/j.pepi.2010.07.005

Paquet, M., Cannat, M., Brunelli, D., Hamelin, C., & Humler, E. (2016). Effect of melt/mantle interactions on MORB chemistry at the easternmost Southwest Indian Ridge (61°–67°E). *Geochemistry, Geophysics, Geosystems*, *17*(11), 4605-4640. doi: 10.1002/2016GC006385

Parnell-Turner, R., Sohn, R., Peirce, C., Reston, T., MacLeod, C., Searle, R., & Simão, N. (2020). Seismicity trends and detachment fault structure at 13°N, Mid-Atlantic Ridge. *Geology*, *49*(3), 320–324. doi: 10.1130/g48420.1

Patterson, S. N., Lynn, K. J., Prigent, C., & Warren, J. M. (2021). High temperature hydrothermal alteration and amphibole formation in Gakkel Ridge abyssal peridotites. *Lithos*, *392-393*, 106107. doi: 10.1016/j.lithos.2021.106107

Pedersen, R. B., Rapp, H. T., Thorseth, I. H., Lilley, M. D., Barriga, F. J. A. S., Baumberger, T., ... Jorgensen, S. L. (2010). Discovery of a black smoker vent field and vent fauna at the Arctic Mid-Ocean Ridge. *Nature Communications*, *1*(1), 126. doi: 10.1038/ncomms1124

Peirce, C., Funnell, M. J., Reston, T. J., & MacLeod, C. J. (2023). Three-dimensional S-wave velocity structure of oceanic core complexes at 13°N on the Mid-Atlantic Ridge. *Geophysical Journal International*, *232*(1), 615–642. doi: 10.1093/gji/ggac350

Peirce, C., Reveley, G., Robinson, A. H., Funnell, M. J., Searle, R. C., Simão, N. M., ... Reston, T. J. (2019). Constraints on crustal structure of adjacent OCCs and segment boundaries at 13°N on the Mid-Atlantic Ridge. *Geophysical Journal International*, *217*(2), 988–1010. doi: 10.1093/gji/ggz074

Peirce, C., Robinson, A. H., Funnell, M. J., Searle, R. C., MacLeod, C. J., & Reston, T. J. (2020). Magmatism versus serpentinization—crustal structure along the 13°N segment at the Mid-Atlantic Ridge. *Geophysical Journal International*, *221*(2), 981–1001. doi: 10.1093/gji/ggaa052

Penrose. (1972). Penrose field conference on ophiolites. *Geotimes*, *17*(12), 24–25.

Pertsev, A. N., Bortnikov, N. S., Vlasov, E. A., Beltenev, V. E., Dobretsova, I. G., & Ageeva, O. A. (2012). Recent massive sulfide deposits of the Semenov ore district, Mid-Atlantic Ridge, 13°31' N: Associated rocks of the oceanic core complex and their hydrothermal alteration. *Geology of Ore Deposits*, *54*(5), 334–346. doi: 10.1134/s1075701512050030

Petersen, S., Kuhn, K., Kuhn, T., Augustin, N., Hékinian, R., Franz, L., & Borowski, C. (2009). The geological setting of the ultramafic-hosted Logatchev hydrothermal field (14°45'N, Mid-Atlantic Ridge) and its influence on massive sulfide formation. *Lithos*, *112*(1), 40–56. doi: 10.1016/j.lithos.2009.02.008

Phipps Morgan, J., & Chen, Y. J. (1993). Dependence of ridge-axis morphology on magma supply and spreading rate. *Nature*, *364*(6439), 706–708. doi: 10.1038/364706a0

Phipps Morgan, J., Parmentier, E. M., & Lin, J. (1987). Mechanisms for the origin of mid-ocean ridge axial topography: Implications for the thermal and mechanical structure of accreting plate boundaries. *Journal of Geophysical Research: Solid Earth*, *92*(B12), 12823–12836. doi: 10.1029/JB092iB12p12823

Picazo, S., Cannat, M., Delacour, A., Escartín, J., Rouméjon, S., & Silantyev, S. (2012). Deformation associated with the denudation of mantle-derived rocks at the Mid-Atlantic

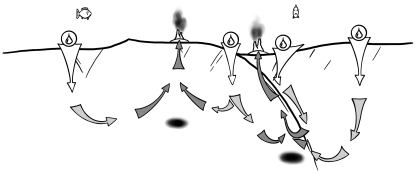

Ridge 13°–15°N: The role of magmatic injections and hydrothermal alteration. *Geochemistry, Geophysics, Geosystems*, *13*(9). doi: 10.1029/2012GC004121

Popov, A., & Kaus, B. (2024). *LaMEM - Lithosphere and Mantle Evolution Model.* Retrieved 2025-01-22, from `https://github.com/UniMainzGeo/LaMEM`

Preiner, M., Igarashi, K., Muchowska, K. B., Yu, M., Varma, S. J., Kleinermanns, K., ... Martin, W. F. (2020). A hydrogen-dependent geochemical analogue of primordial carbon and energy metabolism. *Nature Ecology & Evolution*, *4*(4), 534–542. doi: 10.1038/s41559-020-1125-6

Pruis, M. J., & Johnson, H. P. (2002). Age dependent porosity of young upper oceanic crust: Insights from seafloor gravity studies of recent volcanic eruptions. *Geophysical Research Letters*, *29*(5), 20–1-20-4. doi: 10.1029/2001gl013977

Rabbel, O., Hasenclever, J., Galerne, C. Y., Galland, O., Mair, K., & Palma, O. (2023). Impact of permeability evolution in igneous sills on hydrothermal flow and hydrocarbon transport in volcanic sedimentary basins. *Solid Earth*, *14*(6), 625–646. doi: 10.5194/se-14-625-2023

Reston, T. J. (2018). Flipping detachments: The kinematics of ultraslow spreading ridges. *Earth and Planetary Science Letters*, *503*, 144–157. doi: 10.1016/j.epsl.2018.09.032

Reston, T. J., & McDermott, K. G. (2011). Successive detachment faults and mantle unroofing at magma-poor rifted margins. *Geology*, *39*(11), 1071–1074. doi: 10.1130/g32428.1

Ruh, J. B., Tokle, L., & Behr, W. M. (2022). Grain-size-evolution controls on lithospheric weakening during continental rifting. *Nature Geoscience*, *15*(7), 585–590. doi: 10.1038/s41561-022-00964-9

Ryan, W. B. F., Carbotte, S. M., Coplan, J. O., O'Hara, S., Melkonian, A., Arko, R., ... Zemsky, R. (2009). Global Multi-Resolution Topography synthesis. *Geochemistry, Geophysics, Geosystems*, *10*(3), Q03014. Retrieved 2024-09-18, from `https://www.gmrt.org` (Database) doi: 10.1029/2008GC002332

Rüpke, L. H., & Hasenclever, J. (2017). Global rates of mantle serpentinization and H_2 production at oceanic transform faults in 3-D geodynamic models: Serpentinisation at transform faults. *Geophysical Research Letters*, *44*, 6726–6734. doi: 10.1002/2017gl072893

Sandiford, D., Brune, S., Glerum, A., Naliboff, J., & Whittaker, J. M. (2021). Kinematics of Footwall Exhumation at Oceanic Detachment faults: Solid-Block Rotation and Apparent Unbending. *Geochemistry, Geophysics, Geosystems*, *22*(4), e2021GC009681. doi: 10.1029/2021gc009681

Sauter, D., Cannat, M., Rouméjon, S., Andreani, M., Birot, D., Bronner, A., ... Searle, R. (2013). Continuous exhumation of mantle-derived rocks at the Southwest Indian Ridge for 11 million years. *Nature Geoscience*, *6*(4), 314–320. doi: 10.1038/ngeo1771

Schierjott, J. C., Ito, G., Behn, M. D., Tian, X., Morrow, T., Kaus, B. J. P., & Escartín, J. (2023). How transform fault shear influences where detachment faults form near mid-ocean ridges. *Scientific Reports*, *13*(1), 9259. doi: 10.1038/s41598-023-35714-3

Schouten, H., Smith, D. K., Cann, J. R., & Escartín, J. (2010). Tectonic versus magmatic extension in the presence of core complexes at slow-spreading ridges from a visualization of faulted seafloor topography. *Geology*, *38*(7), 615–618. doi: 10.1130/g30803.1

Schroeder, T., & John, B. E. (2004). Strain localization on an oceanic detachment fault system, Atlantis Massif, 30°N, Mid-Atlantic Ridge. *Geochemistry, Geophysics, Geosystems*, *5*(11). doi: 10.1029/2004GC000728

Seabed 2030. (n.d.). The Nippon Foundation-GEBCO. Retrieved 2025-01-22, from `https://seabed2030.org`

Searle, R. C. (2013). *Mid-Ocean Ridges.* Cambridge University Press. doi: 10.1017/cbo9781139084260

Searle, R. C., MacLeod, C. J., Peirce, C., & Reston, T. J. (2019). The Mid-Atlantic Ridge

Near 13°20'N: High-Resolution Magnetic and Bathymetry Imaging. *Geochemistry, Geophysics, Geosystems*, *20*(1), 295-313. doi: 10.1029/2018GC007940

Seton, M., Müller, R. D., Zahirovic, S., Williams, S., Wright, N. M., Cannon, J., ... McGirr, R. (2020). A Global Data Set of Present-Day Oceanic Crustal Age and Seafloor Spreading Parameters. *Geochemistry, Geophysics, Geosystems*, *21*(10). doi: 10.1029/2020gc009214

Shah, A. K., & Buck, W. (2003). Plate bending stresses at axial highs, and implications for faulting behavior. *Earth and Planetary Science Letters*, *211*(3), 343–356. doi: 10.1016/S0012-821X(03)00187-0

Shaw, P. R., & Lin, J. (1993). Causes and consequences of variations in faulting style at the Mid-Atlantic Ridge. *Journal of Geophysical Research: Solid Earth*, *98*(B12), 21839–21851. doi: 10.1029/93jb01565

Shea, K., Metaxas, A., Young, C. R., & Fisher, C. R. (2008). Processes and Interactions in Macrofaunal Assemblages at Hydrothermal Vents: A Modeling Perspective. In R. Lowell, J. Seewald, A. Metaxas, Perfit, & M.R. (Eds.), *Magma to Microbe: Modeling Hydrothermal Processes at Ocean Spreading Centers* (pp. 259–274). American Geophysical Union (AGU). doi: 10.1029/178GM13

Shewchuk, J. R. (2002). Delaunay refinement algorithms for triangular mesh generation. *Computational Geometry*, *22*(1), 21-74. doi: 10.1016/S0925-7721(01)00047-5

Simão, N. M., Peirce, C., Funnell, M. J., Robinson, A. H., Searle, R. C., MacLeod, C. J., & Reston, T. J. (2020). 3-D P-wave velocity structure of oceanic core complexes at 13°N on the Mid-Atlantic Ridge. *Geophysical Journal International*, *221*(3), 1555–1579. doi: 10.1093/gji/ggaa093

Sinha, M. C., & Evans, R. L. (2004). Gephysical Constraints upon the Thermal Regime of the Ocean Crust. In C. R. German, J. Lin, & L. Parson (Eds.), *Mid-Ocean Ridges* (p. 19-62). American Geophysical Union (AGU). doi: 10.1029/148GM02

Smith, D. K., Cann, J. R., & Escartín, J. (2006). Widespread active detachment faulting and core complex formation near 13° N on the Mid-Atlantic Ridge. *Nature*, *442*(7101), 440–443. doi: 10.1038/nature04950

Smith, D. K., Escartín, J., Schouten, H., & Cann, J. R. (2008). Fault rotation and core complex formation: Significant processes in seafloor formation at slow-spreading mid-ocean ridges (Mid-Atlantic Ridge, 13°–15°N). *Geochemistry, Geophysics, Geosystems*, *9*(3). doi: 10.1029/2007GC001699

Sohn, R., Parnell-Turner, R., Peirce, C., Reston, T., MacLeod, C., & Searle, R. (2020). Microearthquake hypocenter catalog from the detachment faulting system at 13°N, Mid-Atlantic Ridge, obtained using data collected in January 2016. *Interdisciplinary Earth Data Alliance*. (Dataset) doi: 10.26022/IEDA/329824

Speciale, P. A., Behr, W. M., Hirth, G., & Tokle, L. (2020). Rates of Olivine Grain Growth During Dynamic Recrystallization and Postdeformation Annealing. *Journal of Geophysical Research: Solid Earth*, *125*(11), e2020JB020415. doi: 10.1029/2020jb020415

Spiegelman, M., May, D. A., & Wilson, C. R. (2016). On the solvability of incompressible Stokes with viscoplastic rheologies in geodynamics. *Geochemistry, Geophysics, Geosystems*, *17*(6), 2213–2238. doi: 10.1002/2015GC006228

Spiess, F. N., Macdonald, K. C., Atwater, T., Ballard, R., Carranza, A., Cordoba, D., ... Rangin, C. (1980). East Pacific Rise: Hot Springs and Geophysical Experiments. *Science*, *207*(4438), 1421–1433. doi: 10.1126/science.207.4438.1421

Tao, C., Seyfried, W. E., Lowell, R. P., Liu, Y., Liang, J., Guo, Z., ... Li, W. (2020). Deep high-temperature hydrothermal circulation in a detachment faulting system on the ultra-slow spreading ridge. *Nature Communications*, *11*(1), 1300. doi: 10.1038/s41467-020-15062-w

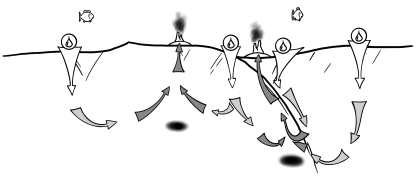

Tao, C., Wu, T., Liu, C., Li, H., & Zhang, J. (2017). Fault inference and boundary recognition based on near-bottom magnetic data in the Longqi hydrothermal field. *Marine Geophysical Research*, *38*(1), 17–25. doi: 10.1007/s11001-016-9283-2

Tapponnier, P., & Francheteau, J. (1978). Necking of the lithosphere and the mechanics of slowly accreting plate boundaries. *Journal of Geophysical Research: Solid Earth*, *83*(B8), 3955–3970. doi: 10.1029/JB083iB08p03955

Theissen-Krah, S., Iyer, K., Rüpke, L. H., & Phipps Morgan, J. (2011). Coupled mechanical and hydrothermal modeling of crustal accretion at intermediate to fast spreading ridges. *Earth and Planetary Science Letters*, *311*(3), 275–286. doi: 10.1016/j.epsl.2011.09.018

Theissen-Krah, S., Rüpke, L. H., & Hasenclever, J. (2016). Modes of crustal accretion and their implications for hydrothermal circulation. *Geophysical Research Letters*, *43*(3), 1124–1131. doi: 10.1002/2015gl067335

Tivey, M. A., & Johnson, H. P. (2002). Crustal magnetization reveals subsurface structure of Juan de Fuca Ridge hydrothermal vent fields. *Geology*, *30*(11), 979–982. doi: 10.1130/0091-7613(2002)030<0979:cmrsso>2.0.co;2

Tucholke, B. E., Behn, M. D., Buck, W. R., & Lin, J. (2008). Role of melt supply in oceanic detachment faulting and formation of megamullions. *Geology*, *36*(6), 455–458. doi: 10.1130/g24639a.1

Vehling, F., Hasenclever, J., & Rüpke, L. (2022). New insights from thermohaline multiphase simulations into the mechanisms controlling vent fluid salinity following a diking event at fast-spreading ridges. *Earth and Planetary Science Letters*, *597*, 117802. doi: 10.1016/j.epsl.2022.117802

Verlaguet, A., Bonnemains, D., Mével, C., Escartín, J., Andreani, M., Bourdelle, F., ... Chavagnac, V. (2021). Fluid Circulation Along an Oceanic Detachment Fault: Insights From Fluid Inclusions in Silicified Brecciated Fault Rocks (Mid-Atlantic Ridge at 13°20'N). *Geochemistry, Geophysics, Geosystems*, *22*(1), e2020GC009235. doi: 10.1029/2020gc009235

Vieira Duarte, J. F., Kaczmarek, M.-A., Vonlanthen, P., Putlitz, B., & Müntener, O. (2020). Hydration of a Mantle Shear Zone Beyond Serpentine Stability: A Possible Link to Microseismicity Along Ultraslow Spreading Ridges? *Journal of Geophysical Research: Solid Earth*, *125*(10). doi: 10.1029/2020jb019509

Villeneuve, M. C., & Heap, M. J. (2021). Calculating the cohesion and internal friction angle of volcanic rocks and rock masses. *Volcanica*, *4*(2), 279–293. doi: 10.30909/vol.04.02.279293

Walker, R. J., Holdsworth, R. E., Armitage, P. J., & Faulkner, D. R. (2013). Fault zone permeability structure evolution in basalts. *Geology*, *41*(1), 59–62. doi: 10.1130/g33508.1

White, R. S., McKenzie, D., & O'Nions, R. K. (1992). Oceanic crustal thickness from seismic measurements and rare earth element inversions. *Journal of Geophysical Research: Solid Earth*, *97*(B13), 19683–19715. doi: 10.1029/92JB01749

Zhao, M., Qiu, X., Li, J., Sauter, D., Ruan, A., Chen, J., ... Niu, X. (2013). Three-dimensional seismic structure of the Dragon Flag oceanic core complex at the ultraslow spreading Southwest Indian Ridge (49°39'E). *Geochemistry, Geophysics, Geosystems*, *14*(10), 4544–4563. doi: 10.1002/ggge.20264

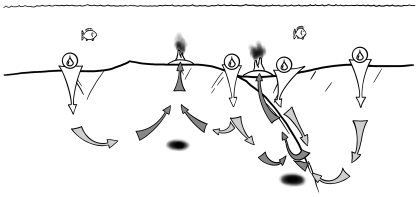

Eidesstattliche Versicherung | Declaration on Oath

I hereby declare and affirm that this doctoral dissertation is my own work and that I have not used any aids and sources other than those indicated.

If electronic resources based on generative artificial intelligence (gAI) were used in the course of writing this dissertation, I confirm that my own work was the main and value-adding contribution and that complete documentation of all resources used is available in accordance with good scientific practice. I am responsible for any erroneous or distorted content, incorrect references, violations of data protection and copyright law or plagiarism that may have been generated by the gAI.

Hamburg, 28.07.2025

Ort, den | City, date

Unterschrift | Signature